Size effects in crystal plasticity

Borg, Ulrik

Publication date:
2007

Document Version
Publisher's PDF, also known as Version of record

Size effects in crystal plasticity

by

Ulrik Borg

DEPT. OF MECHANICAL ENGINEERING
Solid Mechanics

TECHNICAL UNIVERSITY OF DENMARK

Preface

This thesis is submitted in partial fulfillment of the requirements for obtaining the degree of PhD in mechanical engineering. The work was carried out at the Department of Mechanical Engineering, Solid Mechanics, Technical University of Denmark in the period January 2004 - January 2007, with Professor Dr.techn. Viggo Tvergaard and Associate Professor PhD Christian F. Niordson as supervisors. The PhD study was financially supported by The Technical University of Denmark and by the Danish Technical Research Council in a project entitled Modeling Plasticity at the Micron Scale.

I am very grateful to my two supervisors for their friendly inspiration and many valuable discussions during the project.

Part of this work was carried out during a 4 months stay at Cambridge University, UK from August 2005 to December 2005 with Professor Norman A. Fleck as host. I am very grateful to Professor Fleck for making this stay possible, and for his inspiring supervision.

I wish to thank my wife, Louise, for her outstanding support and understanding during this study. I am also very grateful to our daughter, Thea, whose happy smiles always gave me renewed energy.

Finally, I would like to thank my colleagues and fellow PhD students at the Department of Mechanical Engineering, Solid Mechanics for creating a friendly and inspiring environment.

Kgs. Lyngby, 15 January 2007

Ulrik Borg

Abstrakt (in Danish)
Størrelseseffekter i krystalplasticitet

Denne afhandling omhandler numeriske analyser af størrelseseffekter for en række problemer. En tøjningsgradient krystalplastisk teori er udviklet og anvendt til analyserne. Teorien benytter højere ordens spændinger som arbejdskonjugerede til gradienten af de krystallografiske slip og kræver højere ordens randbetingelser. De analyserede problemer omfatter lokalisering af plasticitet i et enkeltkrystal, korngrænseeffekter i et bikrystal og kornstørrelseseffekter i et polykrystal. Mikroskopiske huller i enkeltkrystaller er også analyseret under forskellige belastningssituationer. Disse analyser fokuserer på spændings- og deformationsfelterne omkring hullerne, på hulvækst og interaktion med omkringliggende huller samt på en sammenligning mellem den udviklede gradient krystalplastiske model og en model baseret på en diskret modellering af dislokationer. Desuden er huller og inklusioner i et isotrop materiale analyseret med en isotrop tøjningsgradient teori.

Abstract
Size effects in crystal plasticity

Numerical analyses of plasticity size effects have been carried out for different problems using a developed strain gradient crystal plasticiy theory. The theory employs higher order stresses as work conjugates to slip gradients and uses higher order boundary conditions. Problems on localization of plastic flow in a single crystal, grain boundary effects in a bicrystal, and grain size effects in a polycrystal are studied. Single crystals containing micro-scale voids have also been analyzed at different loading conditions with focus on the stress and deformation fields around the voids, on void growth and interaction between neighboring voids, and on a comparison between the developed strain gradient crystal plasticity theory and a discrete dislocation plasticity theory. Furthermore, voids and rigid inclusions in isotropic materials have been studied using a strain gradient plasticity theory for isotropic solids.

Publications

The following publications are part of the thesis:

[P1] Borg, U., Niordson, C.F., Fleck, N.A. and Tvergaard, V., 2006. A viscoplastic strain gradient analysis of materials with voids or inclusions. *International Journal of Solids and Structures* **43**, 4906-4916.

[P2] Borg, U., 2007. Strain gradient crystal plasticity effects on flow localization. *International Journal of Plasticity, to appear.*

[P3] Borg, U. and Fleck, N.A., 2007. Strain gradient effects in surface roughening. *Modelling and Simulation in Materials Science and Engineering* **15**, 1-12.

[P4] Borg, U., 2007. A strain gradient crystal plasticity analysis of grain size effects in polycrystals. *European Journal of Mechanics, A/solids* **26**, 313-324.

[P5] Borg, U. and Kysar, J.W., 2007. Strain gradient crystal plasticity analysis of a single crystal containing a cylindrical void. *International Journal of Solids and Structures, to appear.*

[P6] Borg, U., Niordson, C.F. and Kysar, J.W., 2007. Size effects on void growth in single crystals with distributed voids. *submitted*

[P7] Hussein, M.I., Borg, U., Niordson, C.F. and Deshpande, V.S., 2006. Plasticity size effects in voided crystals. *submitted*

Contents

Chapter 1
Introduction

Within recent years a significant amount of work has been performed on the observation and prediction of size effects in metal plasticity. Several small scale experiments for plastic deformation of metals have shown significant size effects. The measured indentation hardness of metals has been observed to increase with decreasing width of the indenter when the diameter of the indenter is in the micron range (Stelmashenko et al., 1993; Ma and Clarke, 1995; Nix and Gao, 1998). Fleck et al. (1994) observed that the scaled shear strength of polycrystalline copper wires during torsion increases by almost a factor of three when the wire diameter is decreased from 170 μm to 12 μm, whereas the uniaxial tensile behavior of the wires show no significant size effect. Stölken and Evans (1998) observed an increased bending resistance of Nickel foils as the foil thickness is decreased from 50 μm to 12.5 μm. Furthermore, the Hall-Petch relation describing the increase in yield stress for decreasing grain sizes was determined experimentally by Hall (1951) and Petch (1953).

The plastic deformation of metals can be modeled at various length scales. A phenomenological continuum plasticity theory for isotropic materials is applicable for polycrystals containing a large number of grains (single crystals). In a crystal continuum plasticity theory each grain is modeled in a discrete manner, such that a single crystal or a polycrystal with a limited number of grains can be modeled. On the microscopic scale the material behavior can be modeled with the so-called discrete dislocation plasticity theory (Van der Giessen and Needleman, 1995) where the dislocations are treated as continuum entities moving in fields determined by elasticity. Finally, on the nano scale the material behavior can be modeled with direct atomistic simulations which typically can consider hundreds of thousands of atoms, corresponding to a block of material having characteristic dimensions of approximately 0.1 μm. The focus in this thesis is on the continuum plasticity theories.

Classical phenomenological continuum theories and crystal plasticity theories have no characteristic length scale included and therefore exhibit no size dependence. Such plasticity theories are called local, because the stress in a material point only depends on variables in the same point. A theoretical argument for the observed size effects can be found in Nye (1953) and Ashby (1970) who argue that plastic strain gradients induce geometrically necessary dislocations and the interaction of these dislocations with statistically stored dislocations leads to a size effect on the micron scale. The statistically stored dislocations are the randomly trapped dislocations in a uniform strain field, whereas the geometrically necessary dislocations can be thought of as a density measure of net Burgers vector.

A variety of different nonlocal plasticity formulations incorporating work done by plastic strain gradients have been suggested over the last two decades to capture the ex-

perimentally observed size effects. One of the early strain gradient theories was that proposed by Aifantis (1984) where the yield stress depends on gradients of the plastic strain. In the models presented by Acharya and Bassani (2000) and Bassani (2001) the strain gradient effects enter the expression for the tangent modulus only. Thus, this relatively simple gradient theory does not include higher order stresses and boundary conditions, and is therefore referred to as a lower order theory.

In the strain gradient theories of Fleck and Hutchinson (1993, 1997, 2001) the principle of virtual work contains a higher order stress quantity work conjugate to strain gradients. A finite strain generalization of the theory by Fleck and Hutchinson (2001) has been presented by Niordson and Redanz (2004). Also, a modified version by Fleck and Willis (2004) of the theory by Fleck and Hutchinson (2001) has been enhanced with an interfacial potential that penalizes plastic strain at interfaces by Aifantis and Willis (2005). A rate-dependent crystal plasticity formulation as an extension to the theory of Fleck and Hutchinson (1997) has been presented by Shu and Fleck (1999), and later been generalized to finite strains by Shu and Barlow (2000).

In the gradient theory of single crystal viscoplasticity by Gurtin (2000, 2002) a microstress is work conjugate to the slip rate and a gradient microstress is work conjugate to the slip rate gradients. The material length scale is incorporated through the free energy, which is assumed to scale with the net Burgers vector. A gradient theory for isotropic materials following the treatment of single crystal plasticity is given in Gurtin (2003). An equivalent isotropic strain gradient formulation has been presented by Gudmundson (2004).

Other nonlocal theories are the gradient dependent back stress formulations by Groma (1997), Groma et al. (2003), Evers et al. (2004) and Kuroda and Tvergaard (2006), and the so-called 'mechanism-based strain gradient theory' of Gao et al. (1999) and its crystal plasticity counterpart by Han et al. (2005).

Predictions of the nonlocal crystal plasticity theory by Gurtin (2002) have been compared with the behavior obtained from a discrete dislocation plasticity theory by Bittencourt et al. (2003). Also, predictions of the theory by Shu and Fleck (1999) have been compared with results obtained using discrete dislocation plasticity theory by Shu et al. (2001).

The strain gradient plasticity formulations used for the results presented in the present thesis are described in detail in chapter 2. Chapter 3 serves as a summary of the results presented in the seven papers written during the authors PhD study, which are included at the end of the thesis. Subsequently these papers are denoted by [P1]-[P7].

The first paper, 'A viscoplastic strain gradient analysis of materials with voids or inclusions', [P1], is coauthored with Christian F. Niordson, Norman A. Fleck and Viggo Tvergaard. The paper presents a finite strain rate-dependent strain gradient plasticity formulation for isotropic materials. The model is applied to study metals containing either voids or rigid inclusions.

In 'Strain gradient crystal plasticity effects on flow localization', [P2], a rate-dependent strain gradient crystal plasticity formulation for finite strains is presented. It uses the basic formulation of the nonlocal theory by Gurtin (2000, 2002) and the constitutive framework

of Fleck and Hutchinson (2001). Localization in shear bands within single crystals is studied as an application of the model.

The paper 'Strain gradient effects in surface roughening', [P3], is coauthored with Norman A. Fleck and studies the evolution of surface profile near grain boundaries during plastic deformation. Both experimental and numerical results are presented. In the numerical simulation a bicrystal is considered and a grain boundary potential is introduced.

The grain boundary potential is also employed in the paper 'A strain gradient crystal plasticity analysis of grain size effects in polycrystals', [P4], to simulate different higher order boundary conditions at the grain boundaries in a polycrystal with hexagonal grains of varying size.

The stress and deformation fields around a cylindrical void in a single crystal loaded by a far-field equibiaxial tensile stress are studied in the paper 'Strain gradient crystal plasticity analysis of a single crystal containing a cylindrical void', [P5], which is coauthored with Jeffrey W. Kysar.

The paper 'Size effects on void growth in single crystals with distributed voids', [P6], which is coauthored with Christian F. Niordson and Jeffrey W. Kysar, focuses on size effects in void growth and on the interaction between voids in a single crystal containing periodically arranged cylindrical voids subjected to different stress triaxialities.

Finally, the paper 'Plasticity size effects in voided crystals', [P7], which is coauthored with Mahmoud I. Hussein, Christian F. Niordson and Vikram S. Deshpande, compares predictions for a single crystal containing periodically arranged rectangular voids obtained with strain gradient crystal plasticity to predictions obtained with discrete dislocation plasticity.

Chapter 2
Strain gradient plasticity

This chapter gives a description of the strain gradient plasticity theories used for the numerical simulations presented in the present thesis. As mentioned in the introduction, different strain gradient plasticity theories have been presented by several authors. The basic idea behind the theories is that a plastic strain gradient leads to enhanced hardening due to the generation of geometrically necessary dislocations.

Section 2.1 describes a viscoplastic formulation of the strain gradient theory for isotropic materials by Fleck and Hutchinson (2001). In the strain gradient theory by Fleck and Hutchinson (1993, 1997) the work rate per unit volume depends on both the strain, ϵ_{ij}, and the spatial gradient of strain, $\epsilon_{ij,k}$, and a higher order stress emerges as the work conjugate to $\epsilon_{ij,k}$. In the reformulated strain gradient theory by Fleck and Hutchinson (2001) the displacement field, u_i, and the effective plastic strain, ϵ^P, are treated as independent kinematic quantities. The material work rate depends on the elastic strain, on the effective plastic strain and on the spatial gradient of the effective plastic strain, $\epsilon^P_{,i}$. Then, the higher order stress emerges as work conjugate to $\epsilon^P_{,i}$.

Section 2.2 presents a strain gradient crystal plasticity formulation. The basic formulation of the theory is equivalent to the formulation of Gurtin (2002), where the internal virtual power depends on the elastic strain, on the slip rate for each slip system and on the spatial gradient of the slip rate for each slip system. The theory by Gurtin (2002) is based on the fact that the free energy scales with the net Burgers vector and is assumed to depend on the elastic part of the strain tensor and on the density of geometrically necessary dislocations, which is related to the slip gradients through the relation by Nye (1953). Then, in Gurtin's model the constitutive equations are obtained from thermodynamical arguments. In the theory presented here, the constitutive equations are based on the strain gradient theory by Fleck and Hutchinson (2001) and differs significantly from the constitutive framework of Gurtin (2002).

In the following, repeated lower-case Latin indices imply summation over the range 1-3. A bold character denotes a vector or a tensor, and an ascent dot denotes the time derivative.

2.1 A viscoplastic version of Fleck and Hutchinson's theory of 2001

This section presents a viscoplastic formulation that allows for finite strains of the rate-independent strain gradient plasticity theory for isotropic materials presented by Fleck and Hutchinson (2001). The kinematical basis is based on the rate-independent finite strain generalization of the strain gradient theory by Niordson and Redanz (2004) formulated within an updated Lagrangian framework.

2.1.1 Material model

Let u_i denote the displacement vector and $\dot{u}_i$ the velocity field. With $L_{ij} = \dot{u}_{i,j}$ denoting the velocity gradient, the material spin, Ω_{ij}, is given by the skew symmetric part of the velocity gradient as

$$\Omega_{ij} = \frac{1}{2}\left(L_{ij} - L_{ji}\right) \tag{2.1}$$

The strain rate is defined as the symmetric part of the velocity gradient, and is decomposed into an elastic and plastic part as

$$\dot{\epsilon}_{ij} = \frac{1}{2}\left(L_{ij} + L_{ji}\right) = \dot{\epsilon}^E_{ij} + \dot{\epsilon}^P_{ij} \tag{2.2}$$

The direction of the plastic strain rate is given by $m_{ij} = \frac{3}{2}S_{ij}/\sigma_e$, where $S_{ij} = \sigma_{ij} - \frac{1}{3}\delta_{ij}\sigma_{kk}$ denotes the stress deviator and $\sigma_e = \sqrt{\frac{3}{2}S_{ij}S_{ij}}$ is Von Mises effective stress with σ_{ij} being the Cauchy stress tensor and δ_{ij} the Kronecker delta function. The plastic strain rate components can then be written as a product of its magnitude, $\dot{\epsilon}^P = \sqrt{\frac{2}{3}\dot{\epsilon}^P_{ij}\dot{\epsilon}^P_{ij}}$, and its direction

$$\dot{\epsilon}^P_{ij} = m_{ij}\dot{\epsilon}^P \tag{2.3}$$

A nonlocal measure of the effective plastic strain rate is defined on the basis of the conventional effective plastic strain rate and the gradient of the conventional effective plastic strain rate through the incremental relation

$$\dot{E}^{P^2} = \dot{\epsilon}^{P^2} + l_*^2\dot{\epsilon}^P_{,i}\dot{\epsilon}^P_{,i} \tag{2.4}$$

where l_* is a material length parameter introduced for dimensional consistency. The theory by Fleck and Hutchinson (2001) also exist in a version with three length scale parameters, but the present theory is only formulated using the single parameter version related to the theory by Aifantis (1984).

Following Fleck and Hutchinson (2001), assuming that the plastic strain gradients contribute to the internal work, the principle of virtual power in total form in the deformed configuration may be formulated as

$$\int_V \left(\sigma_{ij}\delta\dot{\epsilon}^E_{ij} + Q\delta\dot{\epsilon}^P + \tau_i\delta\dot{\epsilon}^P_{,i}\right)\mathrm{d}V = \int_S \left(T_i\delta\dot{u}_i + t\delta\dot{\epsilon}^P\right)\mathrm{d}S \tag{2.5}$$

Where Q is a generalized effective stress which is work-conjugate to the plastic strain rate magnitude, $\dot{\epsilon}^P$, and τ_i is a higher order stress which is work-conjugate to the gradient of the plastic strain rate magnitude, $\dot{\epsilon}^P_{,i}$. The current volume and surface are denoted V and S, respectively. The surface traction is denoted by T_i and t denotes the higher order surface traction. The formulation can also be written as

$$\int_V \left(\sigma_{ij}\delta\dot{\epsilon}_{ij} + \left(Q - \sigma_e\right)\delta\dot{\epsilon}^P + \tau_i\delta\dot{\epsilon}^P_{,i}\right)\mathrm{d}V = \int_S \left(T_i\delta\dot{u}_i + t\delta\dot{\epsilon}^P\right)\mathrm{d}S \tag{2.6}$$

The strong form of the field equations is found by requiring the principle of virtual power to hold for all admissible variations in $\dot{u}_i$ and $\dot{\epsilon}^P$. The classical force balance law and boundary conditions are obtained as

$$\sigma_{ij,j} = 0, \qquad T_i = \sigma_{ij} n_j \tag{2.7}$$

where n_i is the surface unit normal in the deformed configuration. In addition, the consistency condition and higher order boundary condition read as

$$Q - \sigma_e - \tau_{i,i} = 0, \qquad t = \tau_i n_i \tag{2.8}$$

To obtain an expression of the principle of virtual power in the reference configuration, Kirchhoff stress measures are now defined as (defining J as the determinant of the metric tensor)

$$\varsigma_{ij} = J\sigma_{ij}, \quad \sigma_e^{\varsigma} = J\sigma_e, \quad q = JQ, \quad \rho_i = J\tau_i \tag{2.9}$$

Introducing the Jaumann rate of the Kirchhoff stress, $\overset{\triangledown}{\varsigma}_{ij} = \dot{\varsigma}_{ij} - \varsigma_{kj}\Omega_{ik} - \varsigma_{ik}\Omega_{jk}$, and the convected rate of the higher order Kirchhoff stress, $\overset{\vee}{\rho}_i = \dot{\rho}_i - L_{ik}\rho_k$, the incremental version of the principle of virtual power, in an updated Lagrangian framework (where the deformed configuration is taken as a reference), can be expressed as (Niordson and Redanz, 2004)

$$\begin{aligned}&\int_{V_0} \left(\overset{\triangledown}{\varsigma}_{ij}\, \delta\dot{\epsilon}_{ij} - \sigma_{ij}\left(2\dot{\epsilon}_{ik}\delta\dot{\epsilon}_{kj} - L_{kj}\delta L_{ki}\right) + \left(\dot{q} - \dot{\sigma}_e^{\varsigma}\right)\delta\dot{\epsilon}^P + \overset{\vee}{\rho}_i\, \delta\dot{\epsilon}^P_{0,i} \right) \mathrm{d}V_0 \\ &= \int_{S_0} \left(\dot{T}_i^0 \delta\dot{u}_i + \dot{t}_0 \delta\dot{\epsilon}^P \right) \mathrm{d}S_0\end{aligned} \tag{2.10}$$

where subscript "0" refers to the reference configuration.

Now, to obtain a viscoplastic version of the theory, a viscoplastic potential is to be defined. In the rate-independent theory by Fleck and Hutchinson (2001) a plastic potential can be defined as

$$\Phi(E^P) = \int_0^{E^P} \sigma_c \left(E^{P\prime} \right) \mathrm{d}E^{P\prime} \tag{2.11}$$

where σ_c is an effective stress which is work-conjugate to the effective plastic strain, E^P. The function $\sigma_c(E^P)$ denotes the uniaxial tensile stress versus plastic strain curve of the material. In this rate-dependent version, a viscoplastic potential is defined as

$$\Phi(\dot{E}^P, E^P) = \int_0^{\dot{E}^P} \sigma_c \left(\dot{E}^{P\prime}, E^P \right) \mathrm{d}\dot{E}^{P\prime} \tag{2.12}$$

where the function $\sigma_c(\dot{E}^P, E^P)$ denotes the uniaxial tensile stress versus plastic strain rate curve, and σ_c is work-conjugate to the effective plastic strain rate, $\dot{E}^P$. Taking the variation of the potential by use of (2.4) gives

$$\delta\Phi = \sigma_c \delta\dot{E}^P = \sigma_c \left(\frac{\dot{\epsilon}^P}{\dot{E}^P}\delta\dot{\epsilon}^P + \frac{l_*^2 \dot{\epsilon}^P_{,i}}{\dot{E}^P}\delta\dot{\epsilon}^P_{,i} \right) = q\delta\dot{\epsilon}^P + \rho_i \delta\dot{\epsilon}^P_{,i} \tag{2.13}$$

with the generalized effective stress, q, and the higher order stress, ρ_i, defined by the constitutive equations

$$q = \frac{\sigma_c}{\dot{E}^P}\dot{\epsilon}^P \tag{2.14}$$

$$\rho_i = \frac{\sigma_c}{\dot{E}^P} l_*^2 \dot{\epsilon}^P_{,i} \tag{2.15}$$

By substituting these expressions into the definition of the effective plastic strain (2.4) it is seen that the effective stress is given as the following quadratic form in q and ρ_i

$$\sigma_c{}^2 = q^2 + l_*^{-2}\rho_i\rho_i \tag{2.16}$$

When excluding the material length scale by setting $l_* = 0$, the effective stress, σ_c, reduces to the Von Mises stress and the effective plastic strain rate, $\dot{E}^P$, equals the conventional effective plastic strain rate, $\dot{\epsilon}^P$.

The viscous material behavior is modeled by a power law for the effective plastic strain rate

$$\dot{E}^P = \dot{\epsilon}_0 \left(\frac{\sigma_c}{g(E^P)} \right)^{1/m} \tag{2.17}$$

Here, m is the strain rate hardening exponent and $\dot{\epsilon}_0$ is a reference strain rate. The hardening function, $g(E^P)$, is evaluated at E^P instead of ϵ^P as it would be in conventional J_2 flow theory. If the strain rate was prescribed such that $\dot{E}^P = \dot{\epsilon}_0$, the hardening function, $g(E^P)$, would be equal to the effective stress, σ_c.

The incremental elastic constitutive equation for the viscoplastic material can be written in the form

$$\overset{\triangledown}{\varsigma}_{ij}\,\Delta t = R_{ijkl}\left(\Delta\epsilon_{kl} - m_{kl}\Delta\epsilon^P\right) \tag{2.18}$$

where Δt is the time step and the elastic stiffness tensor is given by (ν denotes Poisson's ratio and E is Young's modulus)

$$R_{ijkl} = \frac{E}{1+\nu}\left(\frac{1}{2}\left(\delta_{ik}\delta_{jl} + \delta_{il}\delta_{jk}\right) + \frac{\nu}{1-2\nu}\delta_{ij}\delta_{kl}\right) \tag{2.19}$$

The increments of the effective stress and the higher order stress can be obtained from (2.14) and (2.15) using (2.17) and written on the form

$$\dot{q}\Delta t = \frac{\sigma_c}{\dot{E}^P}\left((m-1)\frac{\dot{\epsilon}^P}{\dot{E}^P}\Delta\dot{E}^P + \Delta\dot{\epsilon}^P\right) + \left(\frac{\dot{E}^P}{\dot{\epsilon}_0}\right)^m \frac{\mathrm{d}g}{\mathrm{d}E^P}\dot{\epsilon}^P\Delta t \tag{2.20}$$

$$\overset{\vee}{\rho}_i\,\Delta t = l_*^2\left(\frac{\sigma_c}{\dot{E}^P}\left((m-1)\frac{\dot{\epsilon}^P_{,i}}{\dot{E}^P}\Delta\dot{E}^P + \Delta\dot{\epsilon}^P_{,i}\right) + \left(\frac{\dot{E}^P}{\dot{\epsilon}_0}\right)^m \frac{\mathrm{d}g}{\mathrm{d}E^P}\dot{\epsilon}^P_{,i}\Delta t\right) \tag{2.21}$$

where the change in the effective plastic strain rate is taken as $\Delta\dot{E}^P = \frac{\dot{\epsilon}^P}{\dot{E}^P}\Delta\dot{\epsilon}^P + \frac{l_*^2\dot{\epsilon}^P_{,i}}{\dot{E}^P}\Delta\dot{\epsilon}^P_{,i}$. The values of $\dot{\epsilon}^P$ and $\dot{\epsilon}^P_{,i}$ are taken from the previous increment, such that only $\Delta\epsilon_{ij}$, $\Delta\dot{\epsilon}^P$ and $\Delta\dot{\epsilon}^P_{,i}$ are treated as unknowns.

2.1.2 Numerical formulation

The numerical solutions are obtained using a special kind of finite element method, where increments of the plastic strain rate appear as degrees of freedom on equal footing with displacement increments. The displacement increments, Δu_i, and the change of the effective plastic strain rate, $\Delta\dot{\epsilon}^P$, are interpolated within each element between nodal displacement increments, ΔD^N, and nodal effective plastic strain rate changes, $\Delta\dot{\epsilon}^P_N$, respectively

$$\Delta u_i = \sum_{N=1}^{2k} N_i^N \Delta D^N, \qquad \Delta\dot{\epsilon}^P = \sum_{N=1}^{l} M^N \Delta\dot{\epsilon}^P_N \tag{2.22}$$

where N_i^N and M^N are shape functions and k and l are the number of nodes used for the interpolations. The derivatives of the displacement increments and the effective plastic strain rate increments are taken as

$$L_{ij} = \sum_{N=1}^{2k} N^N_{,j}\dot{D}^N, \quad \Delta\epsilon_{ij} = \sum_{N=1}^{2k} E^N_{ij}\Delta D^N, \quad \Delta\dot{\epsilon}^P_{,i} = \sum_{N=1}^{l} M^N_{,i}\Delta\dot{\epsilon}^P_N \tag{2.23}$$

where $E^N_{ij} = \frac{1}{2}\left(N^N_{i,j} + N^N_{j,i}\right)$. Using these relations in the principle of virtual power, the discretized equations can be written in the following form

$$\begin{bmatrix} \mathbf{K_e} & \mathbf{0} \\ \mathbf{K_{ep}} & \mathbf{K_p} \end{bmatrix} \begin{bmatrix} \mathbf{\Delta D} \\ \mathbf{\Delta\dot{\epsilon}^P} \end{bmatrix} = \begin{bmatrix} \mathbf{\Delta F_1} \\ \mathbf{\Delta F_2} \end{bmatrix} \tag{2.24}$$

where

$$\mathbf{K_e}^{NM} = \int_V \left(E^N_{ij} R_{ijkl} E^M_{kl} + \sigma_{ij}\left(N^M_{k,j}N^N_{k,i} - 2E^M_{ik}E^N_{jk}\right)\right) \mathrm{d}V \tag{2.25}$$

is the elastic stiffness matrix,

$$\mathbf{K_{ep}}^{NM} = -\int_V m_{ij} R_{ijkl} E^M_{kl} M^N \mathrm{d}V \tag{2.26}$$

is the coupling matrix, and

$$\begin{aligned} \mathbf{K_p}^{NM} \;=\; & \int_V \Bigg(\left(\frac{\dot{\epsilon}^P}{\dot{E}^P{}^2}(m-1)q + \frac{\sigma_c}{\dot{E}^P} \right) M^M M^N \\ & + l_*^2 \frac{\dot{\epsilon}^P_{,i}}{\dot{E}^P{}^2}(m-1)qM^M M^N_{,i} + \frac{\dot{\epsilon}^P}{\dot{E}^P{}^2}(m-1)\rho_i M^M_{,i} M^N \\ & + l_*^2 \frac{\dot{\epsilon}^P_{,i}}{\dot{E}^P{}^2}(m-1)\rho_k M^M_{,k} M^N_{,i} + l_*^2 \frac{\sigma_c}{\dot{E}^P} M^M_{,i} M^N_{,i} \Bigg) \mathrm{d}V \end{aligned} \tag{2.27}$$

is the plastic stiffness matrix. The right-hand side in equation (2.24) consists of two components

$$\mathbf{\Delta F_1}^N = \int_S \Delta T_i N_i^N \mathrm{d}S + \Delta t \int_V E^N_{ij} R_{ijkl} m_{kl} \dot{\epsilon}^P \mathrm{d}V \tag{2.28}$$

which is the conventional load increment vector with an added volume force, and

$$\begin{aligned}\mathbf{\Delta F_2}^N &= \int_S \Delta\rho_i n_i M^N \mathrm{d}S - \Delta t \int_V \left(\left(m_{ij} R_{ijkl} m_{kl} \dot{\epsilon}^P + \frac{\dot{\epsilon}^P}{\dot{\epsilon}_0^m} \dot{E^P}^m \frac{\mathrm{d}g}{\mathrm{d}E^P} \right) M^N \right. \\ &\left. + \dot{\epsilon}^P_{,i} \dot{E^P}^m \frac{\mathrm{d}g}{\mathrm{d}E^P} \frac{l_*^2}{\dot{\epsilon}_0^m} M^N_{,i} \right) \mathrm{d}V \end{aligned} \tag{2.29}$$

which is an additional higher order load term with a subtracted volume contribution.

Since the system of equations decouples, it is possible to first solve for the displacement increments and afterwards solve for the effective plastic strain rate increments and hereby exploit the symmetry of $\mathbf{K_e}$ and $\mathbf{K_p}$, respectively.

When the displacement increments and the effective plastic strain rate increments are known, the Jaumann rate of the stress, the generalized effective stress rate and the convected rate of the higher order stress can be found from the constitutive equations (2.18)-(2.21). The increments of the Cauchy stress tensor and the higher order stress vector is then calculated by

$$\Delta\sigma_{ij} = \overset{\triangledown}{\varsigma}_{ij} \Delta t + \Delta t \Omega_{ik}\sigma_{kj} + \Delta t \sigma_{ik}\Omega_{jk} - \sigma_{ij}\Delta\epsilon_{kk} \tag{2.30}$$

$$\Delta\tau_i = \overset{\vee}{\rho}_i \Delta t + \Delta t L_{ik}\tau_k - \tau_i \Delta\epsilon_{kk} \tag{2.31}$$

Subsequently, the effective stress, σ_c, can be calculated from (2.16) and the effective plastic strain rate, $\dot{E}^P$, is given by (2.17). The conventional effective plastic strain rate, $\dot{\epsilon}^P$, and its gradient, $\dot{\epsilon}^P_{,i}$, is now obtained from equations (2.14) and (2.15).

The theory has been applied in papers [P1] and partly [P3] under plane strain assumptions. The elements used for those studies are isoparametric 8-node quadrilaterals with quadratic interpolation of both displacement increments and effective plastic strain rate increments $(k = l = 8)$, as in Niordson and Tvergaard (2005) for a time independent analysis. The integrations (2.25)-(2.29) are carried out using 3×3 point Gaussian integration.

2.2 Strain gradient crystal plasticity

This section presents a strain gradient crystal plasticity theory that allows for finite strains. The basic formulation of the theory is equivalent to the formulation of Gurtin (2000, 2002) but with the constitutive equations based on the strain gradient theory by Fleck and Hutchinson (2001). The kinematical basis is taken from Peirce et al. (1983), where a quantitative description of plastic deformation in single crystals is based on crystallographic shearing.

2.2.1 Material model

It is assumed that a general homogeneous deformation can be represented by the deformation gradient tensor $\boldsymbol{F}$ that maps a line element $\mathrm{d}\boldsymbol{X}$ in the reference configuration to $\mathrm{d}\boldsymbol{x}$

in the deformed configuration as $\mathrm{d}\boldsymbol{x} = \boldsymbol{F} \cdot \mathrm{d}\boldsymbol{X}$. The deformation gradient is decomposed into an elastic and plastic part as introduced by Kröner (1960) and Lee (1969)

$$\boldsymbol{F} = \boldsymbol{F}^* \cdot \boldsymbol{F}^P \tag{2.32}$$

where elastic stretching and rotation of the crystal lattice are embodied in $\boldsymbol{F}^*$, and $\boldsymbol{F}^P$ represents the crystallographic shearing due to dislocation motion along specific slip systems, as illustrated in figure 2.1.

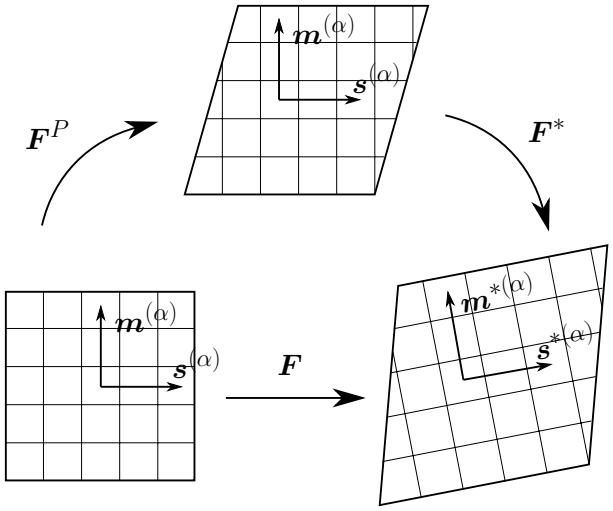

Figure 2.1 Decomposition of the deformation gradient

A slip system (α) in the initial configuration is specified by the orthogonal unit vectors $\boldsymbol{s}^{(\alpha)}$ and $\boldsymbol{m}^{(\alpha)}$, where $\boldsymbol{s}^{(\alpha)}$ is the slip direction and $\boldsymbol{m}^{(\alpha)}$ is the direction normal to the slip plane. The lattice vectors are stretched and rotated according to $\boldsymbol{F}^*$ such that in the deformed lattice the vectors are given by

$$\boldsymbol{s}^{*(\alpha)} = \boldsymbol{F}^* \cdot \boldsymbol{s}^{(\alpha)}, \quad \boldsymbol{m}^{*(\alpha)} = \boldsymbol{m}^{(\alpha)} \cdot \boldsymbol{F}^{*-1} \tag{2.33}$$

In the deformed lattice the vectors $\boldsymbol{s}^{*(\alpha)}$ and $\boldsymbol{m}^{*(\alpha)}$ are still orthogonal, but in general not unit vectors. The velocity gradient $\boldsymbol{L}$ can now by use of (2.32) be expressed as

$$\boldsymbol{L} = \dot{\boldsymbol{F}} \cdot \boldsymbol{F}^{-1} = \dot{\boldsymbol{F}}^* \cdot \boldsymbol{F}^{*-1} + \boldsymbol{F}^* \cdot \dot{\boldsymbol{F}}^P \cdot \boldsymbol{F}^{P-1} \cdot \boldsymbol{F}^{*-1} = \boldsymbol{L}^* + \boldsymbol{L}^P \tag{2.34}$$

where the rate of the plastic part of the deformation gradient, $\dot{\boldsymbol{F}}^P$, can be found by the rate of shearing $\dot{\gamma}^{(\alpha)}$ on each slip system as

$$\dot{\boldsymbol{F}}^P = \sum_\alpha \dot{\gamma}^{(\alpha)} \boldsymbol{s}^{(\alpha)} \boldsymbol{m}^{(\alpha)} \cdot \boldsymbol{F}^P \tag{2.35}$$

The strain rate is taken as the symmetric part of the velocity gradient, $\dot{\epsilon}_{ij} = \frac{1}{2}(L_{ij} + L_{ji})$. Introducing $\mu_{ij}^{*(\alpha)} = \frac{1}{2}\left(s_i^{*(\alpha)} m_j^{*(\alpha)} + s_j^{*(\alpha)} m_i^{*(\alpha)}\right)$ as the classical Schmid orientation

tensor, the overall macroscopic plastic strain rate components can be expressed as

$$\dot{\epsilon}^p_{ij} = \sum_\alpha \dot{\gamma}^{(\alpha)} \mu^{*(\alpha)}_{ij} = \frac{1}{2}\left(L^P_{ij} + L^P_{ji}\right) \tag{2.36}$$

To account for the effects of increased material hardening due to interaction of geometrically necessary dislocations caused by plastic strain gradients with statistically stored dislocations, it is assumed that the slip rates and slip rate gradients contribute to the plastic work, so that the principle of virtual power in total form in the deformed configuration can be written as

$$\int_V \left(\sigma_{ij}\delta\dot{\epsilon}^E_{ij} + \sum_\alpha Q^{(\alpha)}\delta\dot{\gamma}^{(\alpha)} + \sum_\alpha \left(\xi^{(\alpha)}_S s^{*(\alpha)}_i + \xi^{(\alpha)}_T t^{*(\alpha)}_i\right)\delta\dot{\gamma}^{(\alpha)}_{,i} \right) \mathrm{d}V = \int_S \left(T_i \delta\dot{u}_i + \sum_\alpha r^{(\alpha)}\delta\dot{\gamma}^{(\alpha)} \right) \mathrm{d}S \tag{2.37}$$

where σ_{ij} is the Cauchy stress tensor and ϵ^E_{ij} is the elastic part of the strain tensor given by $\dot{\epsilon}^E_{ij} = \frac{1}{2}(L^*_{ij} + L^*_{ji})$. The stress field $Q^{(\alpha)}$ is an effective stress work-conjugate to the slip and $\xi^{(\alpha)}_S$ and $\xi^{(\alpha)}_T$ are higher order stresses work-conjugate to the slip gradients along the slip direction and the transverse direction, respectively. The vector $\boldsymbol{t}^{(\alpha)}$ denotes the transverse direction and thus forms a triad with vectors $\boldsymbol{s}^{(\alpha)}$ and $\boldsymbol{m}^{(\alpha)}$, i.e. $\boldsymbol{t}^{(\alpha)} = \boldsymbol{s}^{(\alpha)} \times \boldsymbol{m}^{(\alpha)}$. The surface stress traction is denoted T_i, while $r^{(\alpha)}$ are the higher order tractions. Following Fleck et al. (1994), the slip gradient in the $\boldsymbol{s}^{(\alpha)}$ direction is related to geometrically necessary edge dislocations, and the slip gradient in the $\boldsymbol{t}^{(\alpha)}$ direction is related to geometrically necessary screw dislocations. A slip gradient in the $\boldsymbol{m}^{(\alpha)}$ direction does not induce any geometrically necessary dislocations and therefore it does not contribute to the plastic work rate. The elastic part of the internal virtual power per unit volume can be rewritten as

$$\sigma_{ij}\delta\dot{\epsilon}^E_{ij} = \sigma_{ij}(\delta\dot{\epsilon}_{ij} - \sum_\alpha \mu^{*(\alpha)}_{ij}\delta\dot{\gamma}^{(\alpha)}) = \sigma_{ij}\delta\dot{\epsilon}_{ij} - \sum_\alpha \tau^{(\alpha)}\delta\dot{\gamma}^{(\alpha)} \tag{2.38}$$

where $\tau^{(\alpha)} = \sigma_{ij}\mu^{*(\alpha)}_{ij}$ is the classical Schmid stress (the resolved shear stress on slip system (α)). The principle of virtual power in total form in the deformed configuration can then be formulated as

$$\int_V \left(\sigma_{ij}\delta\dot{\epsilon}_{ij} + \sum_\alpha \left(Q^{(\alpha)} - \tau^{(\alpha)}\right)\delta\dot{\gamma}^{(\alpha)} + \sum_\alpha \left(\xi^{(\alpha)}_S s^{*(\alpha)}_i + \xi^{(\alpha)}_T t^{*(\alpha)}_i\right)\delta\dot{\gamma}^{(\alpha)}_{,i} \right) \mathrm{d}V = \int_S \left(T_i \delta\dot{u}_i + \sum_\alpha r^{(\alpha)}\delta\dot{\gamma}^{(\alpha)} \right) \mathrm{d}S \tag{2.39}$$

This relation must hold for arbitrary variations of $\dot{u}_i$ and $\dot{\gamma}^{(\alpha)}$ which leads to the strong form of the field equations. First we have the classical balance and boundary conditions

$$\sigma_{ij,j} = 0\,, \qquad T_i = \sigma_{ij} n_j \tag{2.40}$$

where n_i is the surface unit normal in the current configuration. Next we have the consistency condition and higher order boundary conditions

$$Q^{(\alpha)} - \tau^{(\alpha)} - \xi_{S,i}^{(\alpha)} s_i^{*(\alpha)} - \xi_{T,i}^{(\alpha)} t_i^{*(\alpha)} = 0 \tag{2.41}$$

$$r^{(\alpha)} = \left(\xi_S^{(\alpha)} s_i^{*(\alpha)} + \xi_T^{(\alpha)} t_i^{*(\alpha)} \right) n_i \tag{2.42}$$

The principle of virtual power in its weak form (2.39) and strong form (2.40-2.42) is a special case of the formulation by Gurtin (2002). However, the formulations diverges significantly with regard to constitutive equations.

To obtain the principle of virtual power in the reference configuration, Kirchhoff stress measures are defined as (with $J = \det(\boldsymbol{F})$)

$$\varsigma_{ij} = J\sigma_{ij}, \quad q^{(\alpha)} = JQ^{(\alpha)}, \quad \tau^{\varsigma(\alpha)} = J\tau^{(\alpha)}, \quad \rho_S^{(\alpha)} = J\xi_S^{(\alpha)}, \quad \rho_T^{(\alpha)} = J\xi_T^{(\alpha)} \tag{2.43}$$

The first Piola-Kirchhoff stress measure, s_{ij}, can be written as

$$s_{ij} = JF_{ik}^{-1}\sigma_{kj} = F_{ik}^{-1}\varsigma_{kj} \tag{2.44}$$

The principle of virtual power in total form in the reference configuration can then be formulated as

$$\int_{V_0} \left(s_{ij}\delta\dot{F}_{ji} + \sum_\alpha \left(q^{(\alpha)} - \tau^{\varsigma(\alpha)} \right) \delta\dot{\gamma}^{(\alpha)} + \sum_\alpha \left(\rho_S^{(\alpha)} s_i^{*(\alpha)} + \rho_T^{(\alpha)} t_i^{*(\alpha)} \right) F_{ik}^{-1} \delta\dot{\gamma}_{0,k}^{(\alpha)} \right) \mathrm{d}V_0 = \int_S \left(T_i^0 \delta\dot{u}_i + \sum_\alpha r_0^{(\alpha)} \delta\dot{\gamma}^{(\alpha)} \right) \mathrm{d}S_0 \tag{2.45}$$

where the subscript "0" refers to the reference configuration. The lattice Jaumann rate of Kirchhoff stress is introduced as

$$\overset{\nabla^*}{\varsigma}_{ij} = \dot{\varsigma}_{ij} - \varsigma_{kj}\Omega_{ik}^* - \varsigma_{ik}\Omega_{jk}^* \tag{2.46}$$

where the lattice rotation rate is given by the skew symmetric part of the elastic part of the velocity gradient, $\Omega_{ij}^* = \frac{1}{2}(L_{ij}^* - L_{ji}^*)$. Then, the incremental principle of virtual power in an updated Lagrangian framework (where the deformed configuration is taken as a reference, thus $\boldsymbol{F}^* = \boldsymbol{F}^P = \boldsymbol{I}$), can be expressed as

$$\int_{V_0} \left(\overset{\nabla^*}{\varsigma}_{ij} \delta\dot{\epsilon}_{ij} - \sigma_{ij} \left(2\dot{\epsilon}_{ik}\delta\dot{\epsilon}_{kj} - \left(L_{kj} - \Omega_{kj}^P \right) \delta L_{ki} + \Omega_{ki}^P \delta L_{jk} \right) + \sum_\alpha \left(\dot{q}^{(\alpha)} - \dot{\tau}^{\varsigma(\alpha)} \right) \delta\dot{\gamma}^{(\alpha)} + \sum_\alpha \left(\dot{\rho}_S^{(\alpha)} s_i^{(\alpha)} - \rho_S^{(\alpha)} \dot{F}_{ik}^P s_k^{(\alpha)} + \dot{\rho}_T^{(\alpha)} t_i^{(\alpha)} + \rho_T^{(\alpha)} \left(\dot{t}_i^{*(\alpha)} - \dot{F}_{ik} t_k^{(\alpha)} \right) \right) \delta\dot{\gamma}_{0,i}^{(\alpha)} \right) \mathrm{d}V_0 = \int_{S_0} \left(\dot{T}_i^0 \delta\dot{u}_i + \sum_\alpha \dot{r}_0^{(\alpha)} \delta\dot{\gamma}^{(\alpha)} \right) \mathrm{d}S_0 \tag{2.47}$$

where $\Omega_{ij}^P = \frac{1}{2}(L_{ij}^P - L_{ji}^P)$ is the plastic spin. The time derivative of $t_i^{*(\alpha)} = e_{ijk} s_j^{*(\alpha)} m_k^{*(\alpha)}$ (where e_{ijk} is the permutation symbol) can be written as

$$\dot{t}_i^{*(\alpha)} = e_{ijk} \left(s_l^{(\alpha)} m_k^{(\alpha)} \dot{F}_{jl}^* - s_j^{(\alpha)} m_l^{(\alpha)} \dot{F}_{lk}^* \right) \tag{2.48}$$

The resolved shear stress rate is given by

$$\dot{\tau}^{\varsigma(\alpha)} = s_i^{(\alpha)} m_j^{(\alpha)} \left(\overset{\nabla^*}{\varsigma}_{ij} - \sigma_{ik} \dot{\epsilon}_{jk}^E + \sigma_{jk} \dot{\epsilon}_{ki}^E \right) \tag{2.49}$$

A nonlocal measure of the effective slip $\gamma_e^{(\alpha)}$ is defined on the basis of the slip rate and the directional derivative of the slip rate through the incremental relation

$$\dot{\gamma}_e^{(\alpha)^2} = \dot{\gamma}^{(\alpha)^2} + \left(l_S \dot{\gamma}_{,i}^{(\alpha)} s_i^{(\alpha)} \right)^2 + \left(l_T \dot{\gamma}_{,i}^{(\alpha)} t_i^{(\alpha)} \right)^2 \tag{2.50}$$

where l_S and l_T are internal material length parameters introduced for dimensional consistency.

A viscoplastic potential similar to (2.12) for the isotropic strain gradient formulation is to be defined. For the present crystal plasticity version the viscoplastic potential is taken as $\Phi = \sum_\alpha \Phi^{(\alpha)}$, where the potential for each slip system is given by

$$\Phi^{(\alpha)}(\dot{\gamma}_e^{(\alpha)}, \gamma_e^{(\alpha)}) = \int_0^{\dot{\gamma}_e^{(\alpha)}} \tau_e^{(\alpha)} \left(\dot{\gamma}_e^{(\alpha)\prime}, \gamma_e^{(\alpha)} \right) \mathrm{d}\dot{\gamma}_e^{(\alpha)\prime} \tag{2.51}$$

where $\tau_e^{(\alpha)}$ is an effective stress work-conjugate to the effective slip rate, $\dot{\gamma}_e^{(\alpha)}$. Taking the variation of the potential one obtains by use of (2.37) and (2.43) that

$$\delta\Phi^{(\alpha)} = \tau_e^{(\alpha)} \delta\dot{\gamma}_e^{(\alpha)} = q^{(\alpha)} \delta\dot{\gamma}^{(\alpha)} + \rho_S^{(\alpha)} s_i^{(\alpha)} \delta\dot{\gamma}_{,i}^{(\alpha)} + \rho_T^{(\alpha)} t_i^{(\alpha)} \delta\dot{\gamma}_{,i}^{(\alpha)} \tag{2.52}$$

Now, by inserting the variation of the effective slip rate given by (2.50) the constitutive equations for the effective stress $q^{(\alpha)}$ and the higher order stresses $\rho_S^{(\alpha)}$ and $\rho_T^{(\alpha)}$ are obtained as

$$q^{(\alpha)} = \tau_e^{(\alpha)} \frac{\dot{\gamma}^{(\alpha)}}{\dot{\gamma}_e^{(\alpha)}} \tag{2.53}$$

$$\rho_S^{(\alpha)} = \tau_e^{(\alpha)} \frac{\dot{\gamma}_{,i}^{(\alpha)} s_i^{(\alpha)}}{\dot{\gamma}_e^{(\alpha)}} l_S^2 \tag{2.54}$$

$$\rho_T^{(\alpha)} = \tau_e^{(\alpha)} \frac{\dot{\gamma}_{,i}^{(\alpha)} t_i^{(\alpha)}}{\dot{\gamma}_e^{(\alpha)}} l_T^2 \tag{2.55}$$

By substituting these expressions for $\dot{\gamma}^{(\alpha)}$, $\dot{\gamma}_{,i}^{(\alpha)} s_i^{(\alpha)}$ and $\dot{\gamma}_{,i}^{(\alpha)} t_i^{(\alpha)}$ into the definition of the effective slip (2.50), the introduced effective stress $\tau_e^{(\alpha)}$ can be expressed in the following quadratic form in $q^{(\alpha)}$, $\rho_S^{(\alpha)}$ and $\rho_T^{(\alpha)}$

$$\tau_e^{(\alpha)^2} = q^{(\alpha)^2} + l_S^{-2} \rho_S^{(\alpha)^2} + l_T^{-2} \rho_T^{(\alpha)^2} \tag{2.56}$$

In the absence of slip gradients, the higher order stress vanishes and the effective stress $q^{(\alpha)}$ equals the classical Schmid stress $\tau^{(\alpha)}$. In that case the theory reduces to the classical rate-dependent crystal plasticity theory as presented by e.g. Peirce et al. (1983).

A power-law creep model is adopted for the effective slip rate $\dot{\gamma}_e^{(\alpha)}$ to model the viscous material behavior

$$\dot{\gamma}_e^{(\alpha)} = \dot{\gamma}_0 \left(\frac{\tau_e^{(\alpha)}}{g^{(\alpha)}} \right)^{1/m} \tag{2.57}$$

where $\dot{\gamma}_0$ is a reference slip rate used as a scaling parameter to normalize the applied strain rate, and m is a strain rate hardening index with $m \to 0$ being the rate-independent limit. The functions $g^{(\alpha)}$, termed the slip resistance, characterize the current strain hardened state of the crystal and harden from an initial value τ_0 according to

$$\dot{g}^{(\alpha)} = \sum_{\beta} h_{\alpha\beta} \dot{\gamma}_e^{(\beta)} \tag{2.58}$$

Here, $h_{\alpha\beta}$ is the hardening matrix. It is noted that the slip resistance $\dot{g}^{(\alpha)}$ depends on $\dot{\gamma}_e^{(\alpha)}$ instead of $|\dot{\gamma}^{(\alpha)}|$ as it would in classical crystal plasticity, meaning that not only the slips but also the slip gradients generate hardening. The form of the hardening matrix is taken as

$$h_{\alpha\beta} = h\delta_{\alpha\beta} + ph\left(1 - \delta_{\alpha\beta}\right) \tag{2.59}$$

where the parameter p is a latent hardening index (usually in the range $1.0 \leq p \leq 1.4$), h is the self-hardening modulus and $\delta_{\alpha\beta}$ denotes the Kronecker delta function. The self-hardening modulus is taken to be a function of the accumulated effective slip, γ_{ea} , specified by $\gamma_{ea} = \sum_{\alpha} \int \dot{\gamma}_e^{(\alpha)} \mathrm{d}t$. Different expressions for the self-hardening modulus have been employed for the results presented in the present thesis.

Increments of the lattice Jaumann rate of Kirchhoff stress are given by the incremental elastic constitutive equation

$$\overset{\nabla^*}{\varsigma}_{ij} \Delta t = R_{ijkl} \left(\Delta\epsilon_{kl} - \Delta t \sum_{\alpha} \dot{\gamma}^{(\alpha)} \mu_{kl}^{(\alpha)} \right) = \Delta\varsigma_{ij} - \Delta t \Omega_{ik}^* \sigma_{kj} - \Delta t \sigma_{ik} \Omega_{jk}^* \tag{2.60}$$

where the elastic stiffness tensor is given by (2.19). The increments of the effective stress

and the higher order stresses can be written as

$$\dot{q}^{(\alpha)} = (m-1)\tau_e^{(\alpha)}\frac{\dot{\gamma}^{(\alpha)}}{\dot{\gamma}_e^{(\alpha)2}}\ddot{\gamma}_e^{(\alpha)} + \tau_e\frac{1}{\dot{\gamma}_e^{(\alpha)}}\ddot{\gamma}^{(\alpha)} + \dot{\gamma}_0^{-m}\dot{\gamma}_e^{(\alpha)m-1}\dot{\gamma}^{(\alpha)}\dot{g}^{(\alpha)} \tag{2.61}$$

$$\begin{aligned}\dot{\rho}_S^{(\alpha)} &= (m-1)l_S^2\tau_e^{(\alpha)}\frac{\left(\dot{\gamma}_{,i}^{(\alpha)}s_i^{(\alpha)}\right)}{\dot{\gamma}_e^{(\alpha)2}}\ddot{\gamma}_e^{(\alpha)} + l_S^2\tau_e^{(\alpha)}\frac{1}{\dot{\gamma}_e^{(\alpha)}}s_i^{(\alpha)}\ddot{\gamma}_{,i}^{(\alpha)} \\ &\quad + l_S^2\dot{\gamma}_0^{-m}\left(\dot{\gamma}_{,i}^{(\alpha)}s_i^{(\alpha)}\right)\dot{\gamma}_e^{(\alpha)m-1}\dot{g}^{(\alpha)}\end{aligned} \tag{2.62}$$

$$\begin{aligned}\dot{\rho}_T^{(\alpha)} &= (m-1)l_T^2\tau_e^{(\alpha)}\frac{\left(\dot{\gamma}_{,i}^{(\alpha)}t_i^{(\alpha)}\right)}{\dot{\gamma}_e^{(\alpha)2}}\ddot{\gamma}_e^{(\alpha)} + l_T^2\tau_e^{(\alpha)}\frac{1}{\dot{\gamma}_e^{(\alpha)}}t_i^{(\alpha)}\ddot{\gamma}_{,i}^{(\alpha)} \\ &\quad + l_T^2\dot{\gamma}_0^{-m}\left(\dot{\gamma}_{,i}^{(\alpha)}t_i^{(\alpha)}\right)\dot{\gamma}_e^{(\alpha)m-1}\dot{g}^{(\alpha)}\end{aligned} \tag{2.63}$$

where the change in the effective slip rate is taken as $\ddot{\gamma}_e^{(\alpha)} = \frac{\dot{\gamma}^{(\alpha)}}{\dot{\gamma}_e^{(\alpha)}}\ddot{\gamma}^{(\alpha)} + \frac{l_S^2\dot{\gamma}_{,k}^{(\alpha)}s_k^{(\alpha)}}{\dot{\gamma}_e^{(\alpha)}}s_i^{(\alpha)}\ddot{\gamma}_{,i}^{(\alpha)} + \frac{l_T^2\dot{\gamma}_{,k}^{(\alpha)}t_k^{(\alpha)}}{\dot{\gamma}_e^{(\alpha)}}t_i^{(\alpha)}\ddot{\gamma}_{,i}^{(\alpha)}$. The values of $\dot{\gamma}_e^{(\alpha)}$, $\dot{\gamma}^{(\alpha)}$ and $\dot{\gamma}_{,i}^{(\alpha)}$ are taken from the previous increment, so that only $\ddot{\gamma}^{(\alpha)}$ and its spacial gradient $\ddot{\gamma}_{,i}^{(\alpha)}$ are unknowns.

2.2.2 Grain boundary energy potential

To account for grain boundary resistances to dislocations crossing them, two surface energy potentials $\phi_-^{(\alpha)}(\gamma_-^{(\alpha)})$ and $\phi_+^{(\alpha)}(\gamma_+^{(\alpha)})$ acting at the two sides of a grain boundary Γ are introduced. It is assumed that the total displacement fields are continuous across the grain boundary, but that the presence of a grain boundary energy term causes jumps in the slips, having $\gamma_-^{(\alpha)}$ on one side of the boundary and $\gamma_+^{(\alpha)}$ on the other side of the boundary. The principle of virtual power on total form in the deformed configuration can then be written as (where $\phi_-^{(\alpha)\prime}$ denotes $\partial\phi_-^{(\alpha)}/\partial\gamma_-^{(\alpha)}$, etc.)

$$\begin{aligned}&\int_V\left(\sigma_{ij}\delta\dot{\epsilon}_{ij}^E + \sum_\alpha Q^{(\alpha)}\delta\dot{\gamma}^{(\alpha)} + \sum_\alpha\left(\xi_S^{(\alpha)}s_i^{*(\alpha)} + \xi_T^{(\alpha)}t_i^{*(\alpha)}\right)\delta\dot{\gamma}_{,i}^{(\alpha)}\right)\mathrm{d}V \\ &+\int_\Gamma\sum_\alpha\left(\phi_-^{(\alpha)\prime}\delta\dot{\gamma}_-^{(\alpha)} + \phi_+^{(\alpha)\prime}\delta\dot{\gamma}_+^{(\alpha)}\right)\mathrm{d}\Gamma = \int_S\left(T_i\delta\dot{u}_i + \sum_\alpha r^{(\alpha)}\delta\dot{\gamma}^{(\alpha)}\right)\mathrm{d}S\end{aligned} \tag{2.64}$$

Full constraint along Γ with $\gamma^{(\alpha)} = 0$ is obtained by letting $\phi_-^{(\alpha)\prime}$ and $\phi_+^{(\alpha)\prime}$ tend to infinity, whereas vanishing surface energy along Γ simulates that dislocations are free to cross the grain boundary. The strong form of the field equations are given by (2.40)-(2.42). Furthermore, the interface conditions are given by

$$[\sigma_{ij}N_j] = 0 \tag{2.65}$$

$$\left(\xi_{S-}^{(\alpha)}s_{i-}^{(\alpha)} + \xi_{T-}^{(\alpha)}t_{i-}^{(\alpha)}\right)N_i = \phi_-^{(\alpha)\prime}(\gamma_-^{(\alpha)}) \tag{2.66}$$

$$\left(\xi_{S+}^{(\alpha)}s_{i+}^{(\alpha)} + \xi_{T+}^{(\alpha)}t_{i+}^{(\alpha)}\right)(-N_i) = \phi_+^{(\alpha)\prime}(\gamma_+^{(\alpha)}) \tag{2.67}$$

where the unit normal vector N_i on Γ is directed from the (-) side to the (+) side and $[f]$ denotes the jump $f_- - f_+$ across Γ. For the results presented in this thesis, the expressions adopted for the grain boundary energy potentials are of the form

$$\phi_-^{(\alpha)} = \frac{1}{2}\kappa(\gamma_-^{(\alpha)})^2, \qquad \phi_-^{(\alpha)\prime} = \kappa\gamma_-^{(\alpha)} \tag{2.68}$$

$$\phi_+^{(\alpha)} = \frac{1}{2}\kappa(\gamma_+^{(\alpha)})^2, \qquad \phi_+^{(\alpha)\prime} = \kappa\gamma_+^{(\alpha)} \tag{2.69}$$

where κ is a material parameter describing the strength of the grain boundary. This quadratic function of $\gamma^{(\alpha)}$ is taken as a simple example. Other functions might give a better description of the physics at the grain boundary, but this is still an open issue. The grain boundary energy potential is employed in papers [P3] and [P4].

2.2.3 Numerical formulation

The numerical solutions are obtained using a special kind of finite element method where the slip rate increments are taken as degrees of freedom on equal footing with the displacement increments. The displacement increments, Δu_i, and the change of the slip rates, $\Delta\dot{\gamma}^{(\alpha)}$, are interpolated within each element between nodal displacement increments, ΔD^N, and nodal slip rate changes, $\Delta\dot{\gamma}_N^{(\alpha)}$, respectively

$$\Delta u_i = \sum_{N=1}^{2k} N_i^N \Delta D^N, \qquad \Delta\dot{\gamma}^{(\alpha)} = \sum_{N=1}^{l} M^N \Delta\dot{\gamma}_N^{(\alpha)} \tag{2.70}$$

where N_i^N and M^N are shape functions and k and l are the number of nodes used for the interpolations. The derivatives of the displacement increments and the slip rate increments are taken as

$$L_{ij} = \sum_{N=1}^{2k} N_{i,j}^N \dot{D}^N, \quad \Delta\epsilon_{ij} = \sum_{N=1}^{2k} E_{ij}^N \Delta D^N, \quad \Delta\dot{\gamma}_{,i}^{(\alpha)} = \sum_{N=1}^{l} M_{,i}^N \Delta\dot{\gamma}_N^{(\alpha)} \tag{2.71}$$

where $E_{ij}^N = \frac{1}{2}\left(N_{i,j}^N + N_{j,i}^N\right)$. Using these relations in the principle of virtual work, the discretized equations can be written in the following form

$$\mathbf{K_e}\boldsymbol{\Delta}\mathbf{D} = \boldsymbol{\Delta}\mathbf{F_1} \tag{2.72}$$

$$\mathbf{K_p}^{(\alpha)}\boldsymbol{\Delta}\dot{\boldsymbol{\gamma}}^{(\alpha)} = \boldsymbol{\Delta}\mathbf{F_2}^{(\alpha)} - \mathbf{K_{ep}}^{(\alpha)}\boldsymbol{\Delta}\mathbf{D} \tag{2.73}$$

where

$$\mathbf{K_e}^{NM} = \int_V \left(E_{ij}^N R_{ijkl} E_{kl}^M + \sigma_{ij}\left(N_{k,j}^M N_{k,i}^N - 2E_{ik}^M E_{jk}^N\right)\right) \mathrm{d}V \tag{2.74}$$

is the elastic stiffness matrix,

$$\begin{aligned}\mathbf{K_{ep}}^{NM^{(\alpha)}} = \int_V \Big(&-s_i^{(\alpha)} m_j^{(\alpha)} \left(R_{ijkl}E_{kl}^N + \sigma_{kj}E_{ik}^N - \sigma_{ik}E_{jk}^N\right) M^M \\ &+\rho_T^{(\alpha)}\left(e_{ijk}\left(s_l^{(\alpha)} m_k^{(\alpha)} N_{j,l}^N - s_j^{(\alpha)} m_n^{(\alpha)} N_{n,k}^N\right) - t_k^{(\alpha)} N_{i,k}^N\right) M_{,i}^M\Big)\,\mathrm{d}V\end{aligned} \tag{2.75}$$

is the coupling matrix, and

$$\begin{aligned}\mathbf{K_p}^{NM^{(\alpha)}} = \int_V \Bigg\{ \Bigg[& (m-1)\tau_e^{(\alpha)} \frac{\dot{\gamma}^{(\alpha)}}{\dot{\gamma}_e^{(\alpha)^3}} \Big(\dot{\gamma}^{(\alpha)} M^N + l_S^2 \dot{\gamma}_{,k}^{(\alpha)} s_k^{(\alpha)} s_i^{(\alpha)} M_{,i}^N \\ & + l_T^2 \dot{\gamma}_{,k}^{(\alpha)} t_k^{(\alpha)} t_i^{(\alpha)} M_{,i}^N \Big) + \tau_e^{(\alpha)} \frac{1}{\dot{\gamma}_e^{(\alpha)}} M^N \Bigg] M^M \\ & + \Bigg[s_i^{(\alpha)} \Bigg((m-1) l_S^2 \tau_e^{(\alpha)} \frac{\dot{\gamma}_{,j}^{(\alpha)} s_j^{(\alpha)}}{\dot{\gamma}_e^{(\alpha)^3}} \Big(\dot{\gamma}^{(\alpha)} M^N + l_S^2 \dot{\gamma}_{,k}^{(\alpha)} s_k^{(\alpha)} s_l^{(\alpha)} M_{,l}^N \\ & + l_T^2 \dot{\gamma}_{,k}^{(\alpha)} t_k^{(\alpha)} t_l^{(\alpha)} M_{,l}^N \Big) + l_S^2 \tau_e^{(\alpha)} \frac{1}{\dot{\gamma}_e^{(\alpha)}} s_k^{(\alpha)} M_{,k}^N \Bigg) \\ & + t_i^{(\alpha)} \Bigg((m-1) l_T^2 \tau_e^{(\alpha)} \frac{\dot{\gamma}_{,j}^{(\alpha)} t_j^{(\alpha)}}{\dot{\gamma}_e^{(\alpha)^3}} \Big(\dot{\gamma}^{(\alpha)} M^N + l_S^2 \dot{\gamma}_{,k}^{(\alpha)} s_k^{(\alpha)} s_l^{(\alpha)} M_{,l}^N \\ & + l_T^2 \dot{\gamma}_{,k}^{(\alpha)} t_k^{(\alpha)} t_l^{(\alpha)} M_{,l}^N \Big) + l_T^2 \frac{\tau_e^{(\alpha)}}{\dot{\gamma}_e^{(\alpha)}} t_k^{(\alpha)} M_{,k}^N \Bigg) \Bigg] M_{,i}^M \Bigg\} \, \mathrm{d}V \end{aligned} \tag{2.76}$$

is the plastic stiffness matrix. The right-hand side vectors in equation (2.72) and (2.73) can be written as

$$\begin{aligned}\mathbf{\Delta F_1}^N &= \int_S \Delta T_i N_i^N \mathrm{d}S \\ &\quad + \Delta t \int_V \left(E_{ij}^N R_{ijkl} \sum_\alpha \dot{\gamma}^{(\alpha)} \mu_{kl}^{(\alpha)} + \sigma_{ij} \left(\Omega_{ki}^P N_{j,k}^N + \Omega_{kj}^P N_{k,i}^N \right) \right) \mathrm{d}V \end{aligned} \tag{2.77}$$

which is the conventional load increment vector with an added volume force, and

$$\begin{aligned}\mathbf{\Delta F_2}^{M^{(\alpha)}} = \Delta t \int_S \dot{r}^{(\alpha)} M^M \mathrm{d}S - \Delta t \int_V \Bigg(\Bigg(& \frac{\dot{\gamma}_e^{(\alpha)^{m-1}}}{\dot{\gamma}_0^m} \dot{\gamma}^{(\alpha)} \sum_\beta h_{\alpha\beta} \dot{\gamma}_e^{(\beta)} \\ & + s_i^{(\alpha)} m_j^{(\alpha)} \left(R_{ijkl} \sum_\beta \dot{\gamma}^{(\beta)} \mu_{kl}^{(\beta)} + \sum_\beta \dot{\gamma}^{(\beta)} \mu_{ki}^{(\beta)} \sigma_{kj} - \sum_\beta \dot{\gamma}^{(\beta)} \mu_{jk}^{(\beta)} \sigma_{ik} \right) \Bigg) M^M \\ & + \Bigg(s_i^{(\alpha)} l_S^2 \frac{\dot{\gamma}_{,k}^{(\alpha)} s_k^{(\alpha)}}{\dot{\gamma}_0^m} \dot{\gamma}_e^{(\alpha)^{m-1}} \sum_\beta h_{\alpha\beta} \dot{\gamma}_e^{(\beta)} - s_k^{(\alpha)} \rho_S^{(\alpha)} \sum_\beta \dot{\gamma}^{(\beta)} s_i^{(\beta)} m_k^{(\beta)} \\ & + t_i^{(\alpha)} l_T^2 \frac{\dot{\gamma}_{,k}^{(\alpha)} t_k^{(\alpha)}}{\dot{\gamma}_0^m} \dot{\gamma}_e^{(\alpha)^{m-1}} \sum_\beta h_{\alpha\beta} \dot{\gamma}_e^{(\beta)} \\ & - \rho_T^{(\alpha)} e_{ijk} \left(s_l^{(\alpha)} m_k^{(\alpha)} \sum_\beta \dot{\gamma}^{(\beta)} s_j^{(\beta)} m_l^{(\beta)} - s_j^{(\alpha)} m_n^{(\alpha)} \sum_\beta \dot{\gamma}^{(\beta)} s_n^{(\beta)} m_k^{(\beta)} \right) \Bigg) M_{,i}^M \Bigg) \mathrm{d}V \end{aligned} \tag{2.78}$$

which is an additional higher order load term with a subtracted volume contribution. If the grain boundary energy potentials of the form (2.68)-(2.69) are included in the analysis, the term

$$\Delta t \int_{\Gamma} \sum_{\alpha} \kappa \left(\dot{\gamma}_{-}^{(\alpha)} + \dot{\gamma}_{+}^{(\alpha)} \right) M^{M} \mathrm{d}\Gamma \tag{2.79}$$

is to be subtracted from (2.78). In that case, double nodes for the slip rate increments are placed at grain boundaries decoupling the slip on either side. The nodal displacement increments are constrained to be equal on either side of the grain boundary.

The update procedure is as follows. When the displacement increments and slip rate increments have been solved for, the stress rate $\dot{\sigma}_{ij}$, the effective stress rate $\dot{q}^{(\alpha)}$ and the two higher order stress rates $\dot{\rho}_S^{(\alpha)}$ and $\dot{\rho}_T^{(\alpha)}$ can be found from the constitutive equations (2.60)-(2.63). The effective stress $\tau_e^{(\alpha)}$ can now be determined by equation (2.56) and the effective slip rate $\dot{\gamma}_e^{(\alpha)}$ is given by (2.57). The slip rate $\dot{\gamma}^{(\alpha)}$ and its gradients $\dot{\gamma}_{,i}^{(\alpha)} s_i^{(\alpha)}$ and $\dot{\gamma}_{,i}^{(\alpha)} t_i^{(\alpha)}$ are now obtained from equations (2.53)-(2.55).

One can argue that the plastic and the total strain fields should have the same degree of interpolation, and therefore the slips, and thereby the plastic strains, should have shape functions of one degree lower than the displacements. The crystal plasticity results presented in this thesis are all plane strain studies. The elements used for the displacements are 8-node quadrilaterals with quadratic shape functions, and the elements used for interpolation of the slip rate increments are 4-node quadrilaterals with bilinear shape functions, i.e. $k = 8$ and $l = 4$. The coordinates of the nodes in the 4-node elements are identical to the coordinates of the corner nodes in the 8-node elements.

The integrations can be carried out either by using the Jacobian from the 8-node elements for the integrations of $\mathbf{K_e}$ and $\mathbf{\Delta F_1}$, and the Jacobian from the 4-node elements for the integrations of $\mathbf{K_{ep}}$, $\mathbf{K_p}$ and $\mathbf{\Delta F_2}$, or by using the same Jacobian for all integrations. Using the first method the coordinates of the integration points in the two elements will not necessarily coincide exactly if the element have high curvatures. This problem is overcome with the latter method, though in that case the location of the integration points may not be optimal for one of the element types. For both methods it is necessary to have the same number of integration points for the two element types.

The studies presented in this thesis are all plane strain problems with in-plane slip systems. Thus, there is no slip in the transverse direction, $\boldsymbol{t}^{(\alpha)}$, and all terms including the length scale, l_T, or the higher order stress, $\rho_T^{(\alpha)}$, are vanishing. The other material length scale, l_S, is in chapter 3 simply denoted as l.

2.2.4 Jaumann rate of Kirchhoff stress based on material rotations

In the previous sections, the elastic constitutive relation is formulated in the lattice Jaumann rate of Kirchhoff stress given by (2.46) and (2.60). This relation is chosen because most work on crystal plasticity follows the presumption by Hill and Rice (1972) that the crystal elasticity is unaffected by slip, so the usual tensor of elastic moduli relates the lattice Jaumann rate of Kirchhoff stress to the elastic rate of stretching. Another choice could

be to formulate the elastic constitutive relation in terms of the Jaumann rate of Kirchhoff stress based on material rotations as

$$\overset{\triangledown}{\varsigma}_{ij} = R_{ijkl}\dot{\epsilon}^E_{kl}, \qquad \overset{\triangledown}{\varsigma}_{ij} = \dot{\varsigma}_{ij} - \varsigma_{kj}\Omega_{ik} - \varsigma_{ik}\Omega_{jk} \tag{2.80}$$

where the material rotation rate is given by the skew symmetric part of the velocity gradient, $\Omega_{ij} = \frac{1}{2}(L_{ij} - L_{ji})$. The material Jaumann rate of Kirchhoff stress can be related to the lattice Jaumann rate of Kirchhoff stress through the plastic spin rate by

$$\overset{\triangledown}{\varsigma}_{ij} = \overset{\triangledown^*}{\varsigma}_{ij} - \varsigma_{kj}\Omega^P_{ik} - \varsigma_{ik}\Omega^P_{jk} \tag{2.81}$$

Thus, there is no difference between the lattice and the material Jaumann rate of Kirchhoff stress when there is no relative rotation of the material and the lattice.

When using the material Jaumann rate of Kirchhoff stress, the first line in the incremental principle of virtual power in the reference configuration (2.47) takes the form

$$\int_{V_0} \left(\overset{\triangledown}{\varsigma}_{ij}\, \delta\dot{\epsilon}_{ij} - \sigma_{ij}\left(2\dot{\epsilon}_{ik}\delta\dot{\epsilon}_{kj} - L_{kj}\delta L_{ki}\right) + \sum_\alpha \left(\dot{q}^{(\alpha)} - \dot{\tau}^{\varsigma(\alpha)}\right)\delta\dot{\gamma}^{(\alpha)} \right.$$

where the resolved shear stress rate is given by

$$\dot{\tau}^{\varsigma(\alpha)} = s^{(\alpha)}_i m^{(\alpha)}_j \left(\overset{\triangledown}{\varsigma}_{ij} - \sigma_{ik}\left(\dot{\epsilon}_{jk} - L^P_{kj}\right) + \sigma_{jk}\left(\dot{\epsilon}_{ik} - L^P_{ki}\right) \right) \tag{2.82}$$

In the discretized equations (2.72)-(2.73), the stiffness matrices $\mathbf{K_e}$, $\mathbf{K_{ep}}^{(\alpha)}$ and $\mathbf{K_p}^{(\alpha)}$ are the same for the material Jaumann rate of Kirchhoff stress as for the lattice Jaumann rate of Kirchhoff stress. However, the right hand side vectors are changed. The volume integral in the conventional load increment vector with an added volume force (2.77) now reads

$$\Delta t \int_V E^N_{ij} R_{ijkl} \sum_\alpha \dot{\gamma}^{(\alpha)} \mu^{(\alpha)}_{kl} \mathrm{d}V \tag{2.83}$$

The parentheses in the second line in the additional higher order load term with a subtracted volume contribution (2.78) now takes the form

$$\left(R_{ijkl} \sum_\beta \dot{\gamma}^{(\beta)} \mu^{(\beta)}_{kl} + \sum_\beta \dot{\gamma}^{(\beta)} s^{(\beta)}_k m^{(\beta)}_i \sigma_{kj} - \sum_\beta \dot{\gamma}^{(\beta)} s^{(\beta)}_j m^{(\beta)}_k \sigma_{ik} \right) \tag{2.84}$$

Near the end of the PhD study the author decided to formulate the elastic constitutive equations in the lattice Jaumann rate of Kirchhoff stress instead of the Jaumann rate of Kirchhoff stress based on material rotations as is common for isotropic plasticity theories, thus following most work on crystal plasticity. Therefore, most of the crystal plasticity work performed during this PhD study is based on the material Jaumann rate of Kirchhoff stress. Papers [P2]-[P5] and [P7] have employed the crystal plasticity formulation with

the Jaumann rate of Kirchhoff stress based on material rotations, whereas paper [P6] has employed the formulation with the Jaumann rate of Kirchhoff stress based on lattice rotations. In chapter 3.2 some results are presented for the problem considered in [P2] for analyses with the lattice Jaumann rate of Kirchhoff stress instead of the material Jaumann rate of Kirchhoff stress, and it is observed that for those analyses the results are only slightly affected by the choice of Jaumann rate. Similar calculations have been carried out for the problems considered in [P3] and [P4], and even smaller differences were observed there. Papers [P5] and [P7] only consider small deformations, so the choice of Jaumann rate will have a negligible effect in those studies.

Chapter 3
Summary of Results

This chapter contains the main results from the papers [P1]-[P7]. The numerical simulations in [P1] and a minor part of [P3] are based on the viscoplastic formulation of the theory by Fleck and Hutchinson (2001) for isotropic materials allowing for finite strains as described in section 2.1. The remaining papers are based on the strain gradient crystal plasticity formulation described in section 2.2.

Section 3.1 presents numerical results on size effects in isotropic materials containing either cylindrical voids or rigid inclusions in the micron range. This section is a summary of [P1].

Plastic flow localization in shear bands in single crystals with a geometrical imperfection subjected to plane strain uniaxial tensile loading is addressed in section 3.2, summarizing the paper [P2].

Experimental and numerical results for grain boundary effects in surface roughening of an aluminium specimen deformed in plane strain tension are presented in section 3.3. This section is a summary of [P3].

Section 3.4 contains strain gradient crystal plasticity results on the influence of grain size on yield and flow stress in polycrystalline metals. Simulations are performed for different higher order boundary conditions at the grain boundaries. The section is based on the results obtained in [P4].

Section 3.5 presents results for single crystals containing voids. In section 3.5.1 the focus is on the stress and deformation fields around a cylindrical void in a single crystal loaded by a far-field equibiaxial tensile stress under plane strain conditions, summarizing the paper [P5]. Results for a single crystal containing periodically arranged cylindrical voids based on [P6] are presented in section 3.5.2. Finally, section 3.5.3 contains a comparison between the strain gradient crystal plasticity theory and a discrete dislocation plasticity formulation for periodically arranged rectangular voids in a single crystal, serving as a summary of [P7].

3.1 Voids or inclusions in isotropic materials, [P1]

Void sizes in metallic materials are often on the order of magnitude of one micron, and therefore strain gradient effects are expected near the voids. Numerical studies have shown that void growth rates are significantly reduced when the void radius is small compared to the material length scale (Fleck and Hutchinson, 1997; Tvergaard and Niordson, 2004). In a material containing rigid inclusions, plastic deformation in the matrix material is restricted near the inclusion when no debonding occurs. In paper [P1] the viscoplastic strain gradient formulation for isotropic materials presented in section 2.1 is applied to

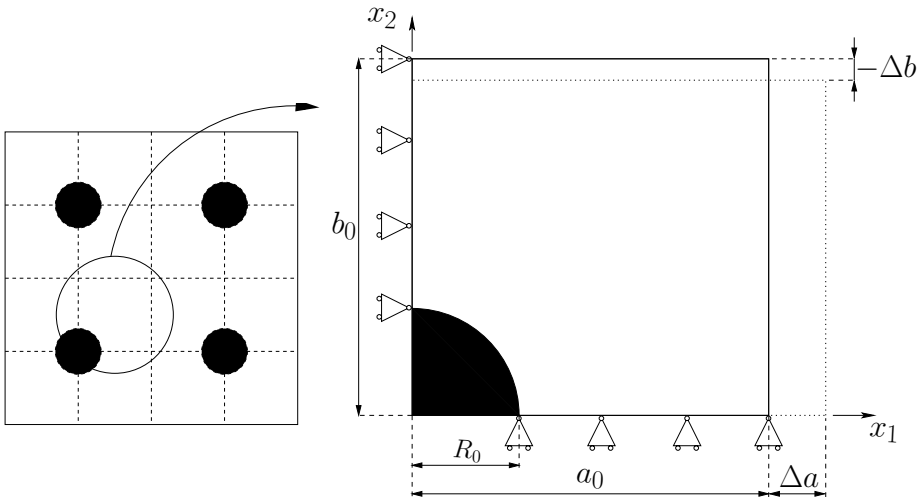

Figure 3.1 The plane strain cell model for a material with rigid inclusions or voids. (a) Periodically arranged inclusions/voids. (b) The unit cell used for the analyses.

study materials containing either voids or rigid inclusions under plane strain assumptions.

Figure 3.1 shows the plane strain cell model used to study the material containing uniformly distributed cylindrical voids or inclusions. The prescribed cell displacement rates are determined such that there is a fixed ratio of the average true stresses, σ_2/σ_1, by use of a special Rayleigh-Ritz finite element method (Tvergaard, 1976). When considering voids we have vanishing stress traction on the void surface, whereas in the case of inclusions we have vanishing displacement rates on the inclusion surface. The dimensions of the unit cell are given by $a_o/b_0 = 1$, and the initial spacings of the voids or inclusions are specified by $R_0/a_0 = 0.3$ corresponding to a volume fraction of 7.1%. The higher order boundary conditions along the four edges of the unit cell are specified by vanishing higher order stress, and when considering voids the higher order stress is also vanishing along the void surface. When considering inclusions results are presented for both vanishing higher order stress and vanishing plastic strain at the inclusion surface. The material parameters are given by the ratio of yield stress to Young's modulus, $\sigma_0/E = 0.003$, the Poisson's ratio, $\nu = 0.3$, the strain hardening exponent, $n = 10$, the strain rate hardening exponent, $m = 0.04$, and the reference strain rate, $\dot{\epsilon}_0 = 0.005$ s^{-1}. The overall strain rate in the x_1-direction is for the results presented here equal to the reference strain rate.

Figure 3.2 shows normalized average true stress, σ_1, in the x_1-direction as a function of the logarithmic strain, ϵ_1, in the x_1-direction for uniaxial tension ($\sigma_2 = 0$) of a material with voids for different values of the material length parameter relative to the void radius. The curve labeled local is obtained by letting $l_* = 0$. It can be seen that decreasing the void size (increasing the material length parameter) gives a more stiff behavior in the plastic range and also seems to increase the material yield stress.

The overall stress-strain curves at two different stress triaxialities for a material with inclusions are shown in figure 3.3 for different values of the material length parameter.

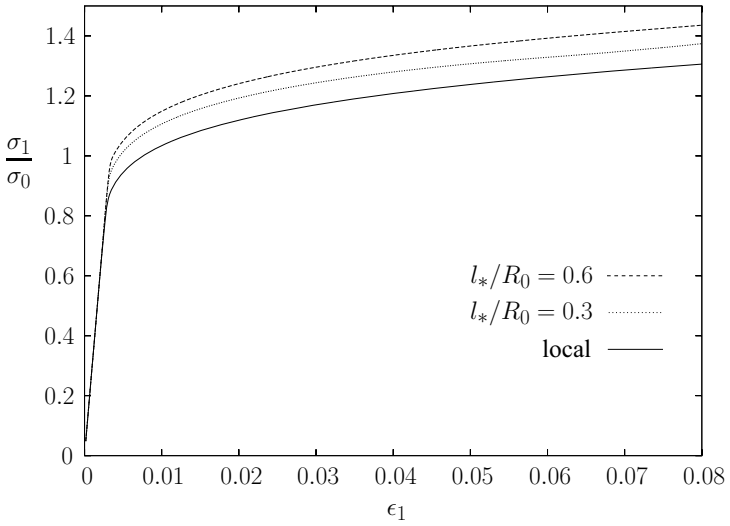

Figure 3.2 Overall uniaxial stress-strain response for a material with voids for different values of the material length scale.

The higher order boundary condition at the inclusion surface is here taken as vanishing plastic strain. The figure shows that the overall yield stress is increased when increasing the material length scale, as was also the case for the material containing voids.

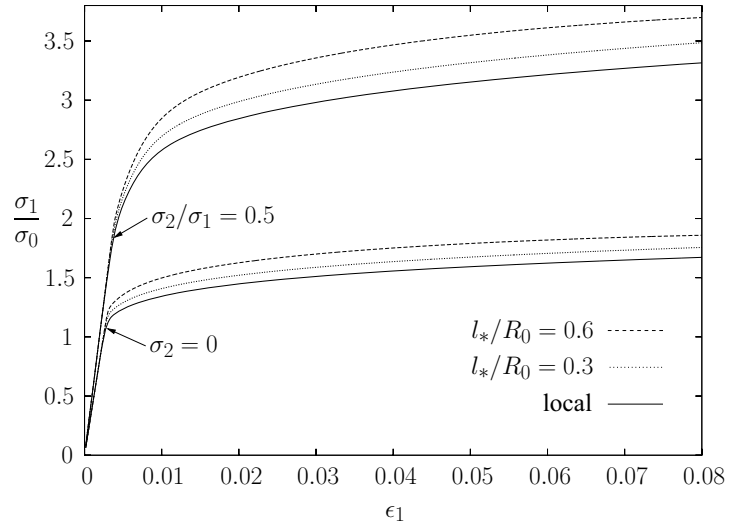

Figure 3.3 Overall stress-strain response for a material with rigid inclusions and two different stress triaxialities for different values of the material length scale.

Figure 3.4 shows uniaxial stress strain curves for a material containing rigid inclusions using two different higher order boundary conditions at the interface between the matrix material and the inclusion for different values of the material length scale. Since there is no higher order boundary conditions in a local formulation, there is only one curve labeled local in the figure. The two higher order boundary conditions used are the two extremes

of full constraint on plastic flow ($\epsilon^P = 0$) or no constraint on plastic flow ($\tau_i n_i = 0$). It can be seen that a full constraint on plastic flow leads to an overall stiffer response when compared to no constraint on plastic flow. Furthermore, there is a higher increase in the overall yield stress due to gradient effects when imposing a full constraint on plastic flow than for imposing no constraint on plastic flow at the inclusion surface.

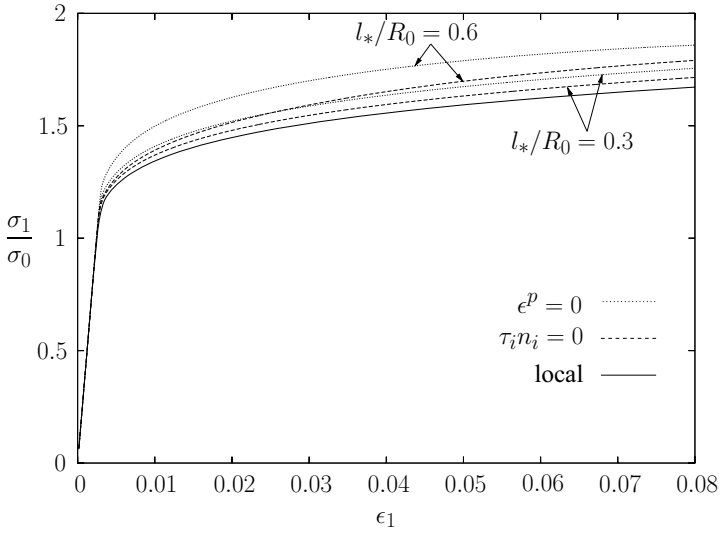

Figure 3.4 Overall uniaxial stress-strain response ($\sigma_2 = 0$) for a material with rigid inclusions using different higher order boundary conditions on the inclusion surface. Results are shown for different values of l_*/R_0.

3.2 Flow localization, [P2]

The localization of plastic flow in shear bands emanating from an initial imperfection in single crystals has been studied by use of classical rate-dependent crystal plasticity by Peirce et al. (1983). The width of the shear bands is entirely mesh dependent in that work. Several works have shown that an internal material length scale sets the width of the shear band and can remove the mesh dependence (Aifantis, 1984; Tvergaard and Needleman, 1995; Mikkelsen, 1999; Sluys and Estrin, 2000). The strain gradient crystal plasticity formulation presented in section 2.2 (using the material Jaumann rate of Kirchhoff stress described in section 2.2.4) has been used to study localization of plastic flow in plane strain tension in paper [P2].

The analyzed specimen is a single crystal with three in-plane slip systems and with a small initial geometrical imperfection given by a cosine function (see figure 3.5). Only the upper right quarter of the specimen is considered due to symmetry. The initial dimensions of the specimen are given by $L_0/b_0 = 3$. The higher order boundary conditions are taken as no constraint on the slips ($r^{(\alpha)} = 0$) on all four boundaries.

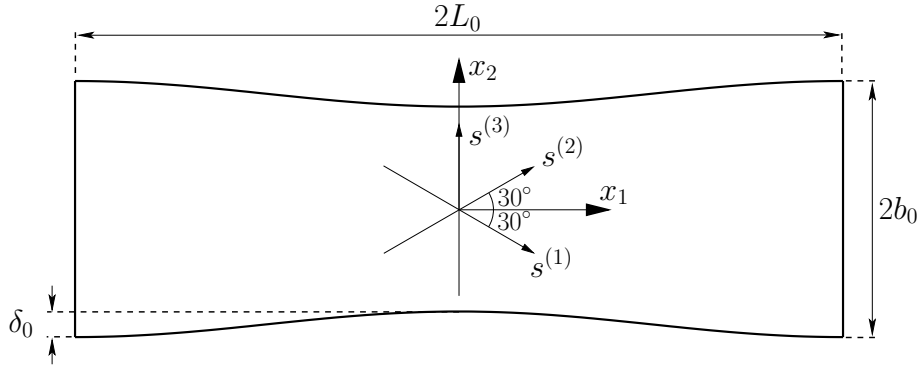

Figure 3.5 The tensile specimen considered with initial dimensions and slip systems. The initial imperfection is greatly exaggerated.

In the results presented here, the self-hardening modulus is taken to be given by

$$h(\gamma_{ea}) = h_0 / \cosh\left(\frac{h_0 \gamma_{ea}}{\tau_s - \tau_0}\right) \tag{3.1}$$

where the constant h_0 represents an initial hardening rate, τ_s is a saturation stress and $h = h_0$ would represent linear hardening. This form of the self-hardening modulus rapidly approaches zero. The material parameters are given by the initial slip resistance relative to the Young's modulus, $\tau_0/E = 0.001$, the Poisson's ratio, $\nu = 0.3$, the initial hardening modulus, $h_0/\tau_0 = 8.9$, the latent hardening index, $p = 1$, the strain rate hardening index, $m = 0.005$, and the reference slip rate, $\dot{\gamma}_0 = 0.001$ s^{-1}. The end displacement rate, $\dot{U}$, is applied such that the average strain rate in the tensile direction equals the reference slip rate.

The normalized overall nominal stress vs. the elongation for a local material ($l = 0$) is shown in figure 3.6. Curves are given for three meshes ranging from 30×10 elements to 90×30 elements, and also for a specimen without initial imperfections (labeled homogeneous). The curve labeled 'lattice Jaumann', 60×20 is for a calculation using the lattice Jaumann rate of Kirchhoff stress instead of the material Jaumann rate of Kirchhoff stress. The two curves for 60×20 elements are almost coinciding, thus the choice of Jaumann rate is not important for the considered analyses. The calculations with the three meshes give an almost identical response until the stress drop due to localization in shear bands begins at $U/L_0 \approx 0.13$. After that point, mesh sensitivity is observed.

Figure 3.7 shows results for a nonlocal material with the material length scale $l/b_0 = 0.02$. As for the local case, stress-strain curves are given for three different meshes and for a specimen with a homogeneous strain field. The curves for all three meshes are identical until the onset of localization in shear bands at $U/L_0 \approx 0.16$. After that, the curves for the two finest meshes are almost coinciding with the curve for the coarsest mesh lying a bit higher. Thus, there is much less mesh sensitivity for the nonlocal material than for the local material. It can also be seen that the nonlocal formulation has delayed the onset of localization in shear bands compared to the local formulation.

Deformed meshes and contours of the accumulated effective slip, γ_{ea}, for different

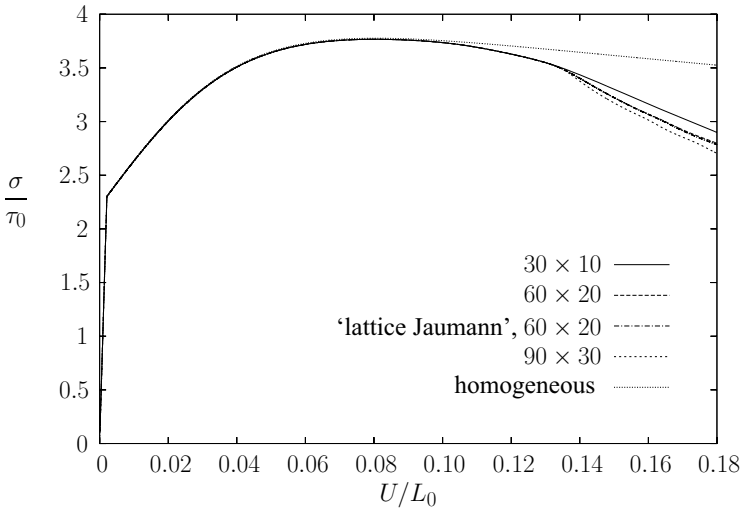

Figure 3.6 Normalized overall stress-strain curves using the conventional theory ($l = 0$) for different meshes.

values of the material length scale is shown in figure 3.8 using a mesh with 60×20 elements. Increasing the material length scale delays the shear band formation, and therefore the contours are not shown at the same elongation value. It is seen that the width of the shear bands increases with the material length scale.

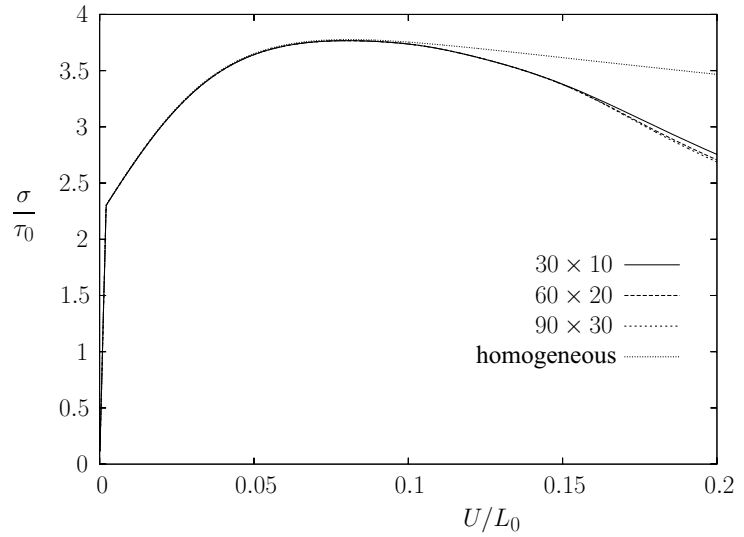

Figure 3.7 Normalized overall stress-strain curves using the nonlocal theory with $l/b_0 = 0.02$ for different meshes.

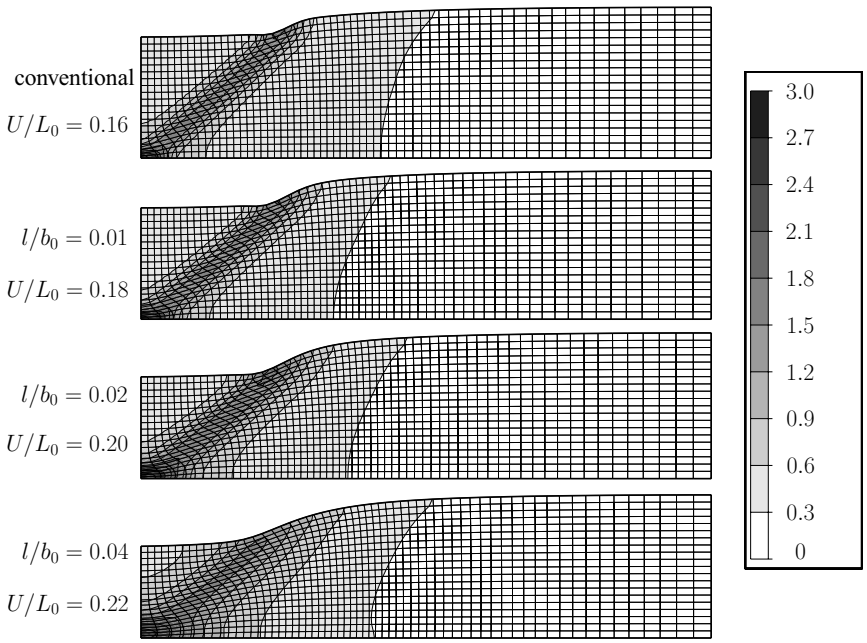

Figure 3.8 Deformed mesh and contours of accumulated effective slip, γ_{ea}, for different values of the internal material length scale relative to the height of the specimen for a mesh with 60×20 elements.

3.3 Grain boundary effects, [P3]

A common undesirable phenomenon in metal forming processes of polycrystalline metals is surface roughening. The effect derives from the crystallographic lattice mismatch from grain to grain and the resulting anisotropy in different grains. Experimental observations on aluminium alloy surfaces deformed in tension, sheet forming and rolling was made by Wilson and Lee (2001). They observed valleys with a width on the order of 3 μm near grain boundaries with grain sizes of 15 μm for a surface rolled to 30% reduction. Crystal plasticity finite element models based on several grains have been widely used to study surface roughening in polycrystals (e.g. Zhao et al. (2004)), but have not focused on the local deformation field near surface grain boundaries. Paper [P3] contains experimental and numerical investigations of the evolution in surface topography near grain boundaries during plastic deformation of metals.

Uniaxial tension tests on commercially pure aluminium sheets have been conducted in order to observe the surface profile near grain boundaries during plastic deformation. The sheets had through-thickness pancake-shaped grains and were mechanically polished prior to deformation. Images from a scanning electron microscope (SEM) of the surface profile near a grain boundary of the aluminium sheet after 10% engineering strain are shown in figure 3.9. A local gradient in surface profile can be observed within a few micrometers from the grain boundary.

The numerical simulations are based on the strain gradient crystal plasticity formulation described in section 2.2 (though with the material Jaumann rate of Kirchhoff stress) including the grain boundary energy potential described in section 2.2.2 with the param-

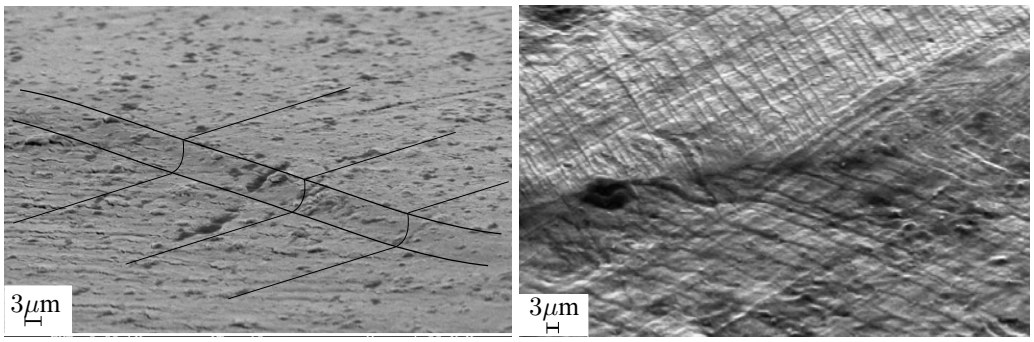

Figure 3.9 SEM images of the surface after 10 percent strain. The left image shows a grain boundary marked to emphasize the change in surface profile, and the right image shows a grain boundary and slip lines on either side of it.

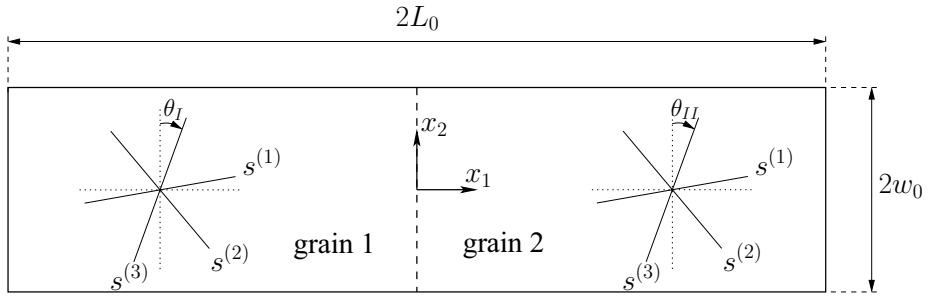

Figure 3.10 The bicrystal considered in the analyses with three slip systems.

eter κ. The studied bicrystal undergoing in-plane tensile deformation is shown in figure 3.10. The two grains are separated by a grain boundary at $x_1 = 0$. Three in-plane slip systems are used at a relative orientation of 60° from one to the next, and their absolute orientation given by the angles θ_I and θ_{II}. The end displacement rate at $x_1 = -L_0$ is set to zero and the end displacement rate at $x_1 = L_0$ is prescribed as $\dot{U}$. Furthermore, the higher order tractions vanish on the external boundary. The material parameters used for the analyses are the initial slip resistance $\tau_0/E = 0.001$, the Poisson's ratio $\nu = 0.3$, the latent hardening index $p = 1$, and the strain rate hardening index $m = 0.02$. Linear hardening is assumed with the hardening modulus $h_0/\tau_0 = 10$. The prescribed end displacement rate is given by $\dot{U}/(2L_0) = \dot{\gamma}_0$.

The results presented here are all taken at the overall strain $\overline{\epsilon}_1 = U/(2L_0) = 5\%$. The surface profile near the grain boundary for a bicrystal with the same orientation of slip systems ($\theta_I = \theta_{II} = 0$) and the same material parameters in each grain is shown in figure 3.11 for $l/w_0 = 0.1$. The profiles are only shown for $x_1 \geq 0$ due to symmetry. Results are displayed for five values of the parameter κ describing the grain boundary. The curve labeled $\kappa \to \infty$ is obtained using $\gamma^{(\alpha)} = 0$ on the grain boundary. It is seen that for $\kappa = 0$ the deformation state is homogeneous throughout the specimen, and that there is an increase in the profile at the grain boundary as the value of κ increases.

Surface profiles for a bicrystal where the two grains have the same orientation of the slip systems but the initial slip resistance in grain one is half that of grain two ($\tau_0^{II}/\tau_0^I = 2$) are shown in figure 3.12 for $l/w_0 = 0.1$. The curve for $\kappa = 0$ decreases monotonically

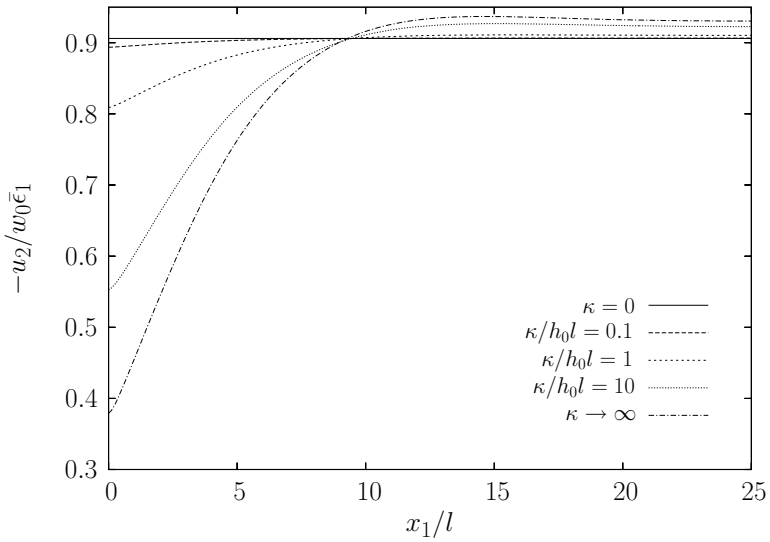

Figure 3.11 The surface profile near the grain boundary for a bicrystal with $\theta_I = \theta_{II} = 0$ and the same material parameters for $l/w_0 = 0.1$ at $\bar{\epsilon}_1 = 5\%$.

from the strong grain to the weak grain, whereas for $\kappa \to \infty$ the profile contact a re-entrant corner at the grain boundary, due to the restriction on slips.

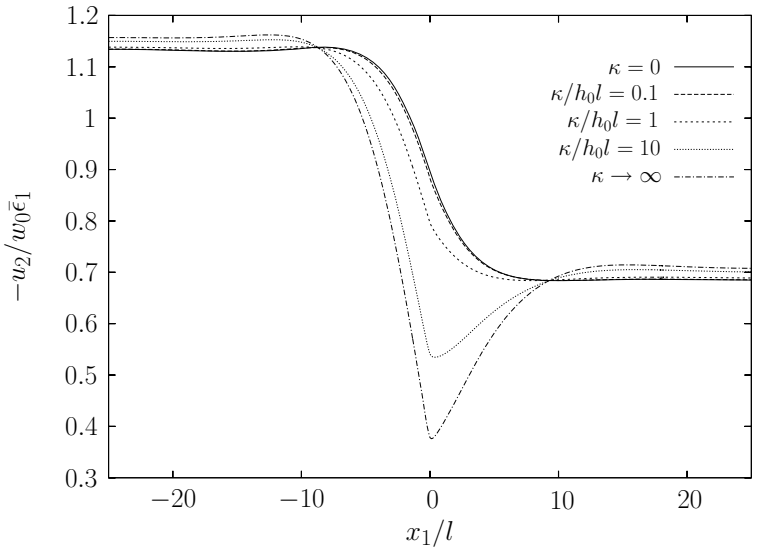

Figure 3.12 The surface profile near the grain boundary for a bicrystal with $\theta_I = \theta_{II} = 0$ and initial slip resistances $\tau_0^{II}/\tau_0^I = 2$ for $l/w_0 = 0.1$ at $\bar{\epsilon}_1 = 5\%$.

Figure 3.13 shows surface profiles for a bicrystal with a lattice mismatch specified by $\theta_I = 0^\circ$ and $\theta_{II} = 15^\circ$. Curves are displayed for the two extreme cases $\kappa = 0$ and $\kappa \to \infty$ using two values of l/w_0. For $\kappa = 0$ there is only a slight difference in the profile for the two considered length scales, whereas the length scale value has a significant influence on the profiles for $\kappa \to \infty$.

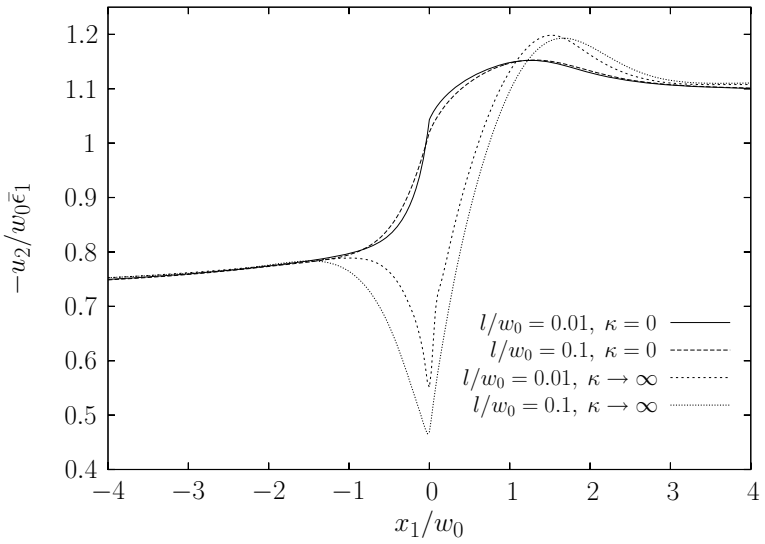

Figure 3.13 The surface profile near the grain boundary for a bicrystal with $\theta_I = 0°$ and $\theta_{II} = 15°$ and the same material parameters for $\kappa \to \infty$ and $\kappa = 0$ at $\bar{\epsilon}_1 = 5\%$ for two values of l/w_0.

3.4 Grain size effects, [P4]

Hall (1951) and Petch (1953) independently found that the yield strength in mild steel varies with the grain size as $\sigma = \sigma_0 + kd^{-1/2}$, where d is the mean grain size, σ_0 is the yield stress in the imaginary situation with infinitely large grains, and k is a material constant. One explanation for the observed grain size dependence is that grain boundaries act as obstructions to dislocation motion. Thus, plastic strain gradient induced geometrically necessary dislocations are expected near the grain boundaries. For decreasing grain sizes the area with an increased density of geometrically necessary dislocations near the grain boundaries relative to the total area of the grain are increased. Strain gradient crystal plasticity analysis including a grain boundary energy potential to simulate different higher order boundary conditions at the grain boundaries of a polycrystal are presented in paper [P4]. The material model used is as described in section 2.2, though with the material Jaumann rate of Kirchhoff stress.

The considered polycrystal including 40 grains (single crystals) of which 24 are six-sided, 8 are five-sided and 8 are four-sided is shown in figure 3.14. The dimensions of the polycrystal are taken as $a_0/b_0 = 1.5$. Each grain has three slip systems at a relative orientation of $60°$ from one to the next and an absolute orientation given by the angle θ. The angle θ in each grain obtained from a random number generator is also shown in the figure. The polycrystal is subjected to plane strain uniaxial loading in the x_1-direction, and the four sides are required to remain straight using a special Rayleigh-Ritz finite element method (Tvergaard, 1976). The higher order boundary conditions on the external boundaries of all the four and five-sided grains are taken as vanishing higher order traction, whereas the external boundaries of the six-sided grains are treated as internal grain boundaries. This is chosen to simulate symmetry boundary conditions along the four external boundaries, even though this can only be achieved in the local case when

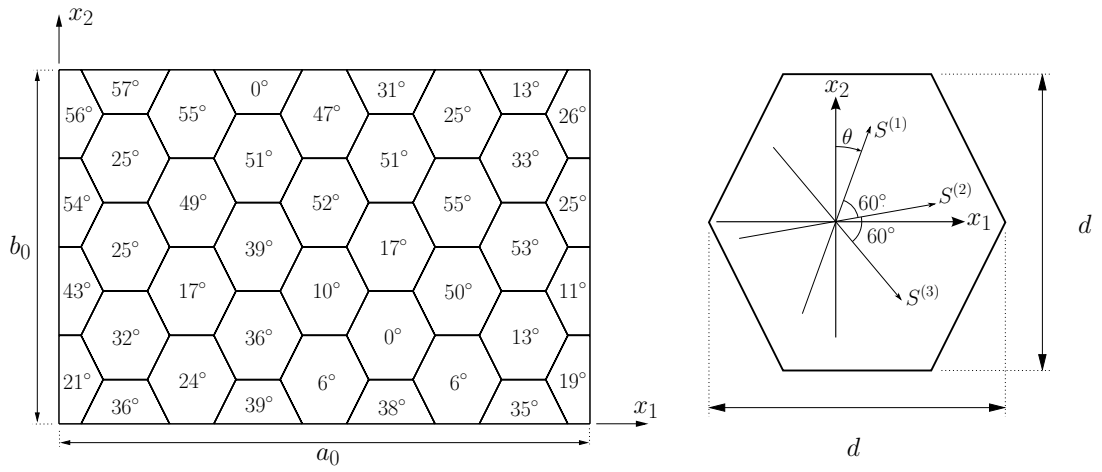

Figure 3.14 The analyzed polycrystal consists of 40 grains with grain size d. The orientation given by the angle θ is given in each grain.

the slip systems in the four an five sided grains are oriented symmetrically around the x_1- and x_2-direction. The grain boundary energy potential described by the parameter κ is applied at all grain boundaries.

The self hardening modulus used for the simulations is given by a power law type of the form

$$h(\gamma_{ea}) = h_0 \left(\frac{h_0 \gamma_{ea}}{\tau_0 n_h} + 1 \right)^{n_h - 1}, \quad \gamma_{ea} = \sum_{\alpha} \int \dot{\gamma}_e^{(\alpha)} \mathrm{d}t \tag{3.2}$$

where the constant h_0 represents an initial hardening rate, n_h is the hardening exponent, and γ_{ea} is the accumulated effective slip. The material parameters used in the calculations are given by the initial slip resistance relative to Young's modulus, $\tau_0/E = 0.001$, the Poisson's ratio, $\nu = 0.3$, the initial hardening rate, $h_0/\tau_0 = 10$, the latent hardening index, $p = 1.4$, the hardening exponent, $n_h = 0.1$, and the strain rate hardening index, $m = 0.01$. The applied end displacement rate, $\dot{U}_1$, is specified so that $\dot{U}_1/a_0 = \dot{\gamma}_0$.

Figure 3.15 shows curves for the average true stress in the x_1-direction, σ, versus average logarithmic strain in the x_1-direction, ϵ, for the polycrystal with grain sizes relative to the material length scale of $d/l = 5$. Results are displayed for five values of κ, ranging from $\kappa = 0$ (vanishing higher order stresses) to $\kappa \to \infty$ (obtained by restricting $\dot{\gamma}^{(\alpha)} = 0$). The two extreme conditions, $\kappa = 0$ and $\kappa \to \infty$, give the lower and upper curve, whereas other values of κ gives intermediate stress strain curves.

Stress strain curves for a polycrystal with different grain sizes are shown in figure 3.16 for the surface energy parameter $\kappa/(\tau_0 l) = 100$. It it seen that the level of the stress strain curves is increasing with decreasing grain sizes. When the increase in flow stress, $(\sigma - \sigma_0)/\tau_0$, at 0.1 logarithmic strain is plotted against the grain size and fitted to a function of the form d^{-n}, the best fit exponent is found to be $n = 0.98$. With the value $\kappa/(\tau_0 l) = 10$ the best fit parameter is $n = 1.09$. Results for the initial yield stress has only been fitted for $\kappa \to \infty$, because the initial yield stress can only be changed for extremely

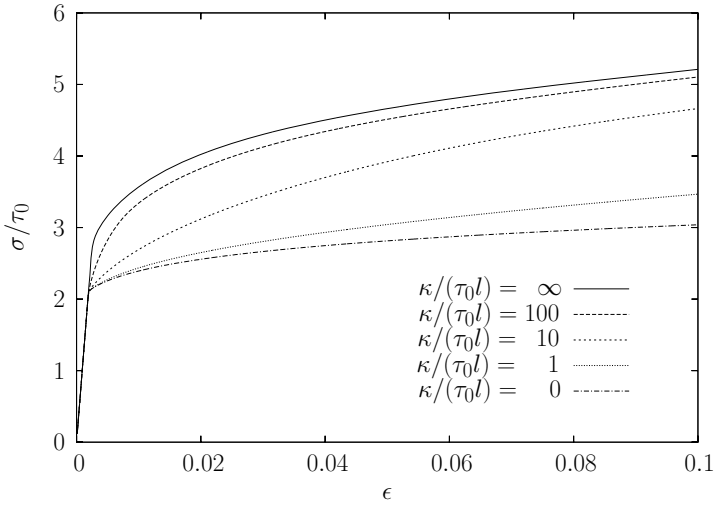

Figure 3.15 Stress strain curves for different grain boundary surface energy parameters for a polycrystal with random grain orientations and grain size $d/l = 5$.

high values of $\kappa/(\tau_0 l)$. For $\kappa \to \infty$ the best fit exponent for the initial yield stress is found to be $n = 1.21$. These values are somewhat higher than what is predicted from the classical Hall-Petch relationship with exponent $n = 0.5$.

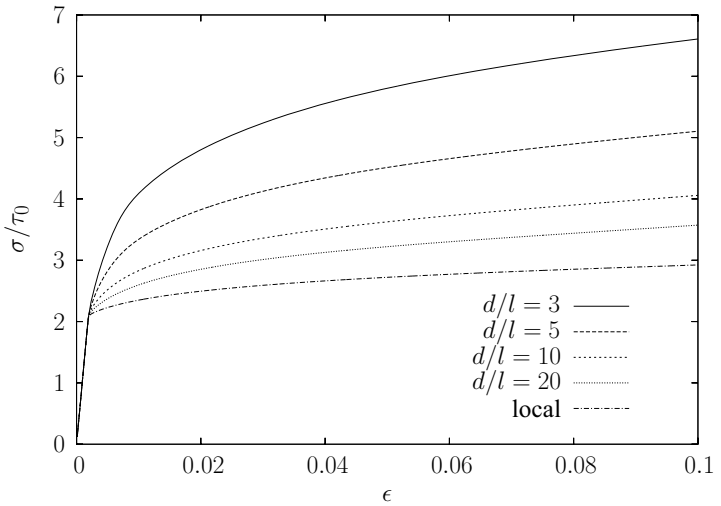

Figure 3.16 Stress strain curves for different grain sizes and randomized grain orientations. The grain boundary surface energy parameter is set to $\kappa/(\tau_0 l) = 100$.

3.5 Voids in single crystals, [P5]-[P7]

Actual void sizes in metals are often so small that they can easily exist inside a single grain of a polycrystalline material. Thus, a crystal plasticity model is suitable to analyze plastically deforming microscopical voids inside a single grain, and also larger voids or several interacting voids within a single crystal.

3.5.1 Stress and deformation fields around a cylindrical void, [P5]

Recent studies (Kysar et al., 2005; Gan and Kysar, 2007) have used anisotropic slip line theory to derive the stress and deformation fields associated with a cylindrical void in a single crystal. Those studies, along with related experimental and numerical studies by Gan et al. (2006), have shown that there are angular regions around the voids within which slip on single slip systems occurs. Paper [P5] studies a cylindrical void in a single crystal loaded by a far-field equibiaxial tensile stress subjected to plane strain conditions using the strain gradient crystal plasticity formulation.

The analyzed square hexagonal close-packed single crystal containing a void with a diameter of one tenth of the side length is shown in figure 3.17. The three slip systems are oriented at the angle 60° from one to the next. The loading is applied as equal end displacements in the x_1- and x_2-direction. The higher order boundary conditions are applied as vanishing higher order stress on the four external edges and on the void surface.

The material parameters used in the calculations are chosen to match the numerical simulations in Gan et al. (2006) and are Young's modulus, $E = 63.9$ GPa, Poisson's ratio, $\nu = 0.36$, initial slip resistance, $\tau_0 = 1$ MPa, reference slip rate, $\dot{\gamma}_0 = 0.001$ s^{-1}, and strain rate hardening index, $m = 0.03$. In the results presented in this section there are no strain hardening ($h_0 = 0$) both for the local and the nonlocal calculations. The prescribed end displacement rates, $\dot{U}$, are given by $\dot{U}/(2a_0) = 0.1\dot{\gamma}_0$, and the results presented are all taken at the deformation level given by $U/(2a_0) = 3.5 \times 10^{-5}$.

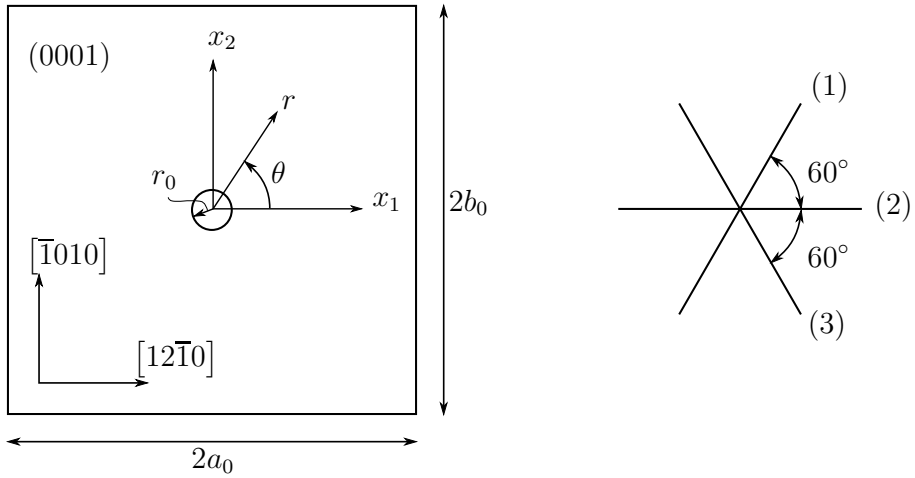

Figure 3.17 The analyzed cylindrical void in an HCP single crystal showing coordinate systems, dimensions, slip systems and crystallographic orientation.

Figure 3.18 shows contours of accumulated slip in the three slip systems and the total slip, $\gamma_{tot} = \gamma^{(1)} + \gamma^{(2)} + \gamma^{(3)}$ for a local material ($l = 0$). It is seen that in the upper right quadrant slip system one is mostly active in the region $0 \leq \theta \leq 30^\circ$, slip system two is mostly active in the region $30^\circ \leq \theta \leq 60^\circ$, and slip system three is mostly active in the region $60^\circ \leq \theta \leq 90^\circ$. The location of angular sectors with only one effective slip system is as predicted by anisotropic slip line theory in Gan and Kysar (2007). Slip contours

for a nonlocal material with a void size relative to the material length scale of $r_0/l = 1$ are shown in figure 3.19. Here, all slip occurs in localized bands in the slip directions to minimize the slip gradients in the slip directions. It is also notable that the magnitude of slip is significantly lower than for the local material.

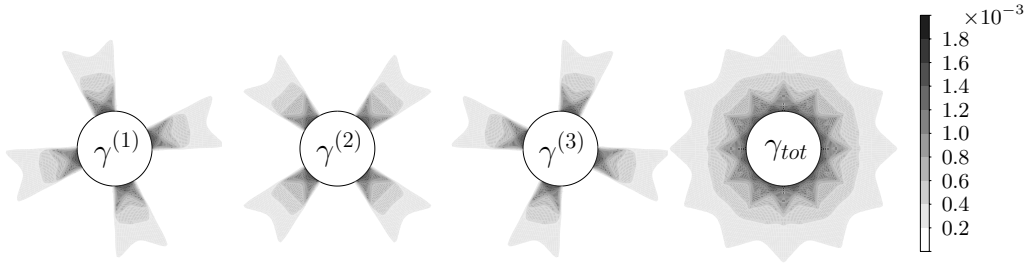

Figure 3.18 Contours of slip in the three slip systems using a local formulation ($l = 0$).

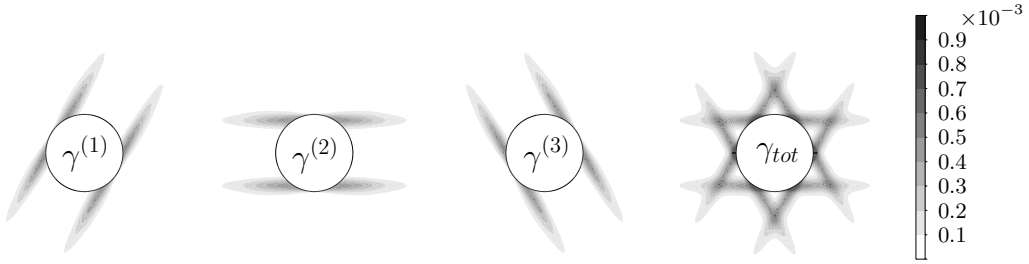

Figure 3.19 Contours of slip in the three slip systems for a nonlocal material with $r_0/l = 1$.

The stress components expressed in polar coordinates around the void surface are shown in figure 3.20 for the local material. The radial stress component, σ_{rr}, and the polar shear stress component, $\sigma_{r\theta}$, vanish on the void surface as expected. The circumferential stress, $\sigma_{\theta\theta}$, is periodic with a period of 30° and with an average value close to $2.3\tau_0$. The analytical slip line solution in Gan and Kysar (2007) predicts $\sigma_{\theta\theta} \approx 2.098\tau$ on the void surface. This difference is mainly due to the viscoplastic effects in the present formulation which are not accounted for in the analytical slip line solution.

Figure 3.21 displays the stress components expressed in polar coordinates around the void surface for a nonlocal material with $r_0/l = 1$. As for the local material the radial stress and the shear stress vanish on the void surface. The magnitude of the circumferential stress is much larger than for the local material. Here, $\sigma_{\theta\theta}$ varies between $4\tau_0$ and $12\tau_0$.

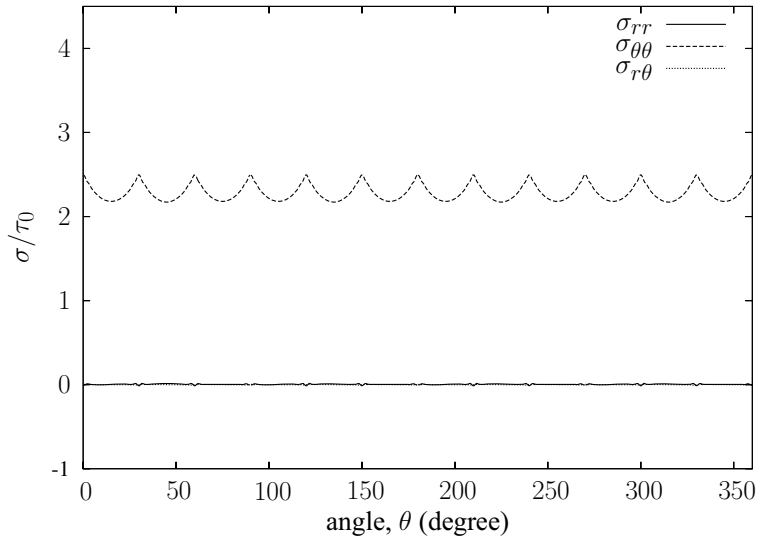

Figure 3.20 Stress components in polar coordinates along the path $r/r_0 = 1.0$ for a local material.

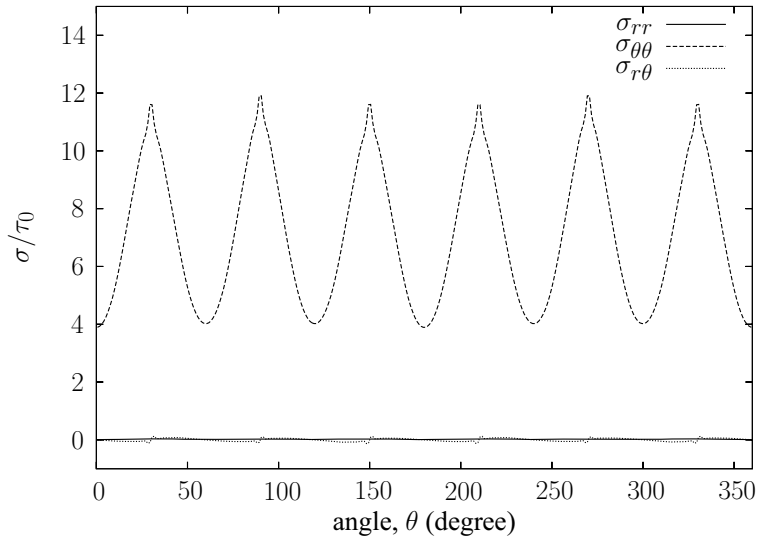

Figure 3.21 Stress components in polar coordinates along the path $r/r_0 = 1.0$ for a nonlocal material with $r_0/l = 1$.

3.5.2 Void growth, [P6]

An important failure mechanism in ductile metals is void growth to coalescence of microscopic voids. Void growth in single crystals have been studied analytically and numerically to investigate e.g. effects of lattice orientation on the overall response and on the shape of the deformed voids (Nemat-Nasser and Hori, 1987; Potirniche et al., 2006). Those studies are size independent. However, as mentioned in chapter 3.1, the void size can have a significant effect on void growth. The effect of void size on void growth in a single crystal with uniformly distributed cylindrical voids is studied in paper [P6].

The analyzed cell model and the orientation of the three slip systems are shown in figure 3.22. The unit cell containing a void with radius r_0 in the center is initially quadratic ($a_0 = b_0$). The cell model is loaded by imposing periodic boundary conditions on the unit cell edges as $\Delta u_i = \overline{\epsilon}_{ij}\Delta x_j$, where Δu_i is the difference between displacements on opposite sides of the unit cell specified by the difference in position vector Δx_j, while $\overline{\epsilon}_{ij}$ is the imposed macroscopic strain. These strain components are specified as $\overline{\epsilon}_{12} = \overline{\epsilon}_{21} = 0$ and $\overline{\epsilon}_{11} = U/a_0$, where U/a_0 is the applied strain in the x_1-direction. The ratio $\overline{\epsilon}_{22}/\overline{\epsilon}_{11}$ is determined by use of a special Rayleigh-Ritz finite element method, such that there is a fixed ratio of the average true stresses $\sigma_2/\sigma_1 = \kappa$. Periodicity for the displacements and stresses and for the slip rates and higher order stresses is enforced at the unit cell edges. Boundary conditions at the void surface are specified by vanishing tractions and higher order tractions.

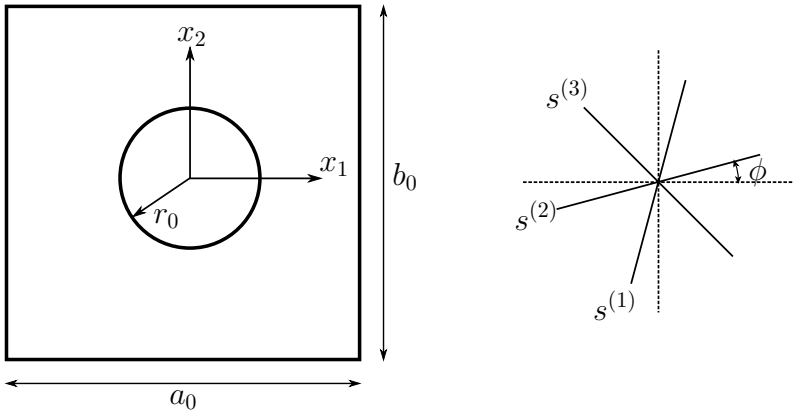

Figure 3.22 The analyzed unit cell with a cylindrical void. The absolute orientation of the three slip systems, with the relative orientation of 60° from one to the next, are given by the angle ϕ.

The material parameters are taken as initial slip resistance relative to Young's modulus $\tau_0/E = 0.001$, Poisson's ratio $\nu = 0.3$, latent hardening index $p = 1.0$, self hardening modulus $h_0/\tau_0 = 10$, power hardening exponent $n = 0.1$, reference slip rate $\dot{\gamma}_0 = 0.001$ s^{-1} and strain rate hardening index $m = 0.03$. The imposed strain rate in the x_1-direction is given by $\dot{U}/a_0 = \dot{\gamma}_0$. The results presented here are for an initial void volume fraction $f_0 = 12.6\%$.

Figure 3.23 shows results for different stress ratios κ and void sizes relative to the material length scale using the slip system orientation given by $\phi = 0^\circ$. The normalized

true stress in the x_1-direction is displayed in figure 3.23a as a function of the logarithmic strain in the x_1-direction, ϵ_1. It is seen that small voids allow much larger overall stress levels for all stress ratios. The maximum attainable stress level is almost independent of the stress ratio, κ, within the range considered here, whereas the strain at this stress maximum decreases considerably with decreasing values of κ. The ratio of void volume to initial void volume is shown as a function of ϵ_1 in figure 3.23b. In accordance with conventional predictions (Koplik and Needleman, 1988) it is observed that more void growth is predicted for larger stress ratios. Furthermore it is seen that the void size has a minor effect on void growth for $\kappa = 1$, and that smaller voids suppress void growth for $\kappa = 0.75$ and 0.5.

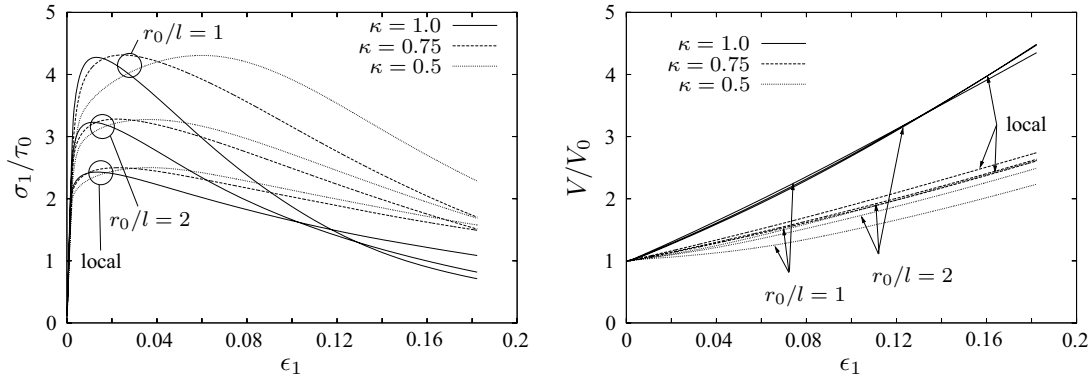

Figure 3.23 Results for the slip system orientation $\phi = 0°$. (a) Overall response in terms of the true stress vs. logarithmic strain. (b) Relative void growth vs. logarithmic strain. Curves are shown for different stress ratios and void sizes.

Figures 3.24 and 3.25 show contour plots of slip at the overall deformation $U/a_0 = 0.1$ for equibiaxial loading ($\kappa = 1.0$) with the lattice orientations $\phi = 0°$ and $\phi = 15°$, respectively. The figures present slip distributions on each of the three slip systems as well as the total slip. For $\phi = 0°$ the local material model predicts equal distributions of total slip between the voids along the x_1 and the x_2-directions (figure 3.24a). The corresponding results for a nonlocal calculation with $r_0/l = 1$ in figure 3.24b shows that gradients are suppressed along the slip planes, as observed in section 3.5.1, and here leads to well developed slip bands on slip systems one and three connecting voids in the x_2-direction. The slip distributions for the crystal orientation rotated $15°$ are presented in figures 3.25a and 3.25b for a local calculation and for a nonlocal calculation with $r_0/l = 1$, respectively. It is seen that both for the local and the nonlocal analysis symmetries exist along lines at a $45°$ angle between the coordinate axes, due to the same symmetry of the slip systems and the equibiaxial loading. For both of the considered crystal orientations more smooth void shapes are observed for micron sized voids, when compared to local predictions.

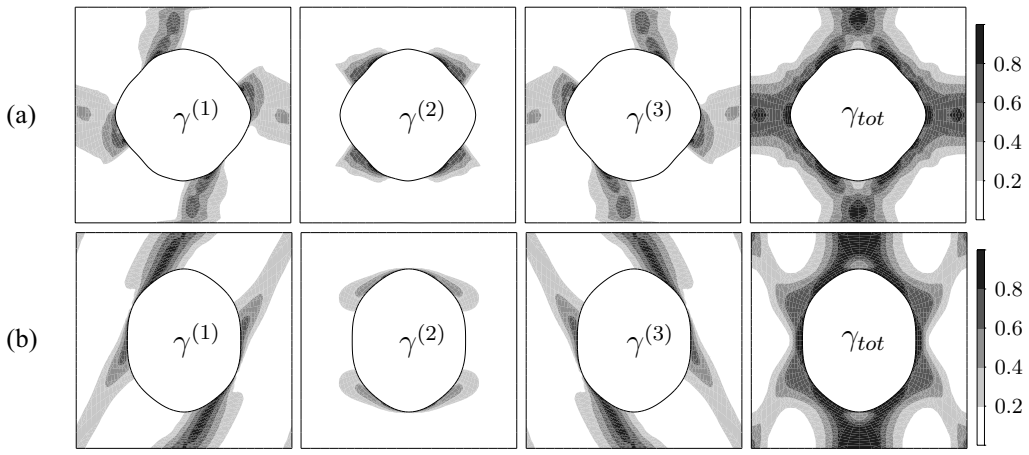

Figure 3.24 Contours of slip on the three slip systems and the total slip at the overall deformation $U/a_0 = 0.1$ for a crystal with slip system orientation $\phi = 0^\circ$ and stress ratio $\kappa = 1.0$. Both results from a local calculation (a) and from a nonlocal calculation with $r_0/l = 1$ (b) are shown.

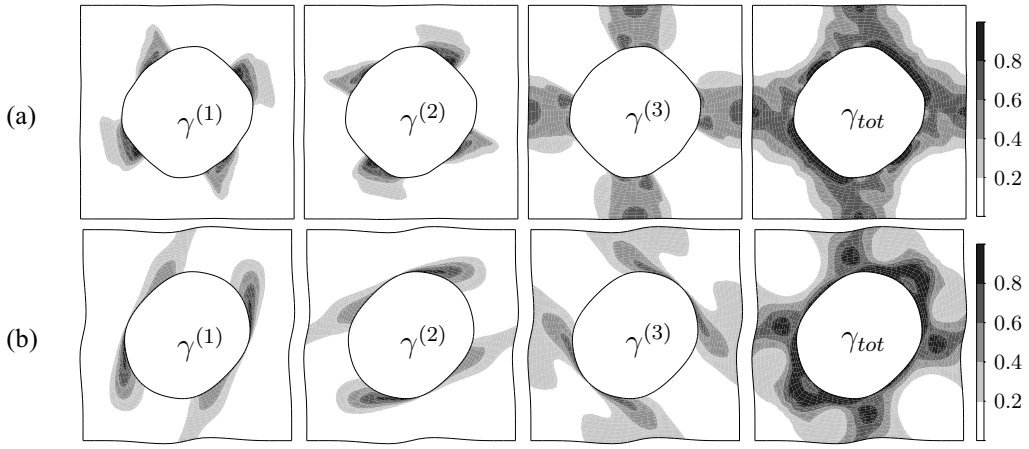

Figure 3.25 Contours of slip on the three slip systems and the total slip at the overall deformation $U/a_0 = 0.1$ for a crystal with slip system orientation $\phi = 15^\circ$ and stress ratio $\kappa = 1.0$. Both results from a local analysis (a) and from a nonlocal analysis with $r_0/l = 1$ (b) are shown.

3.5.3 Comparison to discrete dislocation plasticity predictions, [P7]

Discrete dislocation plasticity is based on the motion of edge dislocations represented as line singularities in an elastic medium. The dislocations can nucleate and glide on active slip systems. The long range interactions of the dislocations are accounted for through their elastic fields while constitutive rules are prescribed for short range interactions. Discrete dislocation plasticity simulations of voided crystals are restricted to the micro-void regime by current computational capabilities. In paper [P7] size effects in periodic voided single crystals are analyzed using both discrete dislocation plasticity and the strain gradient crystal plasticity model described in section 2.2, though using the material Jaumann rate of Kirchhoff stress. The paper focuses on the effect of loading conditions on the void size effect and on employing the discrete dislocation calculations to extract the appropri-

ate length scale for use in the strain gradient crystal plasticity model.

The periodic voided single crystal and the unit cell analyzed are shown in figure 3.26. A crystal with two symmetric slip systems $\phi^{(1)} = -\phi^{(2)} = 54.7^\circ$ and a crystal with three slip systems $\phi^{(1)} = -\phi^{(2)} = 54.7^\circ$ and $\phi^{(3)} = 0^\circ$ are considered, where $\phi^{(\alpha)}$ denotes the orientation with respect to the x_1-axis. The aspect ratio of the unit cell ($d \times d\tan\phi^{(1)}$) ensures periodicity of the motion of the discrete dislocations on discrete slip planes. The rectangular void is centrally located in the unit cell and has the same aspect ratio as the unit cell. The voided crystal is loaded by imposing periodic boundary conditions on the unit cell edges as described in section 3.5.2. Periodicity for the slip rates in the strain gradient calculations and for the motion of the dislocations in the discrete dislocation calculations are also enforced on the unit cell edges. Traction free boundary conditions are imposed on the void surface. Furthermore, in the strain gradient calculations the higher order stress is taken to vanish on the void surface, and in the discrete dislocation calculations the dislocations are assumed to be free to exit the crystal at the void surface. Both shear loading and equibiaxial straining under plane strain conditions are considered here. In shear, the strain components are specified as $\overline{\epsilon}_{12} = \overline{\epsilon}_{21} = \gamma/2$, where γ is the applied shear strain. Under biaxial straining the strain components are specified as $\overline{\epsilon}_{11} = \overline{\epsilon}_{22} = \epsilon_{\mathrm{v}}/2$, where ϵ_v is the imposed two-dimensional volumetric strain.

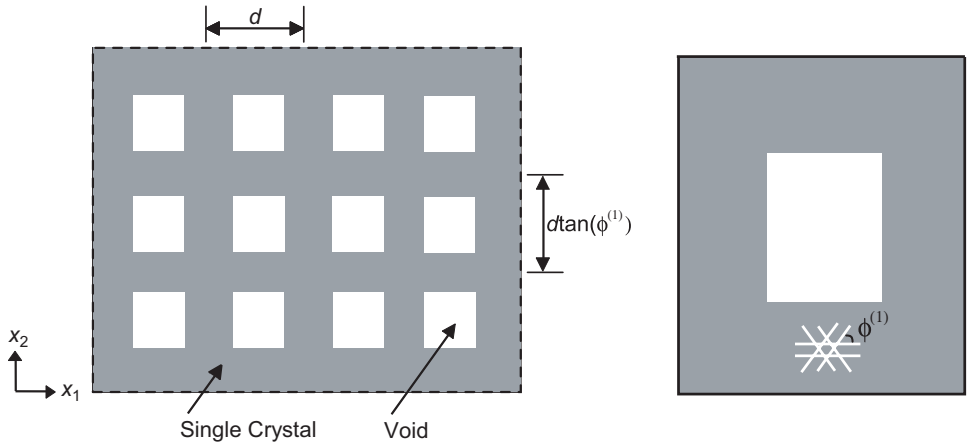

Figure 3.26 The analyzed single crystal with a periodic arrangement of rectangular voids and the unit cell considered.

The elastic material parameters are Young's modulus $E = 70$ GPa and Poisson's ratio $\nu = 0.33$. The material properties used in the discrete dislocation calculations are specified as randomly distributed dislocation sources with a density $300\ \mu\mathrm{m}^{-2}$ on the slip planes spaced $100b$ apart, where b is the Burgers vector taken to be $b = 0.25$ nm. The nucleation strength for each source is taken to be $\tau_{nuc} = 50$ MPa with the nucleation time 10 ns. The drag coefficient for dislocation motion is $B = 10^{-4}$ Pas and the annihilation distance is $6b$. Obstacles of strength 150 MPa are randomly distributed with density $600\ \mu\mathrm{m}^{-2}$. The source and obstacle densities are chosen to ensure that unvoided crystals with unit cells of size $0.5\ \mu\mathrm{m} \leq d \leq 8.0\ \mu\mathrm{m}$, which is the size range for the considered voided crystals, display no size effects. The plasticity parameters in the strain gradient

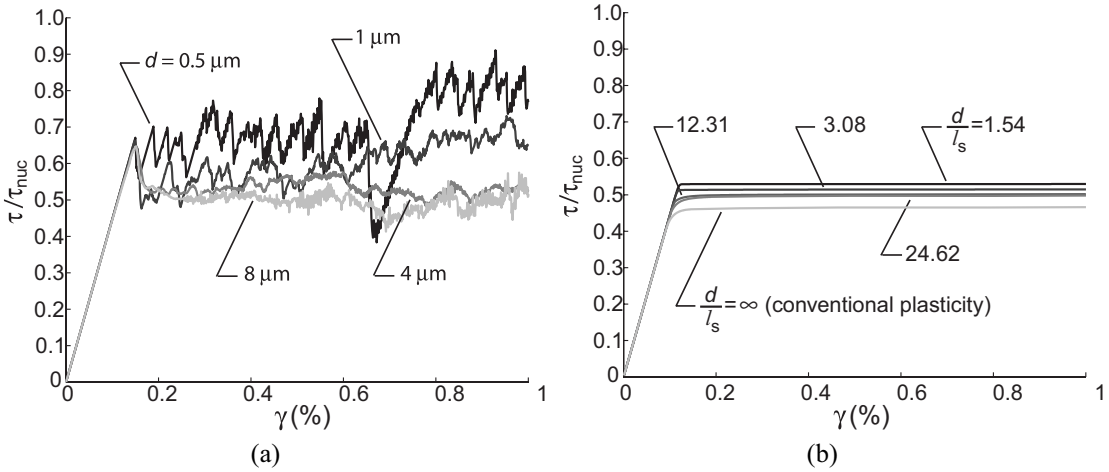

Figure 3.27 The shear response of the three slip system crystal with 4% void volume fraction. (a) Discrete dislocation predictions. (b) Strain gradient plasticity predictions.

calculations were chosen to match the shear response obtained from discrete dislocation calculations in the size independent limit with an unvoided non-hardening crystal using three slip systems. The values chosen are slip resistance $\tau_0 = 30$ MPa, reference slip rate $\dot{\gamma}_0 = 0.001$ s^{-1} and strain rate hardening index $m = 0.02$.

The normalized shear stress versus shear strain response of the voided crystal with three slip systems and initial void volume fraction $v_f = 4\%$ under shear loading is shown in figure 3.27. Results are given both for discrete dislocation calculations and strain gradient calculations for different values of the void spacing d. No clear size effect is observed over the range of void spacings analyzed for the discrete dislocation plasticity predictions (taking into account the inherent variability in the discrete dislocation predictions). Similarly, the strain gradient plasticity predictions of the shear response, only display a small size dependence over the range of void spacings relative to the material length parameter considered here.

Figure 3.28 shows the biaxial stress, σ, versus strain, $\epsilon_{\rm v}$, responses of the voided crystal with three slip systems and initial void volume fraction $v_f = 4\%$ equibiaxially strained. A clear size effect in the stress-strain response is observed both for the discrete dislocation predictions and for the strain gradient predictions. Furthermore, unlike under shear loading the crystals display a hardening response for the smaller void spacings.

A quantitative comparison between discrete dislocation and strain gradient plasticity predictions requires that the material length scale must be specified explicitly in the strain gradient plasticity calculations. The variation of flow strengths of the voided crystals during shear loading and equibiaxial straining are given in figure 3.29 with the choice $l = 0.325$ μm. Both discrete dislocation and strain gradient plasticity predictions are shown for crystals with different void volume fractions and number of slip systems. The strain gradient results are fitted to a power form relation. The flow stress, τ_f, under shear loading is defined as the average value of τ over the strain range $0.0075 \leq \gamma \leq 0.01$. Similarly, the flow strength, σ_f, in equibiaxial straining is defined as the average value of σ over the range $0.0075 \leq \epsilon_{\rm v} \leq 0.01$. It is seen that with the choice $l = 0.325$ μm excellent

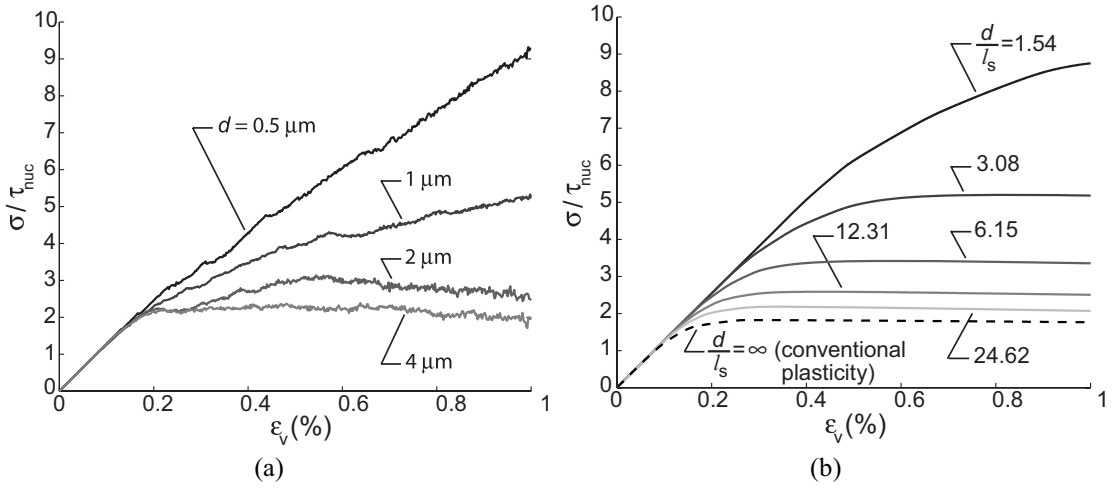

Figure 3.28 The equibiaxial straining response of the three slip system crystal with 4% void volume fraction. (a) Discrete dislocation predictions. (b) Strain gradient plasticity predictions.

agreement is obtained between the discrete dislocation and strain gradient plasticity calculations for both shear and equibiaxial straining of all the voided crystals considered here. This material length scale corresponds to approximately ten times the slip plane spacing in the discrete dislocation calculations. Note that with $l = 0.325$ μm, the $d/l = 3.08$ and $d/l = 12.31$ strain gradient plasticity results in figures 3.27 and 3.28 correspond to $d = 1$ μm and $d = 4.0$ μm, respectively.

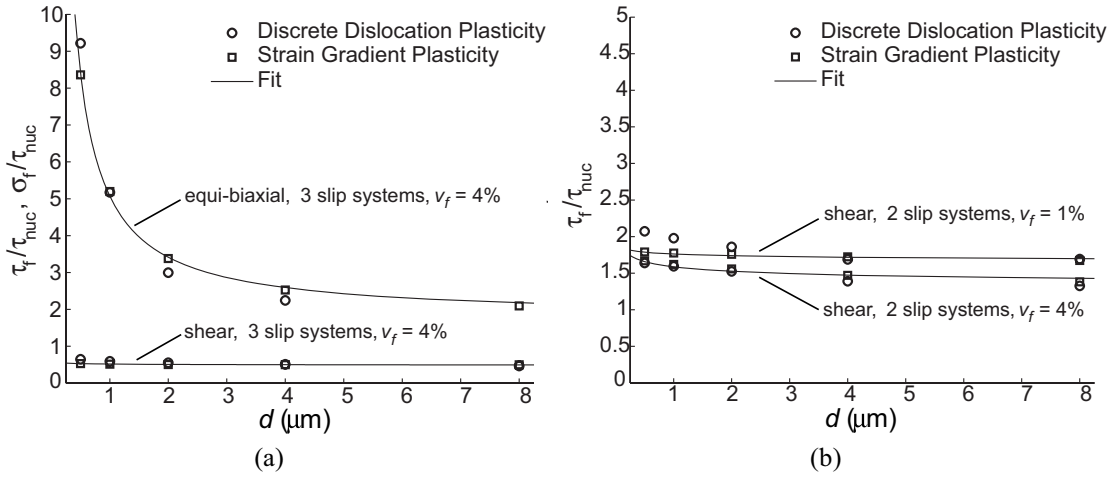

Figure 3.29 Variation of the flow strengths of the voided crystals with void spacing d. (a) Shear and equibiaxial loading of the three slip system crystals with $v_f = 4\%$. (b) Shear loading of the two slip system crystals with $v_f = 1\%$ and 4%. The material length scale in the strain gradient model is assumed to be $l = 0.325$ μm. Fits to the strain gradient plasticity results are also included.

The comparisons presented here indicate that the discrete dislocation and strain gradient plasticity predictions of the responses of the voided crystals compare favorably in terms of the flow strengths. In paper [P7] a favorable comparison in terms of the distributions of the total slip is also presented.

Chapter 4
Concluding Remarks

This thesis focuses on strain gradient plasticity theories and their applications with the main focus on strain gradient crystal plasticity. The thesis contains a summary of an isotropic strain gradient viscoplastic formulation and a summary of a strain gradient crystal plasticity formulation, both allowing for finite strains. The crystal plasticity formulation has also been enhanced by including a grain boundary energy potential to simulate different higher order boundary conditions at the grain boundaries. The numerical implementation of the theories are discussed in details. Various problems are numerically studied by use of the two strain gradient theories, to predict plasticity size effects in the micron range. Seven papers, denoted [P1] through [P7], have been included in the thesis.

The isotropic strain gradient plasticity theory has been applied to analyze materials containing either voids or rigid inclusions in [P1]. It is shown that the overall stress levels increases with decreasing void sizes during uniaxial tension. Similarly for a material containing rigid inclusions there is observed an increase of the overall stress in the main tensile direction with decreasing inclusion size for two different stress triaxialities. Different higher order boundary conditions at the interface between the matrix material and the inclusion was studied, and it was found that the boundary condition representing full constraint on plastic flow gives an overall stiffer response than the other set of boundary conditions, representing no constraint on plastic flow at the interface.

In [P2] the developed strain gradient crystal plasticity formulation was applied to study plastic flow localization in a single crystal loaded in plane strain tension. It was shown how necking started in the middle of the tensile specimen and the larger strains in the neck triggered the formation of shear bands as in Peirce et al. (1983) for conventional crystal plasticity, which is entirely mesh sensitive. The strain gradient crystal plasticity results showed that the gradient effects removed the mesh sensitivity. Furthermore, it was found that the width of the shear bands depends on the material length parameter.

To account for grain boundaries acting as obstacles to dislocation motion, a grain boundary energy potential was included in strain gradient crystal plasticity studies of a bicrystal and a polycrystal in [P3] and [P4], respectively. Experimental and numerical analyses of the evolution in surface topography near grain boundaries during plastic deformation were conducted in [P3]. An aluminium sheet deformed in tension has been examined qualitatively in a scanning electron microscope, and a local gradient in surface profile is observed within a few microns of the grain boundary. The numerical calculations also predicted significant changes in the surface profile near a grain boundary, with the profile being very sensitive to the choice of grain boundary barrier to slip in form of a grain boundary energy potential parameter. The polycrystal in [P4] was analysed to study the flow stress dependence on the grain size under plane strain uniaxial tension. For a random crystallographic orientation of each grain there is only observed a small grain

size effect when there is no restrictions on slip motion at the grain boundaries, whereas a much larger effect is observed when the grain boundaries are restricted to be impenetrable to dislocations (no slip condition). The classical Hall-Petch relationship predicts the flow stress to scale with $d^{-1/2}$, where d is the grain size. The numerical results was fitted to a function of the form d^{-n} for different grain boundary energy parameters, and values of n in the range $0.77 - 1.25$ was found.

Several numerical analyses on voids in single crystals have been conducted in [P5]-[P7] using the strain gradient crystal plasticity formulation. The stress and deformation fields around a cylindrical void in a crystal loaded by a far-field equibiaxial tensile stress was studied in [P5]. Results for the local material model is in agreement with results obtained by Gan and Kysar (2007) using an analytical anisotropic slip line theory. Calculations with the nonlocal material model showed that the stress and deformation fields are dramatically different for micron sized voids when compared to larger voids. Furthermore, the applied stress to activate plastic deformation around the void is observed to increase significantly with decreasing void size. Void growth in a crystal containing uniformly distributed cylindrical voids under different biaxial stress states was analyzed in [P6] by use of a cell model with periodic boundary conditions. The study shows that porous crystals can sustain larger overall stress levels for voids on the micron scale when compared to larger voids. The amount of void growth was found to be suppressed for micron size voids at low stress triaxialities. Also, significant differences were observed on the interaction mechanisms of neighboring voids for the different void sizes considered. A comparison between strain gradient crystal plasticity and discrete dislocation plasticity predictions was performed in [P7] for a crystal with uniformly distributed rectangular voids loaded in shear and equibiaxial straining. Both theories predict a negligible size effect under shear over the length scales considered, whereas both theories predict a strong size dependence under equibiaxial loading. Excellent agreement is obtained between predictions of the two formulations for all crystal types and void volume fractions considered when the strain gradient crystal plasticity material length scale is chosen to be 0.325 μm.

References

Acharya, A. and Bassani, J. L. 2000. Incompatibility and crystal plasticity. *Journal of the Mechanics and Physics of Solids* **48**, 1565–1595.

Aifantis, E. C. 1984. On the microstructural origin of certain inelastic models. *Transactions of the ASME. Journal of Engineering Materials and Technology* **106**, 326–330.

Aifantis, K. E. and Willis, J. R. 2005. The role of interfaces in enhancing the yield strength of composites and polycrystals. *Journal of the Mechanics and Physics of Solids* **53**, 1047–1070.

Ashby, M. F. 1970. The deformation of plastically non-homogeous alloys. *Philosophical Magazine* **21**, 399–424.

Bassani, J. L. 2001. Incompatibility and a simple gradient theory of plasticity. *Journal of the Mechanics and Physics of Solids* **49**, 1983–1996.

Bittencourt, E., Needleman, A., Gurtin, M. E. and Van der Giessen, E. 2003. A comparison of nonlocal continuum and discrete dislocation plasticity predictions. *Journal of the Mechanics and Physics of Solids* **51**, 281–310.

Evers, L. P., Brekelmans, W. A. M. and Geers, M. G. D. 2004. Scale dependent crystal plasticity framework with dislocation density and grain boundary effects. *International Journal of Solids and Structures* **41**, 5209–5230.

Fleck, N. A. and Hutchinson, J. W. 1993. A phenomenological theory for strain gradient effects in plasticity. *Journal of the Mechanics and Physics of Solids* **41**, 1825–1857.

Fleck, N. A. and Hutchinson, J. W.: 1997. Strain gradient plasticity. *in* J. W. Hutchinson and T. Y. Wu (eds), *Advances in Applied Mechanics*. Vol. 33. Academic Press. New York. pp. 295–361.

Fleck, N. A. and Hutchinson, J. W. 2001. A reformulation of strain gradient plasticity. *Journal of the Mechanics and Physics of Solids* **49**, 2245–2271.

Fleck, N. A. and Willis, J. R. 2004. Bounds and estimates for the effect of strain gradients upon the effective plastic properties of an isotropic two-phase composite. *Journal of the Mechanics and Physics of Solids* **52**, 1855–1888.

Fleck, N. A., Muller, G. M., Ashby, M. F. and Hutchinson, J. W. 1994. Strain gradient plasticity: theory and experiment. *Acta Metallurgica et Materialia* **42**, 475–487.

Gan, Y. X. and Kysar, J. F. 2007. Cylindrical void in a rigid-ideally plastic single crystal III: Hexagonal close-packed crystal. *International Journal of Plasticity* **23**, 592–619.

Gan, Y. X., Kysar, J. F. and Morse, T. L. 2006. Cylindrical void in a rigid-ideally plastic single crystal II: Experiments and simulations. *International Journal of Plasticity* **22**, 39–72.

Gao, H., Huang, Y., Nix, W. D. and Hutchinson, J. W. 1999. Mechanism-based strain gradient plasticity-i.theory. *Journal of the Mechanics and Physics of Solids* **47**, 1239–1263.

Groma, I. 1997. Link between the microscopic and mesoscopic length-scale description of the collective behaviour of dislocations. *Physical Review B* **56**, 5807–5813.

Groma, I., Csikor, F. and Zaiser, M. 2003. Spatial correlations and higher-order gradient terms in a continuum description of dislocation dynamics. *Acta Materialia* **51**, 1271–1281.

Gudmundson, P. 2004. A unified treatment of strain gradient plasticity. *Journal of the Mechanics and Physics of Solids* **52**, 1379–1406.

Gurtin, M. E. 2000. On plasticity of crystals: free energy, microforces, plastic strain gradients. *Journal of the Mechanics and Physics of Solids* **48**, 989–1036.

Gurtin, M. E. 2002. A gradient theory of single-crystal viscoplasticity that accounts for geometrically necessary dislocations. *Journal of the Mechanics and Physics of Solids* **50**, 5–32.

Gurtin, M. E. 2003. On a framework for small-deformation viscoplasticity: free energy, microforces, strain gradients. *International Journal of Plasticity* **19**, 47–90.

Hall, E. O. 1951. The deformation and aging of mild steel:iii. discussion of results. *Proceedings of the Physical Society of London B* **64**, 747–753.

Han, C.-S., Gao, H., Huang, Y. and Nix, W. D. 2005. Mechanism-based strain gradient crystal plasticity-I. theory. *Journal of the Mechanics and Physics of Solids* **53**, 1188–1203.

Hill, R. and Rice, J. R. 1972. Constitutive analysis of elastic-plastic crystals at arbitrary strain. *Journal of the Mechanics and Physics of Solids* **20**, 401–413.

Koplik, J. and Needleman, A. 1988. Void growth and coalescence in porous plastic solids. *International Journal of Solids and Structures* **24**, 835–853.

Kröner, E. 1960. Allgemeine kontinuumstheorie der versetzungen und eigenspannungen. *Archive for Rational Mechanics and Analysis* **4**, 273–334.

Kuroda, M. and Tvergaard, T. 2006. Studies of scale dependent crystal viscoplasticity models. *Journal of the Mechanics and Physics of Solids* **54**, 1789–1810.

Kysar, J. F., Gan, Y. X. and Mendez-Arzuza, G. 2005. Cylindrical void in a rigid-ideally plastic single crystal. part I: Anisotropic slip line theory solution for face-centered cubic crystals. *International Journal of Plasticity* **21**, 1481–1520.

Lee, E. H. 1969. Elastic-plastic deformation at finite strains. *Journal of Applied Mechanics* **36**, 1–6.

Ma, Q. and Clarke, D. R. 1995. Size dependent hardness of silver single crystals. *Journal of Materials Research* **10**, 853–863.

Mikkelsen, L. P. 1999. Necking in rectangular tensile bars approximated by a 2-d gradient dependent plasticity model. *European Journal of Mechanics - A/Solids* **18**, 805–818.

Nemat-Nasser, S. and Hori, M. 1987. Void collapse and void growth in crystalline solids. *Journal of Applied Physics* **62**, 2746–2757.

Niordson, C. F. and Redanz, P. 2004. Size-effects in plane strain sheet-necking. *Journal of the Mechanics and Physics of Solids* **52**, 2431–2454.

Niordson, C. F. and Tvergaard, V. 2005. Instabilities in power law gradient hardening materials. *International Journal of Solids and Structures* **42**, 2559–2573.

Nix, W. D. and Gao, H. 1998. Indentation size effects in crystalline materials: a law for strain gradient plasticity. *Journal of the Mechanics and Physics of Solids* **46**, 411–425.

Nye, J. F. 1953. Some geometrical relations in dislocated crystals. *Acta Metallurgica* **1**, 153–162.

Peirce, D., Asaro, R. J. and Needleman, A. 1983. Material rate dependence and localized deformation in crystalline solids. *Acta Metallurgica* **31**, 1951–1976.

Petch, N. J. 1953. The cleavage strength of polycrystals. *Journal of the Iron and Steel Institute* **174**, 25–28.

Potirniche, G. P., Hearndon, J. L., Horstemeyer, M. F. and Ling, X. W. 2006. Lattice orientation effects on void growth and coalescence in fcc single crystals. *International Journal of Plasticity* **22**, 921–942.

Shu, J. Y. and Barlow, C. Y. 2000. Strain gradient effects on microscopic strain field in a metal matrix composite. *International Journal of Plasticity* **16**, 563–591.

Shu, J. Y. and Fleck, N. A. 1999. Strain gradient crystal plasticity: size-dependent deformation of bicrystals. *Journal of the Mechanics and Physics of Solids* **47**, 297–324.

Shu, J. Y., Fleck, N. A., Van der Giessen, E. and Needleman, A. 2001. Boundary layers in constrained plastic flow: comparison of nonlocal and discrete dislocation plasticity. *Journal of the Mechanics and Physics of Solids* **49**, 1361–1395.

Sluys, L. J. and Estrin, Y. 2000. The analysis of shear banding with a dislocation based gradient plasticity model. *International Journal of Solids and Structures* **37**, 7127–7142.

Stelmashenko, N. A., Walls, M. G., Brown, L. M. and Milman, Y. V. 1993. Microindentations on w and mo oriented single crystals: an stm study. *Acta Metallurgica et Materialia* **41**, 2855–2865.

Stölken, J. S. and Evans, A. G. 1998. Microbend test method for measuring the plasticity length scale. *Acta Materialia* **46**, 5109–5115.

Tvergaard, V. 1976. Effect of thickness inhomogeneities in internally pressurized elastic-plastic spherical shells. *Journal of the Mechanics and Physics of Solids* **24**, 291–304.

Tvergaard, V. and Needleman, A. 1995. Effects of nonlocal damage in porous plastic solids. *International Journal of Solids and Structures* **32**, 1063–1077.

Tvergaard, V. and Niordson, C. F. 2004. Nonlocal plasticity effects on interaction of different size voids. *International Journal of Plasticity* **20**, 107–120.

Van der Giessen, E. and Needleman, A. 1995. Discrete dislocation plasticity: a simple planar model. *Modelling and Simulation in materials Science and Engineering* **3**, 689–735.

Wilson, W. R. D. and Lee, W. 2001. Mechanics of surface roughening in metal forming processes. *Journal of Manufacturing Science and Engineering* **123**, 279–283.

Zhao, Z., Radovitzky, R. and Cuitio, A. 2004. A study of surface roughening in fcc metals using direct numerical simulation. *Acta Materialia* **52**, 5791–5804.

P1

A viscoplastic strain gradient analysis of materials with voids or inclusions

International Journal of Solids and Structures
43, 4906-4916, 2006

Available online at www.sciencedirect.com
SCIENCE DIRECT®
International Journal of Solids and Structures 43 (2006) 4906–4916
INTERNATIONAL JOURNAL OF SOLIDS and STRUCTURES
www.elsevier.com/locate/ijsolstr

A viscoplastic strain gradient analysis of materials with voids or inclusions

Ulrik Borg [a], Christian F. Niordson [a,*], Norman A. Fleck [b], Viggo Tvergaard [a]

[a] *Department of Mechanical Engineering, Solid Mechanics, Technical University of Denmark, Nils Koppels Alle, Building 404, Kgs, Lyngby, DK-2800, Denmark*
[b] *Department of Engineering, Cambridge University, Cambridge, UK*

Received 7 April 2005; received in revised form 19 May 2005
Available online 27 July 2005

Abstract

A finite strain viscoplastic nonlocal plasticity model is formulated and implemented numerically within a finite element framework. The model is a viscoplastic generalisation of the finite strain generalisation by Niordson and Redanz (2004) [Journal of the Mechanics and Physics of Solids 52, 2431–2454] of the strain gradient plasticity theory proposed by Fleck and Hutchinson (2001) [Journal of the Mechanics and Physics of Solids 49, 2245–2271]. The formulation is based on a viscoplastic potential that enables the formulation of the model so that it reduces to the strain gradient plasticity theory in the absence of viscous effects. The numerical implementation uses increments of the effective plastic strain rate as degrees of freedom in addition to increments of displacement. To illustrate predictions of the model, results are presented for materials containing either voids or rigid inclusions. It is shown how the model predicts increased overall yield strength, as compared to conventional predictions, when voids or inclusions are in the micron range. Furthermore, it is illustrated how the higher order boundary conditions at the interface between inclusions and matrix material are important to the overall yield strength as well as the material hardening.

Keywords: Strain gradient plasticity; Viscoplastic material; Voids; Size effects

1. Introduction

A number of small scale experiments for metals have shown that size-effects play an important role when strain gradients become large (Fleck et al., 1994; Ma and Clarke, 1995; Stölken and Evans, 1998; Haque

* Corresponding author. Tel.: +45 4525 4287; fax: +45 4593 1475.
E-mail address: cn@mek.dtu.dk (C.F. Niordson).

0020-7683/$ - see front matter © 2005 Elsevier Ltd. All rights reserved.
doi:10.1016/j.ijsolstr.2005.05.022

and Saif, 2003). Such effects are not accounted for in conventional plasticity theories, and several nonlocal material models have been developed to incorporate the influence of a characteristic material length.

For a gradient plasticity theory proposed by Fleck and Hutchinson (2001) a finite strain generalisation has recently been developed by Niordson and Redanz (2004) and a numerical implementation for power law hardening materials has been given by Niordson and Tvergaard (2005). This finite strain model has been used to study necking instabilities in tension as well as buckling instabilities in compression. It was found that the gradient effects delay the onset of localisation and increase the load carrying capacity in compression, in agreement with bifurcation results of Benallal and Tvergaard (1995). Very recently also the effect of the gradient plasticity theory on the occurrence of cavitation instabilities has been analysed (Niordson and Tvergaard, in press). As is known from previous studies (Fleck and Hutchinson, 1997; Huang et al., 2000; Tvergaard and Niordson, 2004), the role of void growth is much reduced when the void radius is small compared to the characteristic material length. This results in an increased peak stress for cavitation, but subsequently the stress decays, as the void grows large relative to the material length scale.

In a viscoplastic theory for isotropic materials strain gradient effects have been incorporated by Gurtin (2003) in a small strain formulation. Also Gudmundson (2004) has proposed a small deformation strain gradient plasticity theory that has an elastic–viscoplastic version, and these viscoplastic constitutive relations have been applied by Fredriksson and Gudmundson (2005) to analyse pure shear and biaxial strain of a thin film.

In the present paper a viscoplastic version of the finite strain model of Niordson and Redanz (2004) is formulated, i.e. a viscoplastic finite strain generalisation of the gradient plasticity theory proposed by Fleck and Hutchinson (2001). This formulation makes use of a viscoplastic potential and the viscous material behaviour is introduced in terms of a power law expression for a nonlocal effective plastic strain rate. Since, in the viscoplastic theory, no internal boundaries exists between elastic and plastic regions, no internal higher order boundary conditions must be specified. Such internal boundary conditions are necessary in a time-independent theory. To illustrate predictions of this viscoplastic nonlocal model, numerical results are presented for elastic–viscoplastic materials containing either voids or rigid inclusions. The results show the effect of different values of the void or inclusion radius relative to the characteristic material length incorporated in the theory. For the material with inclusions different higher order boundary conditions at the inclusion surface are investigated.

2. Material model

Let u_i denote the displacement vector and $\dot{u}_i$ the velocity field. With $\dot{e}_{ij} = \dot{u}_{i,j}$ denoting the velocity gradient, the material spin is given by

$$\dot{\omega}_{ij} = \frac{1}{2}(\dot{e}_{ij} - \dot{e}_{ji}) \tag{1}$$

The symmetric part of the velocity gradient is the strain rate, which is decomposed into an elastic and plastic part

$$\dot{\epsilon}_{ij} = \frac{1}{2}(\dot{e}_{ij} + \dot{e}_{ji}) = \dot{\epsilon}^{\mathrm{E}}_{ij} + \dot{\epsilon}^{\mathrm{P}}_{ij} \tag{2}$$

A nonlocal measure of the effective plastic strain rate is defined on the basis of the conventional effective plastic strain rate and the gradient of the conventional effective plastic strain rate through the incremental relation

$$\dot{E}^{\mathrm{P}^2} = \dot{\epsilon}^{\mathrm{P}^2} + l_*^2 \dot{\epsilon}^{\mathrm{P}}_{,i} \dot{\epsilon}^{\mathrm{P}}_{,i} \tag{3}$$

where l_* is a material length parameter (Fleck and Hutchinson, 2001; Niordson and Redanz, 2004).

The direction of the plastic strain rate is given by $m_{ij} = \frac{3}{2} S_{ij}/\sigma_e$, where $S_{ij} = \sigma_{ij} - \frac{1}{3}\delta_{ij}\sigma_{kk}$ denotes the stress deviator and $\sigma_e = \sqrt{\frac{3}{2} S_{ij} S_{ij}}$ is von Mises effective stress with σ_{ij} being the Cauchy stress tensor. The plastic strain rate components can then be written as a product of its magnitude, $\dot{\epsilon}^{\mathrm{P}} = \sqrt{\frac{2}{3}\dot{\epsilon}^{\mathrm{P}}_{ij}\dot{\epsilon}^{\mathrm{P}}_{ij}}$, and its direction

$$\dot{\epsilon}^{\mathrm{P}}_{ij} = m_{ij}\dot{\epsilon}^{\mathrm{P}} \tag{4}$$

Following (Fleck and Hutchinson, 2001), assuming that the plastic strain gradients contribute to the internal work, the principle of virtual power in total form may be formulated as

$$\int_V (\sigma_{ij}\delta\dot{\epsilon}_{ij} + (Q - \sigma_{(e)})\delta\dot{\epsilon}^{\mathrm{P}} + \tau_i \delta\dot{\epsilon}^{\mathrm{P}}_{,i})\mathrm{d}V = \int_S (T_i \delta\dot{u}_i + \tau_i n_i \delta\dot{\epsilon}^{\mathrm{P}})\mathrm{d}S \tag{5}$$

in the deformed configuration. Here, Q is a generalised effective stress which is work-conjugate to the conventional effective plastic strain rate, $\dot{\epsilon}^{\mathrm{P}}$, and τ_i is a higher order stress which is work-conjugate to the gradient of the conventional effective plastic strain rate, $\dot{\epsilon}^{\mathrm{P}}_{,i}$. The current volume and surface are denoted V and S, respectively. The surface traction is denoted by, $T_i = \sigma_{ij} n_j$, and $\tau_i n_i$ denotes the higher order surface traction.

We now define Kirchhoff stress measures as (defining J as the determinant of the metric tensor)

$$\varsigma_{ij} = J\sigma_{ij}, \quad \sigma^{\varsigma}_{(e)} = J\sigma_{(e)}, \quad q = JQ, \quad \rho_i = J\tau_i \tag{6}$$

Introducing the Jaumann rate of the Kirchhoff stress, $\overset{\triangledown}{\varsigma}_{ij}$, and the convected rate of the higher order Kirchhoff stress, $\overset{\vee}{\rho}_i$, the incremental version of the principle of virtual power, in an updated Lagrangian framework, can be expressed as (Niordson and Redanz, 2004)

$$\int_V (\overset{\triangledown}{\varsigma}_{ij}\delta\dot{\epsilon}_{ij} - \sigma_{ij}(2\dot{\epsilon}_{ik}\delta\dot{\epsilon}_{kj} - \dot{e}_{kj}\delta\dot{e}_{ki}) + (\dot{q} - \dot{\sigma}^{\varsigma}_{(e)})\delta\dot{\epsilon}^{\mathrm{P}} + \overset{\vee}{\rho}_i \delta\dot{\epsilon}^{\mathrm{P}}_{,i})\mathrm{d}V = \int_S (\dot{T}_i \delta\dot{u}_i + \dot{\rho}_i n_i \delta\dot{\epsilon}^{\mathrm{P}})\mathrm{d}S \tag{7}$$

Now, to obtain a viscoplastic version of the theory, a viscoplastic potential is defined as

$$\Phi[\dot{E}^{\mathrm{P}}, E^{\mathrm{P}}] = \int_0^{\dot{E}^{\mathrm{P}}} \sigma_{\mathrm{c}}[\dot{E}^{\mathrm{P}\prime}, E^{\mathrm{P}}]\mathrm{d}\dot{E}^{\mathrm{P}\prime} \tag{8}$$

where σ_{c} is an effective stress which is work-conjugate to the effective plastic strain rate, $\dot{E}^{\mathrm{P}}$. Taking the variation of the potential gives

$$\delta\Phi = \sigma_{\mathrm{c}}\delta\dot{E}^{\mathrm{P}} = \frac{\sigma_{\mathrm{c}}}{\dot{E}^{\mathrm{P}}}\dot{\epsilon}^{\mathrm{P}}\delta\dot{\epsilon}^{\mathrm{P}} + \frac{\sigma_{\mathrm{c}}}{\dot{E}^{\mathrm{P}}} l_*^2 \dot{\epsilon}^{\mathrm{P}}_{,i}\delta\dot{\epsilon}^{\mathrm{P}}_{,i} = q\delta\dot{\epsilon}^{\mathrm{P}} + \rho_i \delta\dot{\epsilon}^{\mathrm{P}}_{,i} \tag{9}$$

with the generalised effective stress, q, and the higher order stress, ρ_i, defined by the constitutive equations

$$q = \frac{\sigma_{\mathrm{c}}}{\dot{E}^{\mathrm{P}}}\dot{\epsilon}^{\mathrm{P}} \tag{10}$$

$$\rho_i = \frac{\sigma_{\mathrm{c}}}{\dot{E}^{\mathrm{P}}} l_*^2 \dot{\epsilon}^{\mathrm{P}}_{,i} \tag{11}$$

By substituting these expressions into the definition of the effective plastic strain (3) it is seen that the effective stress is given as the following quadratic form in q and ρ_i

$$\sigma_{\mathrm{c}}^2 = q^2 + l_*^{-2}\rho_i\rho_i \tag{12}$$

When excluding the material length scale by setting $l_* = 0$, the effective stress, σ_{c}, reduces to the von Mises stress and the effective plastic strain rate, $\dot{E}^{\mathrm{P}}$, equals the conventional effective plastic strain rate, $\dot{\epsilon}^{\mathrm{P}}$.

The viscous material behaviour is modelled by a power law for the effective plastic strain rate

$$\dot{E}^{\mathrm{P}} = \dot{\epsilon}_0 \left(\frac{\sigma_{\mathrm{c}}}{g[E^{\mathrm{P}}]} \right)^{1/m} \tag{13}$$

Here, m is the strain rate hardening exponent and $\dot{\epsilon}_0$ is a reference strain rate. Strain hardening is taken to follow a power law with exponent $1/n$ and initial yield strength $\sigma_0 = E\epsilon_0$ (where E is Young's modulus) given by

$$g[E^{\mathrm{P}}] = \sigma_0 \left(1 + \frac{E^{\mathrm{P}}}{\epsilon_0} \right)^{1/n} \tag{14}$$

where the hardening function is evaluated at E^P instead of ϵ^P as it would be in conventional J_2 flow theory. If the strain rate was prescribed such that $\dot{E}^{\mathrm{P}} = \dot{\epsilon}_0$, the hardening function, $g[E^P]$, would be equal to the effective stress, σ_{c}.

The incremental constitutive equations for the viscoplastic material can be obtained from (10) and (11) using (13) and written in the form

$$\overset{\triangledown}{\varsigma}_{ij}\Delta t = R_{ijkl}(\Delta\epsilon_{kl} - m_{kl}\Delta\epsilon^{\mathrm{P}}) = \Delta\varsigma_{ij} - \Delta\omega_{ik}\sigma_{kj} - \sigma_{ik}\Delta\omega_{jk} \tag{15}$$

$$\dot{q}\Delta t = \frac{\sigma_{\mathrm{c}}}{\dot{E}^{\mathrm{P}}} \left((m-1)\frac{\dot{\epsilon}^{\mathrm{P}}}{\dot{E}^{\mathrm{P}}}\Delta\dot{E}^{\mathrm{P}} + \Delta\dot{\epsilon}^{\mathrm{P}} \right) + \left(\frac{\dot{E}^{\mathrm{P}}}{\dot{\epsilon}_0} \right)^m \frac{\mathrm{d}g}{\mathrm{d}E^{\mathrm{P}}}\dot{\epsilon}^{\mathrm{P}}\Delta t \tag{16}$$

$$\overset{\vee}{\rho}_i\Delta t = l_*^2 \left(\frac{\sigma_{\mathrm{c}}}{\dot{E}^{\mathrm{P}}} \left((m-1)\frac{\dot{\epsilon}^{\mathrm{P}}_{,i}}{\dot{E}^{\mathrm{P}}}\Delta\dot{E}^{\mathrm{P}} + \Delta\dot{\epsilon}^{\mathrm{P}}_{,i} \right) + \left(\frac{\dot{E}^{\mathrm{P}}}{\dot{\epsilon}_0} \right)^m \frac{\mathrm{d}g}{\mathrm{d}E^{\mathrm{P}}}\dot{\epsilon}^{\mathrm{P}}_{,i}\Delta t \right) = \Delta\rho_i - \Delta e_{ik}\rho_k \tag{17}$$

where the change in the effective plastic strain rate is taken as $\Delta\dot{E}^{\mathrm{P}} = \frac{\dot{\epsilon}^{\mathrm{P}}}{\dot{E}^{\mathrm{P}}}\Delta\dot{\epsilon}^{\mathrm{P}} + \frac{l_*^2\dot{\epsilon}^{\mathrm{P}}_{,i}}{\dot{E}^{\mathrm{P}}}\Delta\dot{\epsilon}^{\mathrm{P}}_{,i}$ and the elastic stiffness tensor is given by

$$R_{ijkl} = \frac{E}{1+\nu} \left(\frac{1}{2}\left(\delta_{ik}\delta_{jl} + \delta_{il}\delta_{jk} \right) + \frac{\nu}{1-2\nu}\delta_{ij}\delta_{kl} \right) \tag{18}$$

3. Problem formulation and numerical method

A material containing uniformly distributed cylindrical voids or rigid inclusions, Fig. 1(a), is analysed using a plane strain cell model, Fig. 1(b). The dimensions of the unit cell are given by a_0 and b_0, and the size of the void or inclusion is defined by the radius R_0.

The boundary conditions used for the cell model are

$$\begin{aligned} &\dot{u}_1 = 0, \quad \dot{T}_2 = 0 \text{ at } x_1 = 0 \\ &\dot{u}_1 = \dot{U}_{\mathrm{I}}, \quad \dot{T}_2 = 0 \text{ at } x_1 = a_0 + \Delta a \\ &\dot{u}_2 = 0, \quad \dot{T}_1 = 0 \text{ at } x_2 = 0 \\ &\dot{u}_2 = \dot{U}_{\mathrm{II}}, \quad \dot{T}_1 = 0 \text{ at } x_2 = b_0 + \Delta b \end{aligned} \tag{19}$$

where $\dot{T}_i$ are surface traction rates. Using a special Rayleigh–Ritz finite element method (Tvergaard, 1976), the prescribed cell-side displacement rates, $\dot{U}_{\mathrm{I}}$ and $\dot{U}_{\mathrm{II}}$, are determined such that there is a fixed ratio of the average true stresses

$$\sigma_2 = \kappa\sigma_1 \tag{20}$$

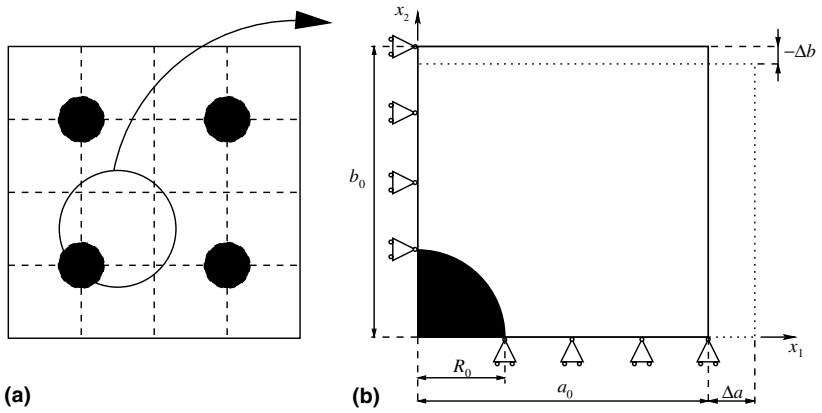

Fig. 1. The plane strain cell model for a material with rigid inclusions or voids: (a) periodically arranged inclusions/voids and (b) the unit cell used for the analyses.

Furthermore, when considering voids we have $\dot{T}_i = 0$ on the void surface, whereas in the case of inclusions we have $\dot{u}_i = 0$ on the inclusion surface.

The numerical solutions are obtained using a special kind of finite element method, where increments of the plastic strain rate appear as degrees of freedom on equal footing with displacement increments. The displacement increments, Δu_i, and the change of the effective plastic strain rate, $\Delta\dot{\epsilon}^{\mathrm{P}}$, are interpolated within each element between nodal displacement increments, ΔD^N, and nodal effective plastic strain rate changes, $\Delta\dot{\epsilon}^{\mathrm{P}}_N$, respectively

$$\Delta u_i = \sum_{N=1}^{2k} N_i^N \Delta D^N, \quad \Delta\dot{\epsilon}^{\mathrm{P}} = \sum_{N=1}^{l} M^N \Delta\dot{\epsilon}^{\mathrm{P}}_N \tag{21}$$

where N_i^N and M^N are shape functions and k and l are the number of nodes used for the interpolations. The elements used are isoparametric eight-node quadrilaterals with quadratic interpolation of both displacement increments and effective plastic strain rate increments ($k = l = 8$), as in Niordson and Tvergaard (2005) for a time independent analysis. The derivatives of the displacement increments and the effective plastic strain rate increments are taken as

$$\Delta e_{ij} = \sum_{N=1}^{2k} N^N_{i,j} \Delta D^N, \quad \Delta\epsilon_{ij} = \sum_{N=1}^{2k} E^N_{ij} \Delta D^N, \quad \Delta\dot{\epsilon}^{\mathrm{P}}_{,i} = \sum_{N=1}^{l} M^N_{,i} \Delta\dot{\epsilon}^{\mathrm{P}}_N \tag{22}$$

where $E^N_{ij} = \frac{1}{2}(N^N_{i,j} + N^N_{j,i})$.

Using these relations in the principle of virtual work, the discretized equations can be written in the following form:

$$\begin{bmatrix} \mathbf{K}_{\mathrm{e}} & \mathbf{0} \\ \mathbf{K}_{\mathrm{ep}} & \mathbf{K}_{\mathrm{p}} \end{bmatrix} \begin{bmatrix} \Delta\mathbf{D} \\ \Delta\dot{\boldsymbol{\epsilon}}^{\mathrm{P}} \end{bmatrix} = \begin{bmatrix} \Delta\mathbf{F}_1 \\ \Delta\mathbf{F}_2 \end{bmatrix} \tag{23}$$

where

$$\mathbf{K}^{NM}_{\mathrm{e}} = \int_V (E^N_{ij} R_{ijkl} E^M_{kl} + \sigma_{ij}(N^M_{k,j} N^N_{k,i} - 2E^M_{ik} E^N_{jk}))\mathrm{d}V \tag{24}$$

is the elastic stiffness matrix

$$\mathbf{K}_{\mathrm{ep}}^{NM} = -\int_V m_{ij} R_{ijkl} E_{kl}^M M^N \,\mathrm{d}V \tag{25}$$

is the coupling matrix, and

$$\mathbf{K}_{\mathrm{p}}^{NM} = \int_V \left(\left(\frac{\dot{\epsilon}^{\mathrm{P}}}{\dot{E}^{\mathrm{P}2}}(m-1)q + \frac{\sigma_{\mathrm{c}}}{\dot{E}^{\mathrm{P}}} \right) M^M M^N + l_*^2 \frac{\dot{\epsilon}^{\mathrm{P}}_{,i}}{\dot{E}^{\mathrm{P}2}}(m-1)q M^M M^N_{,i} + \frac{\dot{\epsilon}^{\mathrm{P}}}{\dot{E}^{\mathrm{P}2}}(m-1)\rho_i M^M_{,i} M^N \right.$$
$$\left. + l_*^2 \frac{\dot{\epsilon}^{\mathrm{P}}_{,i}}{\dot{E}^{\mathrm{P}2}}(m-1)\rho_k M^M_{,k} M^N_{,i} + l_*^2 \frac{\sigma_{\mathrm{c}}}{\dot{E}^{\mathrm{P}}} M^M_{,i} M^N_{,i} \right) \mathrm{d}V \tag{26}$$

is the plastic stiffness matrix. The right-hand side in Eq. (23) consists of two components

$$\mathbf{\Delta F}_{\mathbf{1}}^N = \int_S \Delta T_i N_i^N \,\mathrm{d}S + \Delta t \int_V E_{ij}^N R_{ijkl} m_{kl} \dot{\epsilon}^{\mathrm{P}} \,\mathrm{d}V \tag{27}$$

which is the conventional load increment vector with an added volume force, and

$$\mathbf{\Delta F}_{\mathbf{2}}^N = \int_S \Delta\rho_i n_i M^N \,\mathrm{d}S - \Delta t \int_V \left(\left(m_{ij} R_{ijkl} m_{kl} \dot{\epsilon}^{\mathrm{P}} + \frac{\dot{\epsilon}^{\mathrm{P}}}{\dot{\epsilon}_0^m} \dot{E}^{\mathrm{P}m} \frac{\mathrm{d}g}{\mathrm{d}E^{\mathrm{P}}} \right) M^N + \dot{\epsilon}^{\mathrm{P}}_{,i} \dot{E}^{\mathrm{P}m} \frac{\mathrm{d}g}{\mathrm{d}E^{\mathrm{P}}} \frac{l_*^2}{\dot{\epsilon}_0^m} M^N_{,i} \right) \mathrm{d}V \tag{28}$$

which is an additional higher order load term with a subtracted volume contribution.

Since the system of equations decouples, it is possible to first solve for the displacement increments and afterwards solve for the effective plastic strain rate increments and hereby exploit the symmetry of $\mathbf{K}_{\mathrm{e}}$ and $\mathbf{K}_{\mathrm{p}}$, respectively. The integrations (24)–(28) are carried out using 3×3 point Gaussian integration.

When the displacement increments and the effective plastic strain rate increments are known, the Jaumann rate of the stress, the generalised effective stress rate and the convected rate of the higher order stress can be found from the constitutive equations (15)–(17). The increments of the Cauchy stress tensor and the higher order stress vector is then calculated by

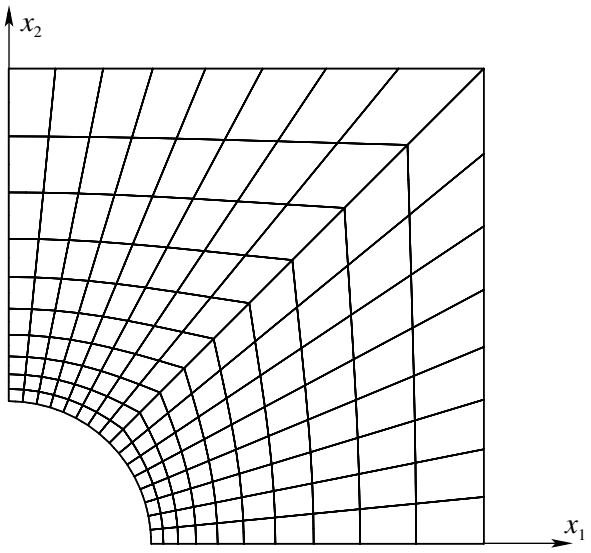

Fig. 2. Initial mesh with $a_0/b_0 = 1$ and $a_0/R_0 = 0.3$ corresponding to a volume fraction of 7.1%.

$$\Delta\sigma_{ij} = \overset{\triangledown}{\varsigma}_{ij}\Delta t + \Delta\omega_{ik}\sigma_{kj} + \sigma_{ik}\Delta\omega_{jk} - \sigma_{ij}\Delta\epsilon_{kk} \tag{29}$$

$$\Delta\tau_i = \overset{\vee}{\rho}_i\Delta t + \Delta e_{ik}\tau_k - \tau_i\Delta\epsilon_{kk} \tag{30}$$

Subsequently, the effective stress, σ_c, can be calculated from (12) and the effective plastic strain rate, $\dot{E}^P$, is given by (13). The conventional effective plastic strain rate, $\dot{\epsilon}^P$, and its gradient, $\dot{\epsilon}^P_{,i}$, is now obtained from Eqs. (10) and (11).

The finite element mesh used for the analyses is shown in Fig. 2.

4. Results

The material parameters used for the numerical analyses are $\sigma_0/E = 0.003$, $n = 10$, $v = 0.3$, $m = 0.04$ and $\dot{\epsilon}_0 = 0.005\ \mathrm{s}^{-1}$. The initial dimensions of the unit cell are specified by $a_0/b_0 = 1$ so that the voids or inclusions have equal spacings in the directions of the coordinate axes. The initial spacing of the voids or inclusions is specified by $R_0/a_0 = 0.3$ corresponding to a volume fraction of 7.1%.

Both for the material containing voids and the material containing inclusions the higher order traction is taken to vanish along the cell boundary ($\tau_i n_i = 0$). This constitutes the appropriate symmetry boundary condition for the problems analysed. Also at the free surface around the voids the higher order stress is imposed to vanish, while for the material containing inclusions the higher order boundary condition is specified by imposing vanishing plastic strain ($\epsilon^P = 0$) unless otherwise stated.

For a material with voids the overall uniaxial stress–strain curve ($\kappa = 0$) is shown in Fig. 3 for different values of the material length parameter relative to the void radius. The solid curve shows results for a conventional material ($l_* = 0$), while the dotted and dashed curves show results for gradient dependent materials with $l_*/R_0 = 0.3$ and $l_*/R_0 = 0.6$, respectively. The figure shows curves of the normalised average true stress, σ_1, in the x_1-direction as a function of the logarithmic strain, ϵ_1. The overall strain rate is equal to the reference strain rate, $\dot{\epsilon}_1 = \dot{\epsilon}_0$. It is seen from the figure how a material with small voids (or conversely a large material length parameter) shows more stiff behaviour in the plastic range. In effect, increasing the material length parameter, apparently increases the overall material yield stress and thus increases the stress level

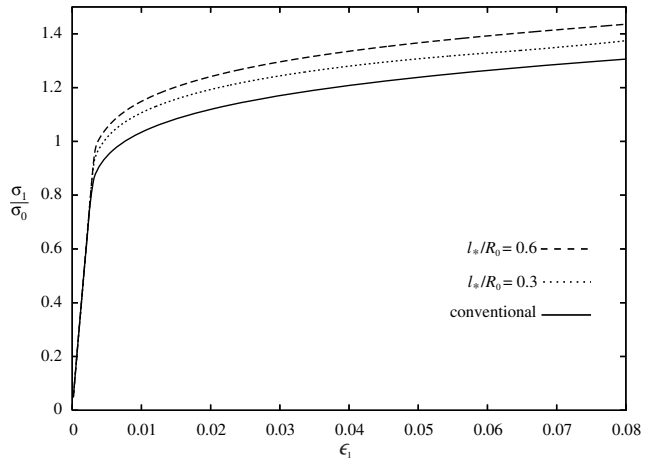

Fig. 3. Overall uniaxial stress–strain response ($\kappa = 0$) for a material with voids. The solid curve shows results from a conventional plasticity model while the dotted and dashed curves show results for plasticity models with $l_*/R_0 = 0.3$ and $l_*/R_0 = 0.6$, respectively. The overall loading rate is given by $\dot{\epsilon}_1 = \dot{\epsilon}_0$.

in the plastic range. Well inside the plastic range ($\epsilon > 0.02$) the stress level is around 6% higher for $l_*/R_0 = 0.3$% and 11% higher for $l_*/R_0 = 0.6$, as compared to the conventional material.

In Fig. 4 results for different overall strain rates are shown both for a conventional material and for a gradient dependent material with $l_*/R_0 = 0.6$. The overall strain rate is varied so that in addition to $\dot{\epsilon}_1 = \dot{\epsilon}_0$ also a 10 times larger and a 10 times smaller strain rate are studied. It is seen from the figure that increasing the overall strain rate for the conventional material from $\dot{\epsilon}_1 = \dot{\epsilon}_0$ to a 10 times larger value has a similar strengthening effect as accounting for gradient hardening using $l_*/R_0 = 0.6$. Moreover, the figure shows that increasing the strain rate by a factor of 10 increases the stress level in the plastic range by around 10%. This is in agreement with the increase expected on the basis of (13) for a homogeneous solid with the value of m used in the present analyses.

Fig. 5 shows the overall stress–strain curves for the material with inclusions under different levels of the overall stress ratio κ and different material length parameters. The size of the cylindrical inclusions is defined by $R_0/a_0 = 0.3$ which corresponds to a reinforcement volume fraction of approximately 7.1%. The solid curves show results for a conventional material ($l_* = 0$), while the dotted and dashed curves show results for gradient dependent materials with $l_*/R_0 = 0.3$ and $l_*/R_0 = 0.6$, respectively. The figure shows that increasing the material length scale leads to an apparent increase in the overall yield stress as was also the case for the material with voids. For all three values of the material length parameter the overall stress level for $\kappa = 0.5$ is approximately a factor of two higher than the stress level for $\kappa = 0$. This is in agreement of what would be expected for a homogeneous solid when ignoring elastic effects.

Results when varying the overall strain rate for the material with inclusions is shown in Fig. 6 for $\kappa = 0$, both for a conventional material and for a gradient dependent material with $l_*/R_0 = 0.6$. As for the material containing voids, increasing the strain rate by a factor of 10 increases the stress level by around 10%, which would be expected in the plastic range for a homogeneous material with the specific value of m used. For the material with inclusions the effect on the overall response by increasing the material length parameter from zero to $l_*/R_0 = 0.6$ is slightly larger than for the material containing voids discussed in relation to Fig. 4.

The higher order boundary condition on the interface between fibers and the matrix material is of significant importance for the overall material response of reinforced materials (see Niordson, 2003). For the

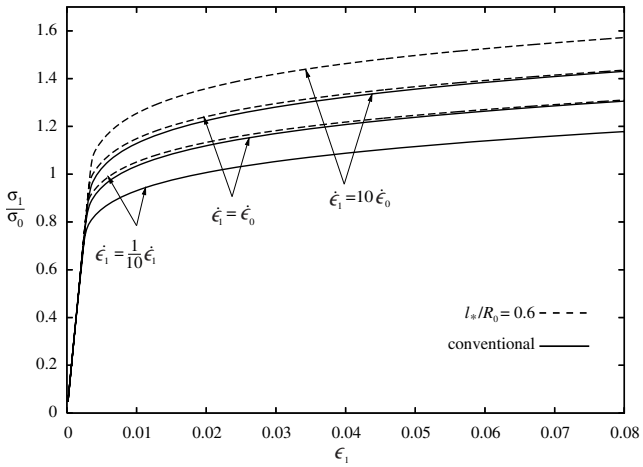

Fig. 4. Overall uniaxial stress–strain response ($\kappa = 0$) for a material with voids. For three different loading rates given by $\dot{\epsilon}_1 = \dot{\epsilon}_0/10$, $\dot{\epsilon}_1 = \dot{\epsilon}_0$ and $\dot{\epsilon}_1 = 10\dot{\epsilon}_0$, results are shown from a conventional plasticity model (solid curves) and from a gradient dependent model with $l_*/R_0 = 0.6$ (dashed curves).

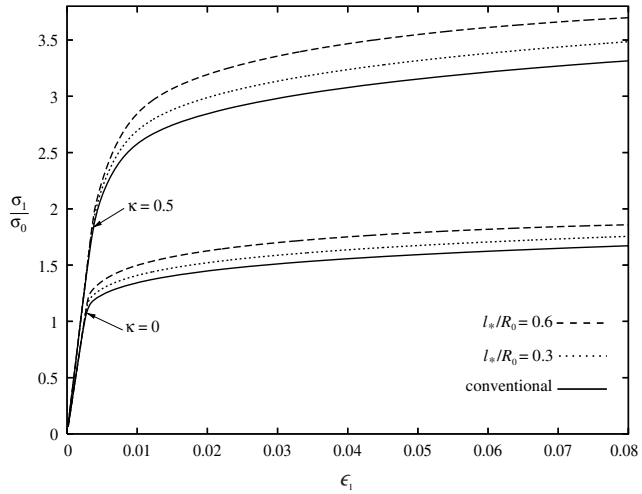

Fig. 5. Overall stress–strain response for a material with rigid inclusions and two different stress triaxialities given by $\kappa = 0$ and $\kappa = 0.5$. The solid curves show results from a conventional plasticity model while the dotted and dashed curves show results for $l_*/R_0 = 0.3$ and $l_*/R_0 = 0.6$, respectively. The overall loading rate is given by $\dot{\epsilon}_1 = \dot{\epsilon}_0$.

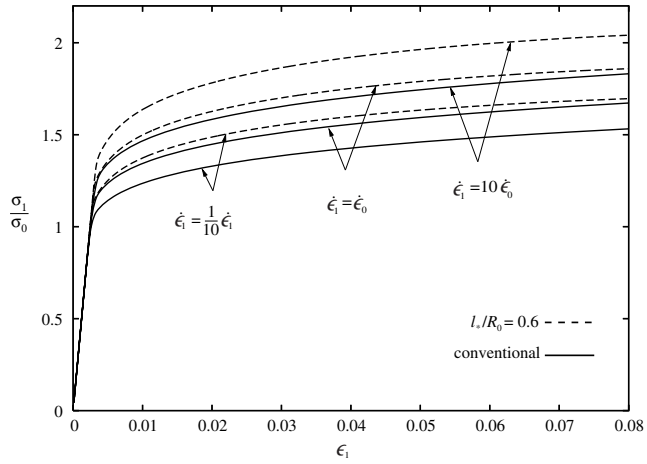

Fig. 6. Overall uniaxial stress–strain response ($\kappa = 0$) for a material with rigid inclusions. For three different loading rates given by $\dot{\epsilon}_1 = \dot{\epsilon}_0/10$, $\dot{\epsilon}_1 = \dot{\epsilon}_0$ and $\dot{\epsilon}_1 = 10\dot{\epsilon}_0$, results are shown from a conventional plasticity model (solid curves) and results from a plasticity model with $l_*/R_0 = 0.6$ (dashed curves).

results presented until now for the reinforced material a full constraint on plastic flow ($\epsilon^{\mathrm{p}} = 0$) has been imposed at the interface between the matrix material and the inclusion. Fig. 7 shows results for the two extreme boundary conditions, which can be imposed at the interface. One is the full constraint on plastic flow represented by the dotted curves ($\epsilon^{\mathrm{p}} = 0$), while the other is no constraint on plastic flow, as represented by the dashed curves ($\tau_i n_i = 0$). It is seen that a full constraint on plastic flow leads to an overall stiffer response when compared to no constraint on plastic flow. Furthermore, it is seen that the apparent increase in the overall material yield stress due to gradient effects, which has been observed in the results presented so far, is not so obvious when imposing vanishing higher order traction at the interface. For this

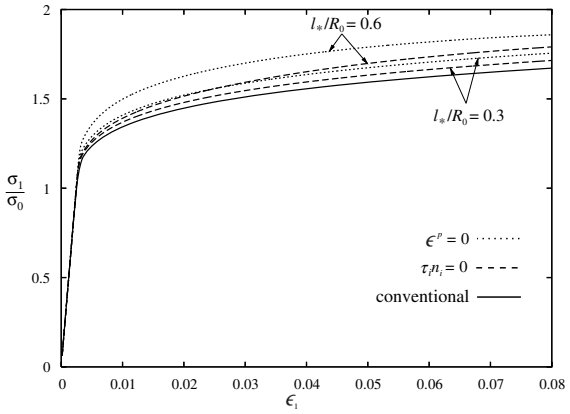

Fig. 7. Overall uniaxial stress–strain response ($\kappa = 0$) for a material with rigid inclusions using different higher order boundary conditions on the inclusion surface. The solid line shows results for a conventional model. The dashed and the dotted lines show results for the higher order traction and the plastic strain set to zero on the inclusion surface, respectively. Results are shown for two different values of l_*/R_0. The overall loading rate is given by $\dot{\epsilon}_1 = \dot{\epsilon}_0$.

boundary condition the strengthening effect seems to stem more from an increased material hardening, which takes place over a longer time in the plastic range and not predominantly in the beginning of plastic deformation.

5. Discussion

An elastic–viscoplastic material model is needed for a number of applications, where strain rate sensitivity of material behaviour is important, e.g. at rapid loading in the room temperature range, or at elevated temperatures, where time dependence of plastic flow tends to get more pronounced. This is the motivation for the constitutive model presented in the present paper.

The strain gradient plasticity theory proposed by Fleck and Hutchinson (2001) has three different material length parameters, each of which has a physical interpretation. Within this framework a theory with a single material length parameter has been formulated, closely related to the strain gradient theory of Aifantis (1984). In the finite strain generalisation developed by Niordson and Redanz (2004), all three material length parameters are incorporated, but results are also shown for the single parameter version of the theory. The present elastic–viscoplastic version of the theory has been formulated so far as a single parameter theory. Since no internal elastic–plastic boundaries exists in the elastic–viscoplastic model, no internal higher order boundary conditions need to be specified.

The results here show that both for the material containing voids and the material containing inclusions the overall stress–strain response is more stiff the larger the value of the ratio l_*/R_0 between the material length and the void or inclusion radius. This result is as expected based on the time independent strain gradient plasticity model. Also, in both cases the strain rate has been varied, and the results have shown the characteristic feature of a strain rate sensitive material that the stress levels are higher the higher the strain rate.

Due to the strongly nonlinear dependence on the stresses in (13), the solution will tend to be numerically unstable at low viscosities. To increase the stable step length at lower viscosities than those considered here, forward gradient methods (Peirce et al., 1984) would be useful.

For rigid inclusions computations using either of the two extreme sets of boundary conditions on the inclusion–matrix interface have been compared (Fig. 7). For both sets of higher order boundary conditions

the response is more stiff than that corresponding to the conventional material with no characteristic material length, as would be expected due to the gradient effects accounted for in either case. Furthermore, the boundary condition representing full constraint on plastic flow at the interface to the material that does not yield gives an overall stiffer response than the other set of boundary conditions, representing no constraint on plastic flow at the interface.

Acknowledgement

This work is financially supported by the Danish Technical Research Council in a project entitled Modeling Plasticity at the Micron Scale.

References

Aifantis, E.C., 1984. On the microstructural origin of certain inelastic models. Transactions of the ASME, Journal of Engineering Materials and Technology 106, 326–330.

Benallal, A., Tvergaard, V., 1995. Nonlocal continuum effects on bifurcation in the plane strain tension–compression test. Journal of the Mechanics and Physics of Solids 43, 741–770.

Fleck, N.A., Hutchinson, J.W., 1997. Strain gradient plasticity. In: Hutchinson, J.W., Wu, T.Y. (Eds.), Advances in applied mechanics, 33. Academic Press, New York, pp. 295–361.

Fleck, N.A., Hutchinson, J.W., 2001. A reformulation of strain gradient plasticity. Journal of the Mechanics and Physics of Solids 49, 2245–2271.

Fleck, N.A., Muller, G.M., Ashby, M.F., Hutchinson, J.W., 1994. Strain gradient plasticity: theory and experiment. Acta Metallurgica et Materialia 42, 475–487.

Fredriksson, P., Gudmundson, P., 2005. Size-dependent yield strength of thin films. International Journal of Plasticity 21, 1834–1854.

Gudmundson, P., 2004. A unified treatment of strain gradient plasticity. Journal of the Mechanics and Physics of Solids 52, 1379–1406.

Gurtin, M.E., 2003. On a framework for small-deformation viscoplasticity: free energy, microforces, strain gradients. International Journal of Plasticity 19, 47–90.

Haque, M.A., Saif, M.T.A., 2003. Strain gradient effect in nanoscale thin films. Acta Materialia 51, 3053–3061.

Huang, Y., Gao, H., Nix, W.D., Hutchinson, J.W., 2000. Mechanism-based strain gradient plasticity—II. Analysis. Journal of the Mechanics and Physics of Solids 48, 99–128.

Ma, Q., Clarke, D.R., 1995. Size dependent hardness of silver single crystals. Journal of Materials Research 10, 853–863.

Niordson, C.F., 2003. Strain gradient plasticity effects in whisker-reinforced metals. Journal of the Mechanics and Physics of Solids 51, 1863–1883.

Niordson, C.F., Redanz, P., 2004. Size-effects in plane strain sheet-necking. Journal of the Mechanics and Physics of Solids 52, 2431–2454.

Niordson, C.F., Tvergaard, V., 2005. Instabilities in power law gradient hardening materials. International Journal of Solids and Structures 42, 2559–2573.

Niordson, C.F., Tvergaard, V., in press. Size-effects on cavitation instabilities. Journal of Applied Mechanics.

Peirce, D., Shih, C.F., Needleman, A., 1984. A tangent modulus method for rate dependent solids. Computers and Structures 18, 875–887.

Stölken, J.S., Evans, A.G., 1998. Microbend test method for measuring the plasticity length scale. Acta Materialia 46, 5109–5115.

Tvergaard, V., 1976. Effect of thickness inhomogeneities in internally pressurized elastic–plastic spherical shells. Journal of the Mechanics and Physics of Solids 24, 291–304.

Tvergaard, V., Niordson, C., 2004. Nonlocal plasticity effects on interaction of different size voids. International Journal of Plasticity 20, 107–120.

P2

Strain gradient crystal plasticity effects on flow localization

To be published in
International Journal of Plasticity

ARTICLE IN PRESS

Available online at www.sciencedirect.com
ScienceDirect

ELSEVIER

International Journal of Plasticity xxx (2007) xxx–xxx

INTERNATIONAL JOURNAL OF Plasticity

www.elsevier.com/locate/ijplas

Strain gradient crystal plasticity effects on flow localization

Ulrik Borg *

Department of Mechanical Engineering, Solid Mechanics, Technical University of Denmark, Kgs. Lyngby, DK-2800, Denmark

Received 18 March 2006; received in final revised form 25 December 2006

Abstract

In metal grains one of the most important failure mechanisms involves shear band localization. As the band width is small, the deformations are affected by material length scales. To study localization in single grains a rate-dependent crystal plasticity formulation for finite strains is presented for metals described by the reformulated Fleck–Hutchinson strain gradient plasticity theory. The theory is implemented numerically within a finite element framework using slip rate increments and displacement increments as state variables. The formulation reduces to the classical crystal plasticity theory in the absence of strain gradients. The model is used to study the effect of an internal material length scale on the localization of plastic flow in shear bands in a single crystal under plane strain tension. It is shown that the mesh sensitivity is removed when using the nonlocal material model considered. Furthermore, it is illustrated how different hardening functions affect the formation of shear bands.

Keywords: Strain gradient plasticity; Crystal plasticity; Shear band

1. Introduction

A significant amount of experimental studies have shown that inhomogeneous plastic flow in metals is size dependent, with smaller generally being harder (see e.g. Fleck

* Tel.: +45 4525 4262; fax: +45 4593 1475.
E-mail address: ub@mek.dtu.dk.

0749-6419/$ - see front matter © 2007 Elsevier Ltd. All rights reserved.
doi:10.1016/j.ijplas.2007.01.003

Please cite this article in press as: Borg, U., Strain gradient crystal plasticity effects on ..., Int. J. Plasticity (2007), doi:10.1016/j.ijplas.2007.01.003

et al., 1994; Haque and Saif, 2003; Stölken and Evans, 1998). It has been argued by Nye (1953) and Ashby (1970) that this size effect is due to the interaction of plastic strain gradient induced geometrically necessary dislocations with statistically stored dislocations. Plasticity theories, where stress in a material point only depends on variables in the same point, cannot capture such observed size effects. Several phenomenological strain gradient plasticity theories have been developed to incorporate the influence of a characteristic material length into the constitutive relations for isotropic materials (Aifantis, 1984; Fleck and Hutchinson, 1997, 2001; Gao et al., 1999; Gudmundson, 2004; Abu Al-Rub and Voyiadjis, 2006). This length scale should be related to for example precipitate spacings in alloys, void spacings, dislocation spacings, grain sizes etc.

When studying the deformation of metals at the grain scale, the anisotropy of each crystal becomes important, and therefore crystal plasticity models can give a better description of the material behavior at this scale. However, classical crystal plasticity formulations like Peirce et al. (1983) have no incorporated length scale. Nonlocal formulations of crystal plasticity have been proposed by several authors. For example, Acharya and Bassani (2000) have presented a formulation where the strain gradients enter through the hardening modulus, Gurtin (2000, 2002) has proposed a formulation based on the fact that the free energy scales with the net Burgers vector and where the constitutive equations are obtained from thermodynamical arguments, and Han et al. (2005a) have presented a crystal plasticity formulation of the so-called mechanism-based strain gradient plasticity theory by Gao et al. (1999). Furthermore, Shu and Fleck (1999) presented a rate-dependent crystal plasticity formulation as an extension to the strain gradient plasticity theory by Fleck and Hutchinson (1997), which has later been generalized to finite deformations by Shu and Barlow (2000). In the Fleck and Hutchinson (1997) gradient theory the higher order stresses build up in the elastic regime, and the plastic part of the strain gradient is not the spatial derivative of the plastic part of the strain. These two deficiencies have been overcome in the reformulated strain gradient theory by Fleck and Hutchinson (2001). Applications of nonlocal crystal plasticity includes microbending of thin beams (Han et al., 2005b), shear of bicrystals (Shu and Fleck, 1999), deformation of whisker-reinforced metal-matrix composite (Shu and Barlow, 2000), analysis of shear banding (Sluys and Estrin, 2000) and the behavior of polycrystals (Cheong et al., 2005).

In the present paper, a rate-dependent strain gradient crystal plasticity formulation for finite strains is presented. The basic formulation of the theory is equivalent to the formulation of Gurtin (2000, 2002), where the crystallographic slip and slip gradient contributes to the plastic work. The principle of virtual power and the extra force balance for each slip system (the strong form of the field equations) is in fact a special case of the formulation by Gurtin (2000, 2002). The constitutive equations are based on the strain gradient theory by Fleck and Hutchinson (2001) and differs significantly from the constitutive framework of Gurtin (2000, 2002). It uses the crystal plasticity framework of Peirce et al. (1983) and includes ideas from the finite strain version of Fleck and Hutchinson (2001) by Niordson and Redanz (2004). Similar to Borg et al. (2006) for an isotropic viscoplastic strain gradient theory, a viscoplastic potential is introduced and the viscous behavior is accounted for by a power-law relationship for a nonlocal effective slip rate.

As an application of the theory, a plane strain tensile test specimen of a single crystal is considered. Here, the localization of plastic flow in shear bands is emanating from an initial geometrical imperfection. This problem has been studied using classical rate-depen-

Please cite this article in press as: Borg, U., Strain gradient crystal plasticity effects on ..., Int. J. Plasticity (2007), doi:10.1016/j.ijplas.2007.01.003

dent crystal plasticity theory by Peirce et al. (1983). Later works have observed size effects in the localization of deformation, where an internal length scale sets the width of a shear band and can remove the mesh dependence (see e.g. Aifantis, 1984; Tvergaard and Needleman, 1995; Mikkelsen, 1999; Sluys and Estrin, 2000). The analysis performed using the presented strain gradient crystal plasticity formulation are in agreement with these results, which supports the presented formulation. Furthermore, the effect of different hardening functions on the localization behavior is studied.

2. Material model

The kinematical basis for the following is taken from Peirce et al. (1983), where a quantitative description of plastic deformation in single crystals is based on crystallographic shearing. In this paper, a Greek superscript in a parentheses denotes a slip system, and repeated lower-case Latin indices imply summation over the range 1–3. A bold character denotes a vector or a tensor and an ascent dot denotes the time derivative. It is assumed that a general homogeneous deformation can be represented by the deformation gradient tensor $\mathbf{F}$ that maps a line element $d\mathbf{X}$ in the reference configuration to $d\mathbf{x}$ in the deformed configuration as $d\mathbf{x} = \mathbf{F} \cdot d\mathbf{X}$. The deformation gradient is decomposed into an elastic and plastic part written as

$$\mathbf{F} = \mathbf{F}^{*} \cdot \mathbf{F}^{\mathrm{P}} \tag{1}$$

where elastic deformation and rigid body rotation are embodied in $\mathbf{F}^{*}$ and $\mathbf{F}^{\mathrm{P}}$ represents the crystallographic shearing due to dislocation motion along specific slip systems. A slip system (α) is specified by the lattice vectors $\mathbf{s}^{(\alpha)}$ and $\mathbf{m}^{(\alpha)}$, where $\mathbf{s}^{(\alpha)}$ is the slip direction and $\mathbf{m}^{(\alpha)}$ is the direction normal to the slip plane. The lattice vectors stretch and rotate by

$$\mathbf{s}^{*(\alpha)} = \mathbf{F}^{*} \cdot \mathbf{s}^{(\alpha)}, \quad \mathbf{m}^{*(\alpha)} = \mathbf{m}^{(\alpha)} \cdot \mathbf{F}^{*-1} \tag{2}$$

The velocity gradient $\mathbf{L}$ can be expressed as

$$\mathbf{L} = \dot{\mathbf{F}} \cdot \mathbf{F}^{-1} = \dot{\mathbf{F}}^{*} \cdot \mathbf{F}^{*-1} + \mathbf{F}^{*} \cdot \dot{\mathbf{F}}^{\mathrm{P}} \cdot \mathbf{F}^{\mathrm{P}-1} \cdot \mathbf{F}^{*-1} = \mathbf{L}^{*} + \mathbf{L}^{\mathrm{P}} \tag{3}$$

where the plastic rate $\dot{\mathbf{F}}^{\mathrm{P}}$ can be found by the rate of shearing $\dot{\gamma}^{(\alpha)}$ on each slip system as

$$\dot{\mathbf{F}}^{\mathrm{P}} = \sum_{\alpha} \dot{\gamma}^{(\alpha)} \mathbf{s}^{(\alpha)} \mathbf{m}^{(\alpha)} \cdot \mathbf{F}^{\mathrm{P}} \tag{4}$$

The strain rate is taken as the symmetric part of the velocity gradient, $\dot{\epsilon}_{ij} = \frac{1}{2}(L_{ij} + L_{ji})$. Introducing $\mu_{ij}^{*(\alpha)} = \frac{1}{2}(s_i^{*(\alpha)} m_j^{*(\alpha)} + s_j^{*(\alpha)} m_i^{*(\alpha)})$ as the classical Schmid orientation tensor, the overall macroscopic plastic strain rate components given as the symmetric part of the plastic part of the velocity gradient can be expressed as

$$\dot{\epsilon}_{ij}^{p} = \frac{1}{2}(L_{ij}^{\mathrm{P}} + L_{ji}^{\mathrm{P}}) = \sum_{\alpha} \dot{\gamma}^{(\alpha)} \mu_{ij}^{*(\alpha)} \tag{5}$$

The plastic strain rate is used to compute the elastic part of the strain rate as $\dot{\epsilon}_{ij}^{\mathrm{E}} = \dot{\epsilon}_{ij} - \dot{\epsilon}_{ij}^{\mathrm{P}}$, with the elastic strain rate given by $\dot{\epsilon}_{ij}^{\mathrm{E}} = \frac{1}{2}(L_{ij}^{*} + L_{ji}^{*})$.

To account for the effects of increased material hardening due to interaction of geometrically necessary dislocations induced by slip gradients with statistically stored dislocations accumulated by slip, it is assumed that both the slip rates and slip rate gradients contribute to the plastic work, so that the plastic dissipation rate $\dot{W}^{\mathrm{P}}$ per unit volume is taken as

Please cite this article in press as: Borg, U., Strain gradient crystal plasticity effects on ..., Int. J. Plasticity (2007), doi:10.1016/j.ijplas.2007.01.003

$$\dot{W}^{\mathrm{P}} = \sum_{\alpha} (Q^{(\alpha)} \dot{\gamma}^{(\alpha)} + \xi_{\mathrm{S}}^{(\alpha)} s_i^{*(\alpha)} \dot{\gamma}_{,i}^{(\alpha)} + \xi_{\mathrm{T}}^{(\alpha)} t_i^{*(\alpha)} \dot{\gamma}_{,i}^{(\alpha)}) \tag{6}$$

where the stress field $\mathrm{Q}^{(\alpha)}$ is an effective stress work-conjugate to the slip and $\xi_{\mathrm{S}}^{(\alpha)}$ and $\xi_{\mathrm{T}}^{(\alpha)}$ are higher order stresses work-conjugate to the slip gradients along the slip direction and the transverse direction, respectively. The vector $t_i^{(\alpha)}$ denotes the transverse direction and thus forms a triad with vectors $s_i^{(\alpha)}$ and $m_i^{(\alpha)}$. A relationship between the density of geometrically necessary dislocations and slip gradients can be obtained via Nye's dislocation density tensor, but the present theory is not directly based on such a relationship. Following Fleck et al. (1994), the slip gradient in the $\mathbf{s}^{(\alpha)}$ direction is related to geometrically necessary edge dislocations, and the slip gradient in the $\mathbf{t}^{(\alpha)}$ direction is related to geometrically necessary screw dislocations. A slip gradient in the $\mathbf{m}^{(\alpha)}$ direction does not induce any geometrically necessary dislocations and therefore it does not contribute to the plastic work rate. The elastic work rate per unit volume $\dot{W}^{\mathrm{E}}$ is taken as

$$\dot{W}^{\mathrm{E}} = \sigma_{ij} \dot{\epsilon}_{ij}^{\mathrm{E}} = \sigma_{ij} \left(\dot{\epsilon}_{ij} - \sum_{\alpha} \dot{\gamma}^{(\alpha)} \mu_{ij}^{*(\alpha)} \right) = \sigma_{ij} \dot{\epsilon}_{ij} - \sum_{\alpha} \tau^{(\alpha)} \dot{\gamma}^{(\alpha)} \tag{7}$$

where σ_{ij} is the Cauchy stress and $\tau^{(\alpha)} = \sigma_{ij} \mu_{ij}^{*(\alpha)}$ is the classical Schmid stress. The principle of virtual power in total form in the deformed configuration can thus be written as

$$\int_V \left(\sigma_{ij} \delta \dot{\epsilon}_{ij} + \sum_{\alpha} (Q^{(\alpha)} - \tau^{(\alpha)}) \delta \dot{\gamma}^{(\alpha)} + \sum_{\alpha} (\xi_{\mathrm{S}}^{(\alpha)} s_i^{*(\alpha)} + \xi_{\mathrm{T}}^{(\alpha)} t_i^{*(\alpha)}) \delta \dot{\gamma}_{,i}^{(\alpha)} \right) \mathrm{d}V$$
$$= \int_{\mathrm{S}} \left(T_i \delta \dot{u}_i + \sum_{\alpha} r^{(\alpha)} \delta \dot{\gamma}^{(\alpha)} \right) \mathrm{d}S \tag{8}$$

with T_i being the surface traction, while $r^{(\alpha)}$ is the higher order traction. The form of (8) is a special case of the principle of virtual power in Gurtin (2000, 2002). The relation must hold for arbitrary variations of $\dot{u}_i$ and $\dot{\gamma}^{(\alpha)}$ which leads to the strong form of the field equations. First we have the classical balance and boundary conditions:

$$\sigma_{ij,j} = 0, \qquad T_i = \sigma_{ij} n_j \tag{9}$$

where n_i is the surface unit normal in the current configuration. Next we have the consistency condition and higher order boundary conditions

$$Q^{(\alpha)} - \tau^{(\alpha)} - \xi_{S,i}^{(\alpha)} s_i^{*(\alpha)} - \xi_{T,i}^{(\alpha)} t_i^{*(\alpha)} = 0 \tag{10}$$

$$r^{(\alpha)} = (\xi_{\mathrm{S}}^{(\alpha)} s_i^{*(\alpha)} + \xi_{\mathrm{T}}^{(\alpha)} t_i^{*(\alpha)}) n_i \tag{11}$$

To obtain the principle of virtual power in the reference configuration, Kirchhoff stress measures are defined as (defining J as the determinant of the deformation gradient)

$$\varsigma_{ij} = J \sigma_{ij}, \qquad q^{(\alpha)} = J Q^{(\alpha)}, \qquad \rho_{\mathrm{S}}^{(\alpha)} = J \xi_{\mathrm{S}}^{(\alpha)}, \qquad \rho_{\mathrm{T}}^{(\alpha)} = J \xi_{\mathrm{T}}^{(\alpha)} \tag{12}$$

When introducing the Jaumann rate of the Kirchhoff stress, $\overset{\nabla}{\varsigma}_{ij}$, the incremental principle of virtual power in an updated Lagrangian framework (where the deformed configuration is taken as a reference, thus $\mathbf{F}^{*} = \mathbf{F}^{\mathrm{P}} = \mathbf{I}$ but $\dot{\mathbf{F}}^{*}$ and $\dot{\mathbf{F}}^{\mathrm{P}}$ are not vanishing), can be expressed as

$$\int_{V_0} (\overset{\nabla}{\varsigma}_{ij} \delta \dot{\epsilon}_{ij} - \sigma_{ij} (2 \dot{\epsilon}_{ik} \delta \dot{\epsilon}_{kj} - L_{kj} \delta L_{ki}) + \sum_{\alpha} (\dot{q}^{(\alpha)} - s_i^{(\alpha)} (\dot{F}_{ki}^{*} \varsigma_{kj} + \dot{\varsigma}_{ij}$$

Please cite this article in press as: Borg, U., Strain gradient crystal plasticity effects on ..., Int. J. Plasticity (2007), doi:10.1016/j.ijplas.2007.01.003

$$-\varsigma_{ik}\dot{F}^{*}_{jk})m^{(\alpha)}_{j})\delta\dot{\gamma}^{(\alpha)}+\sum_{\alpha}(\dot{\rho}^{(\alpha)}_{\mathrm{S}}s^{(\alpha)}_{i}-\rho^{(\alpha)}_{\mathrm{S}}\dot{F}^{\mathrm{P}}_{ik}s^{(\alpha)}_{k}+\dot{\rho}^{(\alpha)}_{\mathrm{T}}t^{(\alpha)}_{i}+\rho^{(\alpha)}_{\mathrm{T}}(\dot{t}^{*(\alpha)}_{i}-\dot{F}_{ik}t^{(\alpha)}_{k}))\delta\dot{\gamma}^{(\alpha)}_{0,i})\mathrm{d}V_{0}$$

$$=\int_{S_0}\left(\dot{T}^{0}_{i}\delta\dot{u}_{i}+\sum_{\alpha}\dot{r}^{(\alpha)_0}\delta\dot{\gamma}^{(\alpha)}\right)\mathrm{d}S_{0} \tag{13}$$

where the subscript "0" refers to the reference configuration. The time derivative of $t^{*(\alpha)}_{i}$ can be written as $\dot{t}^{*(\alpha)}_{i}=e_{ijk}(s^{(\alpha)}_{l}m^{(\alpha)}_{k}\dot{F}^{*}_{jl}-s^{(\alpha)}_{j}m^{(\alpha)}_{l}\dot{F}^{*}_{lk})$, where e_{ijk} is the permutation symbol. The first two terms in the volume integral are identical to the formulation used by Niordson and Redanz (2004) for a strain gradient plasticity theory for isotropic materials, and the rest of the terms are of a similar form.

A nonlocal measure of the effective slip $\gamma^{(\alpha)}_{\mathrm{e}}$ is defined on the basis of the slip rate and the directional derivative of the slip rate through the incremental relation

$$\dot{\gamma}^{(\alpha)^2}_{\mathrm{e}}=\dot{\gamma}^{(\alpha)^2}+(l_{\mathrm{S}}\dot{\gamma}^{(\alpha)}_{,i}s^{(\alpha)}_{i})^{2}+(l_{\mathrm{T}}\dot{\gamma}^{(\alpha)}_{,i}t^{(\alpha)}_{i})^{2} \tag{14}$$

where l_{S} and l_{T} are internal material length parameters introduced for dimensional consistency.

To obtain a viscoplastic version a viscoplastic potential is to be defined. In the rate-independent phenomenological strain gradient theory by Fleck and Hutchinson (2001) a plastic potential, V, is defined as

$$V(E^{\mathrm{P}})=\int_{0}^{E^{\mathrm{P}}}\sigma_{\mathrm{c}}(E^{\mathrm{P}'})\mathrm{d}E^{\mathrm{P}'} \tag{15}$$

where E^{P} is a nonlocal measure of the effective plastic strain and $\sigma_{\mathrm{c}}(E^{\mathrm{P}})$ denotes the uniaxial tensile stress versus plastic strain curve of the material. In the viscoplastic version of the Fleck and Hutchinson (2001) theory presented by Borg et al. (2006), a viscoplastic potential is defined as

$$V(E^{\mathrm{P}},\dot{E}^{\mathrm{P}})=\int_{0}^{\dot{E}^{\mathrm{P}}}\sigma_{\mathrm{c}}(\dot{E}^{\mathrm{P}'},E^{\mathrm{P}})\mathrm{d}\dot{E}^{P'} \tag{16}$$

where the function $\sigma_{\mathrm{c}}(\dot{E}^{\mathrm{P}'},E^{\mathrm{P}})$ denotes the uniaxial tensile stress versus plastic strain rate curve. For the present crystal plasticity version the viscoplastic potential is taken as $V(\dot{\gamma}^{(\alpha)}_{\mathrm{e}},\gamma^{(\alpha)}_{\mathrm{e}})=\sum_{\alpha}\Phi^{(\alpha)}$, where the potential for each slip system is given by

$$\Phi^{(\alpha)}(\dot{\gamma}^{(\alpha)}_{\mathrm{e}},\gamma^{(\alpha)}_{\mathrm{e}})=\int_{0}^{\dot{\gamma}^{(\alpha)}_{\mathrm{e}}}\tau^{(\alpha)}_{\mathrm{e}}(\dot{\gamma}^{(\alpha)'}_{\mathrm{e}},\gamma^{(\alpha)}_{\mathrm{e}})\mathrm{d}\dot{\gamma}^{(\alpha)'}_{\mathrm{e}} \tag{17}$$

where $\tau^{(\alpha)}_{\mathrm{e}}$ is an effective stress work-conjugate to the effective slip rate, $\dot{\gamma}^{(\alpha)}_{\mathrm{e}}$. Taking the variation of the potential one obtains by use of (6) and (12) that

$$\delta\Phi^{(\alpha)}=\tau^{(\alpha)}_{\mathrm{e}}\delta\dot{\gamma}^{(\alpha)}_{\mathrm{e}}=q^{(\alpha)}\delta\dot{\gamma}^{(\alpha)}+\rho^{(\alpha)}_{\mathrm{S}}s^{(\alpha)}_{k}\delta\dot{\gamma}^{(\alpha)}_{,k}+\rho^{(\alpha)}_{\mathrm{T}}t^{(\alpha)}_{k}\delta\dot{\gamma}^{(\alpha)}_{,k} \tag{18}$$

Now, by inserting the variation of the effective slip rate given by (14) the constitutive equations for the effective stress $q^{(\alpha)}$ and the higher order stresses $\rho^{(\alpha)}_{\mathrm{S}}$ and $\rho^{(\alpha)}_{\mathrm{T}}$ are obtained as

$$q^{(\alpha)}=\tau^{(\alpha)}_{\mathrm{e}}\frac{\dot{\gamma}^{(\alpha)}}{\dot{\gamma}^{(\alpha)}_{\mathrm{e}}} \tag{19}$$

$$\rho^{(\alpha)}_{\mathrm{S}}=\tau^{(\alpha)}_{\mathrm{e}}\frac{\dot{\gamma}^{(\alpha)}_{,i}s^{(\alpha)}_{i}}{\dot{\gamma}^{(\alpha)}_{\mathrm{e}}}l^{2}_{\mathrm{S}} \tag{20}$$

Please cite this article in press as: Borg, U., Strain gradient crystal plasticity effects on ..., Int. J. Plasticity (2007), doi:10.1016/j.ijplas.2007.01.003

$$\rho_{\mathrm{T}}^{(\alpha)} = \tau_{\mathrm{e}}^{(\alpha)} \frac{\dot{\gamma}_{,i}^{(\alpha)} t_i^{(\alpha)}}{\dot{\gamma}_{\mathrm{e}}^{(\alpha)}} l_{\mathrm{T}}^2 \tag{21}$$

By substituting these expressions for $\dot{\gamma}^{(\alpha)}$, $\dot{\gamma}_{,i}^{(\alpha)} s_i^{(\alpha)}$ and $\dot{\gamma}_{,i}^{(\alpha)} t_i^{(\alpha)}$ into the definition of the effective slip (14), the introduced effective stress $\tau_{\mathrm{e}}^{(\alpha)}$ can be expressed in the following quadratic form in $q^{(\alpha)}$, $\rho_{\mathrm{S}}^{(\alpha)}$ and $\rho_{\mathrm{T}}^{(\alpha)}$

$$\tau_{\mathrm{e}}^{(\alpha)^2} = q^{(\alpha)^2} + l_{\mathrm{S}}^{-2} \rho_{\mathrm{S}}^{(\alpha)^2} + l_{\mathrm{T}}^{-2} \rho_{\mathrm{T}}^{(\alpha)^2} \tag{22}$$

In the absence of slip gradients, the higher order stress vanishes and the effective stress $q^{(\alpha)}$ equals the classical Schmid stress $\tau^{(\alpha)}$. In that case the theory reduces to the classical rate-dependent crystal plasticity as presented by e.g. Peirce et al. (1983).

A power-law creep model is adopted for the effective slip rate $\dot{\gamma}_{\mathrm{e}}^{(\alpha)}$ to model the viscous material behavior

$$\dot{\gamma}_{\mathrm{e}}^{(\alpha)} = \dot{\gamma}_0 \left(\frac{\tau_{\mathrm{e}}^{(\alpha)}}{g^{(\alpha)}} \right)^{1/m} \tag{23}$$

where $\dot{\gamma}_0$ is a reference slip rate used as a scaling parameter to normalize the applied strain rate, and m is a strain rate hardening index with $m \to 0$ being the rate-independent limit. The functions $g^{(\alpha)}$, termed the slip resistance, characterize the current strain hardened state of the crystal. The slip resistance is taken to be a function of the accumulated effective slip, γ_{ea}, specified by

$$\gamma_{\mathrm{ea}} = \sum_{\alpha} \int \dot{\gamma}_{\mathrm{e}}^{(\alpha)} \, \mathrm{d}t \tag{24}$$

and hardens from an initial value τ_0 according to

$$\dot{g}^{(\alpha)} = \sum_{\beta} h_{\alpha\beta} \dot{\gamma}_{\mathrm{e}}^{(\beta)} \tag{25}$$

Here, $h_{\alpha\beta} = h_{\alpha\beta}(\gamma_{\mathrm{ea}})$ is the hardening matrix. It is noted that the slip resistance $\dot{g}^{(\alpha)}$ depends on $\dot{\gamma}_{\mathrm{e}}^{(\alpha)}$ instead of $|\dot{\gamma}^{(\alpha)}|$ as it would in classical crystal plasticity, meaning that not only the slips but also the slip gradients generate hardening. The form of the hardening matrix used here is given by

$$h_{\alpha\beta} = h\delta_{\alpha\beta} + ph(1 - \delta_{\alpha\beta}) \tag{26}$$

where the parameter p is a latent hardening index (usually in the range $1.0 \leqslant p \leqslant 1.4$), $h = h(\gamma_{\mathrm{ea}})$ is the self-hardening modulus and $\delta_{\alpha\beta}$ denotes the Kronecker delta function. In this work two different expressions for the self-hardening moduli is used. The first one is

$$h(\gamma_{\mathrm{ea}}) = h_0 / \cosh \left(\frac{h_0 \gamma_{\mathrm{ea}}}{\tau_s - \tau_0} \right) \tag{27}$$

where the constant h_0 represents an initial hardening rate, τ_{s} is a saturation stress and $h = h_0$ would represent linear hardening. The other self-hardening modulus used is a power-law type given by

$$h(\gamma_{\mathrm{ea}}) = h_0 \left(\frac{h_0 \gamma_{\mathrm{ea}}}{\tau_0 n} + 1 \right)^{n-1} \tag{28}$$

Please cite this article in press as: Borg, U., Strain gradient crystal plasticity effects on ..., Int. J. Plasticity (2007), doi:10.1016/j.ijplas.2007.01.003

where n is the hardening exponent. The form of the self-hardening modulus given by (27) rapidly approaches zero, whereas the power-law hardening value decays much less rapidly.

Increments of the Jaumann rate of Kirchhoff stress are given by the incremental elastic constitutive equation

$$\overset{\nabla}{\varsigma}_{ij}\Delta t = R_{ijkl}\left(\Delta\epsilon_{kl} - \Delta t\sum_{\alpha}\dot{\gamma}^{(\alpha)}\mu_{kl}^{*(\alpha)}\right) = \Delta\varsigma_{ij} - \Delta\omega_{ik}\sigma_{kj} - \sigma_{ik}\Delta\omega_{jk} \tag{29}$$

where $\dot{\omega}_{ij} = \frac{1}{2}(L_{ij} - L_{ji})$ denotes the material spin rate and the elastic stiffness tensor is given by $R_{ijkl} = \frac{E}{1+\nu}\left(\frac{1}{2}(\delta_{ik}\delta_{jl} + \delta_{il}\delta_{jk}) + \frac{\nu}{1-2\nu}\delta_{ij}\delta_{kl}\right)$. This work is restricted to elastic isotropy, even though the formulation is capable of including elastic anisotropy. The focus in this paper is on localization which occurs after several percent plastic strain, and therefore the elastic behavior plays a minor role. The increments of the effective stress and the higher order stresses can be written as

$$\dot{q}^{(\alpha)} = (m-1)\tau_{\mathrm{e}}^{(\alpha)}\frac{\dot{\gamma}^{(\alpha)}}{\dot{\gamma}_{\mathrm{e}}^{(\alpha)^2}}\ddot{\gamma}_{\mathrm{e}}^{(\alpha)} + \tau_{\mathrm{e}}\frac{1}{\dot{\gamma}_{\mathrm{e}}^{(\alpha)}}\ddot{\gamma}^{(\alpha)} + \dot{\gamma}_0^{-m}\dot{\gamma}_{\mathrm{e}}^{(\alpha)^{m-1}}\dot{\gamma}^{(\alpha)}\dot{g}^{(\alpha)} \tag{30}$$

$$\dot{\rho}_{\mathrm{S}}^{(\alpha)} = (m-1)l_{\mathrm{S}}^2\tau_{\mathrm{e}}^{(\alpha)}\frac{(\dot{\gamma}_{,i}^{(\alpha)}s_i^{(\alpha)})}{\dot{\gamma}_{\mathrm{e}}^{(\alpha)^2}}\ddot{\gamma}_{\mathrm{e}}^{(\alpha)} + l_{\mathrm{S}}^2\tau_{\mathrm{e}}^{(\alpha)}\frac{1}{\dot{\gamma}_{\mathrm{e}}^{(\alpha)}}s_i^{(\alpha)}\ddot{\gamma}_{,i}^{(\alpha)} + l_{\mathrm{S}}^2\dot{\gamma}_0^{-m}(\dot{\gamma}_{,i}^{(\alpha)}s_i^{(\alpha)})\dot{\gamma}_{\mathrm{e}}^{(\alpha)^{m-1}}\dot{g}^{(\alpha)} \tag{31}$$

$$\dot{\rho}_{\mathrm{T}}^{(\alpha)} = (m-1)l_{\mathrm{T}}^2\tau_{\mathrm{e}}^{(\alpha)}\frac{(\dot{\gamma}_{,i}^{(\alpha)}t_i^{(\alpha)})}{\dot{\gamma}_{\mathrm{e}}^{(\alpha)^2}}\ddot{\gamma}_{\mathrm{e}}^{(\alpha)} + l_{\mathrm{T}}^2\tau_{\mathrm{e}}^{(\alpha)}\frac{1}{\dot{\gamma}_{\mathrm{e}}^{(\alpha)}}t_i^{(\alpha)}\ddot{\gamma}_{,i}^{(\alpha)} + l_{\mathrm{T}}^2\dot{\gamma}_0^{-m}(\dot{\gamma}_{,i}^{(\alpha)}t_i^{(\alpha)})\dot{\gamma}_{\mathrm{e}}^{(\alpha)^{m-1}}\dot{g}^{(\alpha)} \tag{32}$$

where the change in the effective slip rate is taken as $\ddot{\gamma}_{\mathrm{e}}^{(\alpha)} = \frac{\dot{\gamma}^{(\alpha)}}{\dot{\gamma}_{\mathrm{e}}^{(\alpha)}}\ddot{\gamma}^{(\alpha)} + \frac{l_{\mathrm{S}}^2\dot{\gamma}_{,k}^{(\alpha)}s_k^{(\alpha)}}{\dot{\gamma}_{\mathrm{e}}^{(\alpha)}}s_i^{(\alpha)}\ddot{\gamma}_{,i}^{(\alpha)} + \frac{l_{\mathrm{T}}^2\dot{\gamma}_{,k}^{(\alpha)}t_k^{(\alpha)}}{\dot{\gamma}_{\mathrm{e}}^{(\alpha)}}t_i^{(\alpha)}\ddot{\gamma}_{,i}^{(\alpha)}$. The values of $\dot{\gamma}_{\mathrm{e}}^{(\alpha)}$, $\dot{\gamma}^{(\alpha)}$ and $\dot{\gamma}_{,i}^{(\alpha)}$ are taken from the previous increment, so that only $\ddot{\gamma}^{(\alpha)}$ and its spacial gradient $\ddot{\gamma}_{,i}^{(\alpha)}$ are unknowns.

3. Problem formulation and numerical method

The specimen to be analyzed here is a single crystal of the FCC type under plane strain tension. In an FCC crystal there are four slip planes of the family $\{1\,1\,1\}$ and each of these have three slip directions of the family $\langle 1\,1\,0\rangle$, giving a total of 12 slip systems. When applying a line load parallel to a $\langle 1\,1\,0\rangle$ direction certain slip systems act cooperatively, which enables plane strain conditions to be achieved (Rice, 1987). In that case, the 12 slip systems can be reduced to three effective in-plane slip systems. In the analysis performed, these three slip systems are oriented at $\pm 30°$ and $90°$ from the tensile axis. Thus, in the

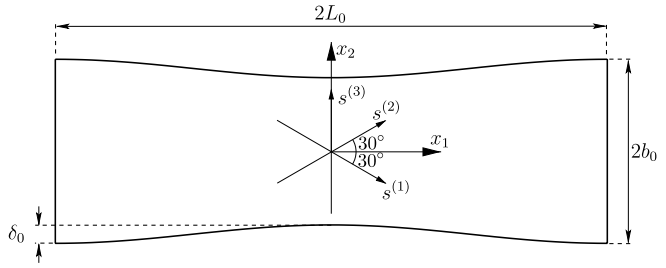

Fig. 1. The tensile specimen considered with initial dimensions and slip systems.

Please cite this article in press as: Borg, U., Strain gradient crystal plasticity effects on ..., Int. J. Plasticity (2007), doi:10.1016/j.ijplas.2007.01.003

undeformed state, the slip systems are symmetrically oriented about the tensile axis. The bar analyzed has a geometrical imperfection as shown in Fig. 1. The initial dimensions of the tensile specimen are given by the length $2L_0$, the width $2b_0$ and a thickness inhomogeneity δ given by $\delta(x_1) = \frac{1}{2}\delta_0(1 + \cos(\frac{\pi x_1}{L_0}))$, where δ_0 is the imperfection magnitude. Due to symmetry, only one quarter (here, the upper right) of the specimen is analyzed. The conventional boundary conditions applied are given by

$$\begin{aligned} &\dot{u}_1 = 0, \quad \dot{T}_2 = 0 \quad \text{at } x_1 = 0 \\ &\dot{u}_1 = \dot{U}, \quad \dot{T}_2 = 0 \quad \text{at } x_1 = L_0 \\ &\dot{u}_2 = 0, \quad \dot{T}_1 = 0 \quad \text{at } x_2 = 0 \\ &\dot{T}_1 = 0, \quad \dot{T}_2 = 0 \quad \text{at } x_2 = b_0 - \delta \end{aligned} \tag{33}$$

where $\dot{T}_i$ are surface traction rates and $\dot{U}$ is the prescribed end displacement rate.

Regarding the higher order boundary conditions, we have the choice of either constraining the slip rates, i.e. setting $\dot{\gamma}^{(\alpha)} = 0$, or having no constrains on the plastic flow by setting $\dot{r}^{(\alpha)} = 0$. Such boundary conditions have been termed microclamped and microfree boundary conditions, respectively (Gurtin and Needleman, 2005). Having $\dot{\gamma}^{(\alpha)} = 0$ simulates a boundary that does not allow dislocations to cross it, which is relevant on the interface between a metal matrix and a stiff inclusion or on the interface between a metallic layer and a ceramic. In the problem considered here, the higher order boundary conditions along the four external boundaries are taken as $\dot{r}^{(\alpha)} = 0$, so that the dislocations do not pile up at the boundaries. In a time independent theory it is necessary to specify higher order boundary conditions at internal elastic–plastic boundaries, but such boundaries do not exist in the elastic-viscoplastic theory.

The numerical solutions are obtained using a special kind of finite element method where the slip rate increments are taken as degrees of freedom on equal footing with the displacement increments. The displacement increments, Δu_i, and the change of the slip rate, $\Delta\dot{\gamma}^{(\alpha)}$, are interpolated within each element between nodal displacement increments, ΔD^N, and nodal slip rate changes, $\Delta\dot{\gamma}_N^{(\alpha)}$, respectively

$$\Delta u_i = \sum_{N=1}^{2k} N_i^N \Delta D^N, \qquad \Delta\dot{\gamma}^{(\alpha)} = \sum_{N=1}^{l} M^N \Delta\dot{\gamma}_{\mathrm{N}}^{(\alpha)} \tag{34}$$

where N_i^N and M^N are shape functions and k and l are the number of nodes used for the interpolations. For the plastic and total strain fields to have the same degree of interpolation, the slips, and thereby the plastic strains, must have shape functions of one degree lower than the displacements. The derivatives of the displacement increments and the slip rate increments are taken as

$$\Delta tL_{ij} = \sum_{N=1}^{2k} N_{i,j}^N \Delta D^N, \quad \Delta\epsilon_{ij} = \sum_{N=1}^{2k} E_{ij}^N \Delta D^N, \quad \Delta\dot{\gamma}_{,i}^{(\alpha)} = \sum_{N=1}^{l} M_{,i}^N \Delta\dot{\gamma}_{\mathrm{N}}^{(\alpha)} \tag{35}$$

where $E_{ij}^N = \frac{1}{2}(N_{i,j}^N + N_{j,i}^N)$.

Using these relations in the principle of virtual work, the discretized equations can be written in the following form

$$\mathbf{K}_{\mathrm{e}}\Delta\mathbf{D} = \Delta\mathbf{F}_1 \tag{36}$$

$$\mathbf{K}_{\mathrm{p}}^{(\alpha)}\Delta\dot{\gamma}^{(\alpha)} = \Delta\mathbf{F}_2^{(\alpha)} - \mathbf{K}_{\mathrm{ep}}^{(\alpha)}\Delta\mathbf{D} \tag{37}$$

Please cite this article in press as: Borg, U., Strain gradient crystal plasticity effects on ..., Int. J. Plasticity (2007), doi:10.1016/j.ijplas.2007.01.003

where

$$\mathbf{K}_{\mathrm{e}}^{NM} = \int_V (E_{ij}^N R_{ijkl} E_{kl}^M + \sigma_{ij}(N_{k,j}^M N_{k,i}^N - 2E_{ik}^M E_{jk}^N))\mathrm{d}V \tag{38}$$

is the elastic stiffness matrix,

$$\mathbf{K}_{\mathrm{ep}}^{NM^{(\alpha)}} = \int_V (-s_i^{(\alpha)} m_j^{(\alpha)} (R_{ijkl} E_{kl}^N + \sigma_{kj} E_{ik}^N - \sigma_{ik} E_{jk}^N) M^M + \rho_{\mathrm{T}}^{(\alpha)} (e_{ijk} (s_l^{(\alpha)} m_k^{(\alpha)} N_{j,l}^N - s_j^{(\alpha)} m_n^{(\alpha)} N_{n,k}^N) - t_k^{(\alpha)} N_{i,k}^N) M_{,i}^M)\mathrm{d}V \tag{39}$$

is the coupling matrix, and

$$\begin{aligned}\mathbf{K}_p^{NM^{(\alpha)}} = \int_V \Bigg\{ & \left[(m-1)\tau_{\mathrm{e}}^{(\alpha)} \frac{\dot{\gamma}^{(\alpha)}}{\dot{\gamma}_{\mathrm{e}}^{(\alpha)^3}} (\dot{\gamma}^{(\alpha)} M^N + l_{\mathrm{S}}^2 \dot{\gamma}_{,k}^{(\alpha)} s_k^{(\alpha)} s_i^{(\alpha)} M_{,i}^N + l_{\mathrm{T}}^2 \dot{\gamma}_{,k}^{(\alpha)} t_k^{(\alpha)} t_i^{(\alpha)} M_{,i}^N) + \tau_{\mathrm{e}}^{(\alpha)} \frac{1}{\dot{\gamma}_{\mathrm{e}}^{(\alpha)}} M^N \right] \\ & \times M^M \left[s_i^{(\alpha)} \left((m-1) l_{\mathrm{S}}^2 \tau_{\mathrm{e}}^{(\alpha)} \frac{\dot{\gamma}_{,j}^{(\alpha)} s_j^{(\alpha)}}{\dot{\gamma}_{\mathrm{e}}^{(\alpha)^3}} \left(\dot{\gamma}^{(\alpha)} M^N + l_{\mathrm{S}}^2 \dot{\gamma}_{,k}^{(\alpha)} s_k^{(\alpha)} s_l^{(\alpha)} M_{,l}^N + l_{\mathrm{T}}^2 \dot{\gamma}_{,k}^{(\alpha)} t_k^{(\alpha)} t_l^{(\alpha)} M_{,l}^N \right) \right. \right. \\ & \left. + l_{\mathrm{S}}^2 \tau_{\mathrm{e}}^{(\alpha)} \frac{1}{\dot{\gamma}_{\mathrm{e}}^{(\alpha)}} s_k^{(\alpha)} M_{,k}^N \right) + t_i^{(\alpha)} \left((m-1) l_{\mathrm{T}}^2 \tau_{\mathrm{e}}^{(\alpha)} \frac{\dot{\gamma}_{,j}^{(\alpha)} t_j^{(\alpha)}}{\dot{\gamma}_{\mathrm{e}}^{(\alpha)^3}} \left(\dot{\gamma}^{(\alpha)} M^N + l_{\mathrm{S}}^2 \dot{\gamma}_{,k}^{(\alpha)} s_k^{(\alpha)} s_l^{(\alpha)} M_{,l}^N \right. \right. \\ & \left. \left. \left. + l_{\mathrm{T}}^2 \dot{\gamma}_{,k}^{(\alpha)} t_k^{(\alpha)} t_l^{(\alpha)} M_{,l}^N \right) + l_{\mathrm{T}}^2 \frac{\tau_{\mathrm{e}}^{(\alpha)}}{\dot{\gamma}_{\mathrm{e}}^{(\alpha)}} t_k^{(\alpha)} M_{,k}^N \right) \right] M_{,i}^M \Bigg\} \mathrm{d}V \end{aligned} \tag{40}$$

is the plastic stiffness matrix. The right-hand side vectors in Eqs. (36) and (37) can be written as

$$\Delta \mathbf{F}_1^N = \int_{\mathrm{S}} \Delta T_i N_i^N \,\mathrm{d}S + \Delta t \int_V E_{ij}^N R_{ijkl} \sum_\alpha \dot{\gamma}^{(\alpha)} \mu_{kl}^{(\alpha)} \,\mathrm{d}V \tag{41}$$

which is the conventional load increment vector with an added volume force, and

$$\begin{aligned}\Delta \mathbf{F}_2^{M^{(\alpha)}} = & \Delta t \int_{\mathrm{S}} \dot{r}^{(\alpha)} M^M \,\mathrm{d}S - \Delta t \int_V \Bigg(\Bigg(\frac{\dot{\gamma}_{\mathrm{e}}^{(\alpha)^{m-1}}}{\dot{\gamma}_0^m} \dot{\gamma}^{(\alpha)} \sum_\beta h_{\alpha\beta} \dot{\gamma}_{\mathrm{e}}^{(\beta)} + s_i^{(\alpha)} m_j^{(\alpha)} \Bigg(R_{ijkl} \sum_\beta \dot{\gamma}^{(\beta)} \mu_{kl}^{(\beta)} \\ & + \sum_\beta \dot{\gamma}^{(\beta)} s_k^{(\beta)} m_i^{(\beta)} \sigma_{kj} - \sum_\beta \dot{\gamma}^{(\beta)} s_j^{(\beta)} m_k^{(\beta)} \sigma_{ik} \Bigg) \Bigg) M^M \\ & + \Bigg(s_i^{(\alpha)} l_{\mathrm{S}}^2 \frac{\dot{\gamma}_{,k}^{(\alpha)} s_k^{(\alpha)}}{\dot{\gamma}_0^m} \dot{\gamma}_{\mathrm{e}}^{(\alpha)^{m-1}} \sum_\beta h_{\alpha\beta} \dot{\gamma}_{\mathrm{e}}^{(\beta)} - s_k^{(\alpha)} \rho_{\mathrm{S}}^{(\alpha)} \sum_\beta \dot{\gamma}^{(\beta)} s_i^{(\beta)} m_k^{(\beta)} \\ & + t_i^{(\alpha)} l_{\mathrm{T}}^2 \frac{\dot{\gamma}_{,k}^{(\alpha)} t_k^{(\alpha)}}{\dot{\gamma}_0^m} \dot{\gamma}_{\mathrm{e}}^{(\alpha)^{m-1}} \sum_\beta h_{\alpha\beta} \dot{\gamma}_{\mathrm{e}}^{(\beta)} - \rho_{\mathrm{T}}^{(\alpha)} e_{ijk} \Bigg(s_l^{(\alpha)} m_k^{(\alpha)} \sum_\beta \dot{\gamma}^{(\beta)} s_j^{(\beta)} m_l^{(\beta)} \\ & - s_j^{(\alpha)} m_n^{(\alpha)} \sum_\beta \dot{\gamma}^{(\beta)} s_n^{(\beta)} m_k^{(\beta)} \Bigg) \Bigg) M_{,i}^M \Bigg) \mathrm{d}V \end{aligned} \tag{42}$$

which is an additional higher order load term with a subtracted volume contribution.

In this plane strain study, the elements used for the displacements are 8-node quadrilaterals with quadratic shape functions, and the elements used for interpolation of the slip

Please cite this article in press as: Borg, U., Strain gradient crystal plasticity effects on ..., Int. J. Plasticity (2007), doi:10.1016/j.ijplas.2007.01.003

rate increments are 4-node quadrilaterals with bilinear shape functions, i.e. $k = 8$ and $l = 4$. The coordinates of the nodes in the 4-node elements are identical to the coordinates of the corner nodes in the 8-node elements. The integrations are carried out using 2×2 point Gaussian integration. The Jacobian from the 8-node elements is used for the integrations of $\mathbf{K}_e$ and $\Delta\mathbf{F}_1$, whereas the Jacobian from the 4-node elements is used for the integrations of $\mathbf{K}_{ep}$, $\mathbf{K}_p$ and $\Delta\mathbf{F}_2$. The coordinates of the integration points in the two elements will not necessarily coincide exactly, but the difference is neglected in the analyses performed.

When the displacement increments and slip rate increments have been solved for, the stress rate $\dot{\sigma}_{ij}$, the effective stress rate $\dot{q}^{(\alpha)}$ and the two higher order stress rates $\dot{\rho}_S^{(\alpha)}$ and $\dot{\rho}_T^{(\alpha)}$ can be found from the constitutive Eqs. (29)–(32). The effective stress $\tau_e^{(\alpha)}$ can now be determined by Eq. (22) and the effective slip rate $\dot{\gamma}_e^{(\alpha)}$ is given by (23). The slip rate $\dot{\gamma}^{(\alpha)}$ and its gradients $\dot{\gamma}_{,i}^{(\alpha)} s_i^{(\alpha)}$ and $\dot{\gamma}_{,i}^{(\alpha)} t_i^{(\alpha)}$ are now obtained from Eqs. (19)–(21).

4. Results

The material parameters used in the calculations are $\tau_0/E = 0.001$, $\nu = 0.3$, $h_0/\tau_0 = 8.9$, $p = 1$ (Taylor hardening), $m = 0.005$ and $\dot{\gamma}_0 = 0.001\ \text{s}^{-1}$. In the first part of the presented results, the hardening modulus is specified by Eq. (27) with $\tau_s/\tau_0 = 1.8$. These material parameters are the same as used in Peirce et al. (1983), and the present formulation without material length scales has been tested against some of the results from that work. For the second part of the presented results, the hardening modulus is specified by Eq. (28) with the hardening exponent $n = 0.05$ or $n = 0.1$. The initial dimensions of the tensile specimen are given by $L_0/b_0 = 3$ and $\delta_0/b_0 = 0.005$, and the applied displacement rate, $\dot{U}$, is specified so that $\dot{U}/L_0 = \dot{\gamma}_0$.

In the considered plane strain problem with in-plane slip systems there is no slip in the transverse direction $\mathbf{t}^{(\alpha)}$, thus all terms including l_T or $\rho_T^{(\alpha)}$ are zero. The other internal material length scale, l_S, is in the following simply denoted as l.

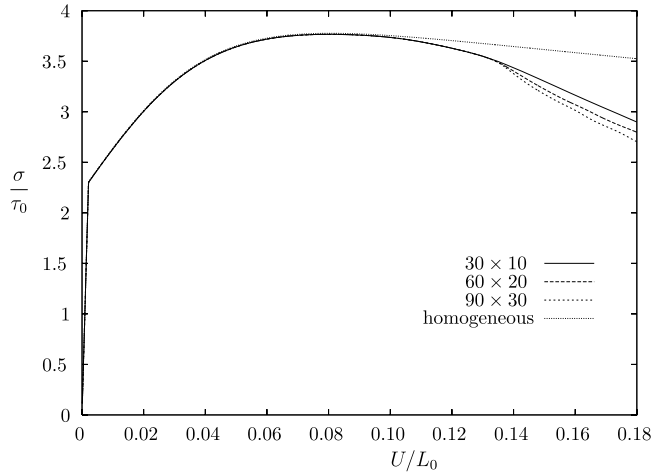

Fig. 2. Normalized overall stress–strain curves using the conventional theory ($l = 0$) for different meshes, and the hardening law given by Eq. (27).

Please cite this article in press as: Borg, U., Strain gradient crystal plasticity effects on ..., Int. J. Plasticity (2007), doi:10.1016/j.ijplas.2007.01.003

Fig. 2 shows normalized overall nominal stress (σ/τ_0) vs. elongation (U/L_0) curves for a conventional material (using $l = 0$), where the nominal stress is defined as $\sigma = T_1/b_0$. Results are shown for three different meshes ranging from 30×10 to 90×30 elements. The mesh size is increasing when moving away from the necking area. The curve labeled homogeneous is obtained from an analysis without any geometrical imperfection ($\delta_0 = 0$) and only one element to make sure that no necking occurs. It can be seen from the figure that necking occurs for all three meshes after the maximum load is reached at $U/L_0 \approx 0.08$. There is good agreement between the calculations with the three meshes until the stress drop due to localization begins at $U/L_0 = 0.13$. After that, mesh sensitivity is observed. Fig. 3 shows deformed meshes and contours of accumulated effective slip, γ_{ea}, for the calculations in Fig. 2. It is clear that the shear band width is very sensitive to the mesh resolution; the finer the mesh, the narrower the shear band.

Fig. 4 is similar to Fig. 2 except that it shows results for a nonlocal material with the internal material length scale $l/b_0 = 0.02$. As for the conventional material there is good agreement between the calculations until the onset of localization in shear bands, which in this case occurs at $U/L_0 \approx 0.16$. In the post-localization region the curves for 60×20 and 90×30 elements are almost coinciding whereas the curve for 30×10 elements lies a little higher. There is much less mesh sensitivity for the nonlocal material than for the conventional material. The deformed mesh and contours of accumulated effective slip for the calculations in Fig. 4 are shown in Fig. 5. Here, the mesh sensitivity on the width of the shear band has been removed for the two finest meshes.

The influence of the internal material length scale on the normalized overall stress–strain response is shown in Fig. 6 for the values $l = 0$, $l/b_0 = 0.01$, $l/b_0 = 0.02$ and $l/b_0 = 0.04$ using a mesh with 60×20 elements. Until the maximum load is reached, the deformation state is almost homogeneous throughout the solid and therefore strain

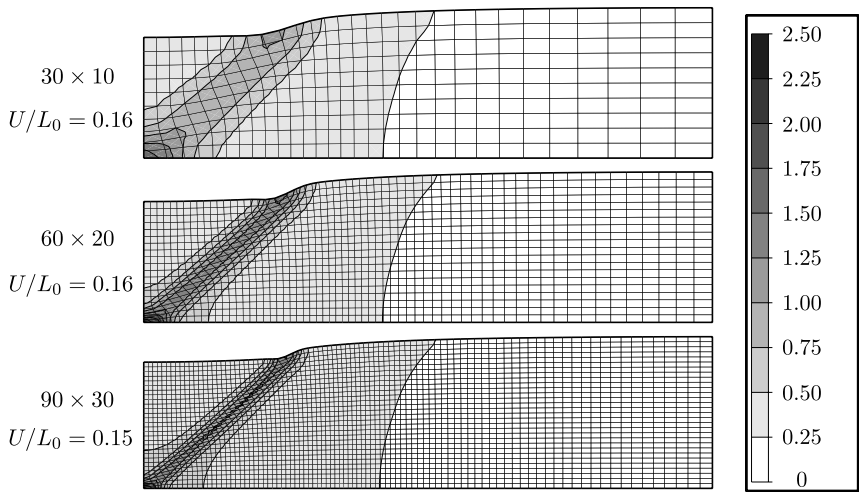

Fig. 3. Deformed mesh and contours of accumulated effective slip, γ_{ea}, using the conventional theory ($l = 0$), and the hardening law given by Eq. (27).

Please cite this article in press as: Borg, U., Strain gradient crystal plasticity effects on ..., Int. J. Plasticity (2007), doi:10.1016/j.ijplas.2007.01.003

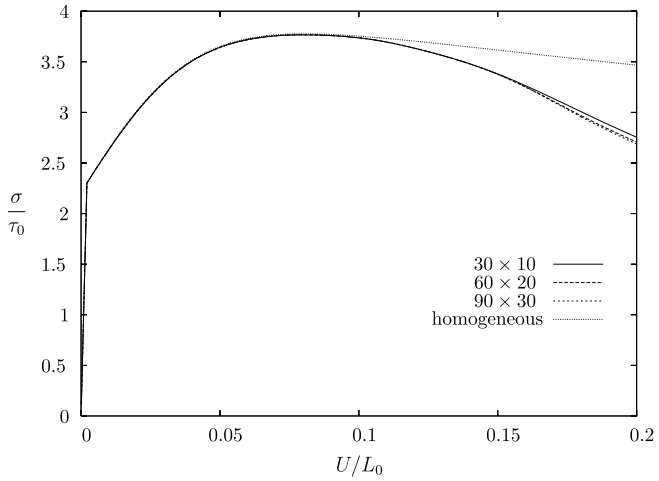

Fig. 4. Normalized overall stress–strain curves using the nonlocal theory with $l/b_0 = 0.02$ for different meshes, and the hardening law given by Eq. (27).

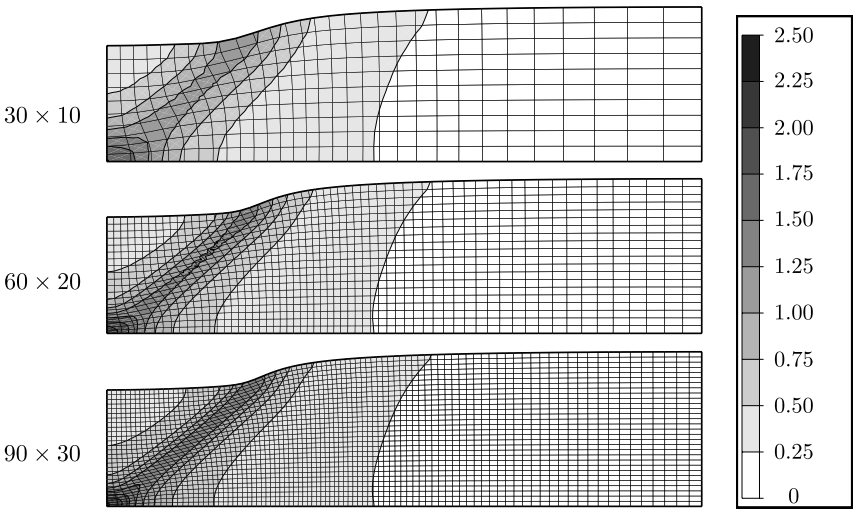

Fig. 5. Deformed mesh and contours of accumulated effective slip, γ_{ea}, using the nonlocal theory with $l/b_0 = 0.02$ at $U/L = 0.18$ for three different meshes, and the hardening law given by Eq. (27).

gradient hardening has no effect on the response. From the maximum load point to the point where there is a stress drop in the curve for the conventional material (where the shear band initiates), only small differences in the response curves are observed. After that point, small specimens (large material length parameter) shows clearly a more stiff behavior. Furthermore, a delay in the initiation of a shear band was observed when increasing the material length scale. Fig. 7 shows deformed meshes and contours of accumulated effective slip for the different material length scales using a mesh with 60×20 elements.

Please cite this article in press as: Borg, U., Strain gradient crystal plasticity effects on ..., Int. J. Plasticity (2007), doi:10.1016/j.ijplas.2007.01.003

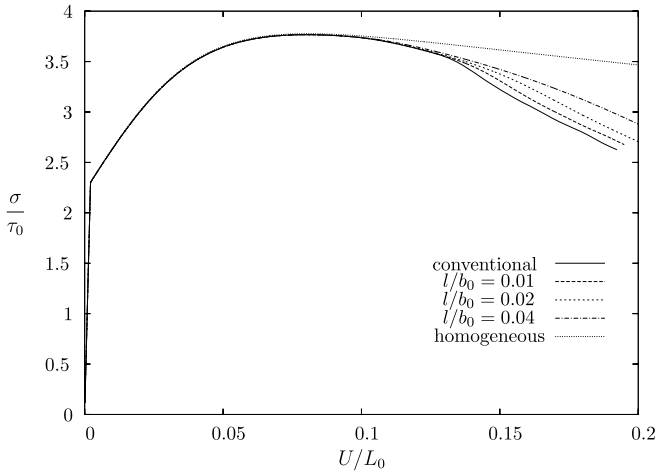

Fig. 6. Normalized overall stress–strain curves for different values of the internal material length scale relative to the height of the specimen for a mesh with 60×20 elements, and the hardening law given by Eq. (27).

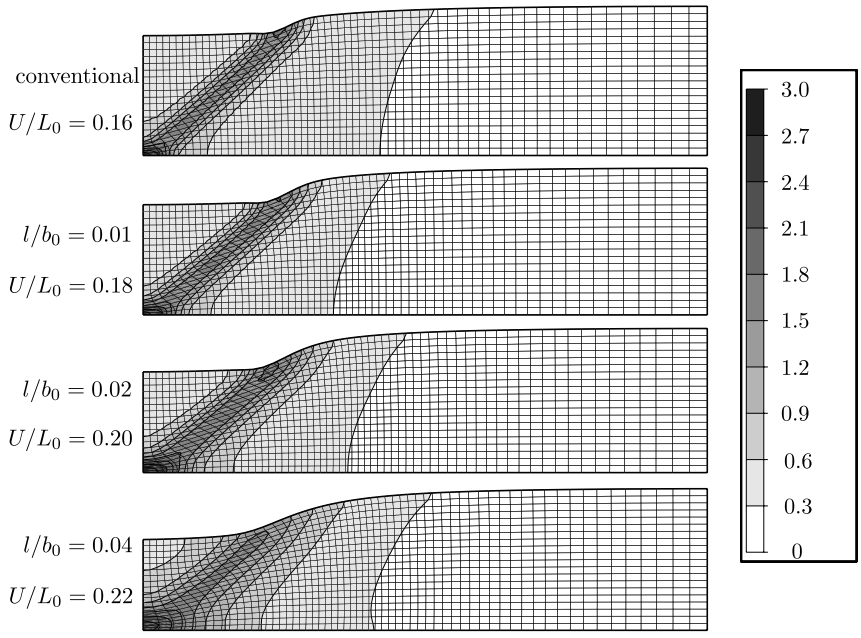

Fig. 7. Deformed mesh and contours of accumulated effective slip, γ_{ea} for different values of the internal material length scale relative to the height of the specimen for a mesh with 60×20 elements, and the hardening law given by Eq. (27).

It is seen that an increasing material length scale is increasing the width of the shear band. The shear band width of the conventional material and the material with $l/b_0 = 0.01$ are almost identical, but for a conventional material the shear band width is highly mesh

Please cite this article in press as: Borg, U., Strain gradient crystal plasticity effects on ..., Int. J. Plasticity (2007), doi:10.1016/j.ijplas.2007.01.003

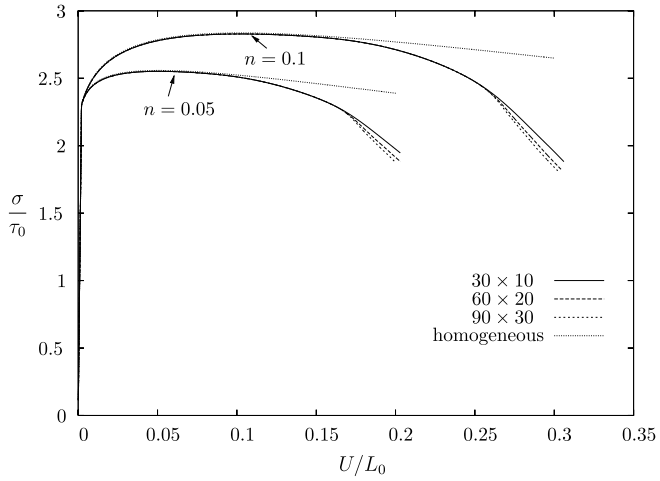

Fig. 8. Normalized overall stress–strain curves using the conventional theory ($l = 0$) with a power hardening law for different meshes and two values of the hardening exponent n.

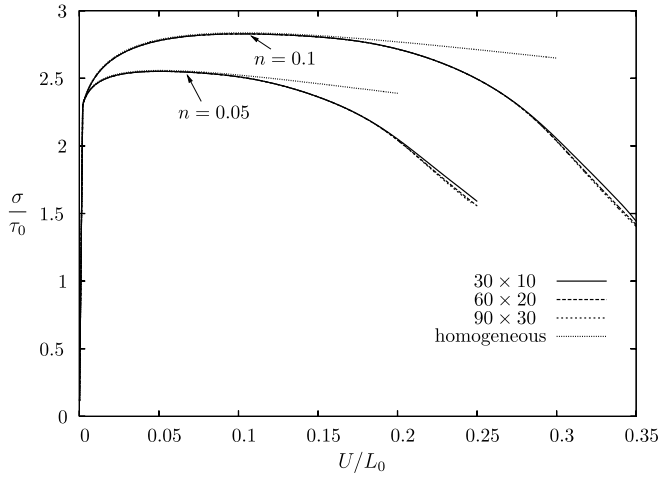

Fig. 9. Normalized overall stress–strain curves using the nonlocal theory with $l/b_0 = 0.02$ with a power hardening law for different meshes and two values of the hardening exponent n.

sensitive, whereas the shear band width with $l/b_0 = 0.01$ has almost converged for the mesh resolution shown.

Figs. 8 and 9 show results for a power law hardening material using the hardening law given by Eq. (28). In Fig. 8 the mesh sensitivity of the normalized overall stress–strain response is shown for a conventional material with two different values of the power hardening exponent, n. For the calculation with $n = 0.05$ the maximum load point is at an end displacement of $U/L_0 = 0.05$ and the response for the three different meshes starts to diverge at $U/L_0 \approx 0.17$ where the shear band initiates for the fine mesh. In the case with $n = 0.1$ (maximum load point at $U/L_0 = 0.1$) the shear band initiates at $U/L_0 \approx 0.26$ for

Please cite this article in press as: Borg, U., Strain gradient crystal plasticity effects on ..., Int. J. Plasticity (2007), doi:10.1016/j.ijplas.2007.01.003

the calculation with the finest mesh. For the nonlocal material shown in Fig. 9 with the hardening exponents $n = 0.05$ and $n = 0.1$, the shear band initiates at $U/L_0 \approx 0.2$ and $U/L_0 \approx 0.29$, respectively. The response curves for the meshes with 60×20 and 90×30 elements are almost coinciding, and the curve for the mesh with 30×10 elements is slightly higher. For the nonlocal material, there is practically no differences on the results for the two finest meshes.

For the calculations using the hardening law given by Eq. (27), the initiation of shear bands occurs at an overall strain of approximately 0.13 and 0.17 for the conventional material and the nonlocal material with $l/b_0 = 0.02$, respectively. The maximum load point in that case is at an overall strain of approximately 0.08. Comparing this to the results obtained with the power hardening law, it is seen that the power hardening law delays the initiation of shear bands, both for the conventional material and for the nonlocal material. Similar results for a conventional rate-independent crystal plasticity model have been obtained by Peirce et al. (1982).

5. Concluding remarks

A plane strain rate-dependent crystal plasticity formulation of a strain gradient plasticity theory for finite deformations has been presented. The theory fits within the framework of the strain gradient plasticity theory by Fleck and Hutchinson (2001) and reduces to the classical crystal plasticity theory by Peirce et al. (1983) in the absence of a characteristic material length scale. Two internal material length parameters were used to account for increased hardening due to slip gradients in the slip direction and in the direction normal to the slip plane as in Shu and Fleck (1999).

The formulation has been applied to study the material response of a single crystal under uniaxial plane strain tension. In all of the simulations necking started to occur soon after that the maximum load point was reached and the larger strains in the neck triggered the formation of shear bands. It was observed that the mesh sensitivity was removed for a nonlocal material compared to a conventional material. Furthermore, it was found that increasing the material length scale delays the formation of shear bands.

As mentioned in the introduction, a number of experimental studies of plasticity on the micron scale are available in the literature (e.g. torsion of thin copper wires, bending of thin beams, micro indentation, etc.). Several workers have determined the microstructural length scale parameters from such experimental results (e.g. Fleck et al., 1994 and Gudmundson, 2004). The analyses here show that the width of the shear bands depend on the material length scale. Using such results, the length scale parameter could also be determined experimentally by measuring the width of shear bands in a specimen deformed in plane strain tension. However, for such an approach more analyses are needed to investigate the evolution of shear band thickness with strain and the implicit coupling to the hardening law.

The effect of the strain hardening was investigated by use of two different hardening laws. The first one with a saturation strength after which there is no increase in the hardening, and the other one a power law type, where there is no such saturation strength. It was found that the power law hardening delayed the formation of shear bands for each value of the hardening exponent.

For the presented results, the internal material length scale did not have a significant effect on the response curves before the initiation of shear bands. This is due to the

Please cite this article in press as: Borg, U., Strain gradient crystal plasticity effects on ..., Int. J. Plasticity (2007), doi:10.1016/j.ijplas.2007.01.003

relatively small value of the material length scale compared to the height of the specimen. Analyses with higher values of the material length scale have been performed, and there the response curves were significantly affected before initiation of shear bands (but after localization into necking). Also, Niordson and Tvergaard (2005) studied tension and compression instabilities for specimens with dimensions in the micron range using a rate-independent phenomenological strain gradient plasticity theory, and they observed a significant effect of the material length scale on the necking behavior using much larger values of l/b_0 than considered here.

Acknowledgements

The author wishes to thank Viggo Tvergaard and Christian F. Niordson for many valuable discussions. This work is financially supported by the Danish Technical Research Council in a project entitled Modeling Plasticity at the Micron Scale.

References

Abu Al-Rub, R.K., Voyiadjis, G.Z., 2006. A physically based gradient plasticity theory. Int. J. Plast. 22, 654–684.
Acharya, A., Bassani, J.L., 2000. Lattice incompatibility and a gradient theory of crystal plasticity. J. Mech. Phys. Solids 48, 1565–1595.
Aifantis, E.C., 1984. On the microstructural origin of certain inelastic models. Trans. ASME J. Eng. Mater. Technol. 106, 326–330.
Ashby, M.F., 1970. The deformation of plastically non-homogeous alloys. Philos. Mag. 21, 399–424.
Borg, U., Niordson, C.F., Fleck, N.A., Tvergaard, V., 2006. A viscoplastic strain gradient analysis of materials with voids or inclusions. Int. J. Solids Struct. 43, 4906–4916.
Cheong, K.S., Busso, E.P., Arsenlis, A., 2005. A study of microstructural length scale effects on the behavior of fcc polycrystals using strain gradient concepts. Int. J. Plast. 21, 1797–1814.
Fleck, N.A., Hutchinson, J.W., 1997. Strain gradient plasticity. In: Hutchinson, J.W., Wu, T.Y. (Eds.), . In: Advances in Applied Mechanics, vol. 33. Academic Press, New York, pp. 295–361.
Fleck, N.A., Hutchinson, J.W., 2001. A reformulation of strain gradient plasticity. J. Mech. Phys. Solids 49, 2245–2271.
Fleck, N.A., Muller, G.M., Ashby, M.F., Hutchinson, J.W., 1994. Strain gradient plasticity: theory and experiment. Acta Metall. Mater. 42, 475–487.
Gao, H., Huang, Y., Nix, W.D., Hutchinson, J.W., 1999. Mechanism-based strain gradient plasticity –I: theory. J. Mech. Phys. Solids 47, 1239–1263.
Gudmundson, P., 2004. A unified treatment of strain gradient plasticity. J. Mech. Phys. Solids 52, 1379–1406.
Gurtin, M.E., 2000. On the plasticity of single crystals: free energy, microforces, plastic strain gradients. J. Mech. Phys. Solids 48, 989–1036.
Gurtin, M.E., 2002. A gradient theory of single-crystal viscoplasticity that accounts for geometrically necessary dislocations. J. Mech. Phys. Solids 50, 5–32.
Gurtin, M.E., Needleman, A., 2005. Boundary conditions in small-deformation, single-crystal plasticity that account for the burgers vector. J. Mech. Phys. Solids 53, 1–31.
Han, C.-S., Gao, H., Huang, Y., Nix, W.D., 2005a. Mechanism-based strain gradient crystal plasticity – I: theory. J. Mech. Phys. Solids 53, 1188–1203.
Han, C.-S., Gao, H., Huang, Y., Nix, W.D., 2005b. Mechanism-based strain gradient crystal plasticity – II: analysis. J. Mech. Phys. Solids 53, 1204–1222.
Haque, M.A., Saif, M.T.A., 2003. Strain gradient effect in nanoscale thin films. Acta Mater. 51, 3053–3061.
Mikkelsen, L.P., 1999. Necking in rectangular tensile bars approximated by a 2-d gradient dependent plasticity model. Eur. J. Mech. A/Solids 18, 805–818.
Niordson, C.F., Redanz, P., 2004. Size-effects in plane strain sheet-necking. J. Mech. Phys. Solids 52, 2431–2454.
Niordson, C.F., Tvergaard, V., 2005. Instabilities in power law gradient hardening materials. Int. J. Solids Struct. 42, 2559–2573.

Please cite this article in press as: Borg, U., Strain gradient crystal plasticity effects on ..., Int. J. Plasticity (2007), doi:10.1016/j.ijplas.2007.01.003

Nye, J.F., 1953. Some geometrical relations in dislocated crystals. Acta Metall. 1, 153–162.
Peirce, D., Asaro, R.J., Needleman, A., 1982. An analysis of nonuniform and localized deformation in ductile single crystals. Acta Metall. 30, 1087–1119.
Peirce, D., Asaro, R.J., Needleman, A., 1983. Material rate dependence and localized deformation in crystalline solids. Acta Metall. 31, 1951–1976.
Rice, J., 1987. Tensile crack tip fields in elastic-ideally plastic crystals. Mech. Mater. 6, 317–335.
Shu, J.Y., Barlow, C.Y., 2000. Strain gradient effects on microscopic strain field in a metal matrix composite. Int. J. Plast. 16, 563–591.
Shu, J.Y., Fleck, N.A., 1999. Strain gradient crystal plasticity: size-dependent deformation of bicrystals. J. Mech. Phys. Solids 47, 297–324.
Sluys, L.J., Estrin, Y., 2000. The analysis of shear banding with a dislocation based gradient plasticity model. Int. J. Solids Structures 37, 7127–7142.
Stölken, J.S., Evans, A.G., 1998. Microbend test method for measuring the plasticity length scale. Acta Mater. 46, 5109–5115.
Tvergaard, V., Needleman, A., 1995. Effects of nonlocal damage in porous plastic solids. Int. J. Solids Struct. 32, 1063–1077.

Please cite this article in press as: Borg, U., Strain gradient crystal plasticity effects on ..., Int. J. Plasticity (2007), doi:10.1016/j.ijplas.2007.01.003

P3

Strain gradient effects in surface roughening

Modelling and Simulation in Materials science and engineering
15, 1-12, 2007

INSTITUTE OF PHYSICS PUBLISHING MODELLING AND SIMULATION IN MATERIALS SCIENCE AND ENGINEERING

Modelling Simul. Mater. Sci. Eng. **15** (2007) S1–S12 doi:10.1088/0965-0393/15/1/S01

Strain gradient effects in surface roughening

Ulrik Borg[1] **and Norman A Fleck**[2]

[1]Department of Mechanical Engineering, Technical University of Denmark, 2800 Kgs. Lyngby, Denmark
[2]Engineering Department, Cambridge University, Trumpington Street, Cambridge CB2 1PZ, UK

E-mail: ub@mek.dtu.dk

Received 4 May 2006, in final form 28 August 2006
Published 6 December 2006
Online at stacks.iop.org/MSMSE/15/S1

Abstract

A thin aluminium sheet comprising of large polycrystals is pulled in uniaxial tension and the resulting surface profile is measured in a scanning electron microscope. The surface profile near the grain boundaries reveals a local deformation pattern of width of a few micrometres and is strong evidence for strain gradient effects. Numerical analyses of a bicrystal undergoing in-plane tensile deformation are also studied using a strain gradient crystal plasticity theory and also by using a strain gradient plasticity theory for an isotropic solid. Both theories include an internal material length scale. An interfacial potential that penalizes the dislocations in crossing the grain boundary is included in the analysis. The results indicate that the surface profile is strongly dependent upon the choice of this potential and on the material length scale.

1. Introduction

Surface roughening of polycrystalline metals during plastic deformation is a common phenomenon in metal forming processes and is commonly referred to as the 'orange peel' effect. In addition to creating cosmetically undesirable surfaces, the inhomogeneities can provide initiation sites for fatigue crack initiation and strain localization. The effect derives from the crystallographic lattice mismatch from grain to grain and the resulting anisotropy in different grains. Incompatibilities of deformation from the interaction between adjacent grains result in the roughening of the free surface.

The surface roughening of polycrystalline Al–Mg alloys during tensile deformation has been experimentally studied by, for example, Stoudt and Ricker (2002). It was observed that the degree of surface roughening increases linearly with both grain size and level of imposed strain. However, an extrapolation of the data to vanishing grain size gives a finite surface roughening and this suggests that an independent material length scale influences the surface roughening in addition to the grain size. Wilson and Lee (2001) made observations of aluminium alloy surfaces deformed in tension, sheet forming and rolling. They observed the

formation of valleys near grain boundaries and concluded that this was a result of the mismatch in the orientation of slip systems of adjacent grains. The width of the valleys were on the order of 3 μm with grain sizes of 15 μm for a surface rolled to 30% reduction.

Numerical simulations based on crystal plasticity finite element models have been widely used to study surface roughening in polycrystals (see e.g. Zhao *et al* (2004) using a three-dimensional conventional crystal plasticity model). The results indicate that the dispersion of crystallographic texture from grain to grain plays an important role in surface roughening. Most of such analyses have been based on several crystals, and have not focused on the local deformation field near surface grain boundaries.

The grain boundary obstructs the motion of dislocations and results in local gradients in plastic strain. In strain gradient plasticity formulations it is possible to introduce an energy term acting at an interface in order to constrain the plastic flow across the interface. Aifantis and Willis (2005) employ the framework of Fleck and Willis (2004) but introduce an interfacial energy potential to penalize the build-up of plastic strain at interfaces. This induces a jump in the higher order tractions and plastic strain gradients but a continuity of plastic strain across the interface. A similar approach has been used by Gudmundson (2004) that allows for jumps in higher order tractions and plastic strains and by Evers *et al* (2004) who uses an enhanced crystal plasticity framework based on various types of dislocation densities allowing for jumps in dislocation densities at grain boundaries. Furthermore, Gurtin and Needleman (2005) have discussed the conditions for a continuous distribution of Burgers vector across a boundary.

The numerical analyses in the present study are based on a rate-dependent strain gradient crystal plasticity formulation as presented by Borg (2006). It sits within the framework of the phenomenological strain gradient theory by Fleck and Hutchinson (2001). Here, the formulation is enhanced by introducing a potential that penalizes crystallographic slip at internal grain boundaries. The potential is a function of the slips on either side of the grain boundary. This formulation admits jumps in the higher order tractions and slips but has continuity of displacement across grain boundaries.

For comparison purposes some of the simulations are obtained using the viscoplastic strain gradient plasticity theory for an isotropic solid based upon Fleck and Hutchinson (2001), as presented in Borg *et al* (2006). No interfacial potential is used in that case, although it would be possible to formulate one.

2. Experiments

Uniaxial tension tests have been conducted on commercially pure aluminium in order to observe the surface profile near grain boundaries during plastic deformation. The specimen was prepared by prescribing 4% tensile pre-strain to an annealed, cold rolled sheet of length 120 mm, width 20 mm and thickness 1.2 mm. The sheet was then given a recrystallization anneal at 540 °C for 15 min, and the resulting grain structure comprised through-thickness pancake-shaped grains of average diameter 5 mm. The surface of the specimens was mechanically polished prior to deformation. A scanning electron microscope (SEM) was used to investigate the surface profile. Figure 1 displays two SEM images of the surface after 10 per cent engineering strain. On the left image a grain boundary has been marked to emphasize the jump in surface profile across the grain boundary. The image on the right shows a grain boundary and slip lines on either side of it. The grains on each side clearly have different crystallographic orientations, and the density of slip lines is increased on one side of the grain boundary.

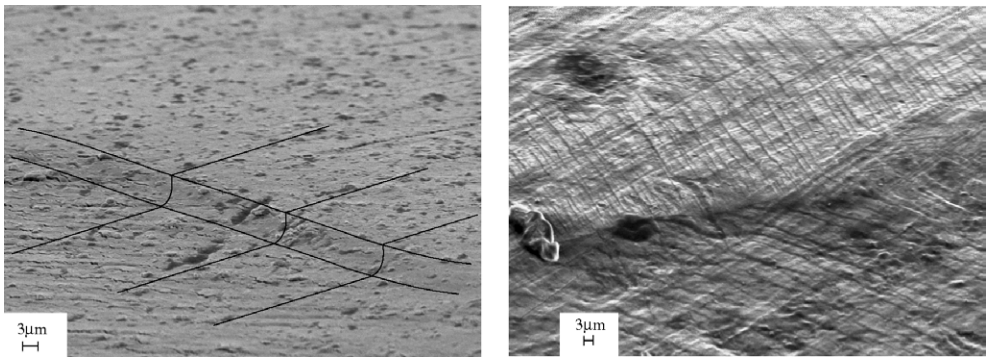

Figure 1. SEM images of the surface after 10% strain.

3. Material model

Results will be based mainly on the strain gradient crystal plasticity theory for finite deformations presented by Borg (2006). The formulation fits within the framework of the strain gradient theory by Fleck and Hutchinson (2001) with the basic formulation equivalent to Gurtin (2002) and reduces to the conventional crystal plasticity theory by, for example, Peirce *et al* (1983) in the absence of strain gradients. A new interfacial potential is introduced to account for the grain boundary resistance to dislocations. For comparison purposes we also present results using a strain gradient plasticity theory for an isotropic solid. The formulation used is a viscoplastic version of the theory by Fleck and Hutchinson (2001) as presented by Borg *et al* (2006). For the isotropic phenomenological solid no interfacial potential is introduced. However, various higher order boundary conditions are assumed to explore their effect upon the surface profile. In the following summaries of the two formulations, the small strain theory is assumed for the sake of simplicity and clarity, although a full finite deformation formulation has been used in all calculations.

3.1. Strain gradient crystal plasticity theory

Plastic deformation by crystallographic slip represents dislocation motion along specific slip systems. A slip system (α) is described by its lattice vectors $s_i^{(\alpha)}$ and $m_i^{(\alpha)}$, where $s_i^{(\alpha)}$ is the slip direction and $m_i^{(\alpha)}$ is the direction normal to the slip plane. Upon introducing $\mu_{ij}^{(\alpha)} = \frac{1}{2}(s_i^{(\alpha)} m_j^{(\alpha)} + s_j^{(\alpha)} m_i^{(\alpha)})$ as the classical Schmid orientation tensor, the overall macroscopic plastic strain rate components can be expressed by the slip $\gamma^{(\alpha)}$ along slip system (α) as

$$\dot{\epsilon}_{ij}^{p} = \sum_{\alpha} \dot{\gamma}^{(\alpha)} \mu_{ij}^{(\alpha)}. \tag{1}$$

An effective slip measure $\gamma_{\mathrm{e}}^{(\alpha)}$ depending on the slip and the slip gradients is introduced as

$$\dot{\gamma}_{\mathrm{e}}^{(\alpha)^2} = \dot{\gamma}^{(\alpha)^2} + (l_S \dot{\gamma}_{,i}^{(\alpha)} s_i^{(\alpha)})^2 + (l_M \dot{\gamma}_{,i}^{(\alpha)} m_i^{(\alpha)})^2 + (l_T \dot{\gamma}_{,i}^{(\alpha)} t_i^{(\alpha)})^2, \tag{2}$$

where $t_i^{(\alpha)}$ is the transverse direction and l_S, l_M and l_T are material length scales introduced for dimensional consistency. Here, $(\,)_{,i} = \partial/\partial x_i$ is the spatial derivative. In this work, only plane problems with in-plane slip systems are considered, and therefore the contribution from the slip gradient in the transverse direction is neglected in the following.

To account for the grain boundary resistance to dislocations crossing them, two surface energy potentials $\phi_{\mathrm{I}}^{(\alpha)}(\gamma_{\mathrm{I}}^{(\alpha)})$ and $\phi_{\mathrm{II}}^{(\alpha)}(\gamma_{\mathrm{II}}^{(\alpha)})$ acting at side 1 and side 2 of the grain boundary Γ,

respectively, are introduced. Then, the principle of virtual power takes the form (where $\phi_{\mathrm{I}}^{(\alpha)\prime}$ denotes $\partial\phi_{\mathrm{I}}^{(\alpha)}/\partial\gamma_{\mathrm{I}}^{(\alpha)}$, etc)

$$\int_V \left(\sigma_{ij}\delta\dot{\epsilon}_{ij} + \sum_\alpha \left(Q^{(\alpha)} - \tau^{(\alpha)}\right)\delta\dot{\gamma}^{(\alpha)} + \sum_\alpha \left(\xi_S^{(\alpha)} s_i^{(\alpha)} + \xi_M^{(\alpha)} m_i^{(\alpha)}\right)\delta\dot{\gamma}_{,i}^{(\alpha)} \right) \mathrm{d}V + \int_\Gamma \sum_\alpha \left(\phi_{\mathrm{I}}^{(\alpha)\prime}\delta\dot{\gamma}_{\mathrm{I}}^{(\alpha)} + \phi_{\mathrm{II}}^{(\alpha)\prime}\delta\dot{\gamma}_{\mathrm{II}}^{(\alpha)}\right) \mathrm{d}\Gamma = \int_S \left(T_i\delta\dot{u}_i + \sum_\alpha r^{(\alpha)}\delta\dot{\gamma}^{(\alpha)} \right) \mathrm{d}S. \quad (3)$$

Here, $Q^{(\alpha)}$ is a stress field work conjugate to the slip rate, and the higher order stresses $\xi_S^{(\alpha)}$ and $\xi_M^{(\alpha)}$ are work conjugate to the slip rate gradients along the slip direction and the direction normal to the slip plane, respectively. T_i is the stress traction and $r^{(\alpha)}$ denotes the higher order traction working on the part of the boundary S where the displacement rates $\dot{u}_i$ and slip rates $\dot{\gamma}^{(\alpha)}$ are not prescribed. The Cauchy stress is denoted σ_{ij} and $\tau^{(\alpha)} = \sigma_{ij}\mu_{ij}^{(\alpha)}$ is the Schmid stress.

It is assumed that the total displacement fields are continuous across the grain boundary but that the presence of a grain boundary energy term causes jumps in the slips. Full constraint along Γ with $\gamma^{(\alpha)} = 0$ is obtained by letting $\phi_{\mathrm{I}}^{(\alpha)\prime}$ and $\phi_{\mathrm{II}}^{(\alpha)\prime}$ tend to infinity, whereas vanishing surface energy along Γ mimics that dislocations are free to cross the grain boundary.

The strong form of the field equations is found by requiring the above relation to hold for all admissible variations in $\dot{u}_i$ and $\dot{\gamma}^{(\alpha)}$. The classical force balance law and boundary conditions read as

$$\sigma_{ij,j} = 0 \qquad T_i = \sigma_{ij}n_j, \quad (4)$$

where n_i is the surface unit normal in the deformed configuration. In addition, we have the consistency condition and higher order boundary conditions

$$Q^{(\alpha)} - \tau^{(\alpha)} - \xi_{S,i}^{(\alpha)} s_i^{(\alpha)} - \xi_{M,i}^{(\alpha)} m_i^{(\alpha)} = 0 \quad (5)$$

$$r^{(\alpha)} = \left(\xi_S^{(\alpha)} s_i^{(\alpha)} + \xi_M^{(\alpha)} m_i^{(\alpha)}\right) n_i. \quad (6)$$

The interface conditions are given by

$$\left[\sigma_{ij}N_j\right] = 0, \quad (7)$$

$$\left(\xi_S^{(\alpha)\mathrm{I}} s_i^{(\alpha)\mathrm{I}} + \xi_M^{(\alpha)\mathrm{I}} m_i^{(\alpha)\mathrm{I}}\right) N_i = \phi_{\mathrm{I}}^{(\alpha)\prime}(\gamma_{\mathrm{I}}^{(\alpha)}), \quad (8)$$

$$\left(\xi_S^{(\alpha)\mathrm{II}} s_i^{(\alpha)\mathrm{II}} + \xi_M^{(\alpha)\mathrm{II}} m_i^{(\alpha)\mathrm{II}}\right) (-N_i) = \phi_{\mathrm{II}}^{(\alpha)\prime}(\gamma_{\mathrm{II}}^{(\alpha)}), \quad (9)$$

where the unit normal vector N_i on Γ is directed from grain 1 to grain 2 and $[f]$ denotes the jump $f_1 - f_2$ across Γ. Simple expressions are adopted for the grain boundary energy potentials of the form

$$\phi_{\mathrm{I}}^{(\alpha)} = \frac{1}{2}\kappa(\gamma_{\mathrm{I}}^{(\alpha)})^2, \qquad \phi_{\mathrm{I}}^{(\alpha)\prime} = \kappa\gamma_{\mathrm{I}}^{(\alpha)}, \quad (10)$$

$$\phi_{\mathrm{II}}^{(\alpha)} = \frac{1}{2}\kappa(\gamma_{\mathrm{II}}^{(\alpha)})^2, \qquad \phi_{\mathrm{II}}^{(\alpha)\prime} = \kappa\gamma_{\mathrm{II}}^{(\alpha)}, \quad (11)$$

with κ being a material parameter describing the strength of the grain boundary.

By use of an effective stress, denoted $\tau_{\mathrm{e}}^{(\alpha)}$, that is work-conjugate to the effective slip rate measure, $\dot{\gamma}_{\mathrm{e}}^{(\alpha)}$, a power-law creep model is formulated as

$$\dot{\gamma}_{\mathrm{e}}^{(\alpha)} = \dot{\gamma}_0 \left(\frac{\tau_{\mathrm{e}}^{(\alpha)}}{g^{(\alpha)}}\right)^{1/m}, \quad (12)$$

where $\dot{\gamma}_0$ is a reference slip rate and m is a strain rate hardening index. The slip resistance $g^{(\alpha)}$ is assumed to harden from an initial value τ_0 according to

$$\dot{g}^{(\alpha)} = \sum_{\beta} h_{\alpha\beta}\dot{\gamma}_{\mathrm{e}}^{(\beta)}, \qquad h_{\alpha\beta} = h\delta_{\alpha\beta} + ph\left(1 - \delta_{\alpha\beta}\right), \tag{13}$$

where p is the latent hardening index, h is the self-hardening modulus and $\delta_{\alpha\beta}$ denotes the Kronecker delta symbol. Here, we use Taylor hardening ($p = 1$) and linear hardening ($h = h_0 =$ constant).

3.2. Strain gradient viscoplastic theory for an isotropic solid

A much simpler, phenomenological strain gradient formulation exists for an isotropic elastic–plastic solid. Introduce a nonlocal measure of the effective plastic strain rate $\dot{E}^P$ on the basis of the conventional effective plastic strain rate $\dot{\epsilon}^P$ and its gradient through the incremental relation

$$\dot{E}^{P^2} = \dot{\epsilon}^{P^2} + l^2\dot{\epsilon}^P_{,i}\dot{\epsilon}^P_{,i}, \tag{14}$$

where l is a material length parameter. The direction of the plastic strain rate is given by $m_{ij} = \frac{3}{2}S_{ij}/\sigma_{\mathrm{e}}$, where $S_{ij} = \sigma_{ij} - \frac{1}{3}\delta_{ij}\sigma_{kk}$ denotes the stress deviator and $\sigma_{\mathrm{e}} = \sqrt{\frac{3}{2}S_{ij}S_{ij}}$ is the von Mises effective stress and σ_{ij} is the Cauchy stress tensor. The plastic strain rate components can then be written as a product of its magnitude, $\dot{\epsilon}^P = \sqrt{\frac{2}{3}\dot{\epsilon}^P_{ij}\dot{\epsilon}^P_{ij}}$ and its direction m_{ij} as $\dot{\epsilon}^P_{ij} = m_{ij}\dot{\epsilon}^P$.

Now follow Fleck and Hutchinson (2001) and assume that the plastic strain gradients contribute to the internal work. Then, the principle of virtual power takes the form

$$\int_V \left(\sigma_{ij}\delta\dot{\epsilon}^{EL}_{ij} + Q\delta\dot{\epsilon}^P + \tau_i\delta\dot{\epsilon}^P_{,i}\right)\mathrm{d}V = \int_S \left(T_i\delta\dot{u}_i + r\delta\dot{\epsilon}^P\right)\mathrm{d}S \tag{15}$$

in the deformed configuration. Here, $\epsilon^{\mathrm{EL}}_{ij}$ is the elastic strain, Q is a generalized effective stress which is work-conjugate to the conventional effective plastic strain rate, $\dot{\epsilon}^P$, and τ_i is a higher order stress which is work-conjugate to the gradient of the conventional effective plastic strain rate, $\dot{\epsilon}^P_{,i}$. Integration by parts of this work equation leads to the identity $Q = \sigma_{\mathrm{e}} + \tau_{i,i}$. The surface stress traction is given by $T_i = \sigma_{ij}n_j$, and r denotes the higher order surface traction.

The viscous material behaviour is modelled by a power law for the effective plastic strain rate

$$\dot{E}^P = \dot{\epsilon}_0\left(\frac{\sigma_{\mathrm{c}}}{g(E^P)}\right)^{1/m}. \tag{16}$$

Here, m is the strain rate hardening exponent, $\dot{\epsilon}_0$ is a reference strain rate and σ_c is an effective stress which is work-conjugate to the effective plastic strain rate $\dot{E}^P$ such that

$$\sigma_{\mathrm{c}}\delta\dot{E}^P = Q\delta\dot{\epsilon}^P + \tau_i\delta\dot{\epsilon}^P_{,i}. \tag{17}$$

The hardening function g is taken as

$$g(E^P) = \sigma_0 + h_0E^P, \tag{18}$$

where σ_0 is the initial yield strength and h_0 is the hardening modulus.

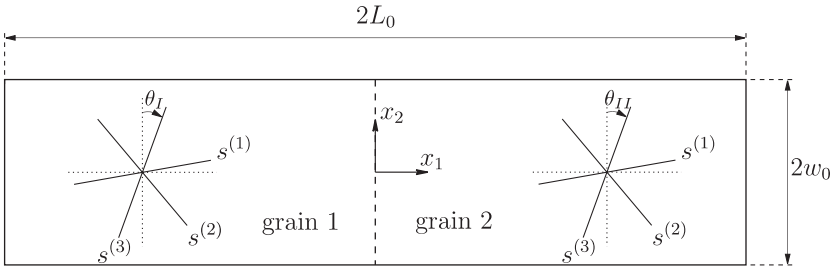

Figure 2. The bicrystal considered in the analyses with three slip systems.

4. Numerical method and modelling details

A bicrystal undergoing in-plane tensile deformation is studied. As shown in figure 2 the bicrystal consists of two grains infinitely long in the x_3-direction separated by a grain boundary at $x_1 = 0$. In the crystal plasticity calculations we use a planar model with three slip systems at a relative orientation of 60° from one to the next. Their absolute orientation is given by the angles θ_{I} and θ_{II} between slip system three and the x_2-direction. The slip system orientation $\theta = 0$ is close to an FCC material under plane strain tension in the $\langle 110 \rangle$ direction which can be simulated with three slip systems oriented at $\pm 35.3°$ and 90° from the tensile axis (see e.g. Rice (1987)). To mimic different crystal orientations, results are presented with varying values of θ.

The applied boundary conditions are given by

$$\begin{aligned} &\dot{u}_1 = 0, \quad \dot{T}_2 = 0 \qquad \text{at } \mathrm{x_1} = -\mathrm{L_0}, \\ &\dot{u}_1 = \dot{U}, \quad \dot{T}_2 = 0 \qquad \text{at } \mathrm{x_1} = \mathrm{L_0}, \\ &\dot{T}_1 = 0, \quad \dot{T}_2 = 0 \qquad \text{at } \mathrm{x_2} = -\mathrm{w_0}, \\ &\dot{T}_1 = 0, \quad \dot{T}_2 = 0 \qquad \text{at } \mathrm{x_2} = \mathrm{w_0}, \end{aligned} \tag{19}$$

where $\dot{U}$ is the applied end displacement rate. Furthermore, the higher order tractions $r^{(\alpha)}$ vanish on the external boundary.

The numerical solutions are obtained using the finite element method. The slip rate increments and plastic strain rate increments for the crystal formulation and isotropic formulation, respectively, are primary unknowns on an equal footing with the displacement increments. These primary unknowns are interpolated within each element between nodal increments as

$$\Delta u_i = \sum_{N=1}^{2k} N_i^N \Delta D^N, \qquad \Delta \dot{\gamma}^{(\alpha)} = \sum_{N=1}^{l} M^N \Delta \dot{\gamma}_N^{(\alpha)} \tag{20}$$

for the crystal formulation, and for the isotropic formulation as

$$\Delta u_i = \sum_{N=1}^{2k} N_i^N \Delta D^N, \qquad \Delta \dot{\epsilon}^P = \sum_{N=1}^{l} M^N \Delta \dot{\epsilon}_N^P, \tag{21}$$

where N_i^N and M^N are shape functions and k and l are the number of nodes used for the interpolations. The elements used for the displacements are 8-node quadrilaterals with quadratic shape functions, and the elements used for interpolation of the slip rate increments or plastic strain rate increments are 4-node quadrilaterals with linear shape functions, i.e. $k = 8$ and $l = 4$.

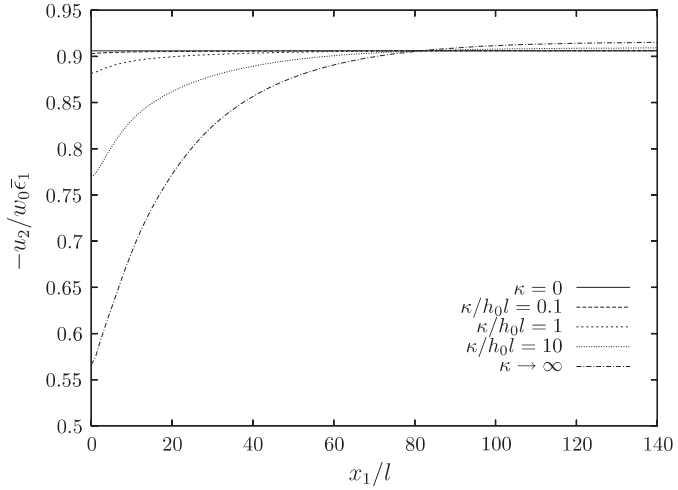

Figure 3. The surface profile near the grain boundary for a bicrystal with $\theta_{\mathrm{I}} = \theta_{\mathrm{II}} = 0$ and the same material parameters for $l/w_0 = 0.01$ at $\bar{\epsilon}_1 = 5\%$.

To allow for discontinuity of slips at the grain boundary, double nodes for the slips must be present at the grain boundary. In this way the slip on each slip system is uncoupled on the two sides of the boundary. In contrast, the displacements are coupled to ensure continuity of the total strain field.

5. Results

The material parameters used for the crystal plasticity calculations are $\tau_0/E = 0.001$, $h_0/\tau_0 = 10$ and $\dot{\gamma}_0 = 0.001\,\mathrm{s}^{-1}$. For the analyses using the isotropic plasticity theory the material parameters are taken as $\sigma_0/E = 0.002$, $h_0/\sigma_0 = 20$ and $\dot{\epsilon}_0 = 0.001\,\mathrm{s}^{-1}$. Using these material data, the stress–strain responses in plane strain tension for (i) an isotropic material and for (ii) a single crystal with slip systems oriented at $\pm 30^\circ$ and 90° from the tensile axis are identical. In both cases the Poisson's ratio $\nu = 0.3$, and the strain rate hardening index is taken as $m = 0.02$ in order to mimic rate-independent plasticity. The dimensions of the bicrystal are chosen such that the ratio w_0/L_0 is small enough to let us neglect specimen end effects. The applied end displacement rate is given by $\dot{U}/2L_0 = \dot{\gamma}_0$ or $\dot{U}/2L_0 = \dot{\epsilon}_0$ for crystal plasticity and isotropic plasticity, respectively.

It can be argued that a slip gradient in the slip direction can be related to edge dislocations, that a slip gradient in the transverse direction (which is absent in this plane problem) can be related to screw dislocations and that a slip gradient in the direction normal to the slip plane, $\gamma^{(\alpha)}_{,i} m^{(\alpha)}_i$, does not induce any geometrical necessary dislocations and thus it should not contribute to the hardening. Therefore we have used $l_M = 0$ in all the calculations, and the other material length scale l_{S} is denoted as l. Unless otherwise stated, the following results have been obtained using the crystal plasticity formulation.

First, a bicrystal is studied such that the two grains have the same orientation of slip systems ($\theta_{\mathrm{I}} = \theta_{\mathrm{II}} = 0$) and the same material parameters. The surface profile at an overall strain $\bar{\epsilon}_1 = U/2L_0 = 5\%$ is shown in figure 3 for $l/w_0 = 0.01$ and in figure 4 for $l/w_0 = 0.1$. Due to symmetry the profiles are only shown for $x_1 \geqslant 0$. In each figure results are displayed for five values of the parameter κ characterizing the grain boundary. For $\kappa = 0$ there is a homogeneous deformation state throughout the specimen, and the surface profile is level.

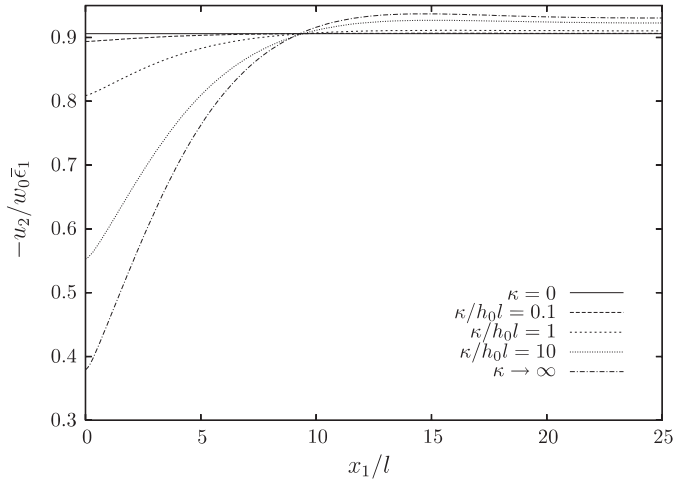

Figure 4. The surface profile near the grain boundary for a bicrystal with $\theta_{\rm I} = \theta_{\rm II} = 0$ and the same material parameters for $l/w_0 = 0.1$ at $\bar{\epsilon}_1 = 5$.

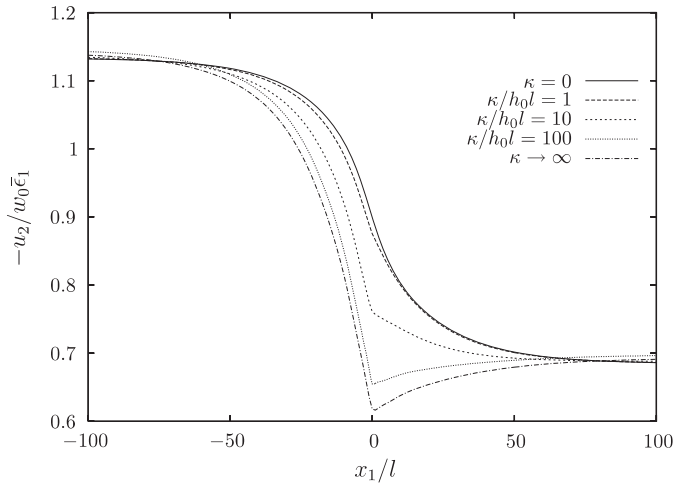

Figure 5. The surface profile near the grain boundary for a bicrystal with $\theta_{\rm I} = \theta_{\rm II} = 0$ and initial slip resistances $\tau_0^{\rm II}/\tau_0^{\rm I} = 2$ for $l/w_0 = 0.01$ at $\bar{\epsilon}_1 = 5\%$.

The curve marked as $\kappa \to \infty$ is obtained using $\gamma^{(\alpha)} = 0$, simulating a grain boundary that is impenetrable to dislocations. Note that an increased value of κ constrains the slips, and thereby the plastic strains, leading to a decrease in the lateral displacement of the specimen at the grain boundary. Figures 3 and 4 illustrate this: there is an increase in the profile at the grain boundary as the value of κ increases.

Figures 5 and 6 show surface profiles for a bicrystal where the two grains have the same crystallographic orientation but the initial slip resistance in grain 1 is half that of grain 2 ($\tau_0^{\rm II}/\tau_0^{\rm I} = 2$), for $l/w_0 = 0.01$ and $l/w_0 = 0.1$. Results are presented for five values of κ at an axial strain of $\bar{\epsilon}_1 = 5\%$. The height of the surface for $\kappa = 0$ (the solid line) decreases monotonically from the strong grain to the weak grain for both values of l/w_0. For $\kappa \to \infty$ the profiles contact a re-entrant corner at the grain boundary, due to the restriction on slips.

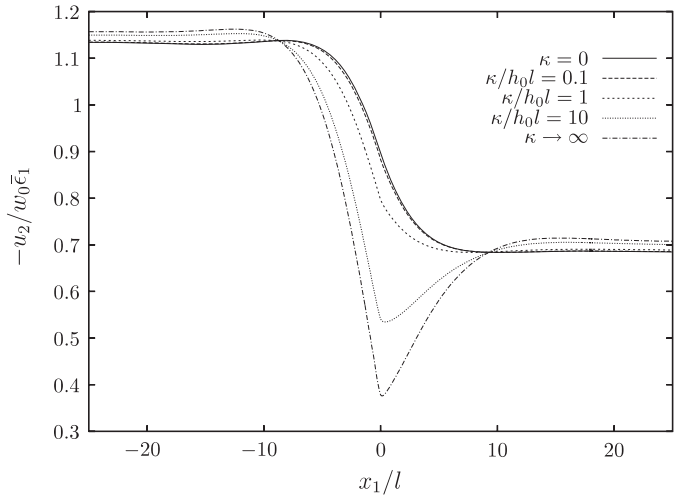

Figure 6. The surface profile near the grain boundary for a bicrystal with $\theta_{\mathrm{I}} = \theta_{\mathrm{II}} = 0$ and initial slip resistances $\tau_0^{\mathrm{II}}/\tau_0^{\mathrm{I}} = 2$ for $l/w_0 = 0.1$ at $\bar{\epsilon}_1 = 5\%$.

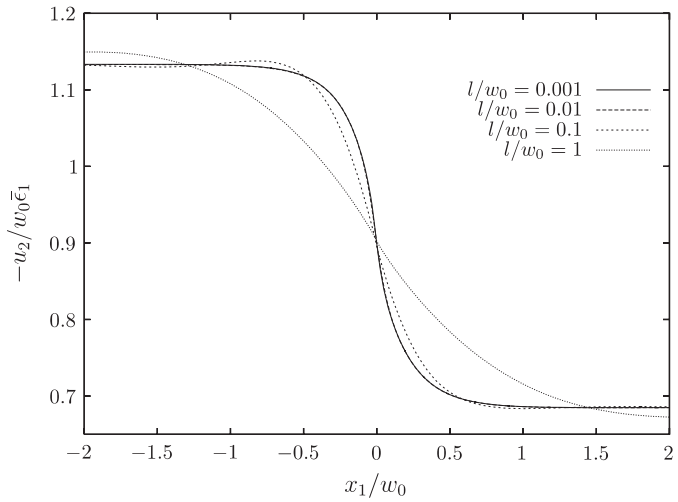

Figure 7. The surface profile near the grain boundary for a bicrystal with $\theta_{\mathrm{I}} = \theta_{\mathrm{II}} = 0$ and initial slip resistances $\tau_0^{\mathrm{II}}/\tau_0^{\mathrm{I}} = 2$ for $\kappa = 0$ at $\bar{\epsilon}_1 = 5\%$.

The sensitivity of the surface profile to the material length scale l/w_0 is shown in figure 7 for $\kappa = 0$ and in figure 8 for $\kappa \to \infty$. These results pertain to the same bicrystal as reported in figures 5 and 6. For the choice $\kappa = 0$ the profile at $l/w_0 = 0.001$ and $l/w_0 = 0.01$ coincide, and only the profile curve for $l/w_0 = 1$ is significantly different from the others. All the profiles with $\kappa = 0$ show a monotonic decrease from the strong grain to the weak grain. In contrast, the value of l/w_0 has a significant effect upon the profiles in figure 8 at $\kappa \to \infty$. For $l/w_0 = 0.001$ the profile is almost constant within the strong grain and decreases within the weak grain, whereas for $l/w_0 = 0.1$ the width of the deformed specimen first increases within the strong grain before it decreases in the weak grain due to the full constraint on slip.

A comparison of surface profiles using strain gradient crystal plasticity and isotropic, phenomenological strain gradient plasticity theory is given in figure 9. The crystal calculations

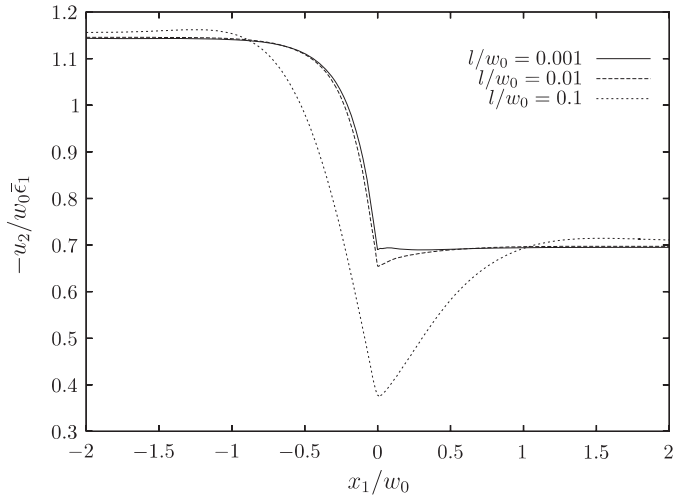

Figure 8. The surface profile near the grain boundary for a bicrystal with $\theta_{\rm I} = \theta_{\rm II} = 0$ and initial slip resistances $\tau_0^{\rm II}/\tau_0^{\rm I} = 2$ for $\kappa \to \infty$ at $\bar{\epsilon}_1 = 5\%$.

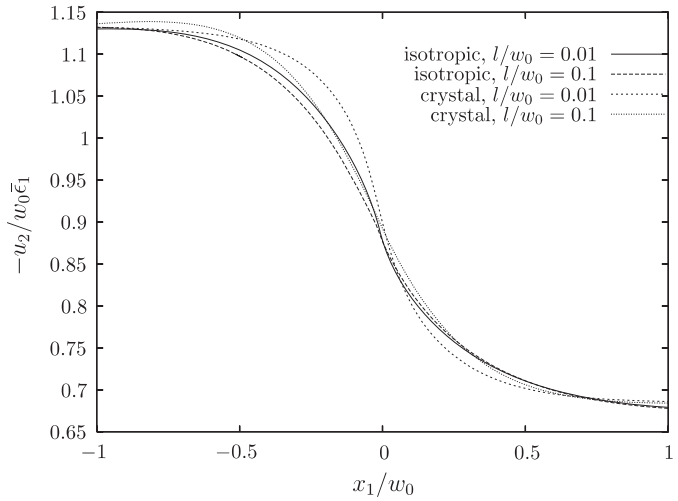

Figure 9. Surface profile near the grain boundary using strain gradient crystal plasticity with $\theta_{\rm I} = \theta_{\rm II} = 0$, initial slip resistances $\tau_0^{\rm II}/\tau_0^{\rm I} = 2$ and continuity of slips and strain gradient plasticity for an isotropic material having continuity of plastic strains at the interface with $\sigma_0^{\rm II}/\sigma_0^{\rm I} = 2$. Both at $\bar{\epsilon}_1 = 5\%$ for two values of l/w_0.

have been carried out for continuity of slips at the grain boundary ($\gamma_{\rm I}^{(\alpha)} = \gamma_{\rm II}^{(\alpha)}$) and $\kappa = 0$, i.e. not using double nodes at the grain boundary. This option is only meaningful when the slip systems in the two grains have the same orientation, which is the case for the results presented in figure 9 ($\theta_{\rm I} = \theta_{\rm II} = 0$). The initial slip resistances are taken as $\tau_0^{\rm II}/\tau_0^{\rm I} = 2$. In the calculations based on the isotropic formulation there is continuity of plastic strains at the grain boundary and the yield strength of the two grains are taken as $\sigma_0^{\rm II}/\sigma_0^{\rm I} = 2$. The results show that there is no significant difference in the surface profiles using the two different formulations, although there is a tendency for the crystal profile to have a locally steeper slope than for the isotropic phenomenological solid.

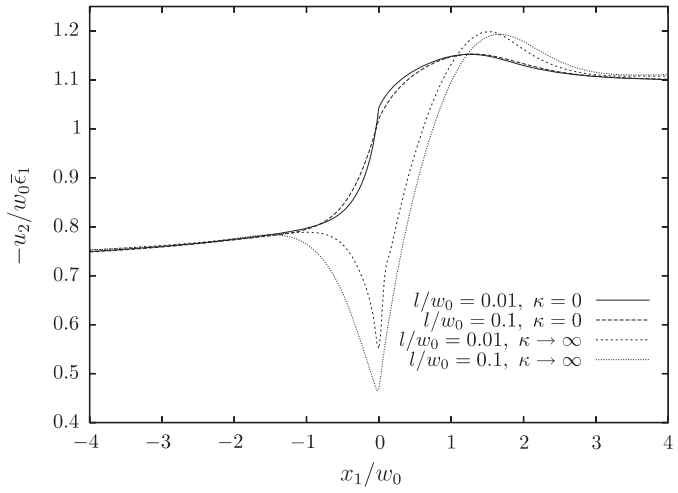

Figure 10. The surface profile near the grain boundary for a bicrystal with $\theta_{\mathrm{I}} = 0^\circ$ and $\theta_{\mathrm{II}} = 15^\circ$ and the same material parameters for $\kappa \to \infty$ and $\kappa = 0$ at $\bar{\epsilon}_1 = 5\%$ for two values of l/w_0.

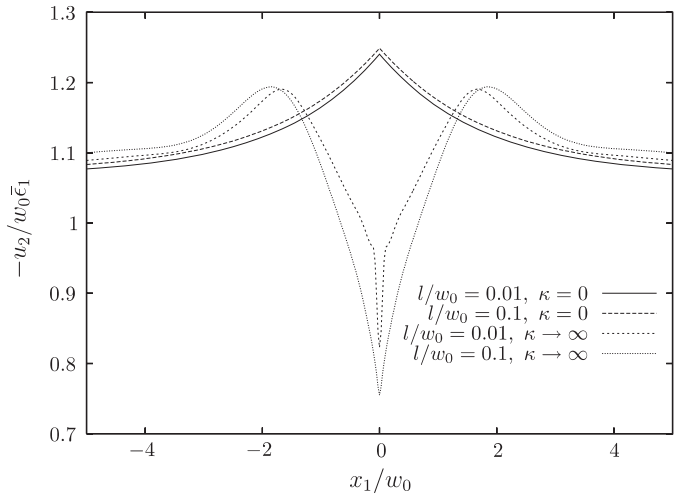

Figure 11. The surface profile near the grain boundary for a bicrystal with $\theta_{\mathrm{I}} = -15^\circ$ and $\theta_{\mathrm{II}} = 15^\circ$ and the same material parameters for $\kappa \to \infty$ and $\kappa = 0$ at $\bar{\epsilon}_1 = 5\%$ for two values of l/w_0.

Next, a bicrystal with a lattice mismatch as specified by $\theta_{\mathrm{I}} = 0^\circ$ and $\theta_{\mathrm{II}} = 15^\circ$ is considered. The surface profile is shown in figure 10 for the case with $\kappa = 0$ (allowing for jumps in the slip) and $\kappa \to \infty$ using two different values of l/w_0. For $\kappa = 0$ there is only a slight difference in the profile for the two considered length scales, whereas the value of l/w_0 has a more major influence on the profiles at $\kappa \to \infty$. The profiles are qualitatively similar to results already displayed in figures 5 and 6 where the grains had the same orientation but different initial slip resistances.

Finally, a bicrystal with the grain orientations $\theta_{\mathrm{I}} = -15^\circ$ and $\theta_{\mathrm{II}} = 15^\circ$ and the same material parameters in each grain is studied. Figure 11 shows the surface profile for the two extreme cases $\kappa = 0$ and $\kappa \to \infty$ using two values of l/w_0. As discussed already for the

profile with $\theta_{\mathrm{I}} = 0^{\circ}$ and $\theta_{\mathrm{II}} = 15^{\circ}$, the value of l/w_0 has only a minor effect upon the surface shape for the choice $\kappa = 0$. An enhanced slip activity is evident near the interface for $\kappa = 0$ in figure 11, where the profile drops at the grain boundary creating a valley. It appears that the interface behaves as a free surface and dislocation activity is enhanced adjacent to it. The profile using $\kappa \to \infty$ creates a tip at the grain boundary. This tip becomes thinner and sharper with decreasing l/w_0.

6. Concluding remarks

The surface profile near a grain boundary of an aluminium sheet deformed in tension has been examined qualitatively in a scanning electron microscope. A local gradient in surface profile is observed within a few micrometres of the grain boundary.

Finite element calculations are reported here on the surface profile adjacent to a grain boundary in a bicrystal. The simulations are reported both for a strain gradient crystal plasticity formulation and for an isotropic, phenomenological strain gradient plasticity solid. A penalty to dislocations on each side of the grain boundaries has been introduced within the crystal plasticity formulation. The predicted profiles are very sensitive to the choice of grain boundary barrier to slip. In order to obtain physically realistic results for the surface profile, slip motion to the grain boundary must occur.

Acknowledgments

The work of UB is financially supported by the Danish Technical Research Council in a project entitled Modeling Plasticity at the Micron Scale.

References

Aifantis K E and Willis J R 2005 *J. Mech. Phys. Solids* **53**, 1047–70
Borg U, Niordson C F, Fleck N A and Tvergaard V 2006 *Int. J. Solids Struct.* **43** 4906–16
Borg U 2006 *Int. J. Plasticity* submitted
Evers L P, Brekelmans W A M and Geers M G D 2004 *Int. J. Solids Struct.* **41** 5209–30
Fleck N A and Hutchinson J W 2001 *J. Mech. Phys. Solids* **49** 2245–71
Fleck N A and Willis J R 2004 *J. Mech. Phys. Solids* **52** 1855–88
Gudmundson P 2004 *J. Mech. Phys. Solids* **52** 1379–406
Gurtin M E 2002 *J. Mech. Phys. Solids* **50** 5–32
Gurtin M E and Needleman A 2005 *J. Mech. Phys. Solids* **53** 1–31
Peirce D, Asaro R J and Needleman A 1983 *Acta Metall.* **31** 1951–76
Rice J R 1987 *Mech. Mater.* **6** 317–35
Stoudt M R and Ricker R E 2002 *Metall. Mater. Trans.* A **33** 2883–9
Wilson W R D and Lee W 2001 *J. Manuf. Sci. Eng.* **123** 279–83
Zhao Z, Radovitzky R and Cuitiño A 2004 *Acta Mater.* **52** 5791–804

P4

A strain gradient crystal plasticity analysis of grain size effects in polycrystals

European Journal of Mechanics, A/solids
26, 313-324, 2007

Available online at www.sciencedirect.com
ScienceDirect
European Journal of Mechanics A/Solids 26 (2007) 313–324

A strain gradient crystal plasticity analysis of grain size effects in polycrystals

Ulrik Borg

Department of Mechanical Engineering, Solid Mechanics, Technical University of Denmark, Kgs. Lyngby, DK-2800, Denmark

Received 9 June 2006; accepted 22 September 2006

Available online 27 October 2006

Abstract

The influence of grain size on yield and flow stress in polycrystalline metals is analyzed using a strain gradient crystal plasticity theory with an internal material length scale. The numerical solutions are obtained with the finite element method considering a polycrystal modeled by 40 individually oriented grains in a unit cell, each having three planar slip systems. An energy potential that penalizes crystallographic slip at grain boundaries is included in the analyzes. The polycrystal is subjected to plane strain tension for various grain sizes and higher order boundary conditions at the grain boundaries. An increase in flow stress with decreasing grain size, d, was obtained on the form d^{-n}, with n in the range 0.82 to 1.25 at initial yield and in the range 0.77 to 1.09 after 0.1 logarithmic strain.

Keywords: Strain gradient plasticity; Grain size effects; Crystal plasticity

1. Introduction

Grain size strengthening in polycrystalline metals has been a subject of research interest for more than 50 years. Hall (1951) and Petch (1953) independently found that the yield strength in mild steel varies with the inverse square root of grain size as

$$\sigma = \sigma_0 + kd^{-1/2} \tag{1}$$

where d is the mean grain size, σ_0 is the yield stress in the imaginary situation with infinitely large grains, and k is a material constant (the Hall–Petch slope). Armstrong et al. (1962) showed experimentally that for a number of metallic polycrystalline aggregates the flow stress at constant strain is related to the grain size, d, by the same form as the Hall–Petch relationship between yield strength and grain size, i.e. σ, σ_0 and k are functions of the strain.

Several models have been proposed to account for the grain size dependency. One theory is that grain boundaries act as obstructions to dislocation motion and therefore dislocations pile-up at grain boundaries giving rise to stress concentrations. Another model based on work hardening assumes an inverse relationship between dislocation density and grain size. A theory that supports the work hardening model was proposed by Ashby (1970) arguing that an in-

E-mail address: ub@mek.dtu.dk (U. Borg).

0997-7538/$ – see front matter
doi:10.1016/j.euromechsol.2006.09.006

crease with strain in the density of geometrically necessary dislocations at a grain boundary affects the work hardening of polycrystals.

Classical crystal plasticity formulations like Peirce et al. (1983) do not include any material length scales in the constitutive equations, and therefore they cannot capture the experimentally observed grain size effects. Within recent years several non-local crystal plasticity formulations have been proposed. Some of these formulations are based on strain gradient plasticity theories that make use of an internal material length scale parameter (Shu and Fleck, 1999; Borg, 2006). Other non-local formulations are continuum theories of dislocations (Acharya and Beaudoin, 2000; Gurtin, 2002; Han et al., 2005; Evers et al., 2004; Kuroda and Tvergaard, 2006). Grain size effects in polycrystals have been predicted with such crystal plasticity formulations by Acharya and Beaudoin (2000) and Evers et al. (2004). Furthermore, discrete dislocation plasticity models have been used to analyze grain size strengthening in the work of Biner and Morris (2002) and Balint et al. (2005).

In this work, the grain size effect in a polycrystal with planar slip systems under plane strain tension is studied using the rate-dependent strain gradient crystal plasticity theory for finite deformations by Borg (2006). It works within the framework of the strain gradient theory by Fleck and Hutchinson (2001). The theory is enhanced with a grain boundary energy potential that penalizes crystallographic slip at internal grain boundaries, following Aifantis and Willis (2005), Gudmundson (2004) and Borg and Fleck (2006). This potential is included to account for the obstruction of dislocations at the grain boundaries.

2. Material model

The material behavior is modeled by a strain gradient crystal plasticity theory for finite strains proposed by Borg (2006) within an updated Lagrangian framework. The formulation fits within the framework of the phenomenological strain gradient theory by Fleck and Hutchinson (2001) and reduces to conventional crystal plasticity theory by e.g. Peirce et al. (1983) in the absence of strain gradients. The theory is further enhanced by an interfacial potential to account for the grain boundary resistance to dislocations. The kinematical basis is taken from Peirce et al. (1983), where a quantitative description of plastic deformation in single crystals is based on crystallographic shearing along specific slip systems. In the following, a Greek superscript in a parentheses denotes a slip system, repeated lower-case Latin indices imply summation over the range 1–3, and a dot denotes the time derivative.

A slip system (α) is specified by the lattice vectors $s_i^{(\alpha)}$ and $m_i^{(\alpha)}$, where $s_i^{(\alpha)}$ is the slip direction and $m_i^{(\alpha)}$ is the direction normal to the slip plane. Introducing $\mu_{ij}^{(\alpha)} = \frac{1}{2}(s_i^{(\alpha)} m_j^{(\alpha)} + s_j^{(\alpha)} m_i^{(\alpha)})$ as the classical Schmid orientation tensor, the overall macroscopic plastic strain rate components can be related to the crystallographic slips, $\gamma^{(\alpha)}$, as

$$\dot{\epsilon}_{ij}^{p} = \sum_{\alpha} \dot{\gamma}^{(\alpha)} \mu_{ij}^{(\alpha)}. \tag{2}$$

To account for the effect of increased material hardening due to geometrically necessary dislocations caused by plastic strain gradients, it is assumed that the slip rates and slip rate gradients, $\dot{\gamma}_{,i}^{(\alpha)}$, contribute to the plastic work. Introducing two surface energy potentials $\phi_{-}^{(\alpha)}(\gamma_{-}^{(\alpha)})$ and $\phi_{+}^{(\alpha)}(\gamma_{+}^{(\alpha)})$ acting at the two sides of a grain boundary Γ, the principle of virtual power on total form in the deformed configuration can thus be written as (where $\phi_{-}^{(\alpha)\prime}$ denotes $\partial\phi_{-}^{(\alpha)}/\partial\gamma_{-}^{(\alpha)}$, etc.)

$$\begin{aligned}
&\int_V \left(\sigma_{ij} \delta \dot{\epsilon}_{ij}^{E} + \sum_{\alpha} Q^{(\alpha)} \delta \dot{\gamma}^{(\alpha)} + \sum_{\alpha} \left(\xi_S^{(\alpha)} s_i^{(\alpha)} + \xi_M^{(\alpha)} m_i^{(\alpha)} + \xi_T^{(\alpha)} t_i^{(\alpha)} \right) \delta \dot{\gamma}_{,i}^{(\alpha)} \right) \mathrm{d}V \\
&\quad + \int_{\Gamma} \sum_{\alpha} \left(\phi_{-}^{(\alpha)\prime} \delta \dot{\gamma}_{-}^{(\alpha)} + \phi_{+}^{(\alpha)\prime} \delta \dot{\gamma}_{+}^{(\alpha)} \right) \mathrm{d}\Gamma = \int_S \left(T_i \delta \dot{u}_i + \sum_{\alpha} r^{(\alpha)} \delta \dot{\gamma}^{(\alpha)} \right) \mathrm{d}S
\end{aligned} \tag{3}$$

where σ_{ij} is the Cauchy stress and $\dot{\epsilon}_{ij}^{E}$ is the elastic part of the strain rate. The stress field $Q^{(\alpha)}$ is a stress measure work-conjugate to the slip, $\gamma^{(\alpha)}$, and $\xi_S^{(\alpha)}$, $\xi_M^{(\alpha)}$ and $\xi_T^{(\alpha)}$ are higher order stresses work-conjugate to the slip gradients along the slip direction, the direction normal to the slip plane and the transverse direction, respectively. The vector $t_i^{(\alpha)}$ denotes the transverse direction and thus forms a triad with vectors $s_i^{(\alpha)}$ and $m_i^{(\alpha)}$. For simplicity and clarity it is

assumed that the slip gradient in the transverse direction does not contribute to the plastic work, which is the case for plane strain problems with in-plane slip systems, and therefore the term $\xi_T^{(\alpha)} t_i^{*(\alpha)} \delta\dot{\gamma}_{,i}^{(\alpha)}$ is excluded in the following. The surface stress traction is denoted T_i, and $r^{(\alpha)}$ is the higher order traction working on the external boundary S. In the absence of the grain boundary term, Eq. (3) has the same form as the principle of virtual power in Gurtin (2002).

The presence of the grain boundary energy term causes jumps in the slips, having $\gamma_-^{(\alpha)}$ on one side of the boundary and $\gamma_+^{(\alpha)}$ on the other side of the boundary. Full constraint along Γ with $\gamma^{(\alpha)} = 0$ is obtained by letting $\phi_-^{(\alpha)\prime}$ and $\phi_+^{(\alpha)\prime}$ tend to infinity, whereas vanishing surface energy along Γ simulates that dislocations are free to cross the grain boundary. Here, the expressions adopted for the grain boundary energy potentials are of the form

$$\phi_-^{(\alpha)} = \frac{1}{2}\kappa\left(\gamma_-^{(\alpha)}\right)^2, \qquad \phi_-^{(\alpha)\prime} = \kappa\gamma_-^{(\alpha)}, \tag{4}$$

$$\phi_+^{(\alpha)} = \frac{1}{2}\kappa\left(\gamma_+^{(\alpha)}\right)^2, \qquad \phi_+^{(\alpha)\prime} = \kappa\gamma_+^{(\alpha)} \tag{5}$$

where κ is a material parameter describing the strength of the grain boundary. This quadratic function of $\gamma^{(\alpha)}$ is taken as a simple example. Other functions might give a better description of the physics at the grain boundary, but this is still an open issue.

To obtain the principle of virtual power on incremental form in the reference configuration, Kirchhoff stress measures are defined as (defining J as the determinant of the deformation gradient)

$$\varsigma_{ij} = J\sigma_{ij}, \quad q^{(\alpha)} = J\,Q^{(\alpha)}, \quad \rho_S^{(\alpha)} = J\xi_S^{(\alpha)}, \quad \rho_M^{(\alpha)} = J\xi_M^{(\alpha)}. \tag{6}$$

The incremental elastic constitutive equation is taken in terms of the Jaumann rate of Kirchhoff stress, $\overset{\triangledown}{\varsigma}_{ij}$, as

$$\overset{\triangledown}{\varsigma}_{ij}\,\Delta t = R_{ijkl}\left(\Delta\epsilon_{kl} - \Delta t\sum_\alpha \dot{\gamma}^{(\alpha)}\mu_{kl}^{(\alpha)}\right) = \Delta\varsigma_{ij} - \Delta\omega_{ik}\sigma_{kj} - \sigma_{ik}\Delta\omega_{jk} \tag{7}$$

where $\dot{\omega}_{ij}$ denotes the material spin rate and the elastic stiffness tensor is given by $R_{ijkl} = \frac{E}{1+\nu}(\frac{1}{2}(\delta_{ik}\delta_{jl} + \delta_{il}\delta_{jk}) + \frac{\nu}{1-2\nu}\delta_{ij}\delta_{kl})$, where E is the elastic modulus, ν is Poisson's ratio and δ_{ij} denotes the Kronecker delta symbol.

A non-local measure of the effective slip, $\gamma_e^{(\alpha)}$, is defined on the basis of the slip rate and its directional derivative through the incremental relation

$$\dot{\gamma}_e^{(\alpha)2} = \dot{\gamma}^{(\alpha)2} + \left(l_S\dot{\gamma}_{,i}^{(\alpha)}s_i^{(\alpha)}\right)^2 + \left(l_M\dot{\gamma}_{,i}^{(\alpha)}m_i^{(\alpha)}\right)^2 \tag{8}$$

where l_S and l_M are internal material length parameters introduced for dimensional consistency. An effective stress $\tau_e^{(\alpha)}$ is defined to be work conjugate to the effective slip rate, $\gamma_e^{(\alpha)}$, such that

$$\tau_e^{(\alpha)}\delta\dot{\gamma}_e^{(\alpha)} = q^{(\alpha)}\delta\dot{\gamma}^{(\alpha)} + \rho_S^{(\alpha)}s_i^{(\alpha)}\delta\dot{\gamma}_{,i}^{(\alpha)} + \rho_M^{(\alpha)}m_i^{(\alpha)}\delta\dot{\gamma}_{,i}^{(\alpha)}. \tag{9}$$

A power-law creep model is adopted for the effective slip rate, $\dot{\gamma}_e^{(\alpha)}$, to model the viscous material behavior

$$\dot{\gamma}_e^{(\alpha)} = \dot{\gamma}_0\left(\frac{\tau_e^{(\alpha)}}{g^{(\alpha)}}\right)^{1/m} \tag{10}$$

where $\dot{\gamma}_0$ is a reference slip rate and m is a strain rate hardening index. The slip resistances $g^{(\alpha)}$ characterize the current strain hardened state of the crystal, and harden from an initial value τ_0 according to

$$\dot{g}^{(\alpha)} = \sum_\beta h_{\alpha\beta}\dot{\gamma}_e^{(\beta)}, \qquad h_{\alpha\beta} = h\delta_{\alpha\beta} + ph(1-\delta_{\alpha\beta}). \tag{11}$$

Here, p is the latent hardening index and h is the self-hardening modulus given by

$$h(\gamma_a) = h_0\left(\frac{h_0\gamma_a}{\tau_0 n_h} + 1\right)^{n_h - 1}, \quad \gamma_a = \sum_\alpha \int \dot{\gamma}_e^{(\alpha)}\,\mathrm{d}t, \tag{12}$$

where the constant h_0 represents an initial hardening rate, n_h is the hardening exponent, and γ_a is the accumulated effective slip.

3. Numerical method and modeling details

This work is based on the assumption of plane strain and three in-plane slip systems at a relative orientation of 60° from one to the next (see Fig. 1). The absolute orientation of a crystal is given by the angle θ between slip system one and the x_2-direction.

The numerical calculations are carried out using a finite element method where the slip rate increments are taken as state variables on equal footing with the displacement increments. The displacement increments, Δu_i, and the slip rate changes, $\Delta\dot{\gamma}^{(\alpha)}$, are interpolated within each element between nodal displacement increments, ΔD^N, and nodal slip rate changes, $\Delta\dot{\gamma}_N^{(\alpha)}$, respectively

$$\Delta u_i = \sum_{N=1}^{2k} N_i^N \Delta D^N, \qquad \Delta\dot{\gamma}^{(\alpha)} = \sum_{N=1}^{l} M^N \Delta\dot{\gamma}_N^{(\alpha)} \tag{13}$$

where N_i^N and M^N are shape functions and k and l are the number of nodes used for the interpolations. For the plastic and total strain fields to have the same degree of interpolation, the slips, and thereby the plastic strains, must have shape functions of one degree lower than the displacements. The elements used for the displacements are 8-node quadrilaterals with quadratic shape functions, and the elements used for interpolation of the slip rate increments are 4-node quadrilaterals with linear shape functions, i.e. $k = 8$ and $l = 4$. The coordinates of the nodes in the 4-node elements are identical to the coordinates of the corner nodes in the 8-node elements.

The discretized equations are obtained by use of these relations in the principle of virtual work. The equation system decouples relations from slip rate increments to displacement increments. The approach is as follows: first solve for the displacement increments, and then solve for slip rate increments for each slip system using the displacement increments. The integrations are carried out using 2×2 point Gaussian integration for both element types.

The polycrystal model to be analyzed is shown in Fig. 2. It includes 40 grains (single crystals) of which 24 are six-sided, 8 are five-sided and 8 are four-sided. The initial dimensions of the polycrystal are given by $a_0/b_0 = 1.5$. The absolute orientation of each grain, given by the angle θ obtained from a random number generator is shown on the figure, though the same orientation of all grains ($\theta = 0°$) is used for some of the calculations reported on here.

The symmetry boundary conditions applied on the polycrystal are given by

$$\begin{aligned}
&\dot{u}_1 = 0, \quad \dot{T}_2 = 0 \quad \text{at } x_1 = 0,\\
&\dot{u}_1 = \dot{U}_1, \quad \dot{T}_2 = 0 \quad \text{at } x_1 = a_0,\\
&\dot{u}_2 = 0, \quad \dot{T}_1 = 0 \quad \text{at } x_2 = 0,\\
&\dot{u}_2 = \dot{U}_2, \quad \dot{T}_1 = 0 \quad \text{at } x_2 = b_0
\end{aligned} \tag{14}$$

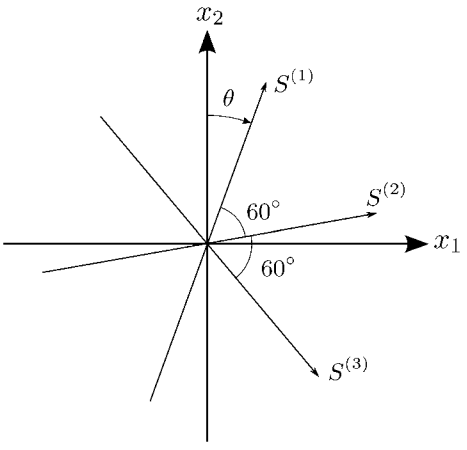

Fig. 1. The three slip systems used have 60° between each and an absolute orientation given by the angle θ.

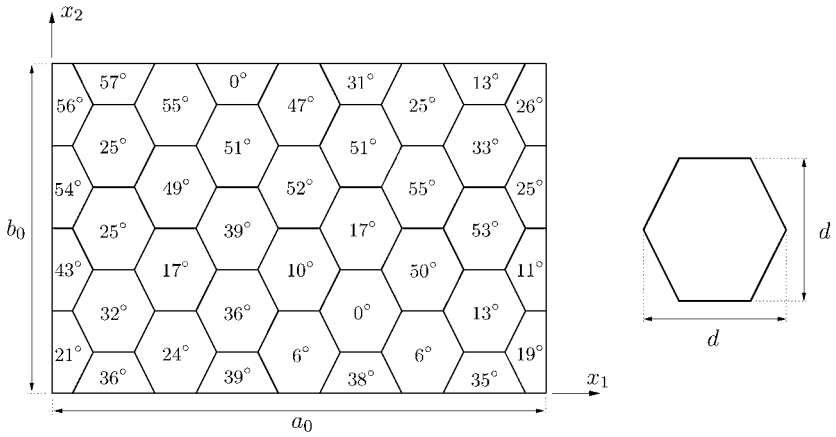

Fig. 2. The analyzed polycrystal consists of 40 grains with grain size d. The orientation given by the angle θ is given in each grain.

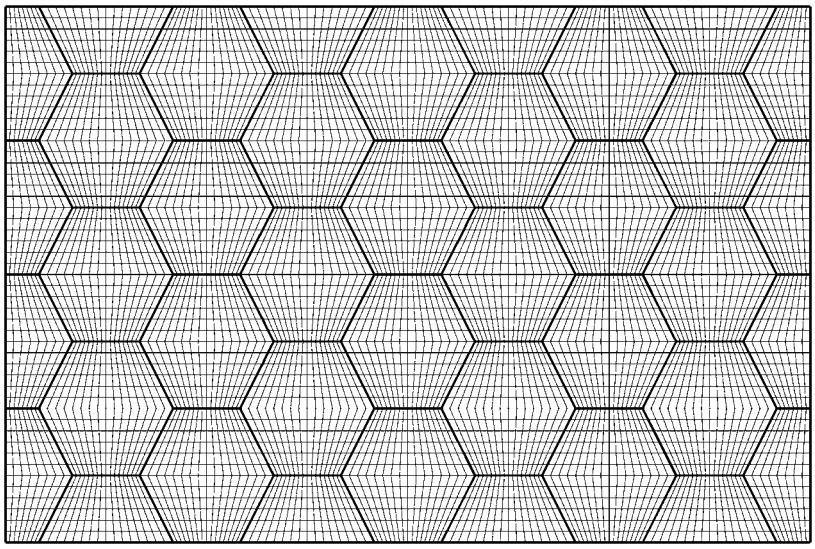

Fig. 3. Example of a finite element mesh used for the numerical analyzes.

where $\dot{T}_i$ are surface traction rates. Using a special Rayleigh–Ritz finite element method (Tvergaard, 1976), the prescribed cell-side displacement rates, $\dot{U}_1$ and $\dot{U}_2$, are determined such that the average true stress in the x_2-direction is zero.

The higher order boundary conditions are applied as vanishing higher order traction, $r^{(\alpha)} = 0$, on the external boundaries of all the four and five-sided grains. The external boundaries of the six-sided grains are treated as internal grain boundaries. This is chosen to simulate symmetry boundary conditions along the four external boundaries, even though this can only be achieved when the slip systems in the four and five-sided grains are oriented symmetrically around the x_1- and x_2-direction. To allow for a discontinuity in slips across grain boundaries, the slips in adjacent grains are uncoupled by placing double nodes for the 4-node elements at grain boundaries. Continuity of the displacement field is ensured through coupling of the displacements at nodes on the grain boundaries. The grain boundary energy potential makes it possible to simulate different conditions at the grain boundaries. The two extreme cases are letting the grain boundaries be impenetrable to dislocations by restricting the slips to vanish ($\kappa \to \infty$), or letting the higher order stresses vanish ($\kappa = 0$). Intermediate conditions can be achieved by using other values of κ.

An example of a finite element mesh used is shown in Fig. 3, where each hexagonal grain consists of a grid 16 elements wide and 12 elements high, giving a total of 6144 elements for the polycrystal. In all cases studied it has been checked that a sufficiently refined mesh has been used.

4. Results

The material parameters used in the calculations are given by the initial slip resistance, $\tau_0/E = 0.001$, Poisson's ratio, $\nu = 0.3$, the initial hardening rate, $h_0/\tau_0 = 10$, the latent hardening index, $p = 1.4$, the hardening exponent, $n_h = 0.1$, the strain rate hardening index, $m = 0.01$ and the reference slip rate, $\dot{\gamma}_0 = 0.001\ \mathrm{s}^{-1}$. The applied end displacement rate, $\dot{U}_1$, is specified so that $\dot{U}_1/a_0 = \dot{\gamma}_0$.

A slip gradient in the direction normal to the slip plane, $\gamma^{(\alpha)}_{,i} m^{(\alpha)}_i$, does not induce any geometrically necessary dislocations, and therefore it can be argued that it should not contribute to the strain hardening of the material. Thus, the length scale related to the gradient in the direction normal to the slip plane is set to zero, $l_M = 0$, for all of the results presented here. The other material length scale, l_S, is in the following simply denoted as l.

For the results presented in Fig. 4 all 40 grains have the same absolute orientation given by $\theta = 0°$. The figure shows curves for the average true stress in the x_1-direction, σ, normalized by the initial slip resistance, τ_0, as a function of the average logarithmic strain in the x_1-direction, $\epsilon = \ln(1 + U_1/a_0)$. The grain boundaries are modeled as impenetrable to dislocations using $\kappa \to \infty$ (obtained by restricting $\gamma^{(\alpha)} = 0$). Results are shown for grain sizes reaching from infinity (labeled local) down to three times the internal material length parameter. The curve labeled local is obtained with $l = 0$ and with no restrictions on the slips at grain boundaries ($\kappa = 0$), corresponding to a conventional crystal plasticity formulation. It is seen that the initial yield strength and the hardening increase with decreasing grain size.

Figs. 5 and 6 display contours of accumulated slip, $\sum_\alpha \int \dot{\gamma}^{(\alpha)}\,\mathrm{d}t$, for some of the calculations presented in Fig. 4 with $d/l = 20$ and $d/l = 3$, respectively. The contours are plotted after 0.05 logarithmic strain in the x_1-direction. For both grain sizes the accumulated slip has the highest value in the middle of the grains and decreases to zero at the grain boundaries. The accumulated slip gradients from the "vertical" grain boundaries are much higher for $d/l = 20$ than for $d/l = 3$. This is due to the contribution from the slip gradients to the internal plastic work and to the hardening of the material. Thus, when the grain size to material length parameter ratio is increased, the slip gradients are reduced to minimize the internal work done by the material. Because of the absolute orientation of the grains ($\theta = 0°$), almost all slip will occur along the two slip systems oriented at $\pm 30°$ from the x_1-direction. This explains why the slip gradients along the x_2-direction are almost independent of the grain size.

Instead of the physically rather unrealistic condition of identical orientation of slip systems in all grains, all of the following results are obtained using the random grain orientation shown in Fig. 2. Fig. 7 is similar to Fig. 4, but now for randomized grain orientations. The slips are again restricted to vanish along the grain boundaries (except for the curve labeled local). The results are qualitatively equal to the results obtained with all grains having the same orientation.

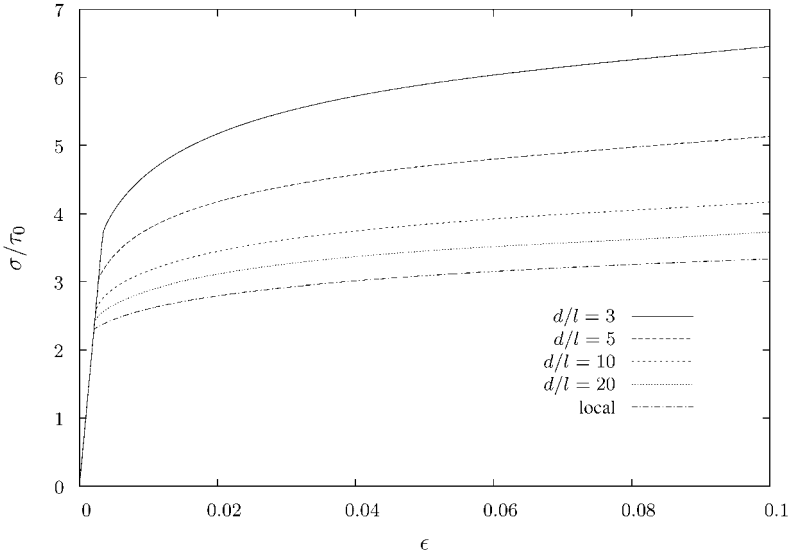

Fig. 4. Stress strain curves for different grain sizes with the same slip system orientation, $\theta = 0°$, in all grains. The slip, $\gamma^{(\alpha)}$, is prescribed to be zero on all grain boundaries ($\kappa \to \infty$).

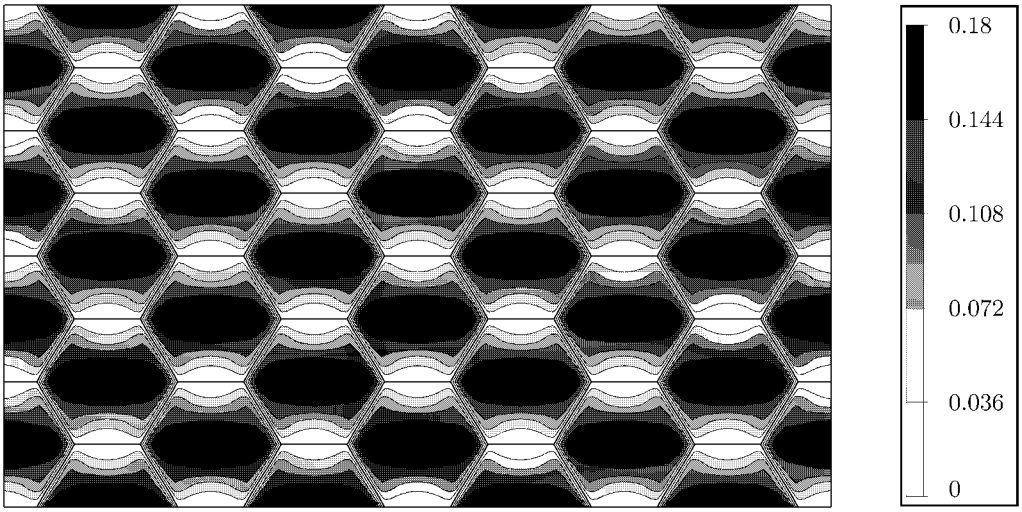

Fig. 5. Contours of the accumulated slip after 0.05 logarithmic strain with grain size $d/l = 20$ and the same slip system orientation in each grain. The slip, $\gamma^{(\alpha)}$, is prescribed to be zero on all grain boundaries ($\kappa \to \infty$).

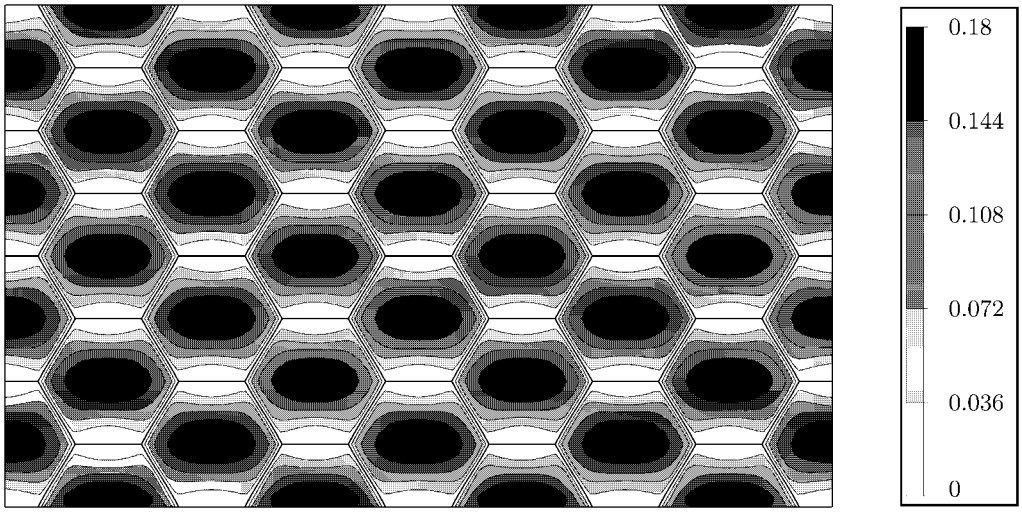

Fig. 6. Contours of the accumulated slip after 0.05 logarithmic strain with grain size $d/l = 3$ and the same slip system orientation in each grain. The slip, $\gamma^{(\alpha)}$, is prescribed to be zero on all grain boundaries ($\kappa \to \infty$).

Fig. 8 shows the increase in flow stress normalized by the initial slip resistance for decreasing grain size. Curves are shown at initial yield (labeled $\epsilon^p = 0.0002$) and also at $\epsilon = 0.1$, both for a polycrystal with the same orientation in all grains and for a polycrystal with randomly oriented grains. The flow stress, σ, is taken as the average true stress in the x_1-direction. Initial yield is taken at 0.0002 plastic strain defined by $\epsilon = 0.0002 + \sigma(1 - \nu^2)/E$, where the elastic strain is taken as $\sigma(1 - \nu^2)/E$ due to the plane strain conditions. In Fig. 8 σ_0 denotes the average true stress in the x_1-direction at either $\epsilon^p = 0.0002$ or $\epsilon = 0.1$ for a polycrystal with infinitely large grains, in practice obtained from a local calculation. Having the same orientation of all grains or a random orientation of the grains seems to have a minor influence on the increase in initial yield stress for all grain sizes. However, at $\epsilon = 0.1$ the level of the curve obtained with the random orientation of the grains is higher than the level of the curve obtained with the same orientation of all grains. All four curves have been fitted with a function of the form d^{-n}, where a and b are the fitting parameters. The values of n giving the best fit are shown in the figure.

Fig. 9 shows stress strain curves for different grain sizes with randomly oriented grains, where the higher order stresses are vanishing on grain boundaries ($\kappa = 0$). In this case the grain size effect is much smaller than for the case

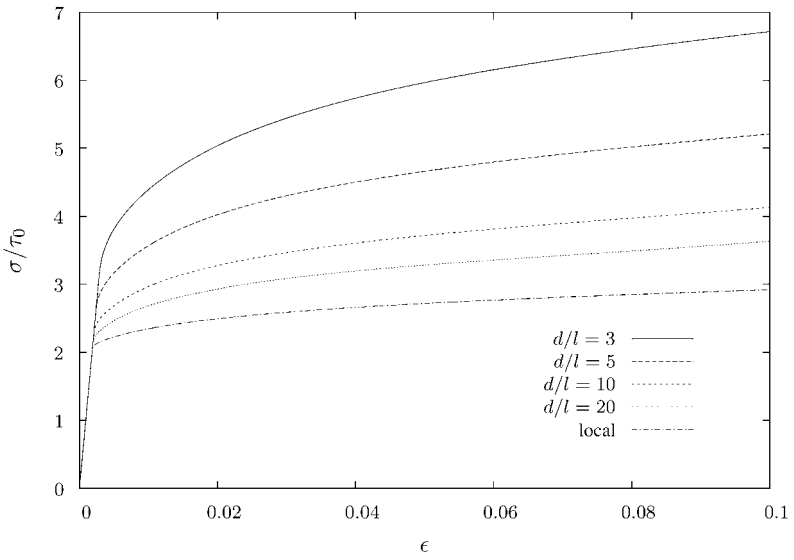

Fig. 7. Stress strain curves for different grain sizes and randomized grain orientations. The slip, $\gamma^{(\alpha)}$, is prescribed to be zero on all grain boundaries ($\kappa \to \infty$).

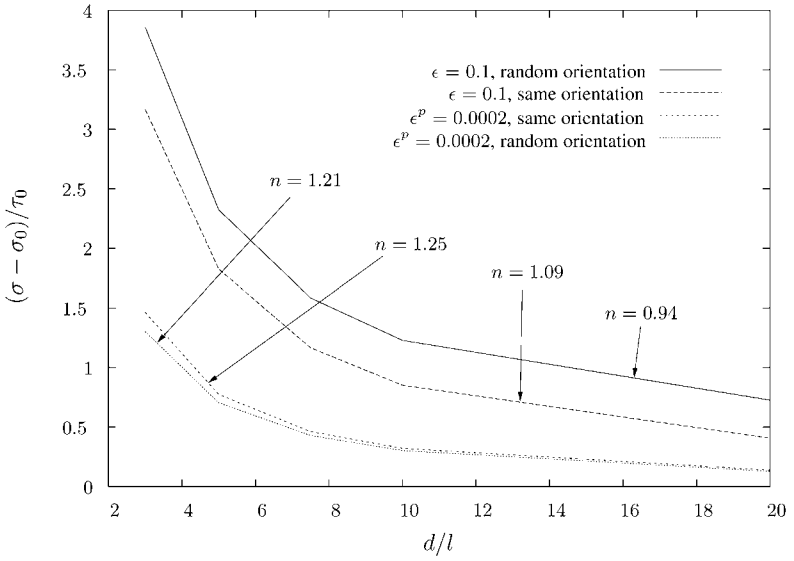

Fig. 8. The increase in flow strength vs. grain size at initial yield and after 0.1 logarithmic strain. The slip, $\gamma^{(\alpha)}$, is prescribed to be zero on all grain boundaries ($\kappa \to \infty$).

with vanishing slip at grain boundaries. The only size effect is due to the different orientation of adjacent grains, causing an inhomogeneous strain field in the polycrystal which gives a gradient effect in the non-local theories.

The increase in flow stress for the calculations shown in Fig. 9 is shown in Fig. 10. As in Fig. 8 for vanishing slip at grain boundaries, results are given after 0.0002 plastic strain (initial yield) and at $\epsilon = 0.1$. The curves are fitted with a function of the form d^{-n} and the best fit parameters are shown in the figure.

In the previous results only two extreme boundary conditions at grain boundaries have been considered. That is either no slip ($\kappa \to \infty$) or no higher order stresses ($\kappa = 0$). Applying other values of the surface energy potential parameter, κ, some intermediate conditions can be achieved. Fig. 11 shows stress strain curves for a polycrystal with randomly oriented grains for grain sizes $d/l = 5$ at different values of the grain boundary surface energy parameter, κ.

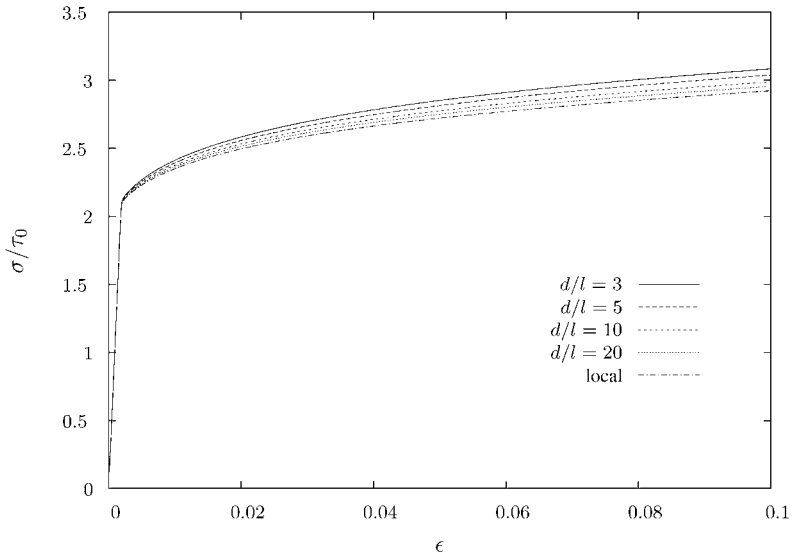

Fig. 9. Stress strain curves for different grain sizes and randomized grain orientations. The higher order stresses are prescribed to be zero on all grain boundaries ($\kappa = 0$).

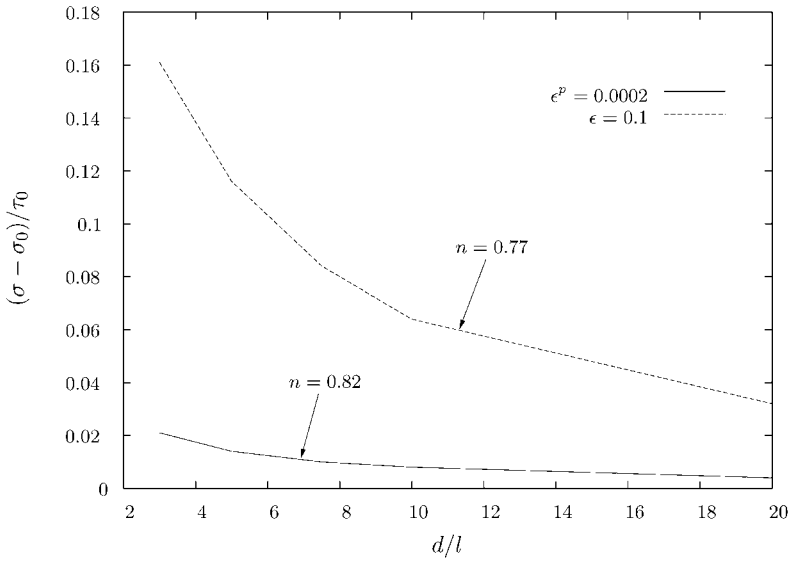

Fig. 10. The increase in flow stress vs. grain size at initial yield and after 0.1 logarithmic strain. The higher order stresses are prescribed to vanish on all grain boundaries ($\kappa = 0$).

The two extreme conditions, $\kappa = 0$ and $\kappa \to \infty$, give the lower and the upper curve, whereas other values of κ give stress strain curves between them.

Figs. 12 and 13 show stress strain curves for varying grain sizes with grain boundary surface energy parameters $\kappa/(\tau_0 l) = 10$ and $\kappa/(\tau_0 l) = 100$, respectively. In both cases, the level of the stress strain curves is increasing with decreasing grain sizes.

The increase in flow stress at $\epsilon = 0.1$ is shown in Fig. 14 for the two values of the grain boundary surface energy parameter used in Figs. 12 and 13. Results for the increase in initial yield stress are not shown, because the initial yield stress can only be changed for extremely high values of $\kappa/(\tau_0 l)$. The reason for this is that the surface energy is taken to be a linear function of the slips, which are very small at initial yield. The best fit parameters to a function of the form d^{-n} are shown on the figure.

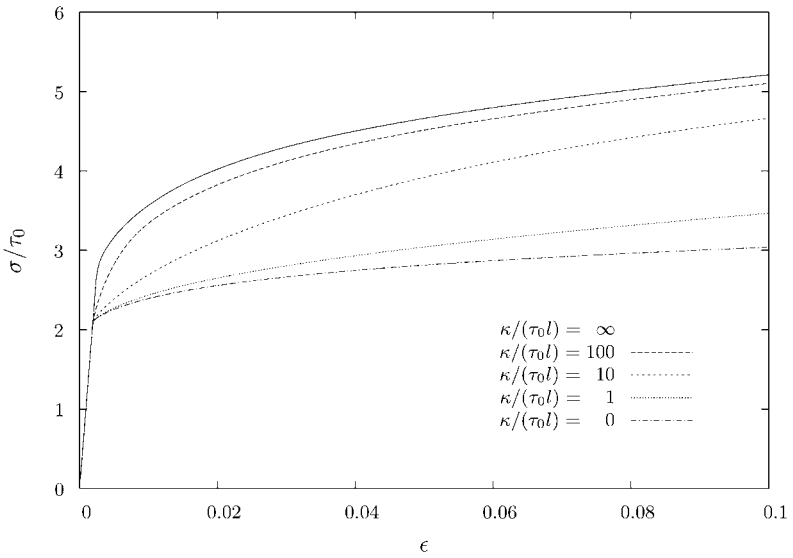

Fig. 11. Stress strain curves for different grain boundary surface energy parameters for a polycrystal with random grain orientations and grain size $d/l = 5$.

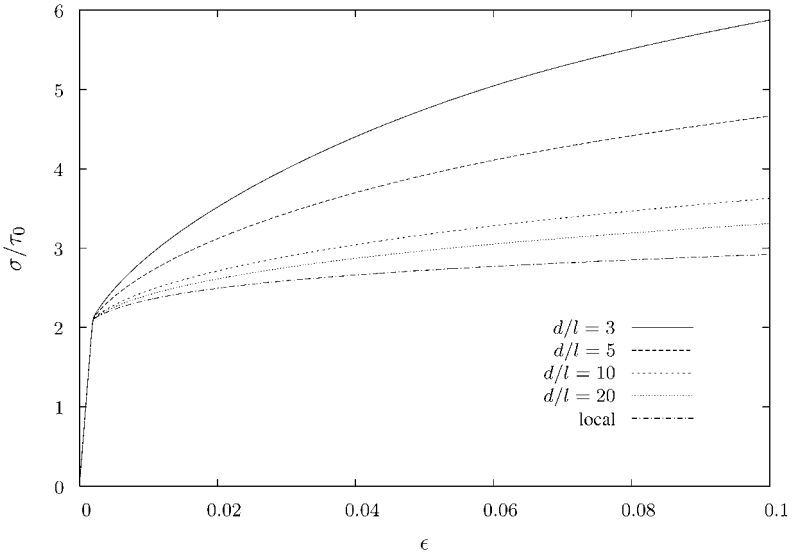

Fig. 12. Stress strain curves for different grain sizes and randomized grain orientations. The grain boundary surface energy parameter is set to $\kappa/(\tau_0 l) = 10$.

5. Conclusion

In this study, the flow stress dependence on the grain size under plane strain uniaxial tension has been analyzed using a strain gradient crystal plasticity theory. A penalty to dislocation pile up on each side of grain boundaries has been used in the form of a grain boundary energy potential. The grain boundary energy parameter, κ, has been varied from $\kappa = 0$, simulating a grain boundary with vanishing higher order stresses, up to $\kappa \to \infty$, simulating a grain boundary impenetrable to dislocations.

The analyzed polycrystal consists of 40 grains, and results are presented both for the same slip system orientation in all grains and for a random slip system orientation. In the case with the same slip system orientation in all grains, there is only a grain size effect for $\kappa \neq 0$. In the case with the random slip system orientation, there is a grain size

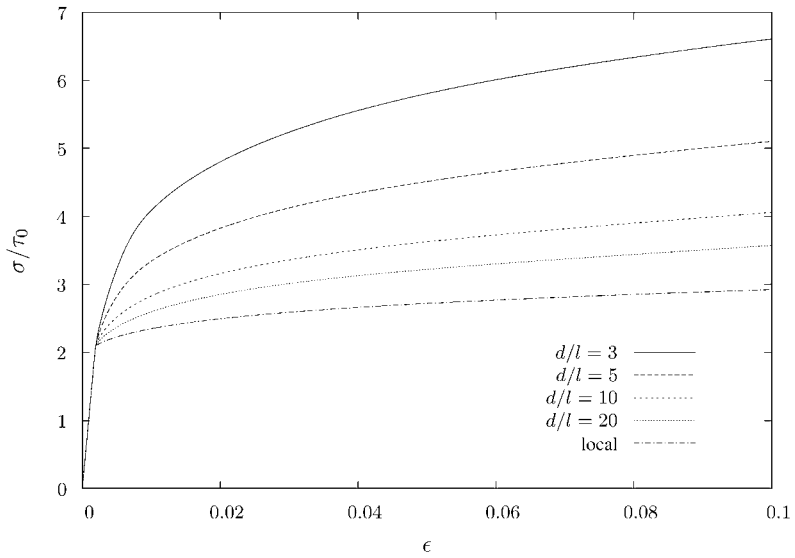

Fig. 13. Stress strain curves for different grain sizes and randomized grain orientations. The grain boundary surface energy parameter is set to $\kappa/(\tau_0 l) = 100$.

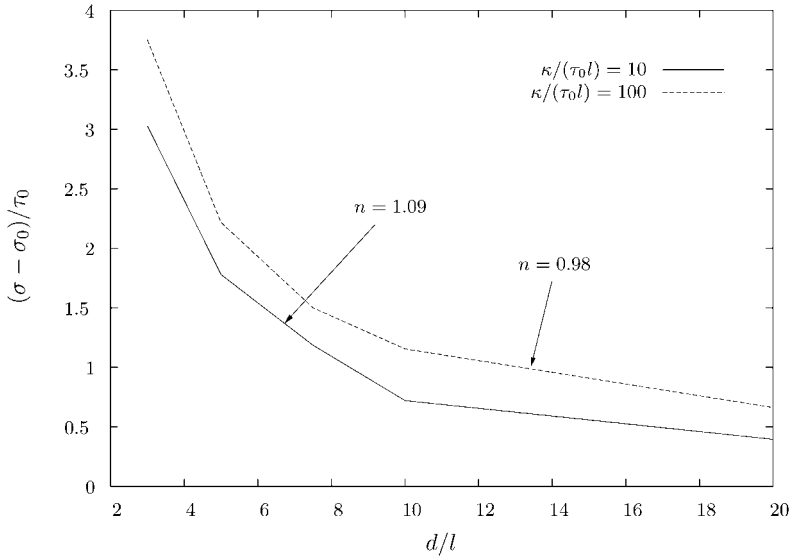

Fig. 14. The increase in flow stress vs. grain size after 0.1 logarithmic strain for two different grain boundary surface energies.

effect for all values of κ. The reason for this is the slip gradients caused by different crystallographic orientation of neighboring grains. The grain size effect due to the random orientation of the grains is small compared to the effect of restricting the grain boundaries to be impenetrable to dislocations. Contours of accumulated slip shows that the largest slips are found in the middle of the crystals, due to the obstruction of crystallographic slip at the grain boundaries. Furthermore, it is observed that the slip gradients are reduced when the specimen size is decreased.

The increase in flow stress as a function of the grain size was fitted to a function in the form of d^{-n} for different grain boundary energy parameters. Exponents, n, in the range 0.82 to 1.25 at initial yield and in the range 0.77 to 1.09 after 0.1 logarithmic strain was observed. These values are somewhat higher than what is predicted from the classical Hall–Petch relationship with exponent $n = 0.5$. In the study of Evers et al. (2004) using a scale dependent model to predict grain size effects in a polycrystal under plane stress loading conditions, they found a Hall–Petch exponent in the range 1.19 to 1.50. Biner and Morris (2002) and Balint et al. (2005) used discrete dislocation plasticity models

to analyze the dependence of shear yield strength on grain size, and observed Hall–Petch exponents in the range 0.4 to 1.0.

Acknowledgements

The author wishes to thank Viggo Tvergaard and Christian F. Niordson for many valuable discussions. This work is financially supported by the Danish Technical Research Council in a project entitled Modeling Plasticity at the Micron Scale.

References

Acharya, A., Beaudoin, A., 2000. Grain-size effect in viscoplastic polycrystals at moderate strains. J. Mech. Phys. Solids 48, 2213–2230.
Aifantis, K., Willis, J., 2005. The role of interfaces in enhancing the yield strength of composites and polycrystals. J. Mech. Phys. Solids 53, 1047–1070.
Armstrong, R., Codd, I., Douthwaite, R., Petch, N., 1962. Plastic deformation of polycrystalline aggregates. Phil. Mag. 7, 45–58.
Ashby, M.F., 1970. The deformation of plastically non-homogeneous alloys. Phil. Mag. 21, 399–424.
Balint, D., Deshpande, V., Needleman, A., Van der Giessen, E., 2005. A discrete dislocation plasticity analysis of grain-size strengthening. Mater. Sci. Eng. A 400–401, 186–190.
Biner, S., Morris, J., 2002. A two-dimensional discrete dislocation simulation of the effect of grain size on strengthening behaviour. Model. Simul. Mater. Sci. Eng. 10, 617–635.
Borg, U., 2006. Strain gradient crystal plasticity effects on flow localization, in press.
Borg, U., Fleck, N., 2006. Strain gradient effects in surface roughening, Model. Simul. Mater. Sci. Eng., in press.
Evers, L., Brekelmans, W., Geers, M., 2004. Scale dependent crystal plasticity framework with dislocation density and grain boundary effects. Int. J. Solids Struct. 41, 5209–5230.
Fleck, N.A., Hutchinson, J.W., 2001. A reformulation of strain gradient plasticity. J. Mech. Phys. Solids 49, 2245–2271.
Gudmundson, P., 2004. A unified treatment of strain gradient plasticity. J. Mech. Phys. Solids 52, 1379–1406.
Gurtin, M.E., 2002. A gradient theory of single-crystal viscoplasticity that accounts for geometrically necessary dislocations. J. Mech. Phys. Solids 50, 5–32.
Hall, E., 1951. The deformation and aging of mild steel: iii. Discussion of results. Proc. Phys. Soc. Lond. B 64, 747–753.
Han, C.-S., Gao, H., Huang, Y., Nix, W.D., 2005. Mechanism-based strain gradient crystal plasticity – I. Theory. J. Mech. Phys. Solids 53, 1188–1203.
Kuroda, M., Tvergaard, V., 2006. Studies of scale dependent crystal viscoplasticity models. J. Mech. Phys. Solids 54, 1789–1810.
Peirce, D., Asaro, R.J., Needleman, A., 1983. Material rate dependence and localized deformation in crystalline solids. Acta Metall. 31, 1951–1976.
Petch, N., 1953. The cleavage strength of polycrystals. J. Iron Steel Inst. 174, 25–28.
Shu, J.Y., Fleck, N.A., 1999. Strain gradient crystal plasticity: size-dependent deformation of bicrystals. J. Mech. Phys. Solids 47, 297–324.
Tvergaard, V., 1976. Effect of thickness inhomogeneities in internally pressurized elastic-plastic spherical shells. J. Mech. Phys. Solids 24, 291–304.

P5

Strain gradient crystal plasticity analysis of a single crystal containing a cylindrical void

To be published in
International Journal of Solids and Structures

Strain gradient crystal plasticity analysis of a single crystal containing a cylindrical void

Ulrik Borg [a,*] and Jeffrey W. Kysar [b]

[a] *Department of Mechanical Engineering, Solid Mechanics, Technical University of Denmark, Kgs. Lyngby, DK-2800, Denmark*

[b] *Department of Mechanical Engineering, Fu Foundation School of Engineering and Applied Science, Columbia University, 500 West 120th Street, New York, NY 10027, USA*

Abstract

The effects of void size and hardening in a hexagonal close-packed single crystal containing a cylindrical void loaded by a far-field equibiaxial tensile stress under plane strain conditions are studied. The crystal has three in-plane slip systems oriented at the angle 60° with respect to one another. Finite element simulations are performed using a strain gradient crystal plasticity formulation with an intrinsic length scale parameter in a non-local strain gradient constitutive framework. For a vanishing length scale parameter the non-local formulation reduces to a local crystal plasticity formulation. The stress and deformation fields obtained with a local non-hardening constitutive formulation are compared to those obtained from a local hardening formulation and to those from a non-local formulation. Compared to the case of the non-hardening local constitutive formulation, it is shown that a local theory with hardening has only minor effects on the deformation field around the void, whereas a significant difference is obtained with the non-local constitutive relation. Finally, it is shown that the applied stress state required to activate plastic deformation at the void is up to three times higher for smaller void sizes than for larger void sizes in the non-local material.

Key words: Void, Strain gradient plasticity, Single crystal

* Corresponding author. Tel.:+45 4525 4262; fax: +45 4593 1475.
Email address: ub@mek.dtu.dk (Ulrik Borg).

1 Introduction

It is well accepted that crack growth in many ductile materials occurs by the mechanisms of void nucleation, growth and coalescence. Voids typically nucleate from second phase particles which exist within the material. The sizes of the voids are often of the order of one micrometer. Elastic-plastic continuum analyses to model the subsequent growth of the voids have traditionally employed isotropic material properties (see e.g. Koplik and Needleman (1988) and Tvergaard (1990)). However since the size of the voids is often smaller than the grain size in a polycrystalline material, it is more appropriate to assume anisotropic elastic-plastic properties.

There are two regimes in which plasticity around a void in an anisotropic single crystal have been studied analytically. The first is for voids that are sufficiently small so that the continuum plasticity approximation is not valid. Several authors (e.g. Stevens et al., 1972; Lubarda et al., 2004; Ahn et al., 2006) have considered the interaction between voids and individual dislocation loops for cylindrical voids as well as spherical voids. The focus of these studies was to calculate the applied stress state at which discrete dislocation loops are nucleated from the void, which leads to void growth.

The other regime is for void sizes for which the continuum approximation is valid. Recent studies (Kysar et al., 2005; Gan and Kysar, 2007) have used continuum anisotropic slip line theory to derive the stress and deformation fields associated with a cylindrical void in a single face centered cubic crystal as well as a hexagonal close packed crystal, along with related experimental and numerical studies by Gan et al. (2006). The constitutive properties considered for the analytical studies are rigid, ideally plastic. The studies have shown that there are angular regions around such voids within which slip on single slip systems occurs. The stress states were also derived and it was shown that the average pressure necessary to activate plastic deformation around a void in a face centered cubic crystal can be up to 50% higher than that for an isotropic material, although for a hexagonal close packed material the average pressure necessary to activate plastic deformation around the void is approximately the same as for isotropic plastic materials. These analyses are applicable for voids which are significantly larger than the voids treated by discrete dislocation plasticity.

The emphasis of the present study is to extend the anisotropic slip line studies, which assume ideal plasticity, to material constitutive models which account for hardening of plastic slip systems and void size effects. Two different material models will be considered. The first includes strain hardening which is typically associated with the creation and accumulation of so-called statistically-stored dislocations. This type of strain hardening is implemented in a local

constitutive formulation which has no intrinsic length scale. The other material model includes strain gradient effects which are typically associated with the segregation of so-called geometrically necessary dislocations. This type of material model is implemented in a non-local constitutive formulation–or strain gradient plasticity formulation–which has an intrinsic length scale. Simulations are performed with both types of material models and the resulting stress and deformation fields are compared to each other as well as to the analytical solution for plastic deformation around voids.

The formulation of the continuum single crystal plasticity theory with no intrinsic length scale is similar to that employed by Peirce et al. (1983). The strain gradient formulation employed in this study is as presented by Borg (2007). The basic formulation is equivalent to that of Gurtin (2002) and the constitutive equations are based on the theory by Fleck and Hutchinson (2001). A representative material length scale of about $5\mu m$ has been estimated by Fleck et al. (1994) from fitting experimental data on a copper wire torsion test to strain gradient plasticity theory results. Also, Fredriksson and Gudmundson (2005) have compared results by a strain gradient plasticity theory with experimental results, which have given estimates of the material length scale ranging from $0.45\mu m$ to $2.7\mu m$. These estimates are performed with strain gradient formulations different from the one used in the present study, however the present length scale is also expected to be on that order. Furthermore, recent work which compares simulations which utilize strain gradient crystal plasticity theory employed in the present study to discrete dislocation plasticity simulations suggests the material length scale to be approximately $0.33\mu m$ (Hussein et al., 2006).

For the local case there is no length scale so the size of the void does not enter into consideration. However for the non-local case the size of the void must be specified. The two void sizes to be considered have radii $r_0/l = 10$ and $r_0/l = 1$, where r_0 and l are the initial radius and the length scale of the constitutive relationship, respectively.

The effect of hardening behaviors within the framework of a non-local constitutive model and also the framework of a local constitutive model are investigated separately. It will be shown that the addition of hardening to the local model mainly reduces the amount of slip which occurs near a void; the extent and boundaries of the single slip angular sectors are not affected. The non-local formulation, on the other hand, introduces a significant change in the extent and boundaries of the single slip sectors. In fact, the sector structure changes significantly so that regions of double slip develop. It is also shown that the critical stress to activate plastic deformation around the void is up to three times higher for the smaller void size than for the larger void size, at least for the non-local constitutive formulation chosen for this study.

This paper is organized as follows. Section 2 discusses the material model used in this study. This will be followed by a discussion of the numerical implementation of the material model in Section 3. The results of the simulations are presented in Section 4. Concluding discussions are in Section 5.

2 Material model

The material model used for this study is a strain gradient crystal plasticity theory for finite strains proposed by Borg (2007). The theory is based on the constitutive framework of the isotropic strain gradient plasticity theory by Fleck and Hutchinson (2001) including ideas from the finite strain version by Niordson and Redanz (2004), and with the basic formulation equivalent to the formulation of Gurtin (2002). In the absence of strain gradients the model reduces to conventional crystal plasticity theory by e.g. Peirce et al. (1983). For simplicity, the following summary of the model is only valid for small strains, even though a formulation that allows for finite strains has been used for the analyses.

In crystal plasticity the quantitative description of plastic deformation is based on crystallographic shearing that represents dislocation motion along specific slip systems. A slip system is described by its unit lattice vectors $s_i^{(\alpha)}$ and $m_i^{(\alpha)}$, where $s_i^{(\alpha)}$ is the slip direction and $m_i^{(\alpha)}$ is the direction normal to the slip plane. By use of the classical Schmid orientation tensor

$$\mu_{ij}^{(\alpha)} = \frac{1}{2}(s_i^{(\alpha)} m_j^{(\alpha)} + s_j^{(\alpha)} m_i^{(\alpha)}) \tag{1}$$

the overall macroscopic plastic strain rate components can be expressed by the slip $\gamma^{(\alpha)}$ along slip system (α) as

$$\dot{\epsilon}_{ij}^{p} = \sum_{\alpha} \dot{\gamma}^{(\alpha)} \mu_{ij}^{(\alpha)} \tag{2}$$

To account for the effect of increased material hardening due to the presence of geometrically necessary dislocations caused by plastic strain gradients, the plastic dissipation rate does not only depend on slip rates but also on slip rate gradients. Following Fleck et al. (1994), the slip gradient in the slip direction is related to geometrically necessary edge dislocations, and a slip gradient in the transverse direction is related to geometrically necessary screw dislocations. Based on this, an effective slip measure, $\gamma_e^{(\alpha)}$, depending on the slip and the slip gradients is introduced as

$$\dot{\gamma}_e^{(\alpha)^2} = \dot{\gamma}^{(\alpha)^2} + \left(l_S \dot{\gamma}_{,i}^{(\alpha)} s_i^{(\alpha)}\right)^2 + \left(l_T \dot{\gamma}_{,i}^{(\alpha)} t_i^{(\alpha)}\right)^2 \tag{3}$$

where $t_i^{(\alpha)}$ is a unit vector in the transverse direction (with $\boldsymbol{t}^{(\alpha)} = \boldsymbol{s}^{(\alpha)} \times \boldsymbol{m}^{(\alpha)}$) and l_S and l_T are material length scales introduced for dimensional consistency. Here, $(\,)_{,i} = \partial/\partial x_i$ is the spatial derivative. The principle of virtual power takes the form

$$\int_V \left(\sigma_{ij}\delta\dot{\epsilon}_{ij} + \sum_\alpha \left(Q^{(\alpha)} - \tau^{(\alpha)} \right) \delta\dot{\gamma}^{(\alpha)} + \sum_\alpha \left(\xi_S^{(\alpha)} s_i^{(\alpha)} + \xi_T^{(\alpha)} t_i^{(\alpha)} \right) \delta\dot{\gamma}_{,i}^{(\alpha)} \right) dV = \int_S \left(T_i \delta\dot{u}_i + \sum_\alpha r^{(\alpha)} \delta\dot{\gamma}^{(\alpha)} \right) dS \tag{4}$$

where $Q^{(\alpha)}$ is a stress field work conjugate to the slip rate, and the higher order stresses $\xi_S^{(\alpha)}$ and $\xi_T^{(\alpha)}$ are work conjugate to the slip rate gradients along the slip direction and the transverse direction, respectively. T_i is the stress traction and $r^{(\alpha)}$ denotes the higher order traction working on the boundary S. The Cauchy stress is denoted σ_{ij} and $\tau^{(\alpha)} = \sigma_{ij}\mu_{ij}^{(\alpha)}$ is the Schmid stress. The virtual power relation (4) is a special case of the virtual power relation in Gurtin (2002).

By use of an effective stress, denoted $\tau_e^{(\alpha)}$, which is work-conjugate to the effective slip rate measure, $\dot{\gamma}_e^{(\alpha)}$, constitutive equations are obtained for the effective stress $Q^{(\alpha)}$ and the higher order stresses $\xi_S^{(\alpha)}$ and $\xi_T^{(\alpha)}$ as

$$Q^{(\alpha)} = \tau_e^{(\alpha)} \frac{\dot{\gamma}^{(\alpha)}}{\dot{\gamma}_e^{(\alpha)}} \tag{5}$$

$$\xi_S^{(\alpha)} = \tau_e^{(\alpha)} \frac{\dot{\gamma}_{,i}^{(\alpha)} s_i^{(\alpha)}}{\dot{\gamma}_e^{(\alpha)}} l_S^2, \quad \xi_T^{(\alpha)} = \tau_e^{(\alpha)} \frac{\dot{\gamma}_{,i}^{(\alpha)} t_i^{(\alpha)}}{\dot{\gamma}_e^{(\alpha)}} l_T^2 \tag{6}$$

Then, the introduced stress $\tau_e^{(\alpha)}$ can be expressed in the following quadratic form

$$\tau_e^{(\alpha)^2} = Q^{(\alpha)^2} + l_S^{-2} \xi_S^{(\alpha)^2} + l_T^{-2} \xi_T^{(\alpha)^2} \tag{7}$$

The viscous material behavior is modeled by use of a power-law creep model formulated as

$$\dot{\gamma}_e^{(\alpha)} = \dot{\gamma}_0 \left(\frac{\tau_e^{(\alpha)}}{g^{(\alpha)}} \right)^{1/m} \tag{8}$$

where $\dot{\gamma}_0$ is a reference slip rate and m is a strain rate hardening index. The slip resistances $g^{(\alpha)}$ characterize the current strain hardened state of the crystal, and harden from an initial value τ_0 according to

$$\dot{g}^{(\alpha)} = \sum_\beta h_{\alpha\beta} \dot{\gamma}_e^{(\beta)}, \quad h_{\alpha\beta} = h\delta_{\alpha\beta} + ph\left(1 - \delta_{\alpha\beta}\right) \tag{9}$$

Here, p is the latent hardening index, $\delta_{\alpha\beta}$ denotes the Kronecker delta function, and h is the self-hardening modulus given empirically by

$$h(\gamma_a) = h_0 / \cosh\left(\frac{h_0 \gamma_a}{\tau_s - \tau_0}\right), \quad \gamma_a = \sum_\alpha \int \dot{\gamma}_e^{(\alpha)} \mathrm{d}t \tag{10}$$

where the constant h_0 represents an initial hardening rate, τ_s is a saturation stress, and γ_a is the accumulated effective slip.

3 Numerical method

The numerical solutions are obtained using the finite element method. The slip rate increments are taken as nodal degrees of freedom on an equal footing with the displacement increments. These primary unknowns are interpolated within each element between nodal increments as

$$\Delta u_i = \sum_{N=1}^{2k} N_i^N \Delta D^N, \qquad \Delta \dot{\gamma}^{(\alpha)} = \sum_{N=1}^{l} M^N \Delta \dot{\gamma}_N^{(\alpha)} \tag{11}$$

where N_i^N and M^N are shape functions and k and l are the number of nodes used for the interpolations. For this plane strain study, the elements used for the displacements are 8-node quadrilaterals with quadratic shape functions, and the elements used for interpolation of the slip rate increments are 4-node quadrilaterals with linear shape functions, i.e. $k = 8$ and $l = 4$. The integrations are carried out using 2×2 point Gaussian integration for both element types. To ensure the integration points for the two element types to coincide, the same Jacobian is used for both element types.

The specimen considered in this study is shown in Figure 1. It is a square ($a_0 = b_0$) single hexagonal close packed crystal containing a cylindrical void in the center with a diameter of one tenth of the side length ($r_0 = 0.1a_0$). The axis of the cylindrical void is chosen to be parallel to the basal plane normal [0001] as in Gan and Kysar (2007). The three active slip systems, each oriented at the angle 60° with respect to the others, are also shown in Figure 1.

For a local material it is possible to consider only a quarter of the crystal due to symmetry, whereas for the nonlocal material the higher order boundary conditions make such an approach difficult. In this study the full crystal is considered for all analyses. The boundary conditions applied to the single

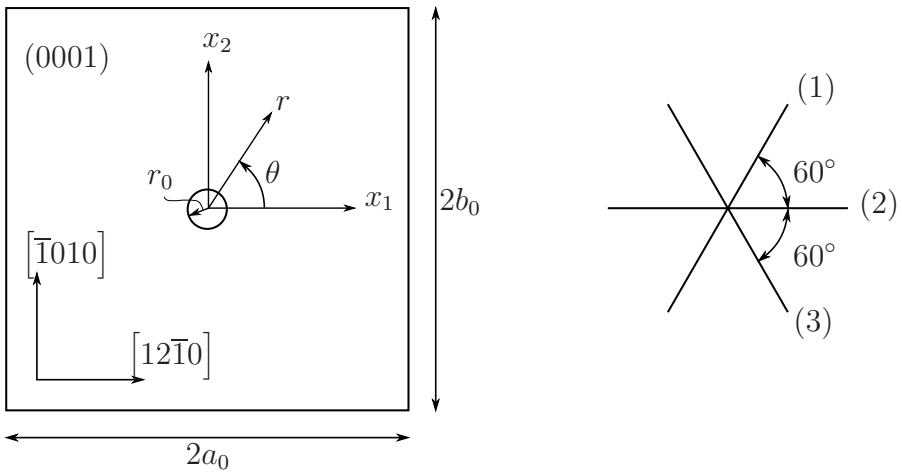

Fig. 1. Cylindrical void in an HCP single crystal showing coordinate systems, dimensions, slip systems and crystallographic orientation.

crystal are given by

$$\begin{aligned} &\dot{u}_1 = 0, \quad \dot{T}_2 = 0 \text{ at } x_1 = -a_0 \\ &\dot{u}_1 = \dot{U}_1, \, \dot{T}_2 = 0 \text{ at } x_1 = a_0 \\ &\dot{u}_2 = 0, \quad \dot{T}_1 = 0 \text{ at } x_2 = -b_0 \\ &\dot{u}_2 = \dot{U}_2, \, \dot{T}_1 = 0 \text{ at } x_2 = b_0 \end{aligned} \tag{12}$$

where $\dot{T}_i$ are surface traction rates and $\dot{U}_i$ are the prescribed end displacement rates. Furthermore, the higher order boundary conditions are applied as vanishing higher order tractions, $r^{(\alpha)} = 0$, on the four external edges and on the void surface. Another possibility for the higher order boundary conditions is to let the slips vanish, i.e. letting the boundaries be impenetrable to dislocations. That would be appropriate at a stiff inclusion but not for a void. The mesh used for the presented results consists of 16224 elements and is finest at the void surface with 312 elements around the void.

For the plane strain problem considered, with in-plane slip systems, there are no slip gradients in the transverse direction, and therefore the length scale parameter, l_T, has no influence on the results. The other length scale parameter, l_S, is denoted l in the following.

4 Results

The material parameters used in the calculations are Young's modulus, $E = 63.9$ GPa, Poisson's ratio, $\nu = 0.36$, initial slip resistance, $\tau_0 = 1$ MPa, reference slip rate, $\dot{\gamma}_0 = 0.001$ s^{-1}, and strain rate hardening index, $m = 0.03$. Re-

sults using the local constitutive formulation are presented both with and without strain hardening. For the results with hardening the following hardening parameters are used: self-hardening modulus, $h_0 = E/100$, saturation stress, $\tau_s = 1.8\tau_0$, and latent hardening index, $p = 1.0$. All the presented results using the non-local formulation are without strain hardening, i.e. $h_0 = 0$. The prescribed end displacement rates are given by $\dot{U}_1/(2a_0) = \dot{U}_2/(2a_0) = 0.0001\ \mathrm{s}^{-1}$. The results presented in this section are taken at the deformation state given by $U_1/(2a_0) = U_2/(2a_0) = 3.5 \times 10^{-5}$.

Contours of slip in the three slip systems and the total slip, $\gamma_{tot} = \gamma^{(1)} + \gamma^{(2)} + \gamma^{(3)}$, are shown in Figure 2 for a non-hardening local material, i.e. using the internal material length scale $l = 0$ and the hardening modulus $h_0 = 0$. It is seen that the slip contours are periodic with a period of 90°. Slip system one is mostly active in the region $0 \leq \theta \leq 30°$, slip system two is mostly active in the region $30° \leq \theta \leq 60°$, and slip system three is mostly active in the region $60° \leq \theta \leq 90°$ of the upper right quadrant. The location of angular sectors with only one effective slip system is as predicted by anisotropic slip line theory in Gan and Kysar (2007), where they are denoted as *slip sectors*.

The slip contours using a local formulation with hardening are shown in Figure 3. The slip sectors are very similar to the results for the non-hardening material, except that the magnitudes of the accumulated slips are less than for the non-hardening case.

Figure 4 shows the slip in the three slip systems and the total slip, $\gamma_{tot} = \gamma^{(1)} + \gamma^{(2)} + \gamma^{(3)}$, plotted along the path $r/r_0 = 1.0$ for a non-hardening local material. It can be seen that the boundaries between two active slip sectors around $\theta = 0°$, 30°, 60° etc. are very thin. Within each slip sector the level of slip is almost constant along the void surface. The analogous plot is shown in Figure 5 for a hardening local material. Here, the slip sector boundaries are also very thin as for the non-hardening local material.

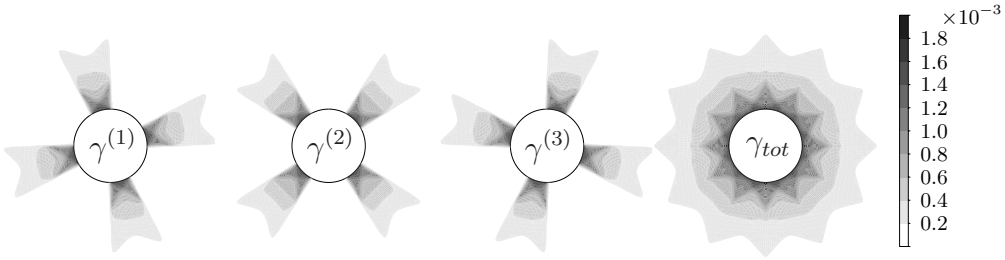

Fig. 2. Contours of slip in the three slip systems using a local formulation without hardening ($l = 0$, $h_0 = 0$).

Stress contours expressed in polar coordinates (σ_{rr}, $\sigma_{\theta\theta}$ and $\sigma_{r\theta}$) are shown in Figure 6 for the non-hardening local material. The left column shows contours over the entire specimen, and the right column shows contours in the vicinity of the void. The results are very similar to those obtained by Gan

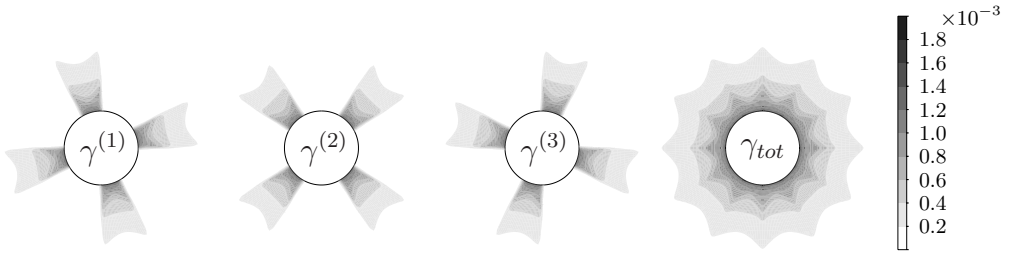

Fig. 3. Contours of slip in the three slip systems using a local formulation with hardening ($l = 0$, $h_0 = E/100$).

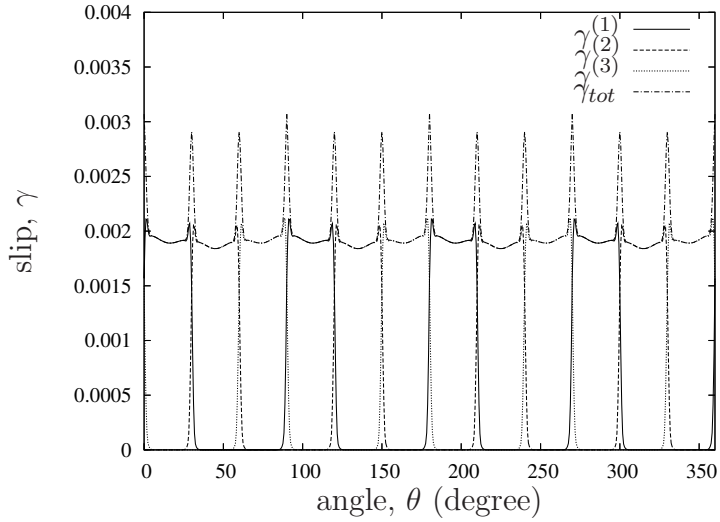

Fig. 4. Slip along the path $r/r_0 = 1.0$ using a local formulation without hardening.

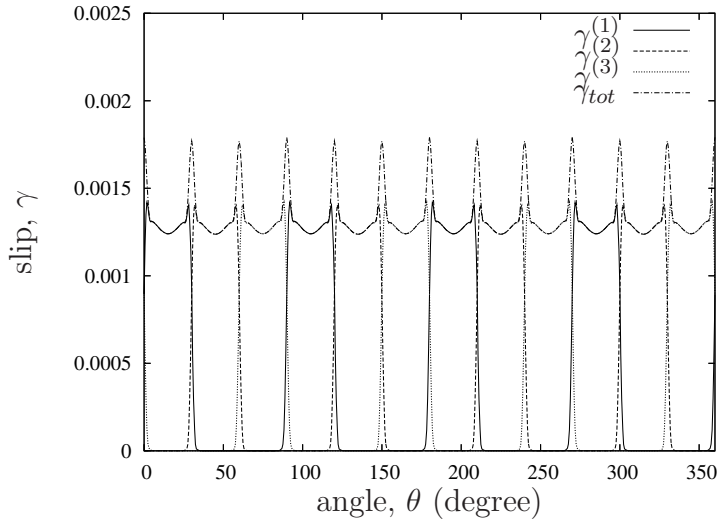

Fig. 5. Slip along the path $r/r_0 = 1.0$ using a local formulation with hardening.

and Kysar (2007) using anisotropic slip line theory for a rigid-ideally plastic crystal. However, here we have edge effects and purely elastic deformations far from the void, so the results are only directly comparable near the void. The radial stress, σ_{rr}, has a 12-point 'star' structure, whereas the circumfer-

ential stress, $\sigma_{\theta\theta}$, has a more smooth variation. The magnitude of the polar shear stress, $\sigma_{r\theta}$, is much smaller than the two other stress components and displays an interesting pattern with alternating positive and negative values. In addition, the anisotropic slip line theory solution predicts values of $\sigma_{r\theta}$ that are periodic with angle on logarithmic spirals which emanate from the void surface.

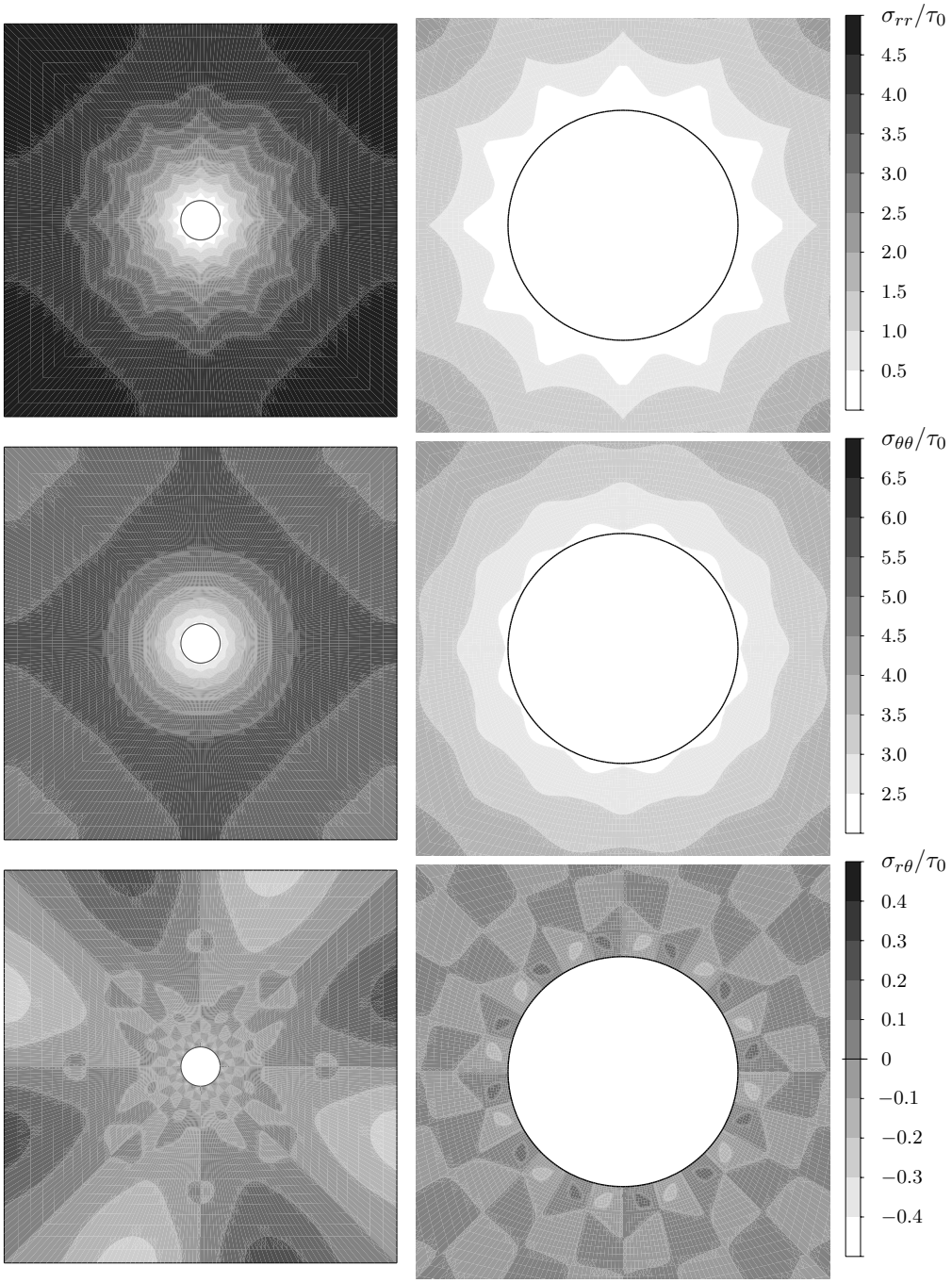

Fig. 6. Contours of stresses expressed in polar coordinates for a non-hardening local material.

Figure 7 shows the stress components expressed in Cartesian coordinates along the path $r/r_0 = 1.0$ for the non-hardening local material; they are periodic with a period of 180°. The shear stress is constant, $|\sigma_{12}/\tau_0| \approx 1.08$, within the slip sectors where slip system two is active. The slip line solution (Gan and Kysar, 2007) predicts $|\sigma_{12}/\tau_0| = 1.0$ in these slip sectors. This difference is mainly due to the viscoplastic effects in the present formulation which are not accounted for in the analytical slip line solution. In Figure 8 the stress components expressed in polar coordinates are plotted along the path $r/r_0 = 1.0$. As expected, the radial stress component, σ_{rr}, and the polar shear stress component, $\sigma_{r\theta}$, vanish at the void surface. The average circumferential stress, $\sigma_{\theta\theta}$, on the surface of the void predicted from simulation is close to $2.3\tau_0$, while the slip line solution predicts an average normalized circumferential stress of $6\ln(3)/\pi \approx 2.098$. The value of $\sigma_{\theta\theta}$ is periodic with a period of 30° which is also evident from the contour plots of $\sigma_{\theta\theta}$ in Figure 6. At the radius $r/r_0 = \sqrt{3}$ the slip line solution predicts $\sigma_{rr}/\tau = 2/\sqrt{3} \approx 1.155$ and $\sigma_{r\theta} = 0$. Also, the circumferential stress, $\sigma_{\theta\theta}$, is expected to vary in the same way as on the void surface. The stresses in polar coordinates from the simulation along the path $r/r_0 = \sqrt{3}$ are plotted for the non-hardening local material in Figure 9. The radial shear stress vanishes at all angles for that radius as predicted and the radial stress has the average value $\sigma_{rr}/\tau_0 \approx 1.17$.

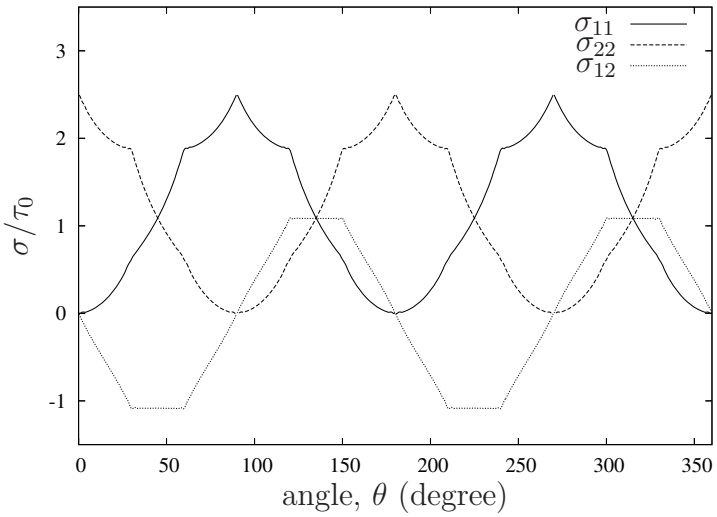

Fig. 7. Stress components in Cartesian coordinates along the path $r/r_0 = 1.0$ for a local material without hardening.

The slip contours shown in Figure 10 for a non-local material with void size relative to the material length scale $r_0/l = 10$ are somewhat different than the results for the local material shown in Figure 2. The magnitudes of the slips are approximately the same which indicates only a very small gradient contribution to the effective slip. The main difference though is that the slip contours are no longer symmetric about the radial center line in each slip sector. This result is not unexpected. Classical continuum single crystal plasticity theory for infinitesimal deformation gradients is invariant to an interchange

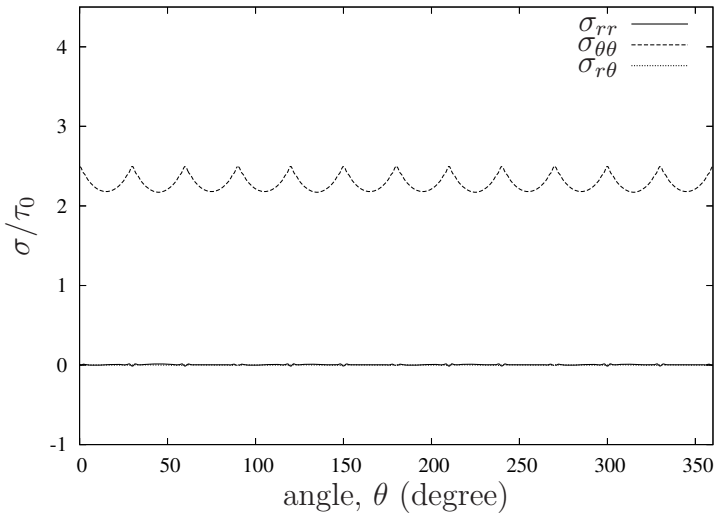

Fig. 8. Stress components in polar coordinates along the path $r/r_0 = 1.0$ for a local material without hardening.

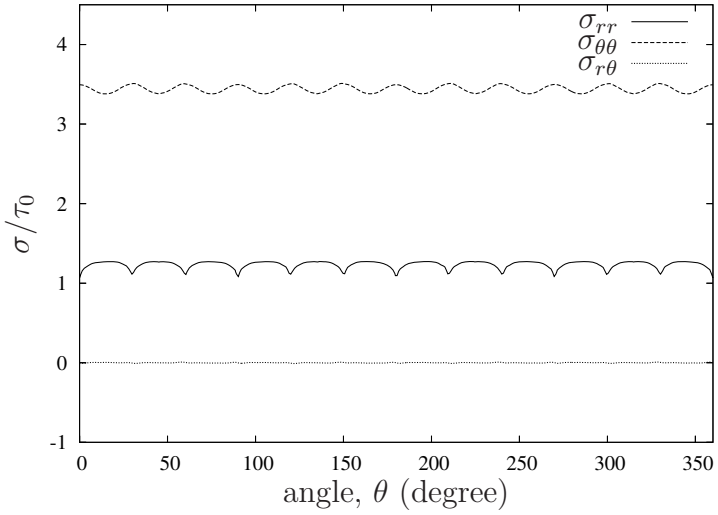

Fig. 9. Stress components in polar coordinates along the path $r/r_0 = \sqrt{3}$ for a local material without hardening.

of the unit lattice vectors $s_i^{(\alpha)}$ and $m_i^{(\alpha)}$. This can be seen in the definition of the Schmid tensor (1) and its subsequent use in the development of the infinitesimal theory in which lattice rotations are negligible. As a consequence of this invariance and the symmetry of the slip systems, the slip distribution about the radial center line of each slip sector is symmetric in spite of the fact that only one effective slip system is active in that region. (N.B. The simulations employ a finite deformation formulation, however the accumulated slips are sufficiently small so that the computed lattice rotation is negligible.) Introduction of the effective slip measure $\gamma_e^{(\alpha)}$ in (3) breaks this symmetry because the directions $s_i^{(\alpha)}$ and $m_i^{(\alpha)}$ are treated differently. Indeed it can be seen for the non-local hardening case in Figure 10 that the slip gradients in

the slip directions are smaller than the slip gradients in the directions normal to the slip planes which can be explained as a consequence of the differences in contributions of slip gradients in the slip directions and slip plane normal directions to the internal plastic work. The reduction of symmetry is also evident in that the slip contours for the non-local material are periodic with a period of 180°, whereas the slip contours in Figure 2 for the local material have a period of 90°.

The slip contours for a non-local material with a small void size—here taken to be $r_0/l = 1$ and shown in Figure 11—are very different from the results for the local material shown in Figure 2 and also from the non-local material with a larger void size, $r_0/l = 10$, in Figure 10. All slip occurs in localized bands in the slip directions, so the slip gradients in the slip directions are much smaller than the slip gradients in the directions normal to the slip planes. Again the symmetry is broken and it is notable that the magnitude of slip is significantly lower than for the other cases. The plastic slip is localized near the void surface, and as before the smallest magnitude of slip gradient is in the direction of slip rather than the transverse direction.

It is interesting to note that the plastic slip contours for the case of $r_0/l = 1$ bear a resemblance to the slip expected due to dislocation emission and motion from a cylindrical void by Lubarda et al. (2004) in an analytical study. In that work, the void is assumed to exist in an initially dislocation-free crystal so that any plastic deformation must be due to dislocations nucleated from the void surface. Similarly, for the high strain gradient case in the present study, the strain gradients lead to very rapid hardening response which would tend to "shut down" the active slip systems, allowing only those slip systems which can operate under relatively low gradients of slip to become active. It should be noted that there is an important difference between the analytical predictions of Lubarda et al. (2004) and the results herein. In the dislocation emission analyses, the presumed active dislocation is that with a slip direction which intersects the void surface with an angle of 45°, which is not the case in the present simulations.

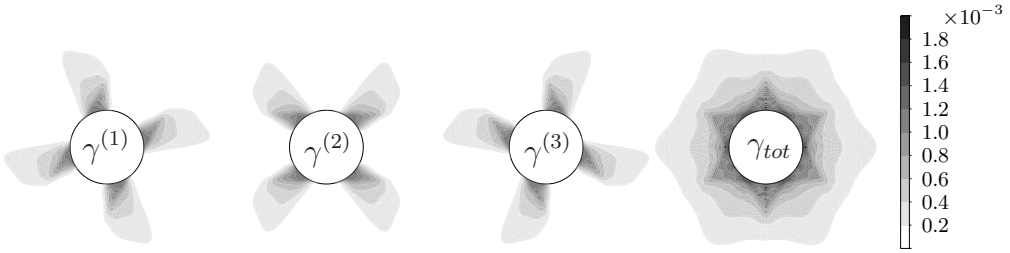

Fig. 10. Contours of slip in the three slip systems for a non-local material with $r_0/l = 10$.

Figure 12 shows slip sector boundaries (areas with double slip), defined as areas where the slip magnitudes in at least two slip systems are higher than

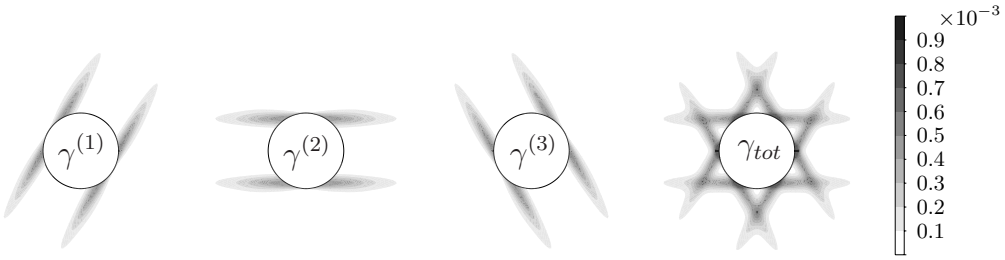

Fig. 11. Contours of slip in the three slip systems for a non-local material with $r_0/l = 1$.

10^{-4}. It can be seen that the slip sector boundaries are very similar for the hardening and the non-hardening local formulation. This is to be expected since the introduction of hardening in a local formulation does not break the invariance due to interchange of $s_i^{(\alpha)}$ and $m_i^{(\alpha)}$ of the kinematical structure and constitutive relations for the case of infinitesimal deformation gradients, which is effectively the case for the very modest magnitudes of strain encountered in these simulations. The reduced symmetry for the case of non-local formulation manifests itself in a broadened slip sector boundary for the void size $r_0/l = 10$. It is presumed that the enhanced local hardening associated with the region of double slip might serve to further modify the sector boundary structure around a void, an effect which is not modelled in the present simulation. Finally the significant change in slip behavior associated with the small void size case $r_0/l = 1$ is evident in Figure 12.

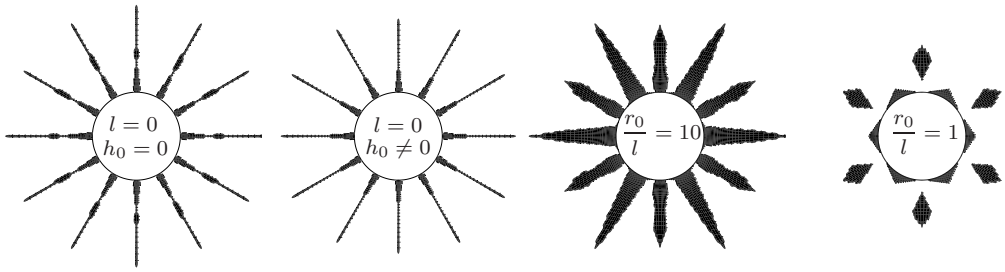

Fig. 12. Areas with double slip for the local formulation with and without hardening and for two void sizes using the non-local formulation.

The slips around the void surface are plotted in Figure 13 for the void size $r_0/l = 10$. The slip magnitudes are significantly lower than the slip magnitudes for the local material shown in Figure 4, and also the curves are smoother in the non-local case. Another significant difference is that the slip sector boundaries are much wider than for the local material (as shown in Figure 12), and there are even areas where all three slip systems are active; however, within these areas of triple slip the slip magnitude on one of the three slip systems is very small. Figure 14 shows the slips around the void surface for the void size $r_0/l = 1$. It can be seen that there are large variations in the total slip around the void surface; there are even material points which suffer almost no plastic deformation.

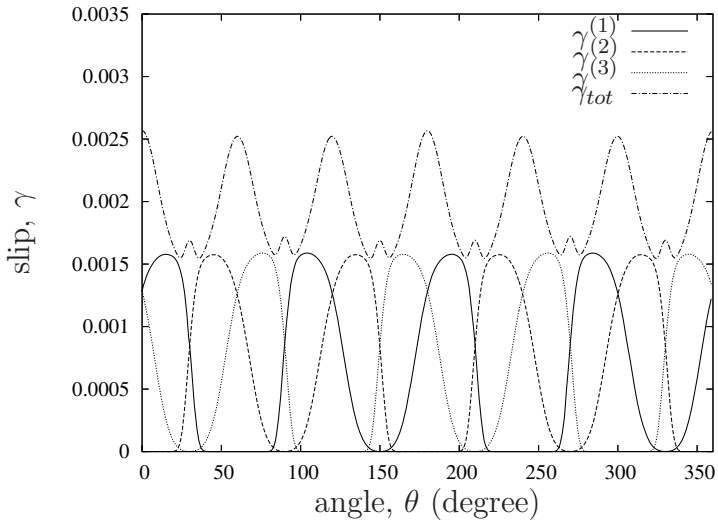

Fig. 13. Slip along the path $r/r_0 = 1.0$ for a non-local material with void size $r_0/l = 10$.

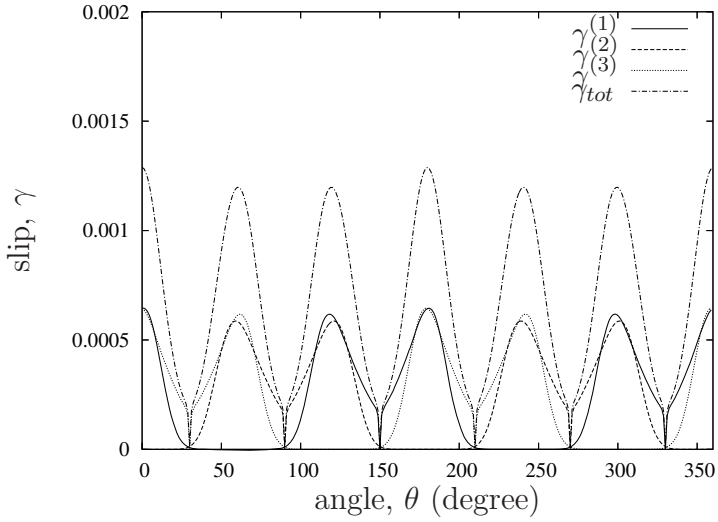

Fig. 14. Slip along the path $r/r_0 = 1.0$ for a non-local material with void size $r_0/l = 1$.

Contours of stresses expressed in polar coordinates for the non-local material with void size $r_0/l = 10$ are shown in Figure 15 and can be compared to those for the local material in Figure 6. The reduction in symmetry from 12-fold to 6-fold rotation is evident around the void. Two points stand out. One is that the magnitude of the stress components does not change dramatically from that of the local non-hardening case for the void size $r_0/l = 10$. In addition, as discussed above, the slip line solution predicts that $\sigma_{r\theta} = 0$ and $\sigma_{rr} = constant$ on $r/r_0 = \sqrt{3}$ so that the stress field exhibits self-similarity in the radial direction for a non-hardening local crystal. The contours of $\sigma_{r\theta}$ in Figure 15, though, demonstrate that the radial self-symmetry is lost in addition to a reduction of the rotational symmetry. The polar stress contours

are shown in Figure 16 for the small void sizes ($r_0/l = 1$). The stresses exhibit a 6-fold rotational symmetry and the magnitudes are larger.

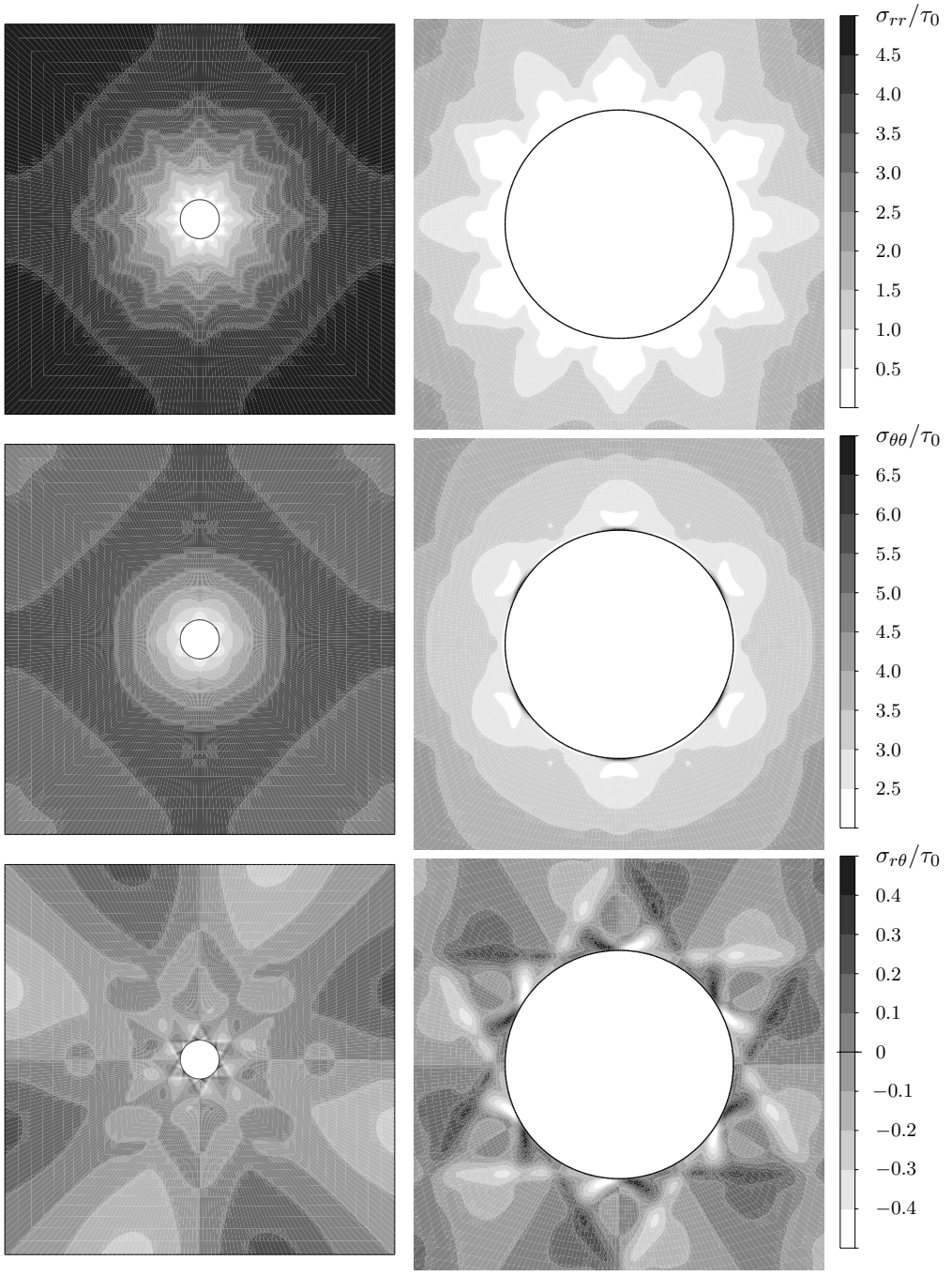

Fig. 15. Contours of stresses expressed in polar coordinates for a non-local material with void size $r_0/l = 10$.

The stresses expressed in Cartesian coordinates for the larger void size ($r_0/l = 10$) are shown in Figure 17 along the path given by $r/r_0 = 1.0$. It is seen that the shear stress, σ_{12}, is not constant in the sectors where slip system

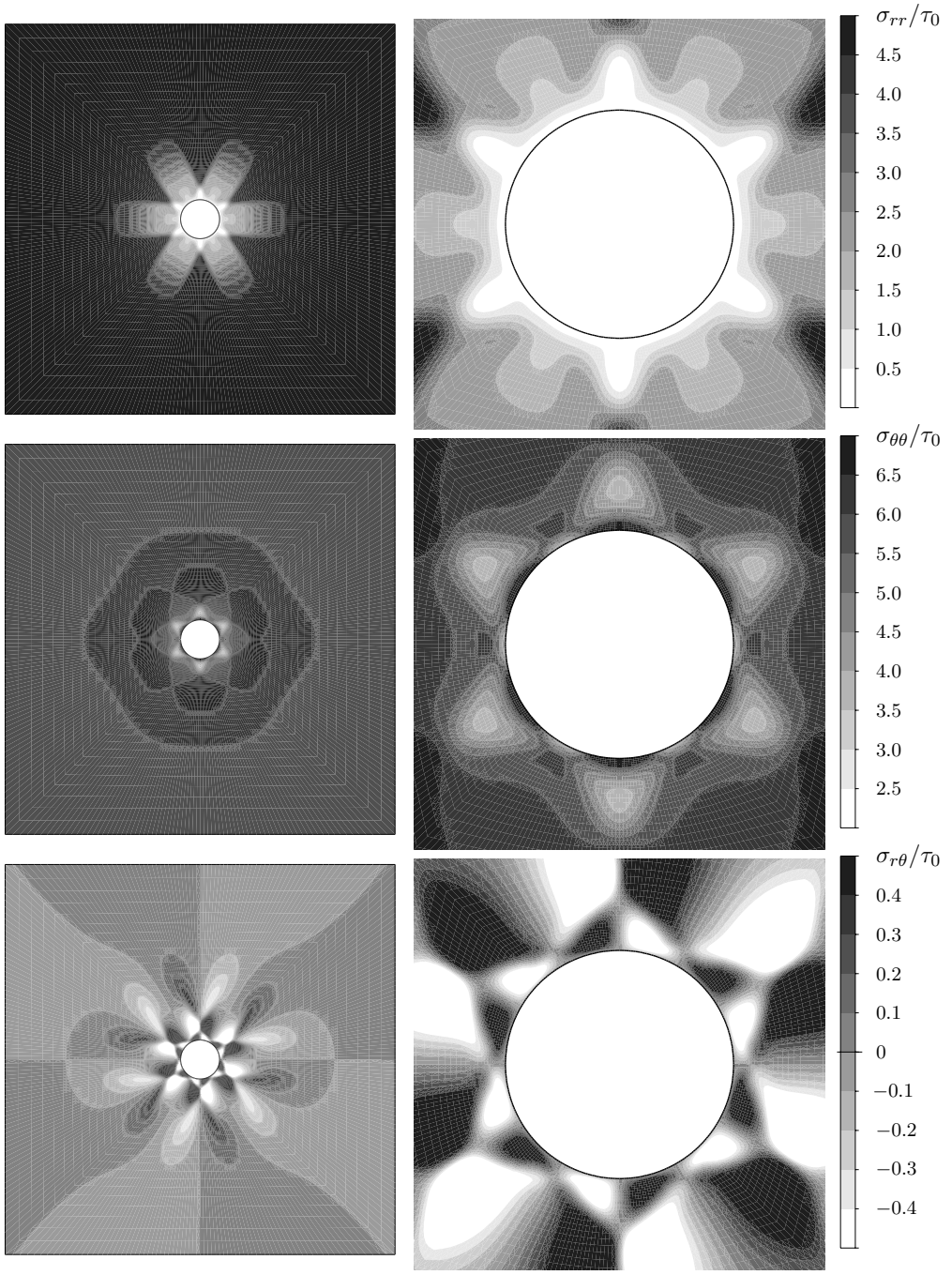

Fig. 16. Contours of stresses expressed in polar coordinates for a non-local material with void size $r_0/l = 1$.

two is active as it was the case for the local material. Figure 18 shows the stress components expressed in polar coordinates for the non-local case with $r_0/l = 10$ along the path given by $r/r_0 = 1.0$. The radial stress and the polar shear stress both vanish at the void surface. The circumferential stress, $\sigma_{\theta\theta}$, has its peaks near $\theta = 30°$, $90°$, $150°$, $210°$, $270°$ and $330°$. The stress level of the peaks is about $10\tau_0$, whereas the circumferential stress for the local

material varies between approximately $2.1\tau_0$ and $2.5\tau_0$. Thus even the larger void sizes ($r_0/l = 10$) can dramatically increase the necessary stress level on the void surface to effect plastic deformation. It is interesting to note that the regions of high $\sigma_{\theta\theta}$ do not extend very far radially from the void surface into the surrounding crystal, and that these regions are separated by regions which have a zero $\sigma_{\theta\theta}$ which implies that the material in these regions on the void surface are devoid of stress.

For the case of small voids ($r_0/l = 1$), the stresses exhibit a 6-fold rotational symmetry and the magnitudes are larger. The stresses on the void surface are shown in Figure 19. Again the radial stress and the shear stress vanish, whereas the circumferential stress varies between approximately $4\tau_0$ and $12\tau_0$. Thus, there are no material points around the void surface with zero stress as there were with the void size $r_0/l = 10$.

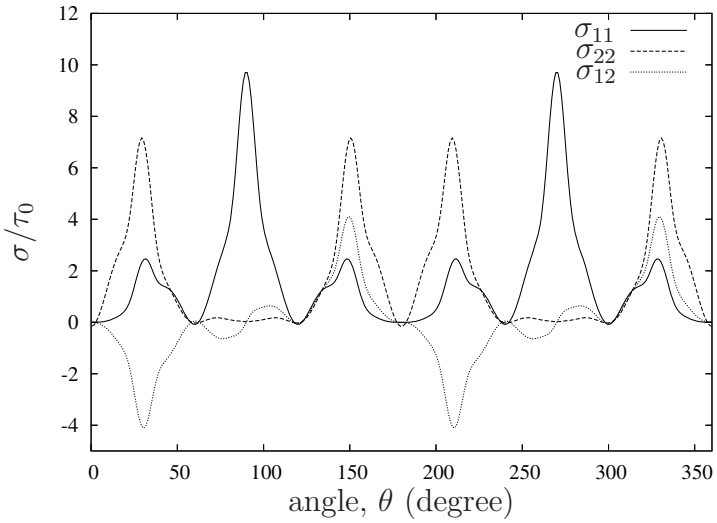

Fig. 17. Stress components in Cartesian coordinates along the path $r/r_0 = 1.0$ for a non-local material with $r_0/l = 10$.

Figure 20 shows the equibiaxial stress level, σ, at which plastic deformation initiates as a function of the void size. The initiation of plastic deformation is here defined as the far-field stress level where the effective shear stress, $\tau_e^{(\alpha)}$, exceeds the slip resistance, τ_0, in any part of the crystal. For a void in an elastic medium subjected to an equibiaxial tensile stress, σ, applied at a remote distance from the void, the analytical stress solution at the void surface predicts a circumferential stress $\sigma_{\theta\theta} = 2\sigma$ and vanishing radial and polar shear stresses. The resolved shear stress on a slip system is highest when the circumferential stress direction is 45° from the slip direction. In that case, the resolved shear stress, $\tau^{(\alpha)}$, equals half the circumferential stress ($\tau^{(\alpha)} = \sigma$). Thus, for a local material where $\tau_e^{(\alpha)} = \tau^{(\alpha)}$ purely elastic considerations predict that plastic deformation initiates at $\sigma/\tau_0 \approx 1$. Furthermore, the slip line solution predicts the average value of $\sigma_{\theta\theta}$ around the void surface at which

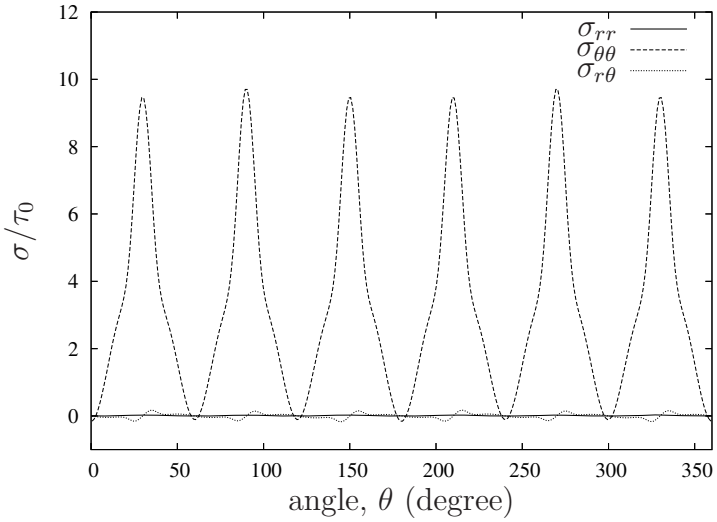

Fig. 18. Stress components in polar coordinates along the path $r/r_0 = 1.0$ for a non-local material with $r_0/l = 10$.

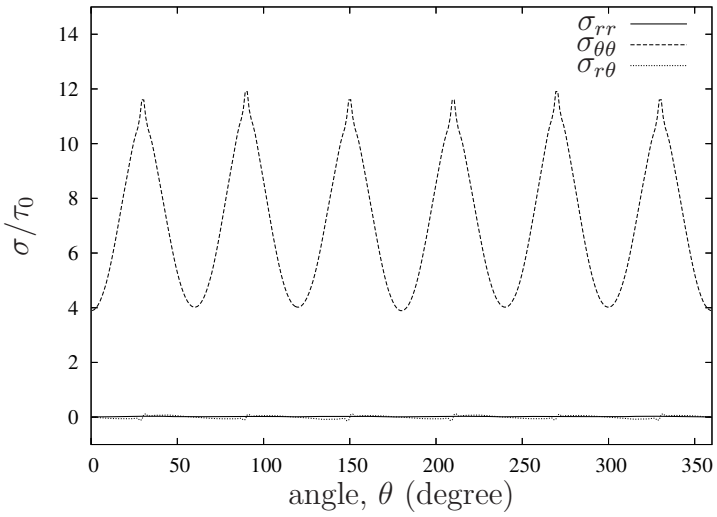

Fig. 19. Stress components in polar coordinates along the path $r/r_0 = 1.0$ for a non-local material with $r_0/l = 1$.

plastic deformation has initiated at all angles as $3\ln(3)\tau/\pi \approx 1.049\tau$. It is seen in Figure 20 that this is in fact the case for $l = 0$. When the void size is decreased relative to the material length scale, the stress level required to initiate plastic deformation is increased. For a void radius, r_0, equal to the internal material length scale, l, the required stress level has increased to approximately three times the slip resistance.

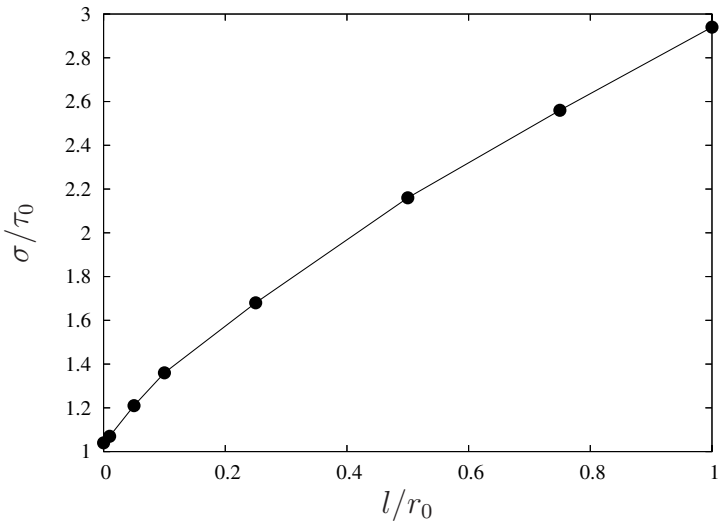

Fig. 20. The overall equibiaxial stress level, σ, that causes an effective stress $\tau_e > \tau_0$ as a function of the void size.

5 Conclusions

The goal of this study is to study the influence of hardening and void size on the stress and deformation fields around a cylindrical void in a single crystal. Hardening within the framework of a local constitutive formulation is considered which corresponds physically to an accumulation of statistically stored dislocations. In addition, strain gradient effects within the framework of a non-local constitutive formulation is considered, which corresponds physically to a segregation of geometrically necessary dislocations. A combination of strain hardening and strain gradient effects is not considered in this study.

The results show that the introduction of hardening in the local constitutive relationship has very little effect on the slip fields around the void when compared to the case of a non-hardening local material. The overall extent of the angular sectors of single slip is unaffected, but the magnitude of the slip is decreased.

When a non-local constitutive relation is used, however, the results are significantly different from the non-hardening local case. For the case of void size $r_0/l = 10$, the boundaries between the angular slip sectors broaden so that there are regions in which multiple slip systems are activated simultaneously. The magnitudes of the slip change very little between the two cases.

For the case of small void size ($r_0/l = 1$), the form of the deformation field changes dramatically. The deformation localizes into regions which intersect the void surface and are parallel to the slip system. This localization is reminiscent of the type of dislocation activity associated with dislocation nucleation from a void in a crystal which is free of dislocations or other dislocation sources

as discussed in Lubarda et al. (2004).

Finally, the applied stress state to activate plastic deformation around the void associated with the non-local material can be as high as three times that of the non-hardening local case. The study by Kysar et al. (2005) concluded that the stress state necessary to activate plastic deformation in face centered cubic crystals can be up to 50% higher than that of an isotropic material, however there was very little difference for hexagonal closed packed crystals (Gan and Kysar, 2007). This discrepancy exists because the effective Schmid factors for the slip systems of a hexagonal close packed crystal are higher than the analogous Schmid factors for the slip systems of a face centered cubic crystal. Therefore, one can conclude that the anisotropy of the material properties as well as the non-local constitutive formulation act to increase the externally applied stress required to activate void growth in single crystals. This has potential implications in the development of theories of effective porous media which are used to model crack growth in ductile materials.

Acknowledgements

The work of U.B. is financially supported by the Danish Technical Research Council in a project entitled Modeling Plasticity at the Micron Scale. J.W.K acknowledges support from AFOSR FA9550-06-1-0214. The authors express gratitude for stimulating conversations with Christian F. Niordson and Viggo Tvergaard.

References

Ahn, D. C., Sofronis, P. and Minich, R. (2006), 'On the micromechanics of void growth by prismatic-dislocation loop emission', *J. Mech. Phys. Solids* **54**(4), 735–755.

Borg, U. (2007), 'Strain gradient crystal plasticity effects on flow localization', *Int. J. Plasticity, in press.*

Fleck, N. A. and Hutchinson, J. W. (2001), 'A reformulation of strain gradient plasticity', *J. Mech. Phys. Solids* **49**, 2245–2271.

Fleck, N. A., Muller, G. M., Ashby, M. F. and Hutchinson, J. W. (1994), 'Strain gradient plasticity: theory and experiment', *Acta Metall. Mater.* **42**, 475–487.

Fredriksson, P. and Gudmundson, P. (2005), 'Size-dependent yield strength of thin films', *Int. J. Plasticity* **21**, 1834–1854.

Gan, Y. X. and Kysar, J. F. (2007), 'Cylindrical void in a rigid-ideally plastic single crystal III: Hexagonal close-packed crystal', *Int. J. Plasticity* **23**, 592–619.

Gan, Y. X., Kysar, J. F. and Morse, T. L. (2006), 'Cylindrical void in a rigid-ideally plastic single crystal II: Experiments and simulations', *Int. J. Plasticity* **22**, 39–72.

Gurtin, M. E. (2002), 'A gradient theory of single-crystal viscoplasticity that accounts for geometrically necessary dislocations', *J. Mech. Phys. Solids* **50**, 5–32.

Hussein, M. I., Borg, U., Niordson, C. F. and Deshpande, V. S. (2006), 'Plasticity size effects in voided crystals', *to be published*.

Koplik, J. and Needleman, A. (1988), 'Void growth and coalescence in porous plastic solids', *Int. J. Solids Struct.* **24**, 835–853.

Kysar, J. F., Gan, Y. X. and Mendez-Arzuza, G. (2005), 'Cylindrical void in a rigid-ideally plastic single crystal. part I: Anisotropic slip line theory solution for face-centered cubic crystals', *Int. J. Plasticity* **21**, 1481–1520.

Lubarda, V. A., Schneider, M. S., Kalantar, D. H., Remington, B. A. and Meyers, M. A. (2004), 'Void growth by dislocation emission', *Acta Mater.* **52**(6), 1397–1408.

Niordson, C. F. and Redanz, P. (2004), 'Size-effects in plane strain sheet-necking', *J. Mech. Phys. Solids* **52**, 2431–2454.

Peirce, D., Asaro, R. J. and Needleman, A. (1983), 'Material rate dependence and localized deformation in crystalline solids', *Acta Metall.* **31**, 1951–1976.

Stevens, A. L., Davison, L. and Warren, W. E. (1972), 'Spall fracture in aluminum monocrystals - dislocation-dynamics approach', *J. Appl. Phys.* **43**(12), 4922–4927.

Tvergaard, V. (1990), 'Material failure by void growth to coalescence', *Adv. Appl. Mech.* **27**, 83–151.

P6

Size effects on void growth in single crystals with distributed voids

Submitted, 2007

Size effects on void growth in single crystals with distributed voids

Ulrik Borg [a,*] , Christian F. Niordson [a] and Jeffrey W. Kysar [b]

[a] *Department of Mechanical Engineering, Solid Mechanics, Technical University of Denmark, Kgs. Lyngby, DK-2800, Denmark*

[b] *Department of Mechanical Engineering, Fu Foundation School of Engineering and Applied Science, Columbia University, 500 West 120th Street, New York, NY 10027, USA*

Abstract

The effect of void size on void growth in single crystals with uniformly distributed cylindrical voids is studied numerically using a finite deformation strain gradient crystal plasticity theory with an intrinsic length parameter. A plane strain cell model is analyzed for a single crystal with three in-plane slip systems. It is observed that small voids allow much larger overall stress levels than larger voids for all the stress triaxialities considered. The amount of void growth is found to be suppressed for smaller voids at low stress triaxialities. Significant differences are observed in the distribution of slips and on the shape of the deformed voids for different void sizes. Furthermore, the orientation of the crystalline lattice is found to have a pronounced effect on the results, especially for the smaller void sizes.

Key words: Void growth, Strain gradient plasticity, Single crystal, Size effects

1 Introduction

Failure by nucleation, growth and coalescence of microscopic voids is an important fracture mechanism in ductile materials. After nucleation voids may grow due to plastic straining of the surrounding material, and finally coalescence can occur at a critical strain. Extensive research has been performed in the area of modeling void growth to coalescence in polycrystalline materials (Gurson, 1977; Koplik and Needleman, 1988; Tvergaard, 1990). Also,

* Corresponding author. Tel.:+45 4525 4262; fax: +45 4593 1475.
Email address: ub@mek.dtu.dk (Ulrik Borg).

single crystal void growth analyses have been carried out to study e.g. effects of lattice orientation on the overall behavior and on the shape of deformed voids (Nemat-Nasser and Hori, 1987; O'Reagan et al., 1997; Potirniche et al., 2006*a*).

All of the above mentioned analyses are size independent. However, a significant amount of experimental work has shown that plastic deformation at the micron scale in crystalline solids is size dependent (Fleck et al., 1994; Ma and Clarke, 1995; Stlken and Evans, 1998). Thus, size independent models do not agree with experimental results for void sizes on the micron range. Several size dependent continuum plasticity models have been proposed, and most of them – the so-called strain gradient plasticity theories – accounts for the presence of geometrically necessary dislocations through plastic strain gradients (e.g. Fleck and Hutchinson, 2001; Gurtin, 2002).

Size-dependent void growth of both cylindrical voids and spherical voids in isotropic materials has been studied by use of strain gradient plasticity cell models under different stress triaxialities by several authors (Fleck and Hutchinson, 2001; Tvergaard and Niordson, 2004; Niordson, 2006; Niordson and Tvergaard, 2006; Borg et al., 2006). The general results from these studies are that the load carrying capability is increased with decreasing void size and that void growth rates are significantly reduced for decreasing void sizes. Similar results were observed by Shu (1998) who studied size effects at small strains in a single crystal with a cylindrical void using a strain gradient crystal plasticity model. Strain gradient theories include an internal material length parameter (typically on the micron scale) to be determined by experiments or comparisons to other size dependent models. Single crystal void analyses have also been performed by use of a discrete dislocation plasticity model in Hussein et al. (2007) which focuses on comparisons between strain gradient crystal plasticity and discrete dislocation plasticity predictions. Void growth for very small voids has been studied by Potirniche et al. (2006*b*) using molecular dynamics simulations restricted to voids on the nano-scale by current computational capabilities.

The stress and deformation fields associated with a cylindrical void in a single crystal loaded by a far-field equi-biaxial compressive stress have been studied with an analytical continuum anisotropic slip line theory by Kysar et al. (2005) and Gan and Kysar (2007), along with related experimental and numerical findings by Gan et al. (2006). These studies show that angular regions exist around the void within which slip on single slip systems occurs. A numerical strain gradient crystal plasticity study, using the same material model as for the present work, focusing on size effects in the stress and deformation fields near a cylindrical void within a single crystal loaded by a far-field equi-biaxial tensile stress has been carried out by Borg and Kysar (2007). Significant size effects were observed in that work.

The present study focuses on size effects in void growth for a single crystal with uniformly distributed voids under different stress triaxialities. Numerical simulations are performed using a strain gradient crystal plasticity material model by Borg (2007). A plane strain cell model with three in-plane slip systems is used, and the interaction of neighboring cylindrical voids is accounted for using periodic boundary conditions for displacements and slip rates on the cell edges. The effect of initial void size on the overall stress-strain behavior and on the evolution of void size during deformation is investigated for two void volume fractions. Also, lattice orientation effects at different initial void sizes and stress triaxialities are discussed and contours of slip are shown together with the deformed void shapes. Finally, the influence of void size on the maximum stress and the strain level at this maximum is analyzed.

The paper is organized as follows. Section 2 serves as a summary of the material model used in this study. The numerical implementation of the material model and the unit cell model is discussed in Section 3. Section 4 presents the result of the simulations and Section 5 contains the conclusions.

2 Material model

This section serves as a summary of the material model used for the analyses presented. The material model employed is the strain gradient crystal plasticity model of Borg (2007), which is based on the principle of virtual power introduced by Gurtin (2002) with the constitutive equations motivated from the isotropic strain gradient plasticity theory of Fleck and Hutchinson (2001). It reduces to conventional crystal plasticity by e.g. Peirce et al. (1983) in the absence of strain gradients.

Plastic deformation is based on crystallographic shearing along specific slip systems specified by the slip direction, $s_i^{(\alpha)}$, and the direction normal to the slip plane, $m_i^{(\alpha)}$. The total strain rate, which is taken as the symmetric part of the velocity gradient, is decomposed into an elastic part and a plastic part, $\dot{\epsilon}_{ij} = \dot{\epsilon}_{ij}^e + \dot{\epsilon}_{ij}^p$, where the plastic strain rate components can be related to the crystallographic slip rate, $\dot{\gamma}^{(\alpha)}$, through

$$\dot{\epsilon}_{ij}^p = \sum_\alpha \dot{\gamma}^{(\alpha)} \mu_{ij}^{(\alpha)} \tag{1}$$

Here, $\mu_{ij}^{(\alpha)} = \frac{1}{2}(s_i^{(\alpha)} m_j^{(\alpha)} + s_j^{(\alpha)} m_i^{(\alpha)})$ is the classical Schmid orientation tensor.

To account for the presence of geometrically necessary dislocations caused by slip gradients, the internal plastic dissipation rate is taken to depend on the slip rates as well as the slip rate gradients. One can argue that a slip gradient in

the slip direction is related to geometrically necessary edge dislocations, a slip gradient in the transverse direction is related to geometrically necessary screw dislocations, whereas a slip gradient in the direction normal to the slip plane does not induce any geometrically necessary dislocations (Fleck et al., 1994). In the present work only plane strain situations with in-plane slip systems are considered. Thus, the slip gradient in the transverse direction vanish and the principle of virtual power in the current configuration for a body V takes the form

$$\int_V \left(\sigma_{ij} \delta \dot{\epsilon}^e_{ij} + \sum_\alpha Q^{(\alpha)} \delta \dot{\gamma}^{(\alpha)} + \sum_\alpha \xi_S^{(\alpha)} s_i^{(\alpha)} \delta \dot{\gamma}^{(\alpha)}_{,i} \right) \mathrm{d}V = \int_S \left(T_i \delta \dot{u}_i + \sum_\alpha r^{(\alpha)} \delta \dot{\gamma}^{(\alpha)} \right) \mathrm{d}S \tag{2}$$

where σ_{ij} is the Cauchy stress tensor, $Q^{(\alpha)}$ is a stress field work conjugate to the slip rate and $\xi_S^{(\alpha)}$ is a higher order stress work conjugate to the gradient of the slip rate in the slip direction, $s_i^{(\alpha)} \dot{\gamma}^{(\alpha)}_{,i}$. The surface stress traction is denoted T_i while $r^{(\alpha)}$ are the higher order tractions working on the surface S of the body.

To obtain the principle of virtual power on incremental form in the reference configuration, Kirchhoff stress measures are defined as

$$\varsigma_{ij} = J \sigma_{ij}, \qquad q^{(\alpha)} = J Q^{(\alpha)}, \qquad \rho_S^{(\alpha)} = J \xi_S^{(\alpha)} \tag{3}$$

where J is the determinant of the deformation gradient. The incremental elastic constitutive equation is taken in terms of the lattice Jaumann rate of Kirchhoff stress, $\overset{\nabla^*}{\varsigma}_{ij}$, as

$$\overset{\nabla^*}{\varsigma}_{ij} \Delta t = R_{ijkl} \left(\Delta \epsilon_{kl} - \Delta t \sum_\alpha \dot{\gamma}^{(\alpha)} \mu_{kl}^{(\alpha)} \right) = \Delta \varsigma_{ij} - \Delta t \Omega^*_{ik} \varsigma_{kj} - \Delta t \varsigma_{ik} \Omega^*_{jk} \tag{4}$$

where Ω^*_{ij} denotes the lattice spin rate given by the skew symmetric part of the elastic part of the velocity gradient. The isotropic elastic stiffness tensor is given by $R_{ijkl} = \frac{E}{1+\nu} \left(\frac{1}{2} \left(\delta_{ik} \delta_{jl} + \delta_{il} \delta_{jk} \right) + \frac{\nu}{1-2\nu} \delta_{ij} \delta_{kl} \right)$, where E is the elastic modulus, ν is Poisson's ratio and δ_{ij} denotes the Kronecker delta.

A nonlocal measure of the effective slip, $\gamma_e^{(\alpha)}$, is defined on the basis of the slip rate and its directional derivative through the incremental relation

$$\dot{\gamma}_e^{(\alpha)^2} = \dot{\gamma}^{(\alpha)^2} + \left(l \dot{\gamma}^{(\alpha)}_{,i} s_i^{(\alpha)} \right)^2 \tag{5}$$

where l is the internal material length parameter introduced for dimensional consistency. An effective stress $\tau_e^{(\alpha)}$ is defined to be work conjugate to the effective slip rate, $\dot{\gamma}_e^{(\alpha)}$, and can be expressed as

$$\tau_e^{(\alpha)^2} = q^{(\alpha)^2} + l^{-2}\rho_S^{(\alpha)^2} \tag{6}$$

A power-law model is adopted for the effective slip rate to model the viscous material behavior

$$\dot{\gamma}_e^{(\alpha)} = \dot{\gamma}_0 \left(\frac{\tau_e^{(\alpha)}}{g^{(\alpha)}} \right)^{1/m} \tag{7}$$

where $\dot{\gamma}_0$ is a reference slip rate and m is the viscoplastic exponent. The slip resistances $g^{(\alpha)}$ characterize the current strain hardened state of the crystal, and harden from an initial value τ_0 according to

$$\dot{g}^{(\alpha)} = \sum_{\beta} h_{\alpha\beta}\dot{\gamma}_e^{(\beta)}, \quad h_{\alpha\beta} = h\delta_{\alpha\beta} + ph\left(1 - \delta_{\alpha\beta}\right) \tag{8}$$

Here, p is the latent hardening index and h is the self-hardening modulus given by

$$h(\gamma_a) = h_0 \left(\frac{h_0\gamma_a}{\tau_0 n} + 1 \right)^{n-1}, \quad \gamma_a = \sum_{\alpha} \int \dot{\gamma}_e^{(\alpha)} \mathrm{d}t \tag{9}$$

where the constant h_0 represents an initial hardening rate, n is the hardening exponent, and γ_a is the accumulated effective slip.

3 Numerical method

The numerical solutions are obtained using a special kind of finite element method where the slip rate increments are treated as primary unknowns on equal footing with the displacement increments. These fields are interpolated within each element between nodal increments as

$$\Delta u_i = \sum_{N=1}^{2k} N_i^N \Delta D^N, \qquad \Delta\dot{\gamma}^{(\alpha)} = \sum_{N=1}^{l} M^N \Delta\dot{\gamma}_N^{(\alpha)} \tag{10}$$

where N_i^N and M^N are shape functions and k and l are the number of nodes used for the interpolations. For the present plane strain study, the elements used for the displacements are 8-node quadrilaterals with quadratic shape

functions, and the elements used for interpolation of the slip rate increments are 4-node quadrilaterals with bilinear shape functions, i.e. $k = 8$ and $l = 4$. The integrations are carried out using 2×2 point Gaussian integration for both element types. To ensure that integration points for the two element types coincide, the same Jacobian is used for both element types.

A plane strain cell model with three in-plane slip systems is used to model a periodic arrangement of cylindrical voids within a single crystal (figure 1). The slip systems are oriented 60° with respect to the others, and their absolute orientation are given by the angle ϕ between slip system 2 and the x_1-axis. The void radius is denoted r_0 and the lengths of the cell sides are denoted a_0 and b_0, and are here taken to be equal ($a_0 = b_0$). Two initial void volume fractions, f_0, are considered in the present study; $f_0 \approx 3.1\%$ and $f_0 \approx 12.6\%$ corresponding to $r_0/a_0 = 0.1$ and $r_0/a_0 = 0.2$, respectively.

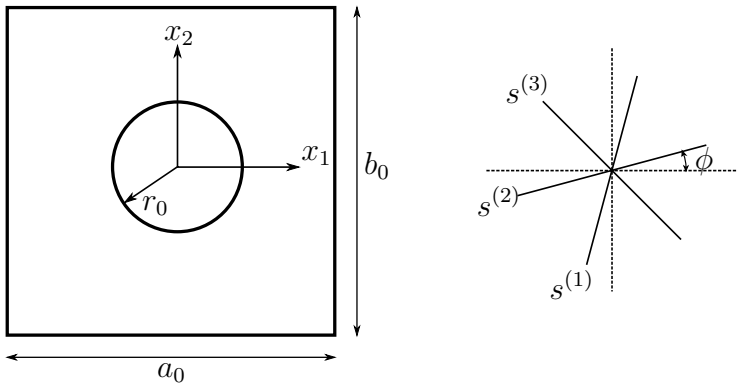

Fig. 1. The analyzed unit cell with a cylindrical void in the center. The absolute orientation of the three slip systems, with the relative orientation of 60° between them, are given by the angle ϕ.

The loading is simulated by imposing periodic boundary conditions on the unit cell edges as

$$\Delta u_i = \overline{\epsilon}_{ij} \Delta x_j \tag{11}$$

where Δu_i is the difference between displacements on opposite sides of the unit cell specified by the difference in position vector Δx_j while $\overline{\epsilon}_{ij}$ is the imposed macroscopic strain, specified as $\overline{\epsilon}_{12} = \overline{\epsilon}_{21} = 0$ and $\overline{\epsilon}_{11} = U/a_0$, where U/a_0 is the applied strain in the x_1-direction. Using a special Rayleigh-Ritz finite element method (Tvergaard, 1976), the ratio of $\overline{\epsilon}_{22}/\overline{\epsilon}_{11}$ is determined such that there is a fixed ratio of the average true stresses $\sigma_2/\sigma_1 = \kappa$. Periodicity for the displacements and stresses is enforced using a penalty method, whereas periodicity for the slip rates is enforced by eliminating nodal degrees of freedom to ensure that slip rates at corresponding points on opposite sides of the unit cell are equal. Boundary conditions at the void surface are specified by vanishing tractions and higher order tractions. The finite element model used for the results presented consists of 1440 elements with 96 elements along the void surface.

4 Results

Numerical results for bi-axial loading of porous crystals with void volume fractions of 12.6% and 3.1% are presented in this section. Two different orientations of the crystal lattice relative to the unit cell are considered; $\phi = 0^\circ$ and $\phi = 15^\circ$. For all analyses the ratio of initial slip resistance to Young's modulus is $\tau_0/E = 0.001$ and Poisson's ratio is $\nu = 0.3$. The deformation hardening behavior is characterized by the self hardening modulus $h_0/\tau_0 = 10$, the power hardening exponent $n = 0.1$ and the latent hardening index $p = 1.0$. The viscous effects are specified by the reference slip rate $\dot{\gamma}_0 = 0.001\text{s}^{-1}$ and the viscoplastic exponent $m = 0.03$. The overall loading rate in the main tensile direction is $\dot{U}/a_0 = \dot{\gamma}_0$.

The normalized true stress is shown as a function of the logarithmic strain in the main tensile direction (x_1) in figure 2a for three different void sizes and three different stress ratios ($\kappa = \sigma_2/\sigma_1 = 0.5; 0.75; 1.0$) with the void volume fraction $f_0 = 12.6\%$ and lattice orientation $\phi = 0^\circ$. The different void sizes are specified by the ratio of the void radius to material length parameter, r_0/l. The curves labeled conv. are for calculations with a vanishing material length parameter, such that the model reduces to conventional crystal plasticity. For all analyses material softening is observed in the form of rapidly decaying response curves after the maximum stress level. The results show enhanced softening behavior for larger stress ratios as is also the case for isotropic plasticity (Koplik and Needleman, 1988). The size of the voids has an important influence on the response of the material, as small voids allow much larger overall stress levels. Furthermore, it is seen that the maximum attainable stress level is almost independent of the bi-axial stress ratio, κ, within the range considered here. On the other hand, the strain at which the maximum stress is attained decreases considerably with increasing values of κ.

The significant softening in the response for the voided crystals observed in figure 2a is due to void growth. This is shown in figure 2b where the void volume relative to the initial void volume is presented as a function of strain. For larger stress ratios more void growth is predicted in accordance with conventional predictions (Koplik and Needleman, 1988). On the other hand, it is observed that the void size (as specified by r_0/l) has almost no effect on the amount of void growth for $\kappa = 1.0$, and it has a minor effect for $\kappa = 0.75$ and 0.5 by suppressing void growth for smaller voids.

For equi-biaxial loading ($\kappa = 1.0$) contour plots of slip at an overall deformation given by $U/a_0 = 0.1$, are shown in the figures 3a and 3b, for a conventional porous crystal and a crystal with micron size voids ($r_0/l = 1$), respectively. The figures present slip distributions on each individual slip plane (as defined

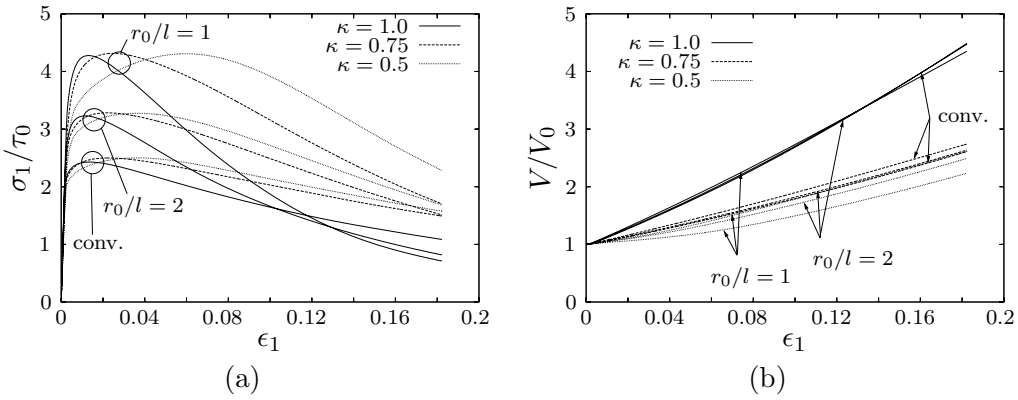

Fig. 2. Results for the initial void volume fraction $f_0 = 12.6\%$ and slip system orientation $\phi = 0°$. (a) Overall response in terms of the true stress vs. logarithmic strain. (b) Relative void growth vs. logarithmic strain. Curves are shown for different stress ratios and void sizes.

in figure 1) as well as the total slip, corresponding to selected analyses in figure 2. It is seen that a conventional crystal model predicts equal distributions of total slip between the voids along the x_1- and the x_2-directions. Furthermore, it is seen that the proper symmetry between the slip systems 1 and 3 for $\phi = 0°$ exists. Figure 3b shows that for a micron scale void modeled by strain gradient crystal plasticity, gradients are suppressed along the slip planes, due to the energetic expenses included in the last term in the volume integral in equation (2). This leads to well developed slip bands on slip systems 1 and 3 connecting voids in the x_2-direction. This implies that the total slip is not equally distributed between voids in the two perpendicular directions, and leads to unequal overall strain in the x_1- and the x_2-directions, as well as ovalizing of the voids, which is not the case for the conventional analyses.

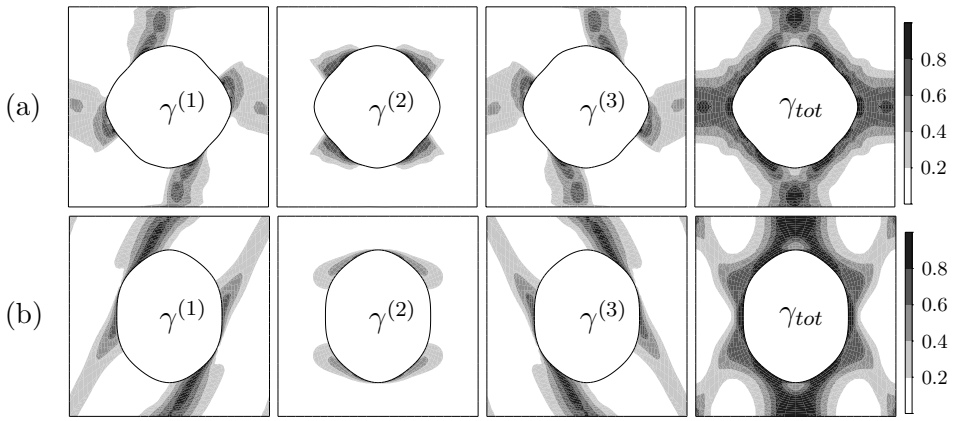

Fig. 3. Contours of slip on the three slip systems and the total slip at the overall deformation $U/a_0 = 0.1$ for a crystal with initial void volume fraction $f_0 = 12.6\%$, slip system orientation $\phi = 0°$ and stress ratio $\kappa = 1.0$. Both results from a conventional calculation (a) and from a gradient-dependent calculation with $r_0/l = 1$ (b) are shown.

Figures 4a and 4b show results corresponding to figures 3a and 3b, respectively, for $\kappa = 0.5$ at the overall deformation $U/a_0 = 0.2$. The figures show that slip concentrates between voids along planes perpendicular to the main loading direction (x_1). Even though the slip bands are not as well developed as for $\kappa = 1.0$, figure 4b illustrates how slip gradients are suppressed along the slip planes when $r_0/l = 1$, as opposed to the conventional results presented in figure 4a. This leads to a more smooth void shape for micron sized voids, when compared to conventional predictions.

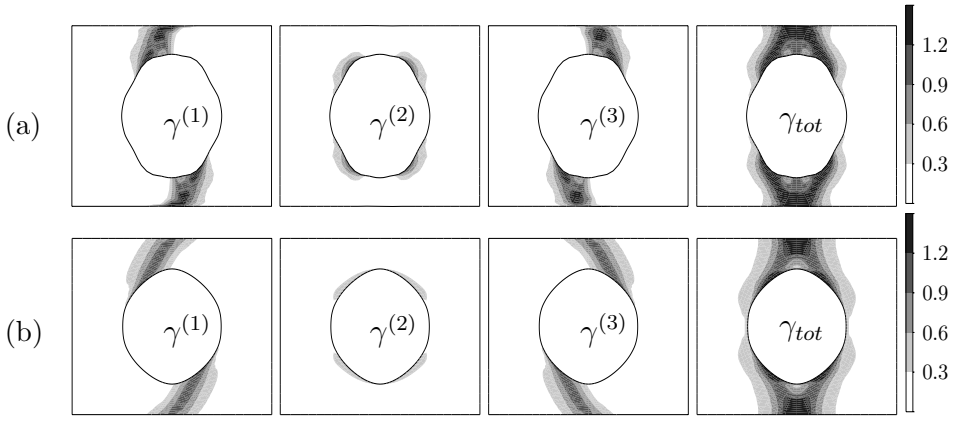

Fig. 4. Contours of slip on the three slip systems and the total slip at the overall deformation $U/a_0 = 0.2$ for a crystal with initial void volume fraction $f_0 = 12.6\%$, slip system orientation $\phi = 0°$ and stress ratio $\kappa = 0.5$. Both results from a conventional calculation (a) and from a gradient-dependent calculation with $r_0/l = 1$ (b) are shown.

Until now only results for $\phi = 0°$ have been discussed. Figures 5a and 5b compare response curves for two different orientations of the crystal lattice relative to the void planes, for $\kappa = 1.0$ and $\kappa = 0.5$, respectively, with the void volume fraction $f_0 = 12.6\%$. It is seen that the overall material response differs at large deformation levels, as softening is more pronounced when $\phi = 0°$. On the other hand, the maximum stress level does not depend strongly on the crystal orientation for either of the void sizes considered here.

For a single void in an infinite equi-biaxially loaded crystal angular sectors of single slip exists around a circular cylindrical void in a hexagonal close-packed crystal as that analyzed here (Gan and Kysar, 2007). For $\phi = 15°$ slip system 3 will be active in a 30° angular band centered around both the x_1- and the x_2-axis. Thus, for a periodical distribution of voids as that in figure 1, there will be a strong interaction between the neighboring voids along the x_1- and the x_2-directions giving rise to increased slip on slip system 3. This is observed in figure 6a, which shows the slip distributions for a conventional material at an overall deformation level of $U/a_0 = 0.1$ for the stress ratio $\kappa = 1.0$ and a void volume fraction of 12.6%. Accounting for gradient hardening decreases the slip gradients along the slip directions and this decreases the interaction between neighboring voids along the x_1- and x_2-directions as seen from figure 6b.

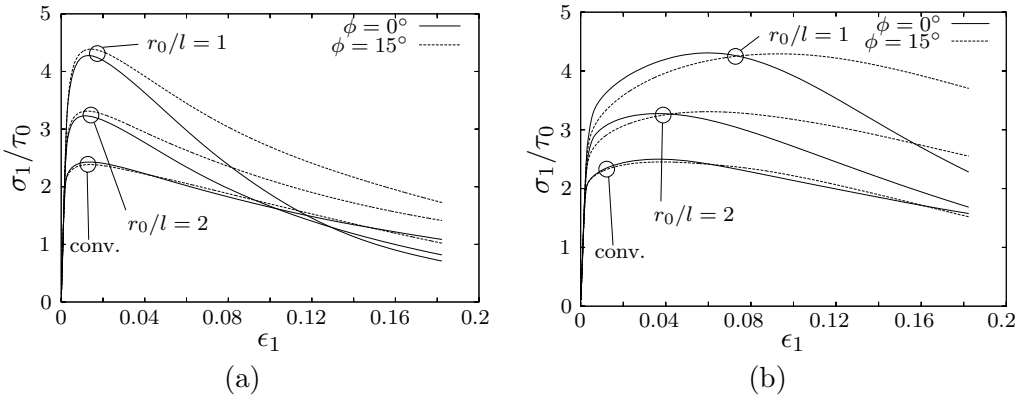

Fig. 5. Overall true stress vs. logarithmic strain for the crystal with initial void volume fraction $f_0 = 12.6\%$ at two slip system orientations. Results are given for the stress ratios $\kappa = 1.0$ (a) and $\kappa = 0.5$ (b) for different void sizes.

For $\phi = 0°$ the symmetry lines for the total slip are oriented along the coordinate axes (see figures 3 and 4), since the slip planes are symmetric across the axes and the loading is oriented along the axes. When the crystal orientation is rotated relative to the void planes, these symmetries will disappear as shown in the figures 6 and 7, where slip distributions are shown for $\phi = 15°$. For $\kappa = 1.0$ results are presented in figures 6a and 6b, for a conventional porous crystal and a crystal with micron scale voids $r_0/l = 1.0$, respectively, while corresponding results are shown in figures 7a and 7b for $\kappa = 0.5$ and $U/a_0 = 0.2$. For $\kappa = 1.0$, the conventional results in figure 6a show that symmetries exist along lines at a 45° angle between the coordinate axes. This is due to the same symmetry of the slip-planes and the equi-biaxial loading. Hence, this symmetry exists even for the gradient dependent solid in figure 6b. For $\kappa = 0.5$ the results in figures 7a and 7b show that these symmetries are broken, due to the lack of symmetric loading.

For a smaller void volume fraction of 3.1% and $\phi = 0°$ response curves and curves of void volume as a function of strain is shown in figures 8a and 8b, respectively. Results are shown for different bi-axial stress ratios and different void sizes. Comparing with figure 2, it is observed that the maximum stress level is significantly larger for the material with the smaller void volume fraction consistent with conventional results for isotropic plasticity (Needleman, 1972). Furthermore, it is seen that material softening is more pronounced for the smaller void volume fraction due to increased void growth. As for the larger void volume fraction, the maximum stress level is almost independent of κ, whereas the strain at the maximum stress level increases with decreasing stress ratio. The suppression of void growth for small voids is observed clearly in figure 8b for all considered stress ratios, with the strongest effect for the smallest stress ratio.

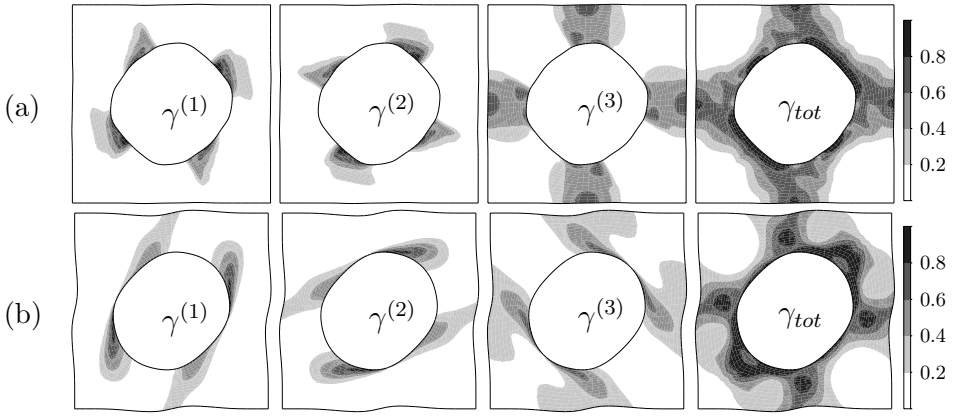

Fig. 6. Contours of slip on the three slip systems and the total slip at the overall deformation $U/a_0 = 0.1$ for a crystal with initial void volume fraction $f_0 = 12.6\%$, slip system orientation $\phi = 15^\circ$ and stress ratio $\kappa = 1.0$. Both results from a conventional analysis (a) and from a gradient-dependent analysis with $r_0/l = 1$ (b) are shown.

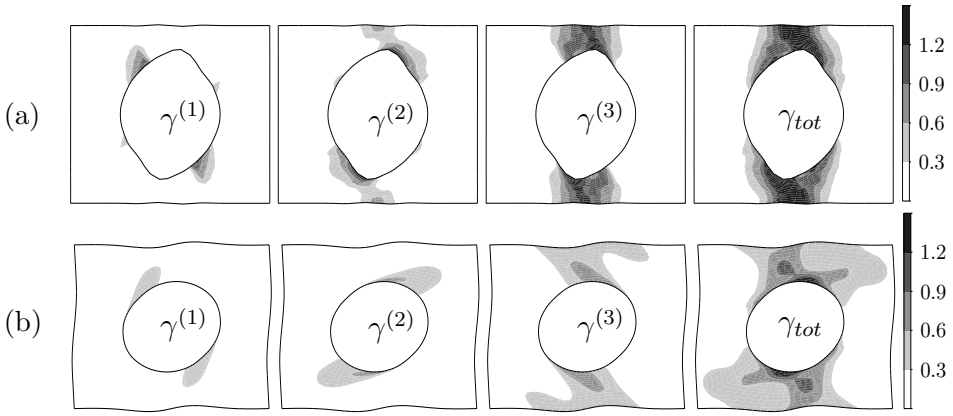

Fig. 7. Contours of slip on the three slip systems and the total slip at the overall deformation $U/a_0 = 0.2$ for a crystal with initial void volume fraction $f_0 = 12.6\%$, slip system orientation $\phi = 15^\circ$ and stress ratio $\kappa = 0.5$. Both results from a conventional analysis (a) and from a gradient-dependent analysis with $r_0/l = 1$ (b) are shown.

5 Conclusions

This study analyzes the size effects in void growth within single crystals containing uniformly distributed cylindrical voids subjected to bi-axial stress states. Numerical analyses for a cell model are performed using a strain gradient crystal plasticity model. The material length scale for the material model used in the present work has been estimated to $l = 0.325\mu$m in Hussein et al. (2007) by fitting strain gradient crystal plasticity results to discrete dislocation plasticity results. With this length scale the two void sizes considered in the present study, $r_0/l = 2$ and $r_0/l = 1$, are both in the sub-micron range.

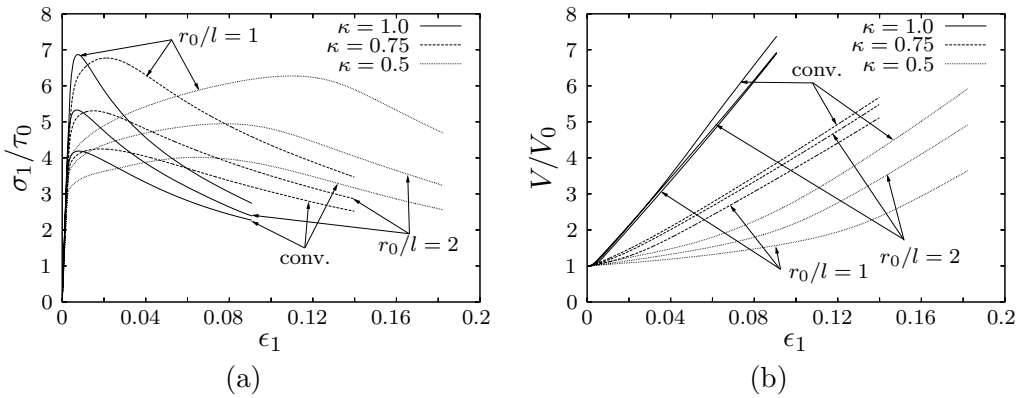

Fig. 8. Results for the initial void volume fraction $f_0 = 3.1\%$ and slip system orientation $\phi = 0°$. (a) Overall response in terms of the true stress vs. logarithmic strain. (b) Relative void growth vs. logarithmic strain. Curves are shown for different stress ratios and void sizes.

The results show that small voids allow much larger overall stress levels for all the stress ratios and initial void volume fractions considered. The strain level at which the maximum stress is achieved was also found to be dependent on the initial void sizes. A summary of the obtained results for the initial void volume fraction $f_0 = 12.6\%$ is shown in figure 9. The highest true stress level in the x_1-direction is shown as a function of void size in figure 9a for two stress ratios, and figure 9b shows the strain level in the x_1-direction at which the maximum stress is achieved. The horizontal curves show results for conventional crystal plasticity, which the gradient-dependent calculations converge to for large void sizes. It is interesting to note that the stress levels for the two stress ratios shown, $\kappa = 1.0$ and $\kappa = 0.5$, are almost identical. For $\kappa = 0.5$ the strain level at the maximum stress increases with decreasing void size, whereas this strain level is much less affected by the initial void size for $\kappa = 1.0$.

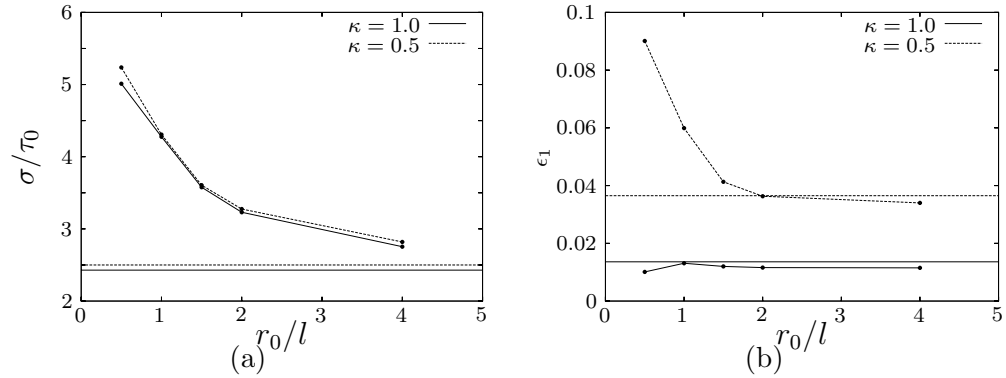

Fig. 9. (a) Maximum true stress in the main tensile direction versus void size and (b) the strain level at which this stress is achieved versus void size. The results are given for two stress ratios and for the initial void volume fraction $f_0 = 12.6\%$ and lattice orientation $\phi = 0°$.

The amount of void growth depends strongly on the stress ratio for both the initial void volume fractions studied. Decreasing the void size to the micron scale is found to suppress void growth for the smaller stress ratios. The interaction on the different slip systems between neighboring voids depends on the lattice orientation relative to the void structure. It is found that gradient effects on the micron scale changes the character of the interaction mechanisms completely by favoring the development of slip bands between neighboring voids.

Contours of slip in the three slip systems are shown for some of the simulations performed at an overall deformation state well beyond the point of maximum true stress in the x_1-direction. These plots also show the deformed void shapes, and significant dependences on both lattice orientation and initial void size are observed, with smaller voids being significantly more smooth than large voids upon deformation.

The strength and the ductility of a metal is limited by void growth to coalescence. This study shows that porous crystals can sustain larger overall stress levels for voids on the micron scale when compared to macroscopic voids. This is due to gradient hardening of the material around the voids and, for moderate stress triaxialities, partly due to the suppression of void growth on the micron scale. Hence, the strength of a crystal increases with decreasing void size for a fixed void volume fraction. Furthermore, increased material ductility for small voids is observed for moderate stress triaxialities, due to suppression of void growth for crystals with micron scale voids.

Acknowledgements

The work of U.B. and C.F.N. is financially supported by the Danish Technical Research Council in a project entitled Modeling Plasticity at the Micron Scale. J.W.K acknowledges support from AFOSR FA9550-06-1-0214.

References

Borg, U. (2007), 'Strain gradient crystal plasticity effects on flow localization', *Int. J. Plasticity, to appear.*

Borg, U. and Kysar, J. W. (2007), 'Strain gradient crystal plasticity analysis of a single crystal containing a cylindrical void', *to be published.*

Borg, U., Niordson, C. F., Fleck, N. A. and Tvergaard, V. (2006), 'A viscoplastic strain gradient analysis of materials with voids or inclusions', *Int. J. Solids Structures* **43**, 4906–4916.

Fleck, N. A. and Hutchinson, J. W. (2001), 'A reformulation of strain gradient plasticity', *J. Mech. Phys. Solids* **49**, 2245–2271.

Fleck, N. A., Muller, G. M., Ashby, M. F. and Hutchinson, J. W. (1994), 'Strain gradient plasticity: theory and experiment', *Acta Metall. Mater.* **42**, 475–487.

Gan, Y. X. and Kysar, J. F. (2007), 'Cylindrical void in a rigid-ideally plastic single crystal III: Hexagonal close-packed crystal', *Int. J. Plasticity* **23**, 592–619.

Gan, Y. X., Kysar, J. F. and Morse, T. L. (2006), 'Cylindrical void in a rigid-ideally plastic single crystal II: Experiments and simulations', *Int. J. Plasticity* **22**, 39–72.

Gurson, A. (1977), 'Continuum theory of ductile rupture by void nucleation and growth: Part i. yield criteria and flow rules for porous ductile media', *J. Eng. Mat. Tech.* **99**, 2–15.

Gurtin, M. E. (2002), 'A gradient theory of single-crystal viscoplasticity that accounts for geometrically necessary dislocations', *J. Mech. Phys. Solids* **50**, 5–32.

Hussein, M. I., Borg, U., Niordson, C. F. and Deshpande, V. S. (2007), 'Plasticity size effects in voided crystals', *to be published*.

Koplik, J. and Needleman, A. (1988), 'Void growth and coalescence in porous plastic solids', *Int. J. Solids Struct.* **24**, 835–853.

Kysar, J. F., Gan, Y. X. and Mendez-Arzuza, G. (2005), 'Cylindrical void in a rigid-ideally plastic single crystal. part I: Anisotropic slip line theory solution for face-centered cubic crystals', *Int. J. Plasticity* **21**, 1481–1520.

Ma, Q. and Clarke, D. R. (1995), 'Size dependent hardness of silver single crystals', *Journal of Materials Research* **10**, 853–863.

Needleman, A. (1972), 'Void growth in an elastic-plastic medium', *J. Appl. Mech.* **39**, 964–970.

Nemat-Nasser, S. and Hori, M. (1987), 'Void collapse and void growth in crystalline solids', *J. Appl. Phys.* **62**, 2746–2757.

Niordson, C. F. (2006), 'Void growth to coalescence in a non-local material', *to be published*.

Niordson, C. F. and Tvergaard, V. (2006), 'Size effects on cavitation instabilities', *J. Appl. Mech.* **73**, 246–253.

O'Reagan, T. L., Quinn, D. F., Howe, M. A. and Mchugh, P. E. (1997), 'Void growth simulations in single crystals', *Comp. Mech.* **20**, 115–121.

Peirce, D., Asaro, R. J. and Needleman, A. (1983), 'Material rate dependence and localized deformation in crystalline solids', *Acta Metall.* **31**, 1951–1976.

Potirniche, G. P., Hearndon, J. L., Horstemeyer, M. F. and Ling, X. W. (2006*a*), 'Lattice orientation effects on void growth and coalescence in fcc single crystals', *Int. J. Plasticity* **22**, 921–942.

Potirniche, G. P., Horstemeyer, M. F., Wagner, G. J. and Gullet, P. M. (2006*b*), 'A molecular dynamics study of void growth and coalescence in single crystal nickel', *Int. J. Plasticity* **22**, 257–278.

Shu, J. Y. (1998), 'Scale-dependent deformation of porous single crystals', *Int. J. Plasticity* **14**, 1085–1107.

Stlken, J. S. and Evans, A. G. (1998), 'Microbend test method for measuring the plasticity length scale', *Acta Materialia* **46**, 5109–5115.

Tvergaard, V. (1976), 'Effect of thickness inhomogeneities in internally pressurized elastic-plastic spherical shells', *J. Mech. Phys. Solids* **24**, 291–304.

Tvergaard, V. (1990), 'Material failure by void growth to coalescence', *Adv. Appl. Mech.* **27**, 83–151.

Tvergaard, V. and Niordson, C. (2004), 'Nonlocal plasticity effects on interaction of different size voids', *Int. J. Plasticity* **20**, 107–120.

P7

Plasticity size effects in voided crystals

Submitted, 2006

Plasticity size effects in voided crystals

M. I. Hussein[1], U. Borg[2], C. F. Niordson[2] and V. S. Deshpande[1]

[1]Department of Engineering, University of Cambridge,

Trumpington Street, Cambridge CB2 1PZ, UK.

[2]Department of Mechanical Engineering, Solid Mechanics, Technical University of Denmark,

2800 Kgs. Lyngby, Denmark.

November 20, 2006

Abstract

The shear and equi-biaxial straining responses of periodic voided single crystals are analysed using discrete dislocation plasticity and a continuum strain gradient crystal plasticity theory. In the discrete dislocation formulation the dislocations are all of edge character and are modelled as line singularities in an elastic material. The lattice resistance to dislocation motion, dislocation nucleation, dislocation interaction with obstacles and annihilation are incorporated through a set of constitutive rules. Over the range of length scales investigated, both the discrete dislocation and strain gradient plasticity formulations predict a negligible size effect under shear loading. By contrast, under equi-biaxial loading both plasticity formulations predict a strong size dependence with the flow strength scaling approximately inversely with the void-spacing. Excellent agreement is obtained between predictions of the two formulations for all crystal types and void volume fractions considered when the material length scale in the non-local plasticity model chosen to be $0.325\mu m$ (around ten times the slip plane spacing in the discrete dislocation models).

Keywords: Dislocations; size effects; voids; plasticity; computer simulation

1 Introduction

There is a considerable body of experimental evidence that plastic deformation in crystalline solids is size dependent at length scales of the order of tens of microns and smaller, (e.g. Ashby, 1970; De Guzman et al., 1993; Fleck et al., 1994; Ma and Clarke, 1995). One well-appreciated source of this size dependence is associated with plastic strain gradients and geometrically necessary dislocations. Such effects are expected to play a significant role in the deformation of voided ductile solids when large plastic strain gradients occur over a micron length scale.

Studies of the deformation of voided ductile solids have focused on the growth of a single void in an infinite length scale independent elastic-plastic solid (e.g. McClintock, 1968; Rice and Tracey, 1969), or on a periodic array of identical voids (e.g. Needleman, 1972; Gurson, 1977; Tvergaard, 1981). Recent experimental investigations by Schlueter et al. (1996) and Khraishi et al. (2001) have shown strong void size effects with micro- and submicron size voids growing at significantly reduced rates compared to larger voids subjected to the same stress levels.

A variety of non-local plasticity theories (mainly strain gradient constitutive formulations) have been proposed to account for the observed size dependence of micro-scale plastic flow in crystalline solids (e.g. Fleck and Hutchinson, 2001; Gurtin, 2002). Numerical and analytical studies employing such phenomenological strain gradient plasticity formulations have consistently predicted reductions in the void growth rates for smaller voids; see for example Fleck and Hutchinson (1997) and Tvergaard and Niordson (2004). More recently, Liu et al. (2003) extended the Rice and Tracey (1969) model for void growth using a flow stress for the matrix material derived from the Taylor (1934) dislocation model that has an internal material length scale. Subsequently, Wen et al. (2005) modified the Gurson (1977) yield surface to account for void size effects by employing the analysis of Liu et al. (2003). All such continuum models need as an input a characteristic material length scale that is typically calibrated from experimental data. By contrast, molecular dynamics simulations of void growth (Potirniche et al., 2006) do not require such calibration but are restricted to the nano-void regime by current computational capabilities.

In principle, discrete dislocation plasticity should be able to bridge the gap between the molecular dynamics simulations and the continuum nonlocal plasticity theories. In this study we investigate the size dependence of the response of voided crystalline materials

using both discrete dislocation and strain gradient crystal plasticity. The focus is on: (i) understanding the effect of loading conditions on the void size effect and (ii) employing the discrete dislocation calculations to extract the appropriate material length scale for use in strain gradient plasticity models of voided crystals.

2 Model formulations

Plane strain analyses of the shear and equi-biaxial responses of periodic voided single crystals (Fig. 1) are carried out. The crystals are elastically isotropic with Young's modulus E and Poisson's ratio ν and have slip systems $\phi^{(\alpha)}$ with respect to the x_1 axis. Two types of crystals are considered: a crystal with two symmetric systems $\phi^{(1)} = -\phi^{(2)} = 54.7^\circ$ and a crystal with three systems $\phi^{(1)} = -\phi^{(2)} = 54.7^\circ$ and $\phi^{(3)} = 0^\circ$. Plane strain conditions are assumed with the plane of deformation being the $x_1 - x_2$ plane, and a small strain approximation is made. We consider two formulations to describe plasticity in the crystals: (i) discrete dislocation plasticity and (ii) the strain gradient crystal plasticity model of Borg (2006).

2.1 Discrete dislocation plasticity formulation

Plasticity in the discrete dislocation formulation originates from the motion of edge dislocations, represented as line singularities in an elastic medium. These dislocations can nucleate and glide on the active slip planes. At each stage of loading, the stress and deformation state is computed using superposition of a singular dislocation field and an image field (Van der Giessen and Needleman, 1995). The singular field ($\tilde{}$) associated with N dislocations is calculated analytically from the isotropic linear elastic dislocation fields in an infinite medium (Hirth and Lothe, 1968). The complete solution is obtained by adding a smooth image field ($\hat{}$) that ensures that the boundary conditions are satisfied (see Sec. 2.3 for details). The displacements u_i, strains ϵ_{ij}, and stresses σ_{ij} are written as

$$u_i = \hat{u}_i + \tilde{u}_i, \quad \epsilon_{ij} = \hat{\epsilon}_{ij} + \tilde{\epsilon}_{ij}, \quad \sigma_{ij} = \hat{\sigma}_{ij} + \tilde{\sigma}_{ij}, \tag{1a}$$

where the ($\tilde{}$) field is the sum of the fields of the individual N dislocations in their current positions, i.e.

$$\tilde{u}_i = \sum_{J=1}^{N} \tilde{u}_i^{(J)}, \quad \tilde{\epsilon}_{ij} = \sum_{J=1}^{N} \tilde{\epsilon}_{ij}^{(J)}, \quad \tilde{\sigma}_{ij} = \sum_{J=1}^{N} \tilde{\sigma}_{ij}^{(J)}. \tag{1b}$$

The image field is obtained by solving a linear elastic boundary value problem using finite elements with the boundary conditions changing as the dislocation structure evolves.

At the beginning of a calculation the crystal is stress- and dislocation-free. The long range interactions of the dislocations are accounted for through their elastic fields while constitutive rules are prescribed for short range interactions. Dislocation dipoles with Burgers vectors $\pm b$ are nucleated at point sources, that simulate Frank-Read sources, randomly distributed on discrete slip planes. Nucleation occurs when the magnitude of the resolved shear stress at the source exceeds a critical value τ_{nuc} during a time period t_{nuc}. The sign of the dipole is determined by the sign of the resolved shear stress along the slip plane while the distance between the two dislocations at nucleation, L_{nuc}, is taken such that the attractive stress that the dislocations exert on each other is equilibrated by a shear stress of magnitude τ_{nuc}. After nucleation, the dislocations glide apart, driven by the Peach-Koehler force acting on them, given by

$$f^{(I)} = m_i^{(I)} \left[\hat{\sigma}_{ij} + \sum_{J \neq I} \tilde{\sigma}_{ij}^{(J)} \right] b_j^{(I)}, \tag{2}$$

where $m_i^{(I)}$ is the unit normal to the slip system on which the dislocation with Burgers vector $b_j^{(I)}$ resides. The magnitude of the glide velocity $V_{\text{gld}}^{(I)}$ along the slip direction of dislocation I is taken to be linearly related to the Peach-Koehler force $f^{(I)}$ through the drag relation

$$V_{\text{gld}}^{(I)} = \frac{1}{B} f^{(I)}, \tag{3}$$

where B is the drag coefficient. Annihilation of two opposite signed dislocations on a slip plane occurs when they are within a material-dependent critical annihilation distance L_{e}. Obstacles to dislocation motion are modelled as points associated with a slip plane that cause dislocations that attempt to pass through them to be pinned. An obstacle releases a pinned dislocation when the Peach-Koehler force on the obstacle exceeds $\tau_{\text{obs}} b$, where τ_{obs} is the obstacle strength.

2.2 Continuum strain gradient crystal plasticity formulation

The strain gradient crystal plasticity model of Borg (2006) is employed here to account for the enhanced hardening in voided crystals due to plastic strain gradients. The model is based on the principle of virtual work introduced by Gurtin (2002) with the constitutive equations motivated from the isotropic strain gradient plasticity model of Fleck and Hutchinson (2001).

Plastic deformation is due to slip on slip systems defined by the slip plane normal, $m_i^{(\alpha)}$, and the slip direction $s_i^{(\alpha)}$. Employing the slip rate $\dot{\gamma}^{(\alpha)}$ on slip system α, we define the plastic strain rate as

$$\dot{\epsilon}_{ij}^{p} = \sum_{(\alpha)} \dot{\gamma}^{(\alpha)} \mu_{ij}^{(\alpha)}, \tag{4a}$$

where $\mu_{ij}^{(\alpha)} = \frac{1}{2}\left(s_i^{(\alpha)} m_j^{(\alpha)} + s_j^{(\alpha)} m_i^{(\alpha)}\right)$ is the Schmid orientation tensor and the total strain rate $\dot{\epsilon}_{ij}$ is written as

$$\dot{\epsilon}_{ij} = \dot{\epsilon}_{ij}^{p} + \dot{\epsilon}_{ij}^{e}, \tag{4b}$$

where $\dot{\epsilon}_{ij}^{e}$ is the elastic strain rate.

Here attention is restricted to plane strain situations where the vectors $s_i^{(\alpha)}$ and $m_i^{(\alpha)}$ lie in the same plane. The principle of virtual work for a body V, subjected to tractions $T_i = \sigma_{ij} n_j$ on the surface S of the body with outward unit normal n_i is expressed as

$$\int_V \left(\sigma_{ij} \delta \dot{\epsilon}_{ij}^{e} + \sum_{(\alpha)} q^{(\alpha)} \delta \dot{\gamma}^{(\alpha)} + \sum_{(\alpha)} \rho_S^{(\alpha)} s_i^{(\alpha)} \delta \dot{\gamma}_{,i}^{(\alpha)} \right) dV = \int_S \left(T_i \delta \dot{u}_i + \sum_{(\alpha)} r^{(\alpha)} \delta \dot{\gamma}^{(\alpha)} \right) dS, \tag{5}$$

where $q^{(\alpha)}$ and $\rho_S^{(\alpha)}$ are the work conjugates to plastic slip and plastic slip-gradient in the slip direction, respectively and $r^{(\alpha)} = \rho_S^{(\alpha)} s_i^{(\alpha)} n_i$ is the higher order surface traction.

With the effective slip rate $\gamma_e^{(\alpha)}$ defined as (Borg, 2006)

$$\dot{\gamma}_e^{(\alpha)^2} = \dot{\gamma}^{(\alpha)^2} + \left(l_S \dot{\gamma}_{,i}^{(\alpha)} s_i^{(\alpha)} \right)^2, \tag{6}$$

the corresponding work-conjugate effective stress is given as

$$\tau_e^{(\alpha)^2} = q^{(\alpha)^2} + l_S^{-2} \rho_S^{(\alpha)^2}, \tag{7}$$

where l_S is the internal material length scale. The constitutive equations for $q^{(\alpha)}$ and $\rho_S^{(\alpha)}$ then follow as

$$q^{(\alpha)} = \tau_e^{(\alpha)} \frac{\dot{\gamma}^{(\alpha)}}{\dot{\gamma}_e^{(\alpha)}}, \quad \text{and} \tag{8}$$

$$\rho_S^{(\alpha)} = \tau_e^{(\alpha)} \frac{\dot{\gamma}_{,i}^{(\alpha)} s_i^{(\alpha)}}{\dot{\gamma}_e^{(\alpha)}} l_S^2. \tag{9}$$

Finally, we specify that strain rate hardening follows a power-law relationship of the form

$$\dot{\gamma}_e^{(\alpha)} = \dot{\gamma}_0 \left(\frac{\tau_e^{(\alpha)}}{\tau_0} \right)^{1/m}, \tag{10}$$

where $\dot{\gamma}_0$ is the reference slip rate, m is the viscoplastic exponent and τ_0 is the slip resistance.

2.3 Periodic voided crystal

A sketch of a crystal with a cubic distribution of rectangular voids with a spacing d and $d \tan \phi^{(1)}$ in the x_1 and x_2 directions, respectively is shown in Fig. 1a. The voided crystals have a volume fraction v_{f} of voids and here we analyse their response by considering a rectangular unit of dimension $d \times d \tan \phi^{(1)}$. The aspect ratio of the unit cell ensures periodicity of the motion of the discrete dislocations on discrete slip planes, i.e. dislocations exiting from one side of the unit cell can re-enter from the corresponding point on the opposite side. The rectangular void (occupying a volume fraction v_f) is centrally located in the unit cell. For simplicity, we restrict attention to the case where the void has the same aspect ratio as the unit cell. The length d which defines the void spacing in the crystal was varied between $0.5\,\mu$m and $8\,\mu$m in the discrete dislocation calculations.

Loading of the voided crystal is simulated by imposing periodic boundary conditions on the unit cell edges as

$$\Delta u_i = \bar{\epsilon}_{ij} \Delta x_j, \tag{11}$$

where Δu_i is the difference between displacements on opposite sides of the unit cell specified by the difference in position vector Δx_j while $\bar{\epsilon}_{ij}$ is the imposed macroscopic strain. Traction free boundary conditions are imposed on the surfaces of the void (including $r^{(\alpha)} = 0$ in the strain gradient plasticity calculation).

In the discrete dislocation plasticity calculations, the individual dislocation fields are the analytically known fields for dislocations in an infinite medium. Thus, the ($\tilde{}$) fields are

not periodic and periodicity is enforced via the ($\hat{}$) fields, such that the boundary conditions, eq. (11), are satisfied. In addition, we also impose periodicity on the motion of the dislocations, i.e. dislocations leaving from one edge re-enter from the opposite edge. This is achieved by removing the exiting dislocation from the calculation (while retaining its contribution to slip) and re-inserting a new dislocation at the corresponding point on the opposite side of the unit cell. It is worth emphasising here that consistent with the $r^{(\alpha)} = 0$ boundary condition employed on teh void surfaces in the strain gradient plasticity calculations, dislocations are assumed to be free to exit the crystal from the traction free surfaces of the void. Similarly, in the strain gradient plasticity calculations, in addition to the periodic displacement fields given by eq. (11), periodicity for the slip rates is also enforced, i.e. nodal degrees of freedom are eliminated to ensure that slip rates at corresponding points on opposite sides of the unit cell are equal.

Two types of loadings are considered here: (i) shear loading (Fig. 1b) and (ii) equi-biaxial straining (Fig. 1c). In shear, the strain components in eq. (11) are specified as $\bar{\epsilon}_{12} = \bar{\epsilon}_{21} = \gamma/2$ and $\bar{\epsilon}_{11} = \bar{\epsilon}_{22} = 0$, where γ the applied shear strain. The work-conjugate applied shear stress is then

$$\tau = \frac{1}{2d^2 \tan\phi^{(1)}} \int_C (T_1 x_2 + T_2 x_1) dC, \tag{12}$$

where $T_i = \sigma_{ij} n_j$ is the traction on the boundary C of the unit cell with n_j the outward unit normal. Under equi-biaxial straining we specify $\bar{\epsilon}_{12} = \bar{\epsilon}_{21} = 0$ and $\bar{\epsilon}_{11} = \bar{\epsilon}_{22} = \epsilon_v/2$, where ϵ_v is the imposed two-dimensional volumetric strain. The work-conjugate applied equi-biaxial stress is then calculated as

$$\sigma = \frac{1}{2d^2 \tan\phi^{(1)}} \int_C (T_1 x_1 + T_2 x_2) dC. \tag{13}$$

A time step of $\Delta t = 0.5\,\mathrm{ns}$ is needed to resolve the dislocation dynamics so rather high loading rates, $\dot{\gamma} = \dot{\epsilon}_{\mathrm{v}} = 1000\,\mathrm{s}^{-1}$, were used in the discrete dislocation calculations, while more realistic loading rates $\dot{\gamma} = \dot{\epsilon}_{\mathrm{v}} = 10^{-3}\,\mathrm{s}^{-1}$ were employed in the strain gradient calculations. Material parameters are chosen (see Section 2.4) such that the crystal exhibits only a small rate sensitivity and hence the results from the discrete dislocation and strain gradient plasticity simulations are comparable even though the applied strain rates in the two formulations differ considerably. The finite element computations of the ($\hat{}$) fields in the discrete dislocation calculations were performed using bilinear elements (54×76 elements for all d values in both the shear and equi-biaxial loading calculations) while in the strain gradient calculations special elements (48×64 and 36×48 elements in the shear and equi-biaxial loading calculations, respectively) with an 8-node quadratic displacement

interpolation and a 4-node bilinear slip rate interpolation were employed; see Borg (2006) for details of the numerical scheme employed in the strain gradient plasticity calculations.

2.4 Material properties: discrete dislocation plasticity

We first describe the material property set used in the discrete dislocation calculations and the resulting stress versus strain response of the single crystal with no voids. The responses of the unvoided crystals are then used to motivate the material property set for the strain gradient plasticity model.

Crystals with two and three active slip systems were considered here. These crystals were elastically isotropic with Young's modulus $E = 70\,\text{GPa}$ and Poisson's ratio $\nu = 0.33$. The crystals were initially stress- and dislocation-free. Dislocation sources were randomly distributed on the slip planes spaced $100b$ apart, with a density ρ_{nuc}. Each source is randomly assigned a nucleation strength from a Gaussian distribution with average $\bar{\tau}_{\text{nuc}} = 50\,\text{MPa}$ and standard deviation $\Delta\tau_{\text{nuc}} = 1.0\,\text{MPa}$; the nucleation time $t_{\text{nuc}} = 10\,\text{ns}$ for all sources. The magnitude of the Burgers vectors is taken to be $b = 0.25\,\text{nm}$ for all dislocations. The drag coefficient for dislocation motion is $B = 10^{-4}\,\text{Pa s}$ and the annihilation distance is $L_e = 6b$. Obstacles of strength $\tau_{\text{obs}} = 150\,\text{MPa}$ are randomly distributed with a density $\rho_{\text{obs}} = 2\rho_{\text{nuc}}$.

The aim of this study is to investigate size effects in voided crystals. In the limit of no voids, the infinite crystal is expected to have a macroscopically homogeneous response and hence not exhibit size effects. In order to investigate the size effect in voided crystals for void spacings in the range $0.5\,\mu\text{m} \leq d \leq 8.0\,\mu\text{m}$, it is essential that the corresponding unit cells with no voids display no size effects. Here we choose the appropriate values of the source and obstacle densities so as to ensure that unvoided crystals with unit cells of size $0.5\,\mu\text{m} \leq d \leq 8.0\,\mu\text{m}$ give statistically indentical responses. The predicted shear stress τ versus strain γ responses of the unvoided three slip system crystal for $\rho_{\text{nuc}} = 300\,\mu\text{m}^{-2}$ are plotted in Fig. 2a for the choices $d = 0.5\,\mu\text{m}$, $2\,\mu\text{m}$ and $8\,\mu\text{m}$. Over the range of unit cell sizes of interest, we observe that the shear response is reasonably size independent. To emphasise the effect of source density in enabling us to achieve a size independent response over the range $0.5\,\mu\text{m} \leq d \leq 8.0\,\mu\text{m}$, the predicted normalised shear flow strength $\tau_{\text{f}}/\tau_{\text{nuc}}$ (τ_{f} is defined as the average shear stress over the shear strain range $0.0075 \leq \gamma \leq 0.01$) is plotted in Fig. 2b as a function of ρ_{nuc} for selected values of d. It is

evident that only for $\rho_{\text{nuc}} > 150\,\mu\text{m}^{-2}$, the predicted responses are reasonably independent of d. All calculations presented subsequently use source and obstacle densities $300\,\mu\text{m}^{-2}$ and $600\,\mu\text{m}^{-2}$, respectively. A similar study also confirmed that the shear response of the unvoided two slip system crystal is also independent of d for $\rho_{\text{nuc}} = 300\,\mu\text{m}^{-2}$.

2.5 Material properties: strain gradient plasticity

The material properties in the strain gradient plasticity calculations were chosen to closely mimic those used in the discrete dislocation plasticity calculations. The elastic properties and crystallographic orientations were chosen to be identical to those in the discrete dislocation model. However, the plasticity parameters which include the strain rate hardening constants and the material length scale, do not have a clear analog in the material parameter set used in the discrete dislocation calculations. We determined the appropriate plasticity constants in the strain gradient plasticity model as follows.

The discrete dislocation calculations of the unvoided three slip system crystals predict a size independent non-hardening shear response with a shear yield strength of 30 MPa. We thus calibrated the plastic properties in the size independent limit ($l_S = 0$) of the strain gradient model to obtain this shear response, i.e. we set the slip system strength $\tau_0 = 30\,\text{MPa}$, the viscoplastic exponent $m = 0.02$ and the reference slip rate $\dot{\gamma}_0 = 10^{-3}\,\text{s}^{-1}$ in all the strain gradient calculations presented here. Subsequently, we shall show that a choice $l_S = 0.325\,\mu\text{m}$ gives good agreement between the discrete dislocation and strain gradient plasticity predictions for all crystallographic geometries, void volume fractions and loading configurations considered. In the following we present results over a range of d/l_S values such that, with $l_S = 0.325\,\mu\text{m}$, the strain gradient calculations correspond exactly to the voided crystals analysed using the discrete dislocation formulation.

3 Numerical results for the voided crystals

Numerical predictions for the shear response of voided two and three slip system crystals with $v_{\text{f}} = 1$ % and 4 % are presented in Section 3.1. In Section 3.2, these results are contrasted with the equi-biaxial straining response of the $v_{\text{f}} = 4$ % three slip system crystals.

3.1 Shear loading

Discrete dislocation plasticity predictions of the normalised shear stress $\tau/\tau_{\rm nuc}$ versus strain γ response of the $v_f = 4$ % three slip system crystals are plotted in Fig. 3a for four values of the void spacing d. The voided crystals display an ideally plastic response with $\tau/\tau_{\rm nuc} \approx 0.6$: taking into account the inherent variability in the discrete dislocation predictions (Needleman et al., 2006), no clear size effect is observed over the range values of d analysed. Consistent with these stress histories, the associated evolution of the dislocation density $\rho_{\rm dis}$ with γ (Fig. 3b) also displays only a small size dependence. The corresponding strain gradient plasticity predictions of the $\tau/\tau_{\rm nuc}$ versus γ response are included in Fig. 3c for values of d/l_S in the range $1.54 \leq d/l_S \leq \infty$. While $d/l_S = \infty$ corresponds to the conventional length scale independent continuum crystal plasticity limit, we shall see subsequently that the other values of d/l_S shown in Fig. 3c are representative of the discrete dislocation predictions plotted in Fig. 3a. Similar to the discrete dislocation results, we observe that the shear flow stress only has a small size dependence over the range of d/l_S values investigated here.

Predicted distributions of the total slip Γ at $\gamma = 0.01$ are shown in Fig. 4 for selected values of d and d/l_S for the discrete dislocation and strain gradient plasticity formulations, respectively. The total slip Γ is defined as

$$\Gamma = \sum_{(\alpha)} |\gamma^{(\alpha)}|, \tag{14a}$$

where the slip $\gamma^{(\alpha)}$ in the strain gradient calculations is the accumulated plastic slip on each slip plane, whereas in the discrete dislocation calculation it is defined as

$$\gamma^{(\alpha)} = s_i^{(\alpha)} \epsilon_{ij} m_j^{(\alpha)}. \tag{14b}$$

In discrete dislocation plasticity, the calculation of $\gamma^{(\alpha)}$[1] involves averaging the displacement jumps across the slip planes by first evaluating the displacements u_i on the finite element mesh and then obtaining the strain field $\epsilon_{ij} = (u_{i,j} + u_{j,i})/2$ by numerical differentiation. Thus, the numerical values of Γ in the Figs. 4a and 4b are mesh size dependent while the strain gradient plasticity results in Figs. 4c-d are mesh size independent. Thus, comparisons between the discrete dislocation and strain gradient plasticity predictions in Fig. 4 should

[1]The quantity $\gamma^{(\alpha)}$ in the discrete dislocation calculations is not the actual slip on slip plane (α) as it includes not only small contributions from the elastic strains but also some contributions from dislocations gliding on all slip systems.

be restricted to the qualitative nature of the distributions of Γ rather than precise numerical comparisons. Both the discrete dislocation and strain gradient plasticity formulations predict that plastic slip localises on the $\phi^{(3)} = 0^\circ$ slip planes intersecting the void. As negligible strain gradients are developed along the slip planes, both the discrete dislocation and strain gradient formulations predict negligible size effects in the shear response of the voided crystals. The corresponding distributions of the lattice rotations Ω are plotted in Fig. 5. In the discrete dislocation calculations the lattice rotation is obtained via the relation

$$\Omega = \frac{1}{2}\left(\hat{u}_{2,1} + \tilde{u}_{2,1} - \hat{u}_{1,2} - \tilde{u}_{1,2}\right), \tag{15a}$$

with the spatial derivatives of the ($\tilde{}$) displacement fields calculated analytically so as to ensure that slip is not included. Analogously, the lattice rotations in the strain gradient crystal plasticity model are obtained by excluding the plastic rotations from the material rotations as

$$\Omega = \frac{1}{2}\left(u_{2,1} - u_{1,2}\right) - \frac{1}{2}\sum_{(\alpha)} \gamma^{(\alpha)} \left(s_2^{(\alpha)} m_1^{(\alpha)} - s_1^{(\alpha)} m_2^{(\alpha)}\right). \tag{15b}$$

The discrete dislocation and strain gradient calculations both predict spatial gradients in the lattice rotations Ω for all cases considered here including the size independent limit of the strain gradient calculations ($d/l_S = \infty$). These spatial gradients indicate the storage of geometrically necessary dislocations (Nye, 1953; Ashby, 1970) even though the τ versus γ response is reasonbaly size independent. We note that the large lattice rotations immediately above and below the void in the discrete dislocation predictions are indicative of the formation of a kink-band on the $\phi^{(3)} = 0^\circ$ planes. The strength of this kink band seems to increase with increasing d.

The size dependence of the shear responses of the voided crystals are summarised in Fig. 6. Results are presented for voided two and three slip system crystals with $v_\mathrm{f} = 1$ % and 4 %. The size dependence is quantified in terms of the flow stress τ_f and the average dislocation density ρ_f, defined as the average values of τ and ρ_dis, respectively over the strain range $0.0075 \leq \gamma \leq 0.01$. Discrete dislocation predictions of τ_f and ρ_f versus d are plotted in Figs. 6a and 6b, respectively while the strain gradient plasticity predictions of τ_f versus d/l_S are included in Fig. 6c. The discrete dislocation predictions are averages over four realisations of source and obstacle distributions and the error bars marked in Figs. 6a and 6b indicate the variations over these realisations. Since the $\phi^{(3)}$ planes of the three slip system crystal are aligned with the applied shear stresses, these voided crystals have a lower flow strength compared to the two slip system voided crystals. Further, consistent with expectations, the $v_f = 1$ % crystals have a higher flow strength compared to the 4 %

crystals. Over the range of d values considered here, both the discrete dislocation plasticity and strain gradient plasticity formulations predict a negligible size dependence of $\tau_{\rm f}$. In line with these predictions, the discrete dislocation plasticity calculations also indicate that the dislocation density $\rho_{\rm f}$ is not strongly dependent on d.

While no qualitative differences between responses of the two and three slip voided crystals were predicted in the calculations reported above, it is worth mentioning that the discrete dislocation predictions of the dislocation distributions in these two cases are markedly different. The dislocation distributions at $\gamma = 0.01$ in the $d = 4.0\,\mu$m voided two and three slip system voided crystals ($v_f = 4$ %) are plotted in Figs. 7a and 7b, respectively. While the two slip system voided crystal has a reasonably uniform dislocation distribution throughout the unit cell, dislocations in the three slip system crystal are localised on a cross centred at the void with the remaining unit cell reasonably dislocation free. These differences are rationalised by recalling that with the $\phi^{(3)} =^\circ$ slip planes aligned with the shearing directions in the three slip system crystal, deformation preferentially occurs by the formation of slip bands along the 0° planes intersecting the void and by the formation of a kink band (see the lattice rotation distributions in Fig. 5) on the 0° planes immediately above and below the void. On the other hand, deformation in the two slip system crystals is more uniform with the crystals undergoing symmetric double slip.

3.2 Equi-biaxial straining

Over the length scale considered here, both the discrete dislocation and strain gradient plasticity formulations predict negligible size effects for voided crystals subjected to shear. We proceed to consider the other extreme loading case of equi-biaxial straining of the voided crystals. For the sake of brevity, attention is restricted to the $v_{\rm f} = 4$ % three slip system crystals.

Discrete dislocation plasticity predictions of the biaxial stress σ and dislocation density $\rho_{\rm dis}$ versus strain $\epsilon_{\rm v}$ responses of the voided crystals are plotted in Figs. 8a and 8b, respectively. Predictions are shown for length scales in the range $0.5\,\mu{\rm m} \leq d \leq 4.0\,\mu{\rm m}$. Note that the $d = 8.0\,\mu$m predictions are omitted here as the biaxial straining calculations for the large unit cells are prohibitively time-consuming. Unlike the shear loading case, a distinct size effect in the σ versus $\epsilon_{\rm v}$ response is observed with the strength of the voided crystals increasing with decreasing d. Moreover, unlike under shear loading the crystals display a

hardening response at least for the smaller values of d considered here. While the strength of the crystals displays a strong size dependence, no clear trend is observed in the variation of ρ_{dis} with d (Fig. 8b). The corresponding strain gradient plasticity predictions of the σ versus ϵ_{v} response are plotted in Fig. 8c. These responses are qualitatively similar to the discrete dislocation predictions over the range of d/l_S values considered here and confirm that the non-hardening response is recovered in the size independent limit $d/l_S = \infty$.

Discrete dislocation (Figs. 9a and 9b) and strain gradient plasticity (Figs. 9c-e) predictions of the distributions of the total slip Γ indicate that under biaxial straining, spatial gradients in the slip magnitude develop along the active slip planes. Thus, unlike under shear loading, these gradients give rise to hardening due to the presence of geometrically necessary dislocations and the consequent size effects in the responses plotted in Figs. 8a and 8c. The strain gradient plasticity calculations clearly show that higher gradients in Γ are present for smaller values of d/l_S, which give rise to the increased strength with decreasing d.

The discrete dislocation and strain gradient plasticity predictions of the size effects under equi-biaxial straining are summarised in Figs. 10a and 10b, respectively. Similar to the shear loading case, the results are summarised in terms of the flow strength σ_{f} and corresponding dislocation density ρ_{f} defined as the average values of σ and ρ_{dis} over the range $0.0075 \leq \epsilon_{\text{v}} \leq 0.01$. Moreover, the discrete dislocation results plotted in Fig. 10a are averages over four realisations of source and obstacle distributions with the error bars showing the ranges of σ_{f} and ρ_{f} obtained in these calculations. Both the discrete dislocation and strain gradient plasticity calculations predict a strong size effect in the flow strength with σ_{f} decreasing with increasing d over the entire range of void spacings considered here. However, such a clear size dependence is not observed in the discrete dislocation predictions of ρ_{f}: we conclude that while the density of geometrically necessary dislocations increases with decreasing d, an interplay between the statistical and geometrically necessary dislocation densities means that this trend is not reflected in the variation of the total dislocation density ρ_{f} with d.

4 Comparison between the discrete dislocation and strain gradient plasticity predictions

While qualitative comparisons between discrete dislocation and strain gradient plasticity predictions are shown above, quantitative comparisons require that the length scale l_S be specified explicitly in the strain gradient plasticity calculations. Comparisons between the discrete dislocation and strain gradient plasticity predictions of $\tau_{\rm f}$ and $\sigma_{\rm f}$ with void spacing d are shown in Fig. 11a for the $v_{\rm f} = 4$ % three slip system crystals and the choice $l_S = 0.325\,\mu$m. Similar comparisons are shown in Fig. 11b for the shear loading of the $v_f = 1$ % and 4 % two slip system crystals again with the choice $l_S = 0.325\,\mu$m. With this choice of l_S, excellent agreement is obtained between the discrete dislocation and strain gradient plasticity predictions for both shear and equi-biaxial straining of all the voided crystals considered here. To illustrate the scaling of the strengths with the void spacing d we fit relations of the form

$$\tau_{\rm f} = k\left(\frac{d}{d_{\rm ref}}\right)^{-n} + \tau_\infty, \tag{16a}$$

and

$$\sigma_{\rm f} = k\left(\frac{d}{d_{\rm ref}}\right)^{-n} + \sigma_\infty, \tag{16b}$$

to strain gradient plasticity predictions of the shear and equi-biaxial flow strengths in Fig. 11. In eq. (16), $d_{\rm ref} = 1\,\mu$m and k are the reference structural length and strength, respectively, τ_∞ and σ_∞ are the strain gradient plasticity predictions of the flow strength in the limit $d/l_S \to \infty$ (i.e. the conventional length scale independent crystal plasticity limit) and n is an exponent characterising the sensitivity of the flow strength to the void spacing d. Least-squares fits to the strain gradient plasticity predictions using eq. (16) are included in Fig. 11 with the corresponding constants listed in Table 1. These fits indicate that while under equi-biaxial loading the flow strength $\sigma_{\rm f}$ exhibits approximately an inverse scaling with d ($n \approx 1.0$), under shear loading the size effect is significantly weaker with $n \approx 0.2$.

Note that with $l_S = 0.325\,\mu$m, the $d/l_S = 3.08$ and 12.31 strain gradient plasticity results in Figs. 4, 5 and 9 correspond to $d = 1\,\mu$m and $4.0\,\mu$m, respectively and thus can be directly compared with the discrete dislocation predictions in the corresponding figures. The comparisons presented in this work indicate that the discrete dislocation and strain gradient plasticity predictions of the responses of the voided crystals compare favourably

not only in terms of the flow strengths but also in terms of the distributions of the total slip Γ though there is some discrepancies between the discrete dislocation and strain gradient plasticity predictions of the lattice rotations (Fig. 5).

5 Discussion

In plastically deforming crystals, the accumulation, interaction and motion of large numbers of dislocations give rise to complex spatiotemporal dynamics, which may lead to organised dislocation structures including, for example, walls, cells, subgrains and persistent slip bands. The characteristic length scales that are associated with the dislocation patterns lead to the now well-appreciated size dependence of plastic response at the micron scale. Conventional plasticity theories predict a size independent response. A variety of non-local plasticity theories (mainly strain gradient constitutive formulations) have been proposed to account for the observed size dependence of micro-scale plastic flow in crystalline solids, (e.g. Fleck and Hutchinson, 2001; Gurtin, 2002). The physical motivation for these typically stems from accounting, in a phenomenological relation, for the effects of geometrically necessary dislocations, (Nye, 1953; Ashby, 1970). These continuum plasticity models assume that plasticity can occur at any point where the flow criterion is met. However, a necessary criterion for plasticity is that sufficient slip can be produced by the available dislocations. This in turn requires the presence of one or more dislocation sources close to that location – this is not always the case as demonstrated in Needleman et al. (2006). In the discrete dislocation calculations presented here we ensured that source limited plasticity effects were negligible by choosing sufficiently high source and obstacle densities. Thus, the origin of the size effect in the calculations presented here was restricted primarily to geometrically necessary dislocations that the strain gradient plasticity theories attempt to model.

In the discrete dislocation formulation, the shear/tensile responses of the crystals are outcomes of the boundary value problem solution, with the dislocation mobility, source and obstacle strength and density all playing a role in setting the yield strength and hardening rates. Here we calibrated the size independent hardening response in the strain gradient plasticity model from the discrete dislocation predictions of the shear response of the unvoided crystals. Good agreement between the discrete dislocation and strain gradient plasticity predictions was obtained with the choice of the material length scale $l_S = 0.325\,\mu$m

in the strain gradient plasticity model. This material length scale corresponds to roughly ten times the slip plane spacing in the discrete dislocation and is consistent with the active slip band spacing found in the discrete dislocation calculations (Figs. 4 and 9). It is worth noting that similar to the findings reported here, Shu et al. (2001) also found good agreement between discrete dislocation and strain gradient predictions of the simple shear response of a constrained strip with the choice of a material length scale approximately ten times the slip plane spacing.

Fleck and Hutchinson (2001) have argued that at least two distinct material length parameters must be introduced in any phenomenological gradient plasticity theory, one parameter characterising problems for which stretch gradients are dominant and the other relevant to problems when rotation gradients (or shearing gradients) are controlling. The indentation and void growth problems are similar in that the stretch gradients play the critical role in determining size effects. Begley and Hutchinson (1998) analysed the size dependence of indentation data for different metals of varying hardness to infer that the stretch gradient length scale usually fell within the range between $0.2\,\mu$m and $0.5\,\mu$m. By contrast, the length scale associated with the shearing gradients is critical in the torsion of wires and Fleck et al. (1994) inferred from their experiments that this length scale is approximately $2\,\mu$m for polycrystalline copper. The comparisons between the discrete dislocation and strain gradient plasticity calculations reported here suggest that a single material length scale $l_S = 0.325\,\mu$m is sufficient to give good agreement between the two sets of simulations for both shear and equi-biaxial loading of a voided crystal. This length scale is in broad agreement with the stretch length scales inferred by Begley and Hutchinson (1998).

6 Concluding remarks

We have carried out plane strain analyses of the shear and equi-biaxial loading responses of periodic voided crystals employing both discrete dislocation plasticity and continuum strain gradient crystal plasticity formulations. The general features that emerge from our analyses include:

- Under shear loading, the formation of strong slip bands reduces the slip gradient along the slip planes in both the discrete dislocation and strain gradient plasticity formulations. Thus, both theories predict a non-hardening response with small size

effects.

- By contrast, under equi-biaxial straining, both formulations predict a strong size dependence with the flow strength displaying approximately an inverse scaling with the void spacing d.

- Excellent agreement between the strain gradient plasticity and discrete dislocation predictions is obtained for all loading cases, crystal types and void volume fractions considered here. This agreement is obtained when the material length scale l_S in the strain gradient formulation is set to approximately ten times the slip plane spacing in the discrete dislocation model.

Acknowledgments

MIH and VSD acknowledge support from the Engineering and Physical Sciences Research Council (EPSRC), UK. The work of UB and CFN is financially supported by the Danish Technical Research Council in a project entitled Modeling Plasticity at the Micron Scale.

References

Ashby, M. F. (1970). The deformation of plastically non-homogeneous materials, *Philosophical Magazine* **21**: 399–424.

Begley, M. R. and Hutchinson, J. W. (1998). The mechanics of size-dependent indentation, *Journal of the Mechanics and Physics of Solids* **46**: 2049–2068.

Borg, U. (2006). Strain gradient crystal plasticity effects on flow localization, *To be published* .

De Guzman, M. S., Neubauer, G., Flinn, P. and Nix, W. D. (1993). The role of indentation depth on the measured hardness of materials, *Materials Research Society Symposium Proceedings*, Vol. 308, pp. 613–618.

Fleck, N. A. and Hutchinson, J. W. (1997). Strain gradient plasticity, *in* J. W. Hutchinson and T. Y. Wu (eds), *Advances in Applied Mechanics*, Vol. 33, Academic Press, New York, pp. 295–361.

Fleck, N. A. and Hutchinson, J. W. (2001). A reformulation of strain gradient plasticity, *Journal of the Mechanics and Physics of Solids* **49**: 2245–2271.

Fleck, N. A., Muller, G. M., Ashby, M. F. and Hutchinson, J. W. (1994). Strain gradient plasticity: Theory and experiment, *Acta Metallurgica et Materialia* **42**: 475–487.

Gurson, A. L. (1977). Continuum theory of ductile rupture by void nucleation and growth: Part I Yield criteria and flow rules for porous ductile media, *Journal of Engineering Materials Technology* **99**: 2–15.

Gurtin, M. E. (2002). A gradient theory of single-crystal viscoplasticity that accounts for geometrically necessary dislocations, *Journal of the Mechanics and Physics of Solids* **50**: 5–32.

Hirth, J. P. and Lothe, J. (1968). *Theory of Dislocations*, McGraw-Hill, New York.

Khraishi, T. A., Khaleel, M. A. and Zbib, H. M. (2001). A parametric-experimental study of void growth in superplastic deformation, *International Journal of Plasticity* **17**: 297–315.

Liu, B., Qiu, X., Huang, Y., Hwang, K. C., Li, M. and Liu, C. (2003). The size effect on void growth in ductile materials, *Journal of the Mechanics and Physics of Solids* **51**: 1171–1187.

Ma, Q. and Clarke, D. R. (1995). Size dependent hardness of silver single crystals, *Journal of Materials Research* **10**: 853–863.

McClintock, F. A. (1968). A criterion for ductile fracture by growth of holes, *Journal of Applied Mechanics* **35**: 363–371.

Needleman, A. (1972). Void growth in an elastic-plastic medium, *Journal of Applied Mechanics* **41**: 964–970.

Needleman, A., Van der Giessen, E. and Deshpande, V. S. (2006). Statistical aspects of discrete dislocation plasticity, *Scripta Materialia* **54**: 729–733.

Nye, J. F. (1953). Some geometrical relations in dislocated crystals, *Acta Metallurgica* **1**: 153–162.

Potirniche, G. P., Horstemeyer, M. F., Wagner, G. J. and Gullett, P. M. (2006). A molecular dynamics study of void growth and coalescence in single crystal nickel, *International Journal of Plasticity* **22**: 257–278.

Rice, J. R. and Tracey, D. M. (1969). On the ductile enlargement of voids in triaxial stress fields, *Journal of the Mechanics and Physics of Solids* **17**: 201–217.

Schlueter, N., Grimpe, F., Bleck, W. and Dahl, W. (1996). Modeling of the damage in ductile steels, *Computational Materials Science* **7**: 27–33.

Shu, J. Y., Fleck, N. A., Van der Giessen, E. and Needleman, A. (2001). Boundary layers in constrained plastic flow: Comparison of nonlocal and discrete dislocation plasticity, *Journal of the Mechanics and Physics of Solids* **49**: 1361–1395.

Taylor, G. I. (1934). The mechanism of plastic deformation of crystals. Part I Theoretical, *Proceedings of the Royal Society of London* **A145**: 362–387.

Tvergaard, V. (1981). Influence of voids on shear band instabilities under plane strain conditions, *International Journal of Fracture* **17**: 389–407.

Tvergaard, V. and Niordson, C. F. (2004). Nonlocal plasticity effects on interaction of different size voids, *International Journal of Plasticity* **20**: 107–120.

Van der Giessen, E. and Needleman, A. (1995). Discrete dislocation plasticity: a simple planar model, *Modelling and Simulation in Materials Science and Engineering* **3**: 689–735.

Wen, J., Huang, Y., Hwang, K. C., Liu, C. and Li, M. (2005). The modified gurson model accounting for the void size effect, *International Journal of Plasticity* **21**: 381–395.

Loading	Material	k (MPa)	n	σ_∞ or τ_∞ (MPa)
Equi-biaxial straining	3 slip systems, $v_\mathrm{f} = 4$ %	99	1.01	88
Shear	3 slip systems, $v_\mathrm{f} = 4$ %	1.6	0.29	23
	2 slip systems, $v_\mathrm{f} = 4$ %	12	0.23	59
	2 slip systems, $v_\mathrm{f} = 1$ %	7.7	0.13	75

Table 1: The parameters used to plot eq. (16) in Fig. 11.

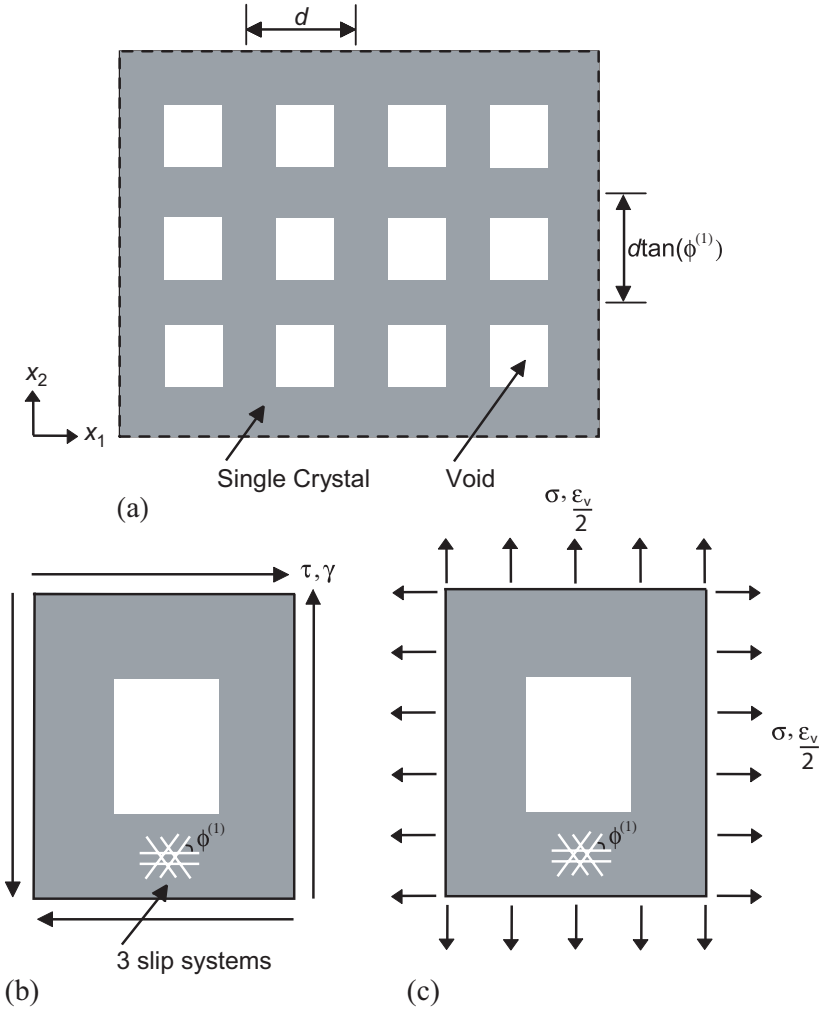

Figure 1: (a) The two-dimensional crystal with a periodic cubic arrangements of rectangular voids. Sketches of the unit cell of the voided crystal subjected to periodic (a) shear loading and (b) equi-biaxial straining.

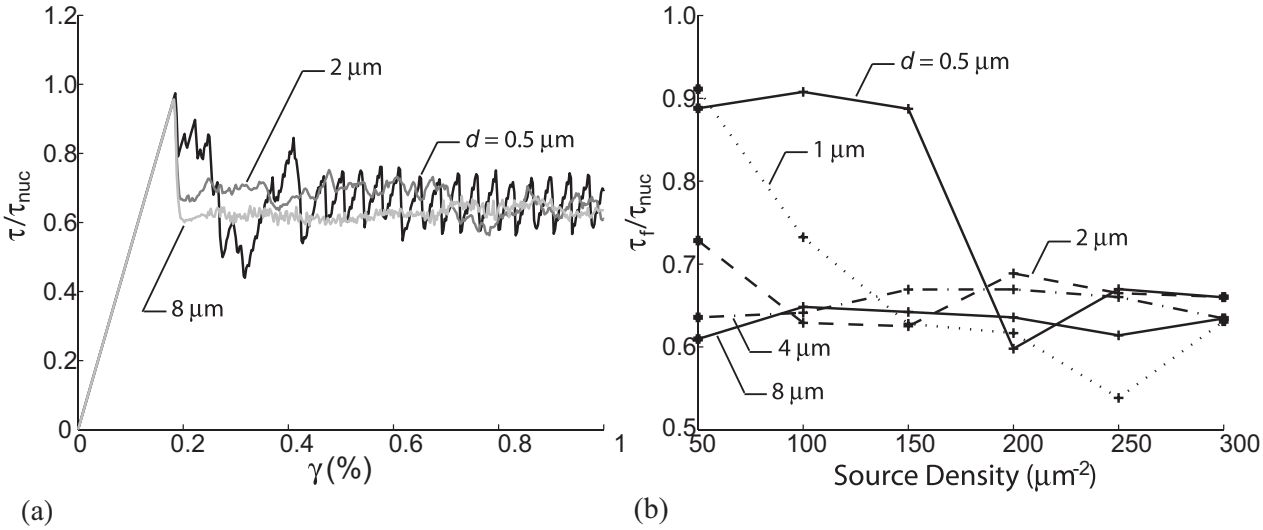

Figure 2: (a) Discrete dislocation predictions of the shear stress τ versus strain γ response of the three slip system single crystal with $\rho_{\text{nuc}} = 300\,\mu\text{m}^{-2}$ and $\rho_{\text{obs}} = 600\,\mu\text{m}^{-2}$. Results are shown for selected values of the unit cell size d. (b) The variation of the shear flow stress τ_{f} of the three slip system single crystals as a function of the source density ρ_{nuc} for selected values of d.

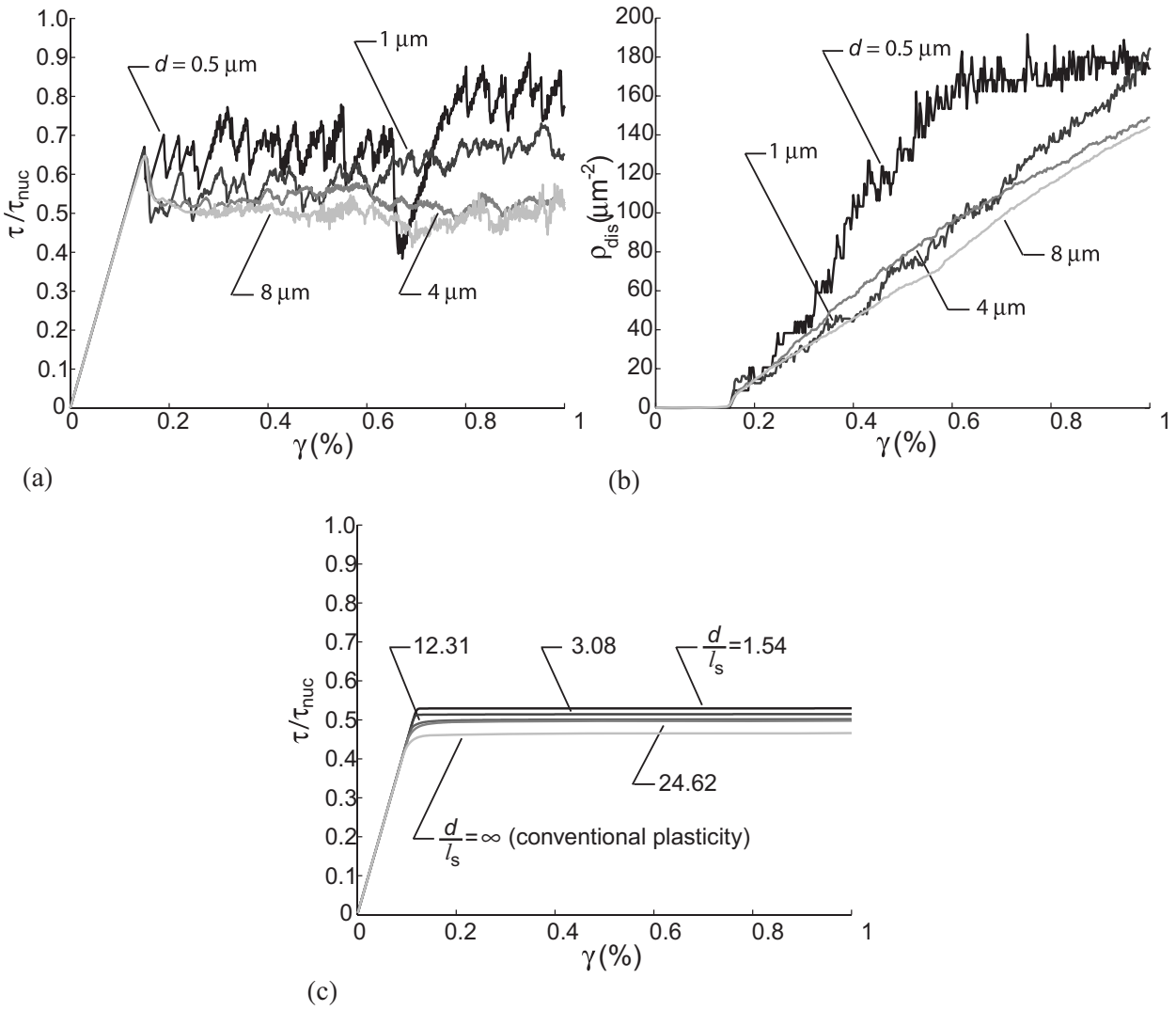

Figure 3: The shear response of the $v_{\mathrm{f}} = 4$ % three slip system voided crystal. Discrete dislocation predictions of the evolution of the (a) shear stress τ and (b) dislocation density ρ_{dis} with shear strain γ for selected values of the void spacing d. (c) Corresponding strain gradient crystal plasticity predictions of the shear stress versus strain response for selected values of the normalised void spacing d/l_S. Predictions of the two formulations are directly comparable with the choice $l_S = 0.325\,\mu$m.

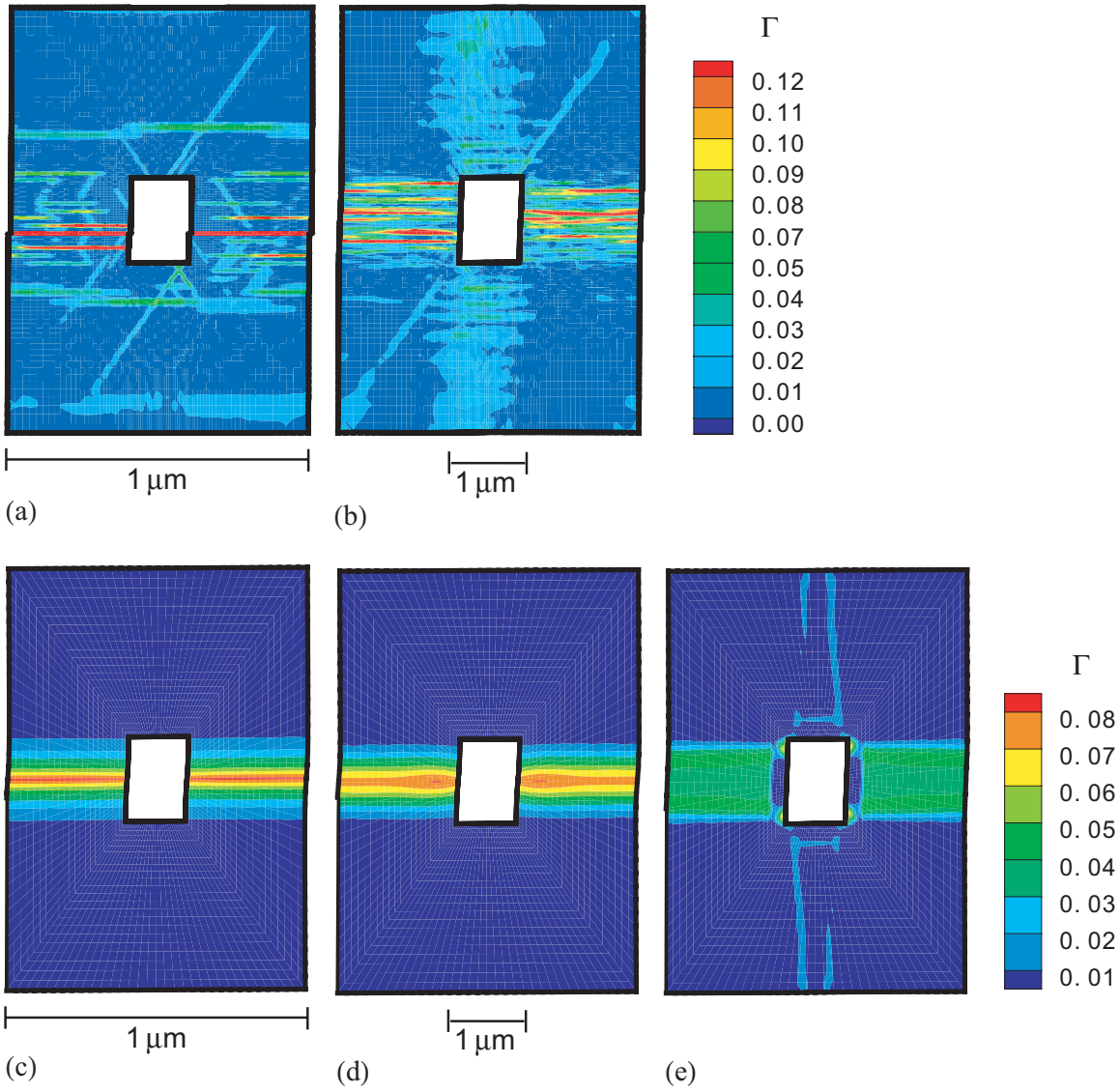

Figure 4: Predictions of the distributions of the total slip Γ in the $v_{\rm f} = 4$ % three slip system voided crystal at an applied shear strain $\gamma = 0.01$. Discrete dislocation plasticity: (a) $d = 1.0\,\mu$m and (b) $d = 4.0\,\mu$m. Strain gradient plasticity: (c) $d/l_S = 3.08$, (d) $d/l_S = 12.31$ and (e) the size independent limit with $d/l_S = \infty$. The scale bars marked in (c) and (d) assume $l_S = 0.325\,\mu$m.

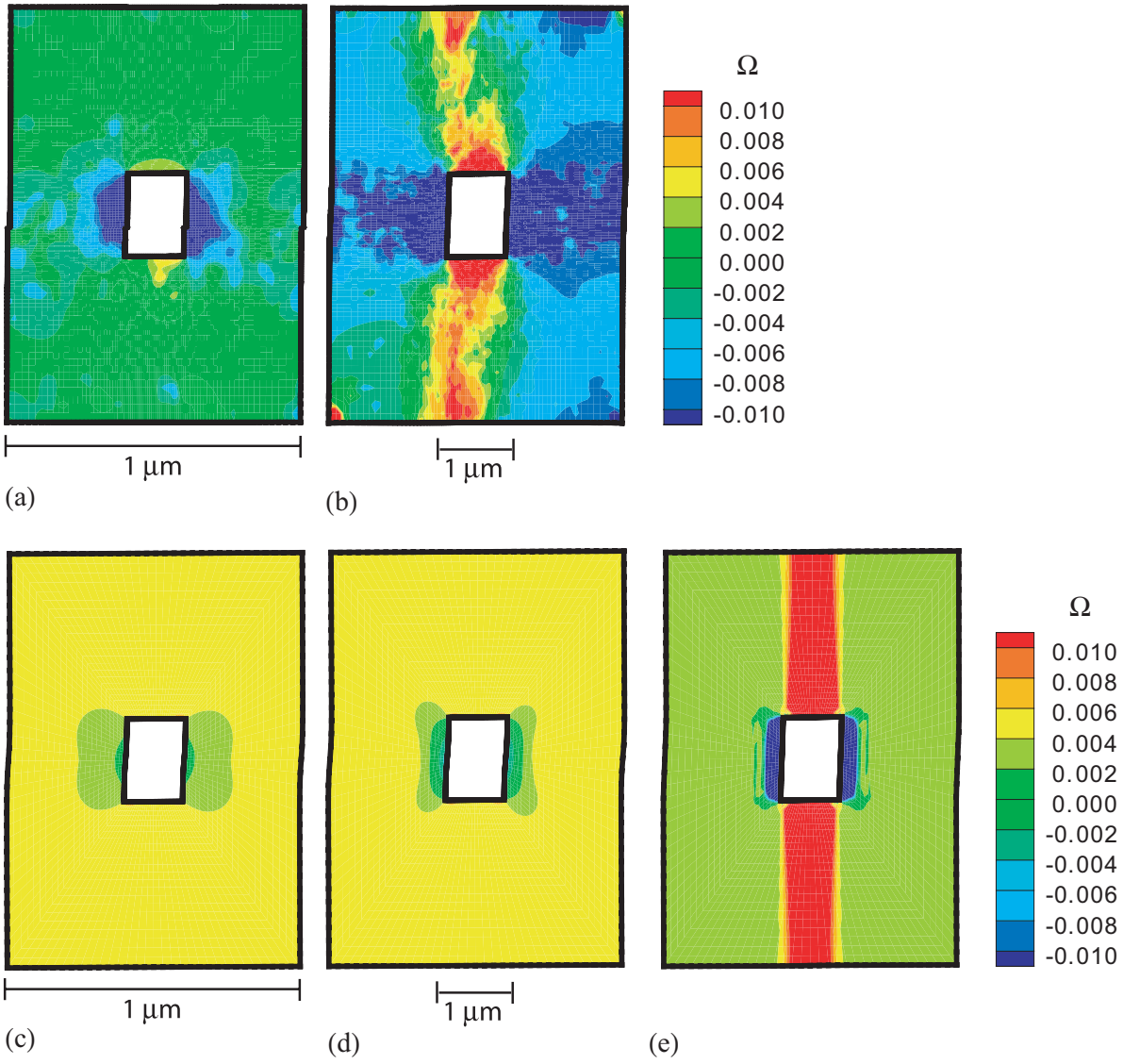

Figure 5: Predictions of the distributions of the lattice rotations Ω in the $v_{\mathrm{f}} = 4\,\%$ three slip system voided crystal at an applied shear strain $\gamma = 0.01$. Discrete dislocation plasticity: (a) $d = 1.0\,\mu$m and (b) $d = 4.0\,\mu$m. Strain gradient plasticity: (c) $d/l_S = 3.08$, (d) $d/l_S = 12.31$ and (e) the size independent limit with $d/l_S = \infty$. The scale bars marked in (c) and (d) assume $l_S = 0.325\,\mu$m.

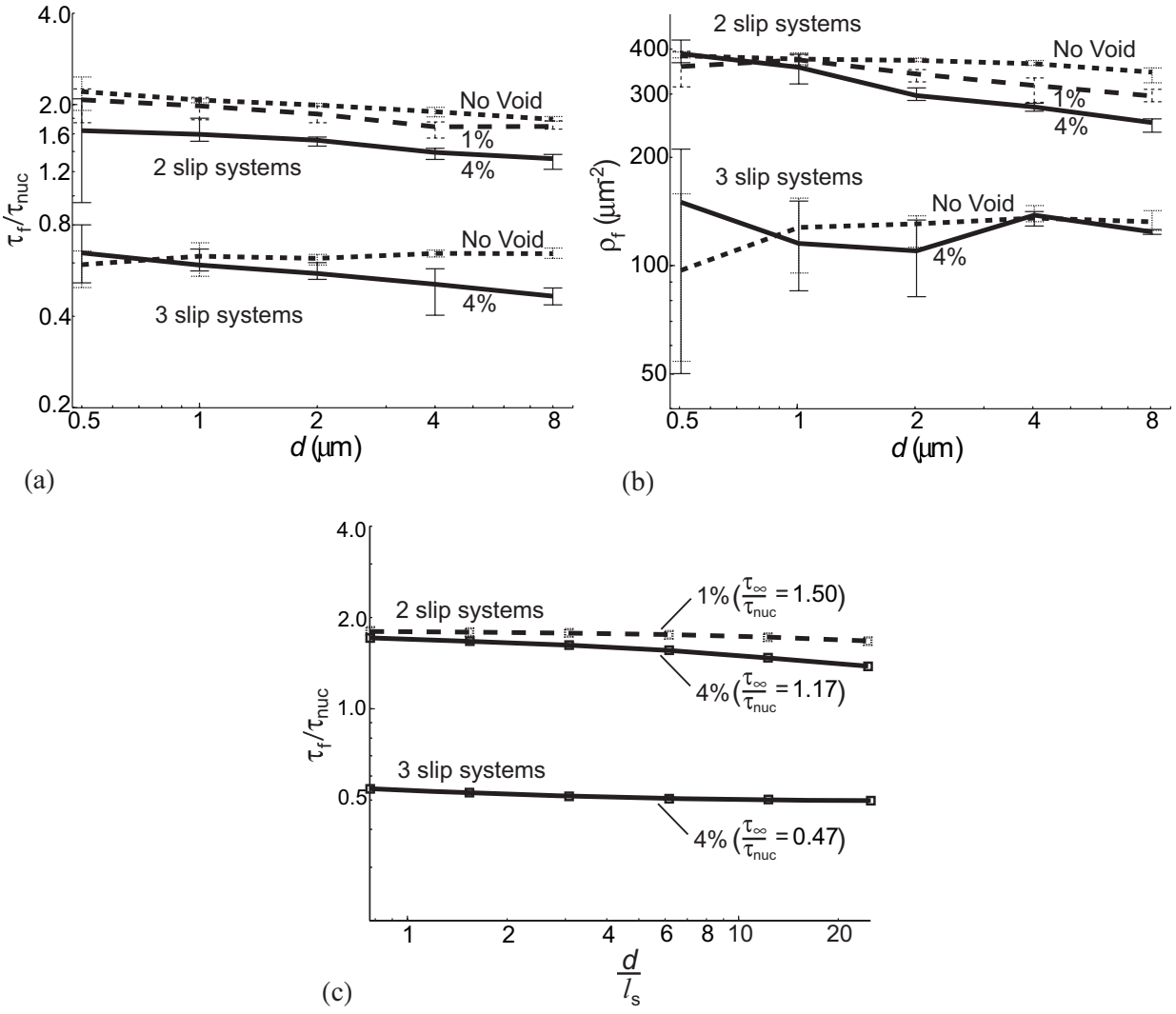

Figure 6: Summary of the predicted size dependence of the shear responses of the $v_{\rm f} = 1$ % and 4 % two and three slip system crystals. Discrete dislocation plasticity: (a) shear flow strength $\tau_{\rm f}$ and (b) corresponding dislocation density $\rho_{\rm f}$ versus void spacing. Strain gradient plasticity: (c) $\tau_{\rm f}$ versus normalised void spacing d/l_S. The flow strength τ_∞ in the size independent limit ($d/l_S = \infty$) is marked in (c) for each case.

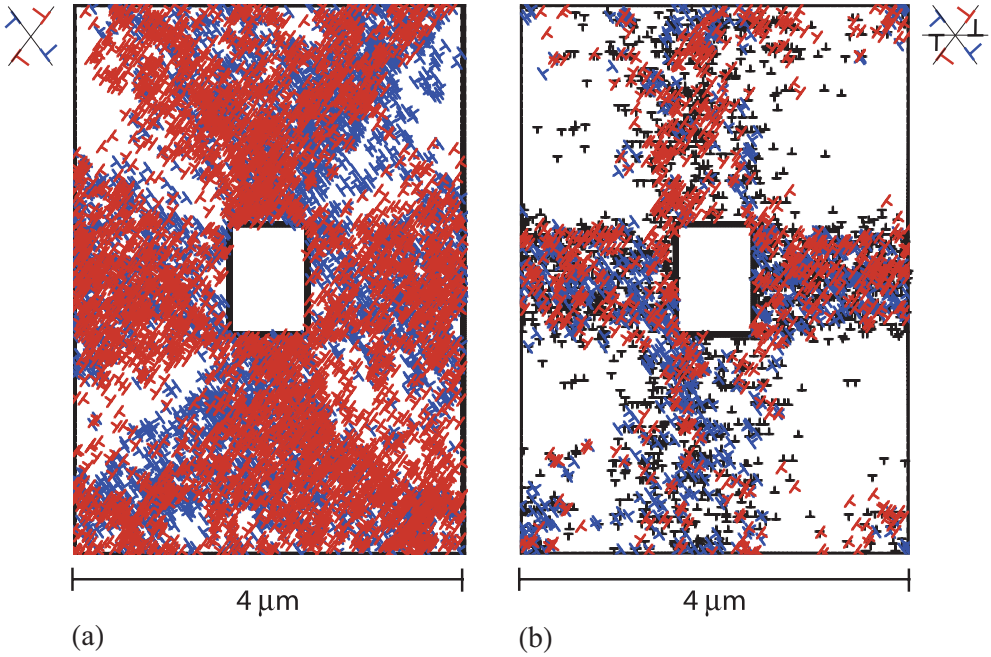

Figure 7: Discrete dislocation plasticity predictions of the dislocation distributions in the (a) two slip system and (b) three slip system crystals ($v_{\mathrm{f}} = 4$ %) at an applied shear strain $\gamma = 0.01$.

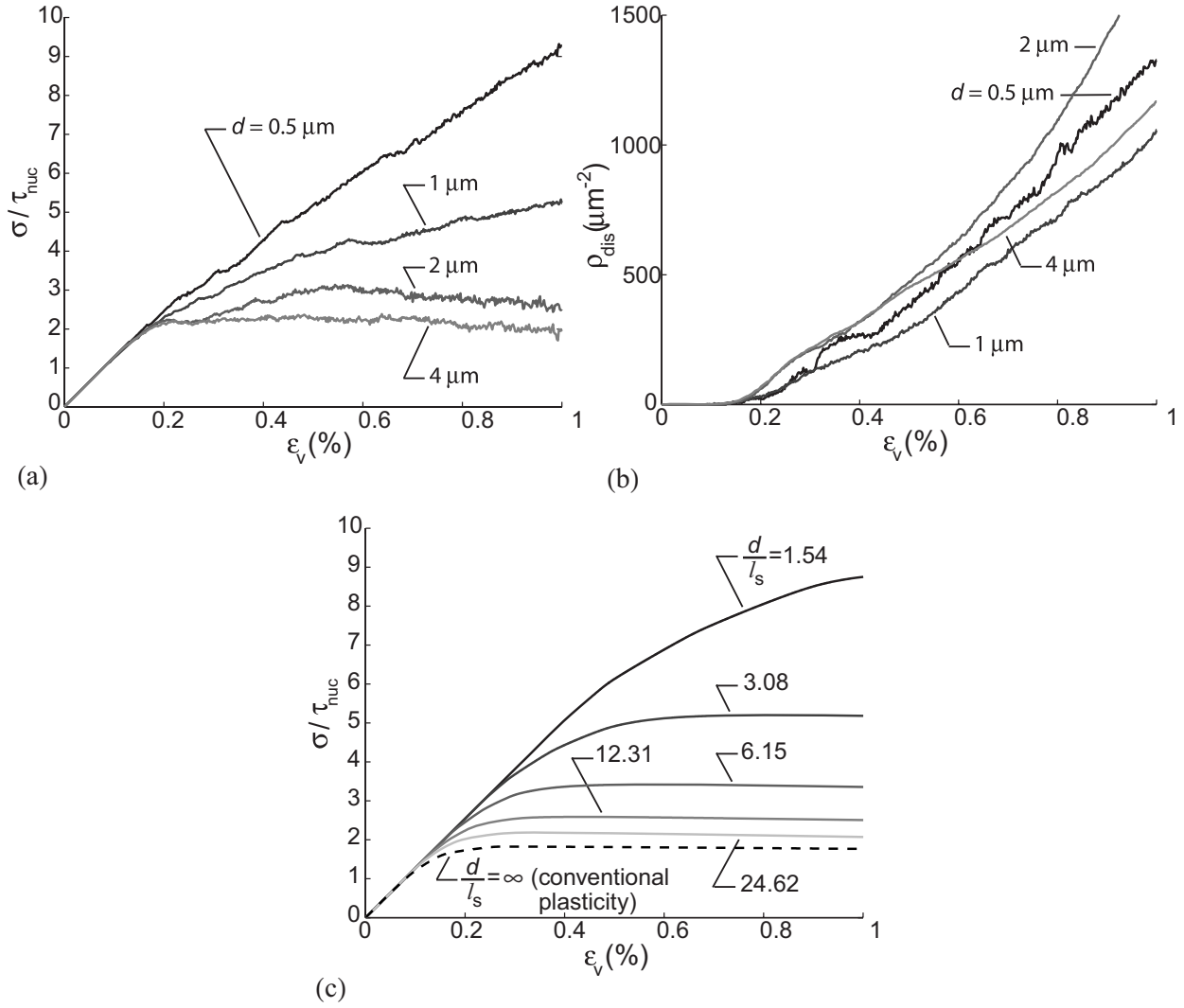

Figure 8: The equi-biaxial straining response of the $v_{\rm f} = 4$ % three slip system crystal. Discrete dislocation predictions of the evolution of the (a) stress σ and (b) dislocation density $\rho_{\rm dis}$ with strain $\epsilon_{\rm v}$ for selected values of the void spacing d. (c) Corresponding strain gradient crystal plasticity predictions of the stress versus strain response for selected values of the normalised void spacing d/l_S. Predictions of the two formulations are directly comparable with the choice $l_S = 0.325\,\mu$m.

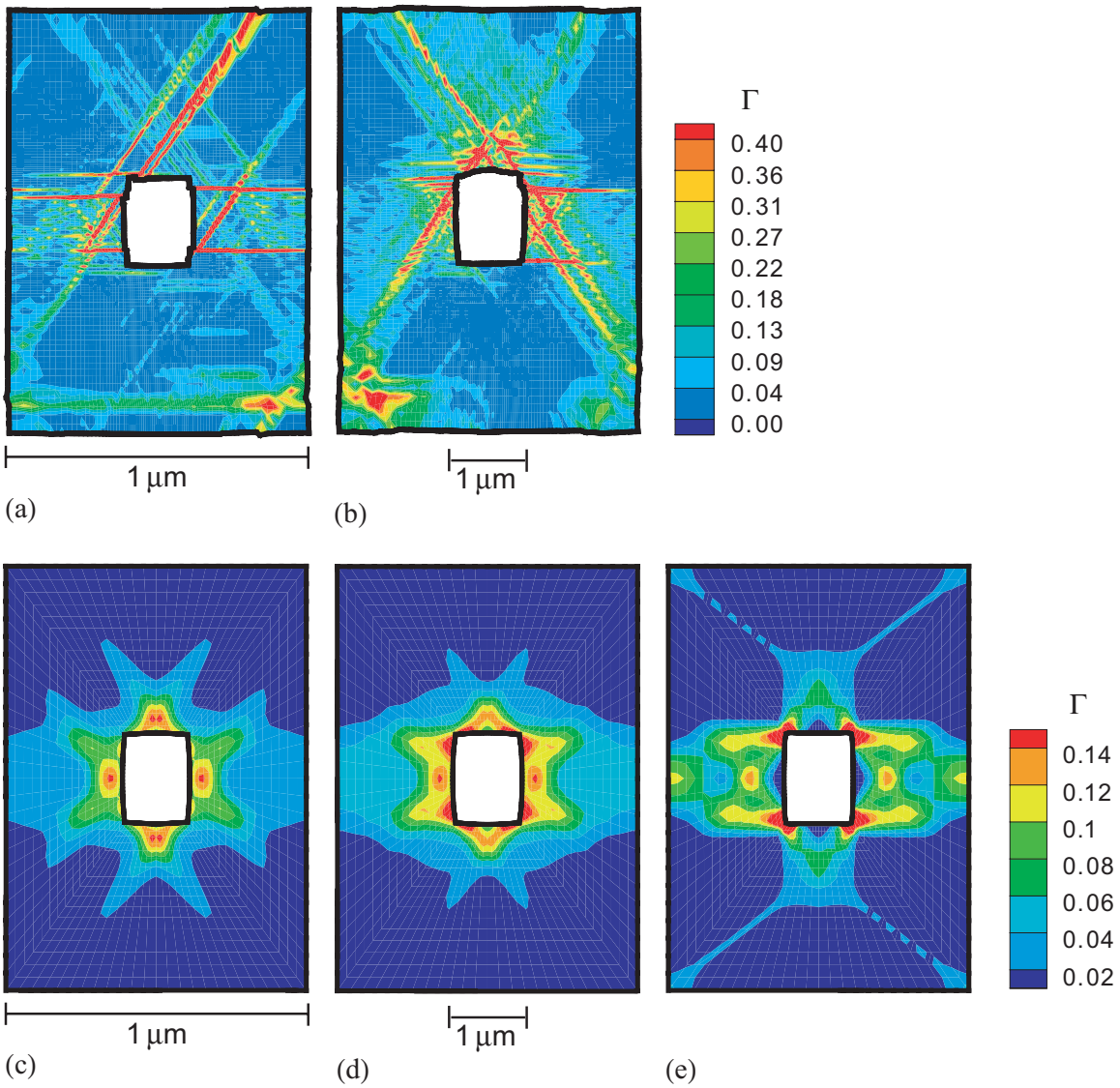

Figure 9: Predictions of the distributions of the total slip Γ in the $v_{\mathrm{f}} = 4$ % three slip system crystal at an applied equi-biaxial strain $\epsilon_{\mathrm{v}} = 0.01$. Discrete dislocation plasticity: (a) $d = 1.0\,\mu$m and (b) $d = 4.0\,\mu$m. Strain gradient plasticity: (c) $d/l_S = 3.08$, (d) $d/l_S = 12.31$ and (e) the size independent limit with $d/l_S = \infty$. The scale bars marked in (c) and (d) assume $l_S = 0.325\,\mu$m.

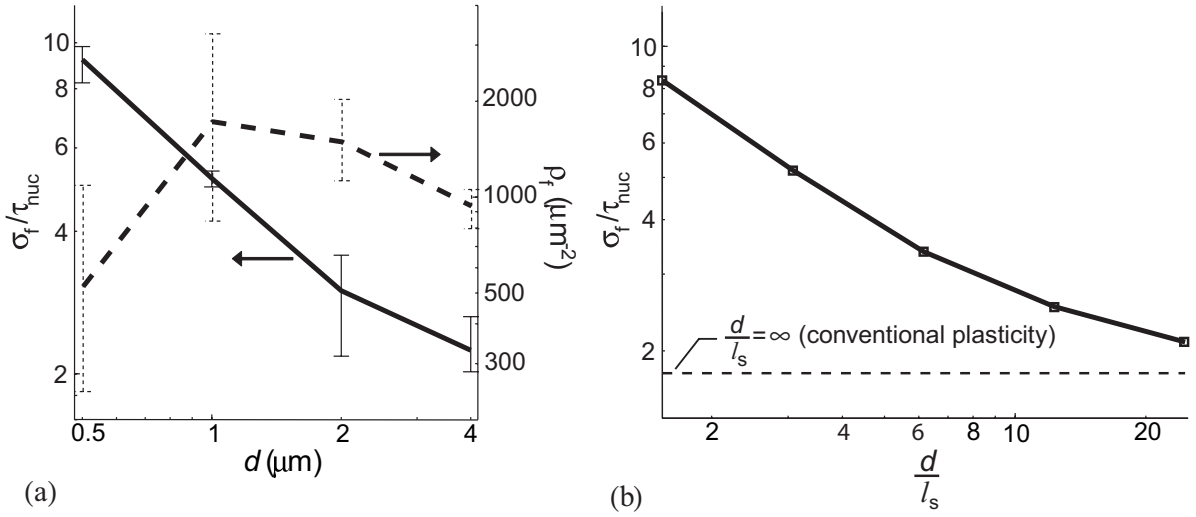

Figure 10: Summary of the predicted size dependence of the equi-biaxial straining response of the $v_f = 4$ % three slip system crystal. Discrete dislocation plasticity: (a) Flow strength σ_f and corresponding dislocation density ρ_f versus void spacing. Strain gradient plasticity: (b) σ_f versus normalised void spacing d/l_S.

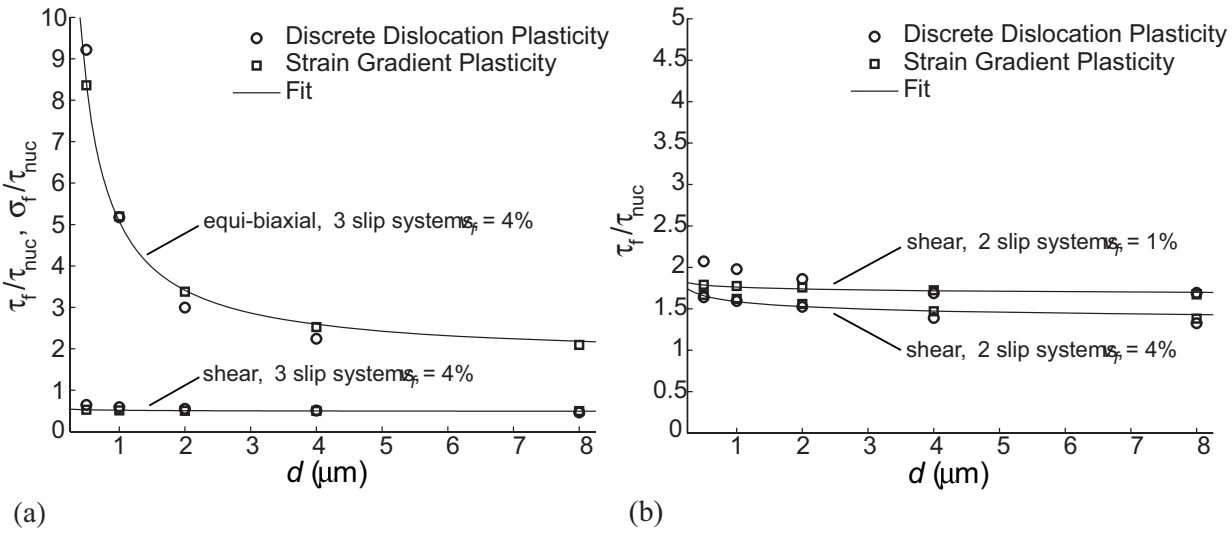

Figure 11: Discrete dislocation and strain gradient plasticity predictions of the variation of the flow strengths of the voided crystals with void spacing d. Results are shown for (a) shear and equi-biaxial flow strengths of the $v_{\rm f} = 4$ % three slip system crystals and (b) the shear flow strengths of the $v_{\rm f} = 1$ % and 4 % two slip system crystals. The material length scale in the strain gradient model is assumed to be $l_S = 0.325\,\mu$m. Fits of the form eq. (16) to the strain gradient plasticity predictions are also included with the constants employed listed in Table 1.